



**HAL**  
open science

# Critical behaviour of superconducting nanowires

Sergei Kozlov

► **To cite this version:**

Sergei Kozlov. Critical behaviour of superconducting nanowires. Superconductivity [cond-mat.supr-con]. Université Paris sciences et lettres, 2024. English. NNT : 2024UPSLS020 . tel-04833415

**HAL Id: tel-04833415**

**<https://pastel.hal.science/tel-04833415v1>**

Submitted on 12 Dec 2024

**HAL** is a multi-disciplinary open access archive for the deposit and dissemination of scientific research documents, whether they are published or not. The documents may come from teaching and research institutions in France or abroad, or from public or private research centers.

L'archive ouverte pluridisciplinaire **HAL**, est destinée au dépôt et à la diffusion de documents scientifiques de niveau recherche, publiés ou non, émanant des établissements d'enseignement et de recherche français ou étrangers, des laboratoires publics ou privés.



**THÈSE DE DOCTORAT**  
**DE L'UNIVERSITÉ PSL**

Préparée à l'École Supérieure de Physique  
et de Chimie Industrielles de la ville de Paris

**Critical Behavior of superconducting nanowires.**  
**Comportement critique des nanofils supraconducteurs.**

Soutenu par

**Sergei Kozlov**

Le 31 janvier 2024

École doctorale n°564

**Physique en Île-de-France**

Spécialité

**Physique**

Préparée au

Laboratoire de Physique et  
d'Étude des Matériaux

Composition du jury :

|  |  |
|--|--|
| Takis KONTOS<br>Directeur de Recherche at CNRS   | <i>Président du jury</i><br><i>Examineur</i> |
| Thierry MARTIN<br>Professeur à Aix-Marseille Université                                  | <i>Rapporteur</i>                            |
| Alejandro SILHANEK<br>Professeur à Université de Liège                                   | <i>Rapporteur</i>                            |
| Julia MEYER<br>Professeure à Université Grenoble-Alpes                                   | <i>Examinatrice</i>                          |
| Tristan CREN<br>Directeur de Recherche at L'Institut des<br>NanoSciences de Paris (INSP) | <i>Examineur</i>                             |
| Dimitri RODITCHEV<br>Professeur à l'ESPCI Paris  | <i>Co-directeur de</i><br><i>thèse</i>       |
| Cheryl FEUILLET-PALMA<br>Maitre de Conférences à l'ESPCI Paris                           | <i>Directrice de thèse</i>                   |



# Remerciements

I would like to first thank my supervisors Dimitri and Cheryl for the opportunity to do interesting physics, for the valuable advice that guided me and brought me to this point. And especially for understanding and believing in me and that I could do this work even when I did not believe in it myself. And of course for the scientific debates with Dimitri who kept me going and Cheryl's inexhaustible optimism even when I was down.

I am also very grateful to my family and especially to my mother Irina, who raised me on her shoulders, aunt Olga, who always helped us, especially in hard times and grandmother Elena, whose accidental gift as a child started my acquaintance with electrical devices.

I am very grateful to my friends Andrei, Sasha and Misha, without whose support I would definitely not have been able to make this journey. They always managed to bring light and warmth even in my darkest and coldest days. I would also like to thank my long-time friend and colleague Dima, who is always ready to help and always tries to infect me with his optimism.

I would also like to thank my previous supervisor, Vasily, from whom I had the pleasure and freedom to pursue tasks that interest me. Without his support and mentorship during my bachelor and master theses, I would not have been able to be here in Paris.

Perhaps this item is not typical, but I would like to thank my doctor Dimitri, who has been helping me fight the disease for almost 10 years now.

Thanks to Thales for sponsoring this project.

Of course, I would also like to thank all those I have been fortunate enough to work with. With Paul, whose responsiveness helped me to enter a new field smoothly. And I am also grateful to him for the way he automated all the measurements and data analysis. This has been a reference point for me throughout the work. I am very grateful to Zoe for her support and tea talks. I am grateful to Jérôme Lesueur for supporting me in my endeavours and providing valuable feedback. Finally, I am grateful to Luca for helping me with resource-intensive computations. And to all LPEM staff for the warm atmosphere in which I enjoyed working. And also all jury members who agreed to participate in my defence.

# Contents

|  |            |
|--|------------|
| <b>Remerciements</b>   | <b>i</b>   |
|  | <b>ii</b>  |
| <b>List of Figures</b>   | <b>iv</b>  |
| <b>List of Tables</b>  | <b>x</b>   |
| <b>List of Abbreviations</b>   | <b>xi</b>  |
| <b>Introduction</b>  | <b>xii</b> |
| <b>1 A pinch of superconductivity</b>  | <b>1</b>   |
| 1 A brief history of superconductivity . . . . .   | 2          |
| 2 London equations . . . . .   | 4          |
| 3 Ginzburg-Landau theory . . . . .   | 6          |
| 3.1 Ginzburg-Landau free energy . . . . .  | 6          |
| 3.2 Ginzburg-Landau equations . . . . .  | 7          |
| 3.3 Two characteristic lengths and two types of superconductors . . . . .                | 8          |
| 4 Abrikosov vortex . . . . .   | 10         |
| 5 Time-dependent Ginzburg-Landau (TDGL) . . . . .  | 14         |
| 6 Conclusion . . . . .   | 17         |
| <b>2 High temperature superconductors</b>  | <b>18</b>  |
| 1 High temperature superconductors: the short story of its discovery . . . . .           | 19         |
| 2 Crystal structures . . . . .   | 20         |
| 3 Properties of $\text{CuO}_2$ planes . . . . .  | 21         |
| 4 Electronic properties of $\text{YBa}_2\text{Cu}_3\text{O}_{7-\delta}$ . . . . .        | 24         |
| 4.1 Phase Diagram . . . . .  | 24         |
| 4.2 Superconducting properties in $\text{YBa}_2\text{Cu}_3\text{O}_{7-\delta}$ . . . . . | 25         |
| 5 Thin Film growth . . . . .   | 26         |
| 6 Conclusion . . . . .   | 30         |
| <b>3 <math>\text{YBa}_2\text{Cu}_3\text{O}_{7-\delta}</math> nanowires</b>               | <b>31</b>  |
| 1 Motivation . . . . .   | 32         |
| 2 State of the art . . . . .   | 33         |
| 3 Fabrication by ion irradiation . . . . .   | 36         |
| 3.1 Disorder effect . . . . .  | 36         |
| 3.2 Ion implantation . . . . .   | 37         |

---

|          |  |            |
|----------|--|------------|
| 3.3      | SRIM Simulations . . . . .                           | 38         |
| 4        | Fabrication workflow . . . . .                       | 39         |
| 5        | Conclusion . . . . .                                 | 43         |
| <b>4</b> | <b>Transport measurements</b>                        | <b>44</b>  |
| 1        | Measurement setup . . . . .                          | 45         |
| 2        | RT measurements . . . . .                            | 46         |
| 3        | IV characteristics . . . . .                         | 50         |
| 3.1      | Switching, returning and critical currents . . . . . | 50         |
| 3.2      | Flux Creep behavior . . . . .                        | 60         |
| 3.3      | Shapiro steps . . . . .                              | 65         |
| 3.3.1    | RF-illumination setup . . . . .                      | 65         |
| 3.3.2    | Shapiro-like steps . . . . .                         | 66         |
| 3.3.3    | Shapiro steps width . . . . .                        | 71         |
| 3.3.4    | Shapiro steps temperature dependence . . . . .       | 78         |
| 4        | Conclusion . . . . .                                 | 78         |
| <b>5</b> | <b>Simulation of vortex dynamics</b>                 | <b>80</b>  |
| 1        | System of equations . . . . .                        | 81         |
| 2        | Discretization scheme . . . . .                      | 83         |
| 2.1      | Link-variables . . . . .                             | 83         |
| 2.2      | Computational grid . . . . .                         | 84         |
| 2.3      | Boundary conditions . . . . .                        | 86         |
| 3        | Conclusion . . . . .                                 | 87         |
| <b>6</b> | <b>Vortex patterns</b>                               | <b>88</b>  |
| 1        | Model . . . . .                                      | 89         |
| 1.1      | One grain boundary . . . . .                         | 91         |
| 1.2      | Two identical grain boundaries . . . . .             | 96         |
| 1.3      | Two different grain boundaries . . . . .             | 101        |
| 2        | Conclusion . . . . .                                 | 108        |
|          | <b>Conclusion</b>                                    | <b>109</b> |
|          | <b>List of publications</b>                          | <b>111</b> |
|          | <b>Bibliography</b>                                  | <b>113</b> |

# List of Figures

|     |  |    |
|-----|--|----|
| 1.1 | Mercury resistance versus temperature from the work [Onnes, 1911]. . . . .   | 2  |
| 1.2 | Timeline of different critical temperatures discovered. Adapted from [Ben-<br>nemann, 2008]. . . . .   | 4  |
| 1.3 | The penetration of the magnetic field into the superconductor for different<br>London penetration depth, according to the equation 1.11 . . . . .  | 6  |
| 1.4 | Phase diagrams of a) the type-I and b) the type-II superconductors. . . . .  | 10 |
| 1.5 | a) The shape of the Abrikosov vortex and the two characteristic scales of a<br>superconductor. b) Experimental observation of Abrikosov vortices by the<br>scanning SQUID microscopy technique, adapted from [Wells, 2015a] . . . . .  | 11 |
| 2.1 | Different classes of superconducting materials shown in colour adapted<br>from wikipedia [Ray, 2015] : BCS (dark green circle), based on heavy<br>fermions (green star), cuprates (blue diamond), based on iron-pnicture<br>(orange square), strontium ruthenate (grey pentagon), nickel (pink cross).<br>YBa <sub>2</sub> Cu <sub>3</sub> O <sub>7-δ</sub> compound has been outlined with its discovery in 1987. . . . . | 20 |
| 2.2 | a) ABX <sub>3</sub> -type perovskite lattice, where A is an alkali metal, alkaline earth or<br>rare earth cation, B is a transition metal cation and X is O <sup>-2</sup> b) YBa <sub>2</sub> Cu <sub>3</sub> O <sub>7-δ</sub><br>unit cell. . . . .   | 21 |
| 2.3 | a) Orbitals of the Cu and O atoms involved in CuO <sub>2</sub> planes. b) Schematic<br>arrangement of Cu-O-Cu bonds in CuO <sub>2</sub> planes. . . . .  | 21 |
| 2.4 | Energy diagram of the 3d Cu and 2p O orbitals, and their hybridisation<br>[Alloul, 2009] . . . . .   | 22 |
| 2.5 | Schematic of the CuO <sub>2</sub> plane in its Mott insulator phase and in the case of<br>hole doping. . . . .   | 22 |
| 2.6 | Band structure of a CuO <sub>2</sub> plane. The Hubbard bands of Cu, and the<br>bonding and non-bonding bands of O-Cu are shown, U is the coulombic<br>interaction energy on Cu. . . . .   | 23 |
| 2.7 | YBCO Unit Cell for Different Doping Levels a) Insulating underdoped<br>YBa <sub>2</sub> Cu <sub>3</sub> O <sub>6</sub> where in the CuO chains there are no oxygen ions. b) Op-<br>timally doped YBa <sub>2</sub> Cu <sub>3</sub> O <sub>7-δ</sub> c) Overdoped YBa <sub>2</sub> Cu <sub>3</sub> O <sub>9</sub> : in this case, the<br>CuO chains are fully occupied by oxygen ions. . . . .                               | 23 |
| 2.8 | Generic phase diagram of cuprates [Vishik, 2018]. . . . .  | 24 |
| 2.9 | Anisotropy of resistivity measured in-plane (a) and out-of-plane (b). [Segawa,<br>2003]. . . . .   | 25 |

|      |   |    |
|------|---|----|
| 2.10 | a) Schematic diagram of the tri-crystalline substrate of $\text{SrTiO}_3$ (100), with four epitaxial $\text{YBa}_2\text{Cu}_3\text{O}_{7-\delta}$ rings. b) Scanning SQUID microscope image of the four superconducting rings, cooled under a magnetic field of approximately 5 mG [Tsuei, 1994]. c) Ordered antiferromagnetic lattice of half-flow quanta spontaneously generated in a zigzag lattice ( $\text{YBa}_2\text{Cu}_3\text{O}_{7-\delta}$ -Au-Nb) [Hilgenkamp, 2003]. . . . .   | 26 |
| 2.11 | a) Pulsed Laser Ablation in Thalès. b) Scheme of the process showing the laser, the target and the heated samples. c) Photos of the interior of the PLD chamber with the target and heated sample holder, courtesy to J. Briatico . . . . .   | 27 |
| 2.12 | Layers of the special samples: on a sapphire substrate, a 40 nm $\text{CuO}_2$ buffer layer allows the deposition of a 30 nm thick $\text{YBa}_2\text{Cu}_3\text{O}_{7-\delta}$ thin film under a partial oxygen vacuum of approximately $10^{-4}$ mbar, on a rotating substrate heated between $650^\circ\text{C}$ and $800^\circ\text{C}$ . The sample is then cooled to room temperature. A mechanical mask is aligned with the sample and heated under a $\sim 10^{-4}$ mbar partial oxygen vacuum, reaching temperatures between $650^\circ\text{C}$ and $800^\circ\text{C}$ to ensure optimal doping of the $\text{YBa}_2\text{Cu}_3\text{O}_{7-\delta}$ layer. Subsequently, a 4 nm capping $\text{CuO}_2$ layer, through this circular stencil mask, is deposited under the same conditions to ensure full stoichiometry of the capping layer. $\text{CuO}_2$ is known to be highly stoichiometric and prevents grabbing oxygen from $\text{YBa}_2\text{Cu}_3\text{O}_{7-\delta}$ , requiring deposition under partial oxygen vacuum. In the last step, the sample is cooled down to room temperature, the mechanical mask removed. In the last step the sample is heated around $650^\circ\text{C}$ under the same partial oxygen vacuum ( $\sim 10^{-4}$ mbar), on a rotating substrate heated between $650^\circ\text{C}$ and $800^\circ\text{C}$ to ensure optimal doping of the uncapped $\text{YBa}_2\text{Cu}_3\text{O}_{7-\delta}$ layer. The sample is cooled down under this partial oxygen pressure. Then 20 nm thick Au thin film is deposited in situ on all the sample in this last step, ensuring ohmic contact with the unprotected $\text{YBa}_2\text{Cu}_3\text{O}_{7-\delta}$ layer around the $\text{CuO}_2$ capping layer. . . . . | 28 |
| 2.13 | Atomic Force Microscopy (AFM) image of the surface of a $\approx 150$ -nm-thick $\text{YBa}_2\text{Cu}_3\text{O}_{7-\delta}$ film with an asymmetric $45^\circ$ [001]-tilt grain boundary. Adapted from [Hilgenkamp, 2002] . . . . .  | 29 |
| 3.1  | a) Operational mechanism originally proposed by Golt'sman <i>et al.</i> [Goltzman, 2001]. The superconducting nanowire is biased just below its critical current (i). When a photon with energy $h\nu$ surpassing the superconducting gap $\Delta$ is absorbed, it disrupts the Cooper pairs and forms a normal region (ii), termed a hot spot. This normal region deflects the supercurrents (iii), which propagate along the wire's edges until they exceed the critical current density. Consequently, the nanowire undergoes a local transition to a resistive state (iv), generating a measurable voltage pulse. To be able to detect such a fast voltage pulse, the superconducting nanowire is in an electrical circuit allowing to separate the Direct Current (DC) and Radio-Frequency (RF) part of the signal. b) Electrical circuit involving a Bias Tee to be able to bias with a DC current and detect the fast voltage pulse through an amplifier towards a counter or an oscilloscope. . . . .   | 32 |

|     |  |    |
|-----|--|----|
| 3.2 | <p>a) Top : optical microscope image of 300 nm wide parallel <math>\text{YBa}_2\text{Cu}_3\text{O}_{7-\delta}</math> nanowires and AFM image of several 130 nm wide YBCO nanowires. Bottom : photoresponse under pulsed optical illumination at 1550 nm wavelength at 8 K. IV characteristics at <math>T = 8</math> K. The three insets show the time-resolved photoresponse signal (red circles) measured at three polarisation currents, adapted from [Arpaia, 2015a]. b) Top : Scanning Electron Microscope (SEM) image of the mask before etching to produce <math>\text{La}_{1.85}\text{Ce}_{0.15}\text{CuO}_4</math> wires 100 nm wide, 10 <math>\mu\text{m}</math> long, 5 nm thick. And <math>I(V)</math> hysteretic at 3 K. Bottom : Transient photoresponse of a 100 nm wide, 10 <math>\mu\text{m}</math> long, 5 nm thick <math>\text{La}_{1.85}\text{Ce}_{0.15}\text{CuO}_4</math> wire at different laser pulse powers. The wire is illuminated by a femtosecond laser pulse of 1.56 <math>\mu\text{m}</math> wavelength at a repetition rate of 100 MHz, and measured at 3 K with <math>I_{bias} = 111 \mu\text{A}</math>, adapted from [Shibata, 2016]. c) Ultra-thin nanowires (10-20 nm thick, 65 nm wide, 200 nm long) of optimally doped unprotected YBCO, taken from [Ejrnaes, 2017a]. IV hysteretic at 4.9 K and pulse associated with a black shot. d) Nanowires made of <math>\text{Bi}_2\text{Sr}_2\text{CaCu}_2\text{O}_{8+\delta}</math> cuprates on the left and LSMO on the right. Detection pulse with single-photon sensitivity in each of the two cuprates [Charaev, 2023]. . . . .</p> | 35 |
| 3.3 | <p>Normalized critical temperature as a function of <math>dpa</math>. Adapted from [Lesueur, 1993]. . . . .</p>  | 36 |
| 3.4 | <p>Simulation of the <math>dpa</math> generated by punctual source of <math>\text{He}^+</math> and <math>\text{O}^+</math> ions with an energy of 30 keV into a stack of <math>\text{CeO}_2</math> (8 nm)/<math>\text{YBa}_2\text{Cu}_3\text{O}_{7-\delta}</math> (30 nm)/<math>\text{CeO}_2</math> (40 nm)/<math>\text{Al}_2\text{O}_3</math> (<math>10^5</math> ions simulation). a) Scheme of the irradiated sample with the axes (<math>x</math>, <math>y</math>, <math>z</math>), the different layers and their thicknesses. Nota Bene: the scales are not respected. b) <math>Dpa</math> averaged along the depth <math>x</math> in the <math>\text{YBa}_2\text{Cu}_3\text{O}_{7-\delta}</math> layer at <math>y = 0</math> as a function of the lateral dimension <math>z</math>. c) <math>dpa</math> at <math>y = 0</math> and <math>z = 0</math> as a function of the depth <math>x</math>. The dose is adjusted such that the maximum <math>dpa</math> in a) are equals for the <math>\text{He}^+</math> ions and the <math>\text{O}^+</math> ions. The black dashed lines separate the different material layers. . . . .</p>  | 37 |
| 3.5 | <p>i) Main structure of the initial samples. ii) Spin coating of a 500-nm thick S1805 photoresist with a first layer of LOR05B to achieve an undercut. iii) Laser lithography to pattern the pre-contact. iv) Development of the photoresist. v) Deposition of a Ti(2nm)/Au(200nm) thin film in a Plassys ultra-high vacuum thin film deposition system. vi) Lift-off. vii) Spin coating of a 500-nm thick MAN 2405 negative electron-sensitive resist. viii) Electron beam lithography to design nanowires and contacts, particularly under the <math>\text{CeO}_2</math> capping layer. ix) Ion Beam Etching (IBE) with Argon ions accelerated at 500 eV at a rate of 25 nm of gold per minute. An optical picture of one of the devices on CS15 after the development of the lithography and before the IBE effect is shown. x) Ion irradiation of all the samples at an energy of 30 keV, a dose of <math>3 \times 10^{14}</math> ions/<math>\text{cm}^2</math>. The parts protected either by the gold layer or the MAN resist are not irradiated and remain superconducting, while in the other non-protected areas, <math>\text{YBa}_2\text{Cu}_3\text{O}_{7-\delta}</math> becomes insulating. This entire process prevents the out-diffusion of oxygen from <math>\text{YBa}_2\text{Cu}_3\text{O}_{7-\delta}</math>, as the thin film remains embedded in the insulating <math>\text{YBa}_2\text{Cu}_3\text{O}_{7-\delta}</math> and between two highly stable and stoichiometric <math>\text{CeO}_2</math> layers (buffer layer and capping layer). . . . .</p>  | 41 |

|      |   |    |
|------|---|----|
| 3.6  | Map of a typical sample with all the nanowire geometries patterned by ion irradiation onto a 30 nm thick $\text{YBa}_2\text{Cu}_3\text{O}_{7-\delta}$ thin film on a single $10 \times 10 \text{ mm}^2$ chip. The region delimited by the purple contact, made by e-beam lithography on negative resist, outlines the $\text{CeO}_2$ capping layer. Orange areas represent the gold contact. . . . .  | 42 |
| 4.1  | Resistance versus temperature curves for different nanowires from the sample CS15 (see Fig.3.6). The exact dimensions of each nanowire are presented in table 4.1 or in Fig.3.6. a) in linear scale, b) in log scale. . . . .   | 46 |
| 4.2  | Fit of the resistance versus temperature dependence for the nanowire A-10 based on the different models: 3D and 2D fluctuations models (Eq.4.1), the Halperin-Nelson model (Eq.4.3) and the vortex entry model (Eq.4.4). a - linear scale, b - log scale. . . . .   | 49 |
| 4.3  | IV curve of the nanowire D-4 from the sample CS15. a - linear scale, b - log scale. . . . .   | 51 |
| 4.4  | Temperature dependencies of the switching current $I_s$ , the critical current $I_c$ and the returning current $I_d$ for the nanowire B-6 of the sample CS16. . . . .   | 52 |
| 4.5  | Fit of the switching current versus temperature dependence based on the depairing current from the Ginzburg-Landau model (Eq.4.7) for the nanowire B-6 from the sample CS16. . . . .  | 53 |
| 4.6  | <i>Frozen vortex rivers</i> adapted from [Silhanek, 2010b]. Vortex configurations, imaged by scanning Hall probe microscopy at $T = 4.2 \text{ K}$ in a superconducting Pb film with a periodic array of pinning sites: (a) field cooled without applied current and (b) field cooled with applied current of 36 mA. The arrows indicate the direction of the applied current. . . . .  | 55 |
| 4.7  | Schematics of a biased current wire in the framework of the SBT thermal model. A normal hot region of length $2y_0$ along the $y$ -axis in red transfers thermal energy laterally to the superconducting wire via heat conduction $\kappa$ , and through the substrate due to the heat transfer $\alpha$ . Depending on the values of $\alpha$ and $\kappa$ , the hot region either expands or self-heals. . . . .  | 56 |
| 4.8  | Fit of the critical currents versus temperature dependence for the nanowire B-6 from the sample CS16, based on the different models described in the main text. a) Model from Griessen <i>et al.</i> [Griessen, 1994] implementing the fluctuations of the critical temperature $\delta T$ or fluctuations of the mean free path length $\delta l$ to the critical current evolution in temperature (Eq.4.12). b) Model from Plain <i>et al.</i> [Plain, 2002] with the contributions of both strong and weak pinning types to the critical current evolution in temperature (Eq.4.13). c) Power $\alpha$ and $\beta$ fits (Eq.4.14) d) Albrecht <i>et al.</i> [Albrecht, 2007] model with two regimes below 40K (vortex pinned on specific pinning shape and morphology) and above 40 K (depinning is thermally activated) . . . . . | 58 |
| 4.9  | IV curves for different temperatures in linear scale a) and log scale b) for the nanowire C-5 from the sample CS15. . . . .   | 61 |
| 4.10 | Fit of IV curves based on the flux creep model (Eq.4.20) for the nanowire B-6 from the sample CS16. . . . .   | 63 |
| 4.11 | The pinning energy $E_p$ and the jump width between pinning sites $\delta_p$ resulting from the flux creep model fit for the nanowire B-6 from the sample CS16. . . . .   | 64 |
| 4.12 | a) IV curves under RF illumination at different temperatures. b) Dynamical resistance $dV/dI$ versus the number of the Shapiro step for different temperatures for the nanowire B-6 of the sample CS16. . . . .   | 66 |

|      |  |    |
|------|--|----|
| 4.13 | Phase diagram of different effects in superconducting nanobridges depicting different cases depending on lateral sizes (length $l$ and width $w$ ) of a weak link. Adapted from [Likharev, 1979]. . . . .  | 68 |
| 4.14 | CPR for various lengths of the superconducting bridge. Adapted from [Likharev, 1975]. . . . .  | 69 |
| 4.15 | Dynamical resistance $dV/dI$ versus the number of Shapiro step a) Experimental measurements of the sample C-8 from CS15 measured at $T = 6$ K at $f = 18.32$ GHz. b) Simulations from RSJ model with Likharev's CPR (Eq.4.23). . . . .   | 70 |
| 4.16 | Color-maps of the dynamic resistance under an RF illumination at $f = 18.32$ GHz as a function of bias current and the RF power for the of the nanowire C-8 from the sample CS15 at $T = 6$ K. . . . .   | 72 |
| 4.17 | a) RF power evolution of the critical current (step 0) and width of the Shapiro steps (step number $> 0$ ) of the nanowire C-8 from the sample CS15 at $T = 6$ K. b) Zoom in $\mu A$ range showing the evolution of the Shapiro steps width with RF power . . . . .  | 73 |
| 4.18 | Series of IV curves at different RF powers of the nanowire C-8 from the sample CS15 at $T = 6$ K. a) Uniform scale, b) log-log scale. . . . .  | 74 |
| 4.19 | Series of IV curves at different RF powers with the corresponding power law fits. a) Linear scale, b) log-log scale. . . . .   | 75 |
| 4.20 | Extracted the power $n$ from the power law fitting of the series of IV curves for a) different RF powers, b) different temperatures $T$ . . . . .  | 76 |
| 4.21 | Color-maps of the dynamic resistance under an RF illumination at $f = 18.32$ GHz as a function of bias current and the RF power for the nanowire C=8 of the sample CS15 at a) 6 K, b) 20 K, c) 50 K, and d) 70 K. . . . .  | 77 |
| 5.1  | Computational grid for the finite-difference method using link variables approach. . . . .   | 85 |
| 6.1  | a) Scanning Electron Microscope image of a typical nanobridge studied in experiments [Amari, ]. b) and c) Two sample geometries studied theoretically, representing the central (narrowest) part of the real device. They contain one (b) or two (c) linear defects (grey regions). Edge defects situated at the ends of linear defects are indicated by black rectangles. The direction of the transport current is shown by arrows. The voltage is calculated between the two blue dashed lines. Further details are provided in the text. . . . .   | 90 |
| 6.2  | Vortex dynamics in single linear defect with no AC current applied ( $I_{AC} = 0$ ). a) Static map of the order parameter amplitude $ \psi(\mathbf{r}) $ at low transport currents $I_{DC} \ll I_c$ . b) Static $ \psi(\mathbf{r}) $ map at $I_{DC} \lesssim I_C$ indicates the presence of one vortex and one anti-vortex at the edge defects, ready to enter. d)-e) Snapshots of $ \psi(\mathbf{r}) $ at different moments of vortex propagation for a fixed $I_{DC} = 0.10 > I_c$ . f) Periodic temporal evolution of the instantaneous voltage $V(t)$ at the same conditions. The dots c, d and e on the graph correspond to snapshots c), d) and e). The period of $V(t)$ oscillations provides the fundamental frequency $f_1$ of the process. g) Fourier spectrum of $V(t)$ . . . . . | 93 |

|      |   |     |
|------|---|-----|
| 6.3  | Transport properties of the nanobridge with one linear defect. Solid lines represents normalized $\langle V \rangle(I_{DC})$ characteristics calculated for different values of the AC component $I_{AC}$ of the total transport current. The right vertical axis displays the numbers of Shapiro plateaus. Dashed line - $V(I)$ characteristic of a SNS Josephson junction calculated within the RSJ model [Stewart, 1968; McCumber, 1968]. To fit the curve into the plot window, its vertical scale was divided by a factor of 10. . . . . | 94  |
| 6.4  | Evolution of the instantaneous voltage $V(t)$ for the Shapiro plateau 1/3 of Fig.3. a) $V(t)$ at constant $I_{DC}$ and $I_{AC}$ for the detuned frequency $f_{AC} = 0.625 f_3$ . The low-frequency envelope due to the beat effect is visible. b) $V(t)$ at the resonance $f_{AC} = f_3$ . c) Frequency spectrum of $V(t)$ in the case (b). . . . .   | 96  |
| 6.5  | $\langle V \rangle(I_{DC})$ characteristics for different values of $I_{AC}$ in the case of two identical linear defects (displayed in Fig. 6.1c). The right vertical axis displays the numbers of Shapiro steps. Dashed lines are used as eye-guides (refer to the text for details). . . . .  | 98  |
| 6.6  | Vortex dynamics in the case of two identical linear defects of Fig. 6.1c. a) and b) Snapshots of the order parameter amplitude in the stable (a) and metastable (b) states near the transition (see in the text). c) Evolution of $V(t)$ at the transition from the metastable to the stable state at $I_{AC} = 0.03$ . The initial DC current $I_{DC} = 0.076$ switches to $I_{DC} = 0.077$ at the moment $t = 500$ . A movie illustrating the oscillatory dynamics of this transition is provided by the <a href="#">link</a> . . . . .     | 99  |
| 6.7  | a) Schematic energy diagram of the states considered in Fig.6. Stable ( $E_0$ ) and metastable ( $E_1$ ) states are presented along with their frequency spectra. b) a sketch of two coupled oscillators . . . . .  | 101 |
| 6.8  | a) $\langle V \rangle(I_{DC})$ characteristics for different values of $\epsilon_2$ with fixed $\epsilon_1 = 0.5$ in the case of two different linear defects (displayed in Fig. 6.1c). b) Corresponding critical current $I_c$ versus $\epsilon_2$ dependency. . . . .   | 102 |
| 6.9  | Color-maps of the superconducting current density $J_s$ distribution when the DC current $I_{DC}$ is set just below the critical current $I_c$ for two cases a) $\epsilon_2 = 0.83$ and b) $\epsilon_2 = \epsilon_1 = 0.5$ . . . . .  | 104 |
| 6.10 | Dynamics of states with (a,c) and without (b,d) NDR for the case $\epsilon_2 = 0.042$ . . . . .   | 105 |
| 6.11 | $\langle V \rangle(I_{DC})$ characteristics for different $I_{AC}$ in the case of two different linear defects, $\epsilon = 0.5$ and $\epsilon = 0.42$ . The right vertical axis displays the numbers of corresponding Shapiro steps. . . . .   | 106 |

# List of Tables

|     |  |    |
|-----|--|----|
| 4.1 | Geometrical parameters for the nanowire's RT curves plotted in Fig.4.1 . . . | 47 |
| 4.2 | RT fit parameters . . . . .  | 48 |

# List of Abbreviations

|              |   |
|--------------|---|
| <b>1D</b>    | One-Dimensional                                 |
| <b>2D</b>    | Two-Dimensional                                 |
| <b>3D</b>    | Three-Dimensional                               |
| <b>AC</b>    | Alternating Current                             |
| <b>AFM</b>   | Atomic Force Microscopy                         |
| <b>AL</b>    | Aslamazov-Larkin                                |
| <b>BCS</b>   | Bardeen Cooper Schrieffer                       |
| <b>BKT</b>   | Berezinskii–Kosterlitz–Thouless                 |
| <b>CPR</b>   | Current Phase Relationship                      |
| <b>DC</b>    | Direct Current                                  |
| <b>FIB</b>   | Focused Ion Beam                                |
| <b>GL</b>    | Ginzburg-Landau                                 |
| <b>HTS</b>   | High-Temperature Superconductors                |
| <b>IBE</b>   | Ion Beam Etching                                |
| <b>IV</b>    | Current versus Voltage                          |
| <b>NDR</b>   | Negative dynamic resistance                     |
| <b>PLD</b>   | Pulsed Laser Ablation                           |
| <b>RCSJ</b>  | Resistive Capacitive Shunted Junction           |
| <b>RF</b>    | Radio-Frequency                                 |
| <b>RSJ</b>   | Resistive Shunted Junction                      |
| <b>SBT</b>   | Skocpol-Beasley-Tinkham                         |
| <b>SEM</b>   | Scanning Electron Microscope                    |
| <b>SNS</b>   | Superconductor-Normal metal-Superconductor      |
| <b>SNSPD</b> | Superconducting Nanowire Single Photon Detector |
| <b>SQUID</b> | Superconducting Quantum Interference Devices    |
| <b>SRIM</b>  | Stopping and Range of Ions in Matter            |
| <b>STM</b>   | Scanning Tunneling Microscope                   |
| <b>TAVM</b>  | Thermally Activated Vortex Motion               |
| <b>TDGL</b>  | Time-Dependent Ginzburg-Landau                  |
| <b>UV</b>    | Ultraviolet                                     |

# Introduction

Superconductivity has attracted the attention of the world community since its discovery. This applies not only to fundamental science but also to many applications that can utilize the unusual properties of superconductors. However, the first superconductors could work only at ultra-low temperatures, which made their use in real devices very difficult. A great step towards applying superconductivity to everyday life was the discovery of [High-Temperature Superconductors \(HTS\)](#) in 1986 [Bednorz, ]. These superconductors can show their superconducting properties already at the temperature of liquid nitrogen (77.4 K), which is much more accessible and easier to use than liquid helium (boiling point 4.2 K). As a result, high-temperature superconductors have found applications in areas where they have no competitors - high magnetic fields and high electric power transmission.

Despite the high critical temperature, the structure of these superconducting crystals is very complex, and their superconducting properties are extremely sensitive to the oxygen ion content. This severely limited their field of application for a long time. With the development of technology, scientists have learnt how to successfully scale down [HTS](#) devices to micro and nano sizes. [Superconducting Quantum Interference Devices \(SQUID\)](#) for ultra-sensitive measurement of magnetic fields [Clarke, 2004], nanowires for the detection of single photons [Esmail Zadeh, 2021] for various applications in astronomy, quantum optics, and quantum informatics have been successfully realized. However, further improvements in the properties of the devices are needed, which requires a better understanding of how electron transport occurs in such systems. It is known that [HTS](#), including  $\text{YBa}_2\text{Cu}_3\text{O}_{7-\delta}$ , are type II superconductors, so Abrikosov vortices play a major role in the transport properties. The present work is devoted to the study of their influence in nanoscale samples.

This work is devoted to the experimental study of transport characteristics of  $\text{YBa}_2\text{Cu}_3\text{O}_{7-\delta}$  nanowires and the theoretical study of how vortex patterns affect the transport characteristics of nanowires. The work is conventionally divided into three parts. The first part contains an introduction to the field of superconductivity and consists of two chapters: Chapter 1 contains a brief history of the study of superconductivity and a more detailed description of the main theoretical concepts actively used in the future, and Chapter 2 describes the history and properties of [HTS](#). Part II presents our experimental results on the transport characteristics of  $\text{YBa}_2\text{Cu}_3\text{O}_{7-\delta}$  nanowires. Chapter 3 gives an overview of the fabrication methods of [HTS](#) nanowires and describes the fabrication process of  $\text{YBa}_2\text{Cu}_3\text{O}_{7-\delta}$  nanowires used in this work. Chapter 4 presents the main experimental

---

results on the measurements of transport properties of our samples. The temperature dependencies of the resistivity, which we analyze by different existing theories, are discussed. The dependencies of the current-voltage characteristics over a wide temperature range are also presented, which we try to explain within the framework of existing vortex motion models. The last section of the chapter is devoted to the Shapiro experiment. The third part, contains our theoretical studies carried out within the framework of [Time-Dependent Ginzburg-Landau \(TDGL\)](#) theory. It opens with [Chapter 5](#) which describes the theoretical formalism and the scheme used in the numerical calculations. [Chapter 6](#) contains our theoretical results. It considers the motion of vortex-antivortex pairs in a nanoscale bridge in the presence of parallel linear defects. The calculated voltage-current characteristics were obtained also in the presence of electromagnetic radiation (the Shapiro experiment). The results include fractional Shapiro steps (that were previously experimentally obtained in [Chapter 4](#)) and sharp discontinuities in the voltage-current characteristics associated with the change of oscillation modes.

# Chapter 1

## A pinch of superconductivity

### Objectives

In this chapter we give a brief description of the phenomenon of superconductivity. Starting with a historical overview, we then outline in more detail the main theoretical concepts used in our work.

### Contents

|     |   |    |
|-----|---|----|
| 1   | A brief history of superconductivity . . . . .                        | 2  |
| 2   | London equations . . . . .  | 4  |
| 3   | Ginzburg-Landau theory . . . . .                                      | 6  |
| 3.1 | Ginzburg-Landau free energy . . . . .                                 | 6  |
| 3.2 | Ginzburg-Landau equations . . . . .                                   | 7  |
| 3.3 | Two characteristic lengths and two types of superconductors . . . . . | 8  |
| 4   | Abrikosov vortex . . . . .  | 10 |
| 5   | Time-dependent Ginzburg-Landau (TDGL) . . . . .                       | 14 |
| 6   | Conclusion . . . . .  | 17 |

## 1 A brief history of superconductivity

On 26 October 1911, Heike Kamerlingh Onnes made a groundbreaking discovery in his laboratory in Leiden: the sudden transition of mercury to zero resistance [Onnes, 1911]. The historical representation of the resistance versus temperature of mercury can be observed in Fig.1.1. This experiment marked the identification of a novel phenomenon, leading to the establishment of a new field known as superconductivity. However, after 22 years, it became evident that zero resistance was not the sole characteristic of the superconducting phase. In 1933, Walther Meissner and Robert Ochsenfeld found that a sample of superconducting tin completely repels a magnetic field [Meissner, 1933].

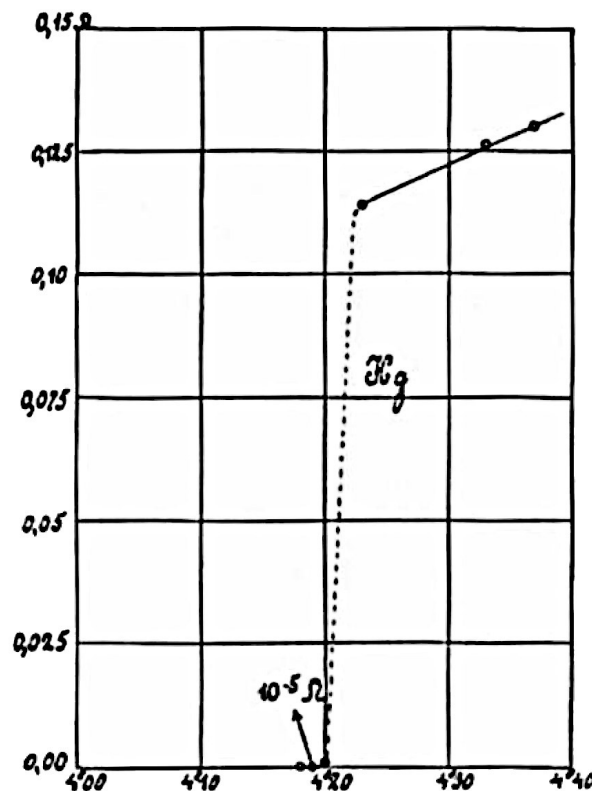


Figure 1.1 – Mercury resistance versus temperature from the work [Onnes, 1911].

The initial theoretical framework for the superconductivity phenomenon was provided by the London brothers Fritz and Heinz London [London, 1935]. They incorporated equations describing zero resistance and magnetic field expulsion into Maxwell's equations. Although this approximation allowed for the description of the electrodynamics of superconductivity, it did not consider its quantum nature and posed a challenge with the negative surface energy problem. A significant advancement in understanding superconductivity occurred in 1950 when Vitaly Ginzburg and Lev Landau introduced a phenomenological theory [Ginzburg, 1950] based on Landau's theory of second-order phase transitions. This approach involved decomposing the free energy into degrees of the order parameter — a complex function whose modulus is proportional to the density of superconducting elec-

trons. Ginzburg and Landau's theory addressed both issues posed by the London brothers' theory simultaneously. It provided predictions for temperature and field dependencies near the transition temperature and introduced a new characteristic of superconducting materials - the coherence length. At the same time, experimental identification of the isotope effect [Maxwell, 1950] played a crucial role in understanding the nature of superconductivity, revealing the connection between lattice vibrations and superconducting electrons. Herbert Fröhlich [Fröhlich, 1950] first expressed this idea, but the final result was obtained by Leon Cooper [Cooper, 1956]. He and his colleagues John Bardeen and John Schrieffer proposed the first successful microscopic theory [Bardeen, 1957]. The core concept was that lattice vibrations could attract electrons, leading to the formation of pairs known as Cooper pairs. This theory successfully explained experimental data and became one of the triumphs of condensed matter physics.

Subsequent works by Lev Gorkov, Alexei Abrikosov [Abrikosov, 1964] and Gerasim Eliashberg [Eliashberg, 1960] further developed this theory within the framework of quantum field approach. Gorkov [Gorkov, 1959] demonstrated that the Ginzburg-Landau theory is a limiting case of the Bardeen Cooper Schrieffer (BCS) theory, establishing a microscopic connection between these two theories. In the same year, Abrikosov [Abrikosov, 1969] analysed the Ginzburg-Landau theory and showed the possibility of superconductors of the second kind, where the magnetic field penetrates in the form of quantum lines known as vortices (Abrikosov's vortices). This analysis was soon experimentally verified, opening up a new field of study into the behaviour of Abrikosov vortices.

In 1962, while still a graduate student, Brian Josephson discovered a completely new effect - the tunnelling of Cooper pairs [Josephson, 1962]. In fact, two effects were predicted: stationary and non-stationary Josephson effects. Both phenomena were soon validated through experimental work [Anderson, 1963; Clark, 1968], and this discovery laid the foundation for an entire scientific field. Furthermore, applications of devices based on the Josephson effect are now commonplace in electronics, medicine, and informatics.

The next breakthrough in superconductivity came from the experimentalists. In 1987, Karl Müller and Johannes Bednorz discovered ceramics with a superconducting transition temperature of 93 K for  $\text{YBa}_2\text{Cu}_3\text{O}_{7-\delta}$  [Wu, 1987b], followed by 107 K for  $\text{Bi}_2\text{Sr}_2\text{CaCu}_2\text{O}_{8+\delta}$  [Maeda, 1988]. The new materials could not be described within the framework of the BCS theory. It also turned out that their properties are extremely sensitive to the concentration of oxygen and exhibited a complex phase diagram, incorporating phenomena such as anti-ferromagnetism, pseudo-gap, and strange metal phenomenon behaviour. This discovery triggered a new wave of experimental and theoretical investigations into the complex nature of these materials.

The evolution of superconductivity does not end here, and with the development of fabrication and measurement equipment, new phenomena are emerging on scales that were previously inaccessible. However, these recent developments belong to current research and do not yet belong to the history of the field, despite its rapid development.

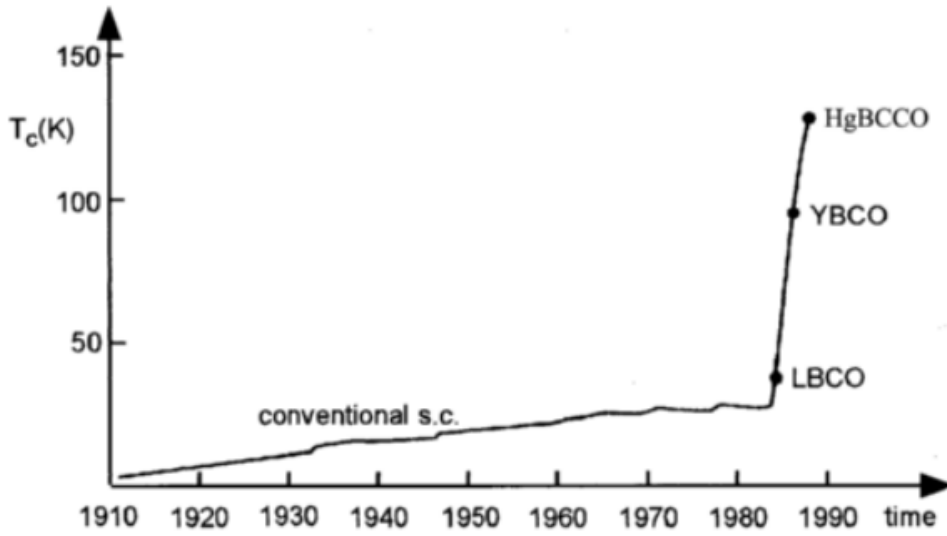


Figure 1.2 – Timeline of different critical temperatures discovered. Adapted from [Benne-  
mann, 2008].

## 2 London equations

The initial successful attempt to provide a theoretical description of the superconduc-  
tivity phenomenon was undertaken by brothers Fritz and Heinz London [London, 1935].  
They formulated the Maxwell equations in a manner that accounted for two crucial ex-  
perimental observations: zero resistance and ideal diamagnetism.

When a current flows without resistance, the external field simply imparts acceleration  
to the electrons. This can be expressed in the form of Newton's second law as:

$$m \frac{d\mathbf{v}}{dt} = -e\mathbf{E}, \quad (1.1)$$

where  $m$  - is an electron mass,  $e$  - is an electron charge,  $\mathbf{E}$  - electric field. The expression  
for the current density,  $\mathbf{j} = -n_e e \mathbf{v}$ , allows us to rewrite the equation using the electron  
density  $n_e$ :

$$\Lambda \frac{d\mathbf{j}}{dt} = \mathbf{E}, \quad (1.2)$$

where  $\Lambda = \frac{m}{n_e e^2}$ . This equation constitutes the first London equation. It elucidates the  
phenomenon that in a stationary case with a constant superconducting current,  $\mathbf{j} = \mathbf{const}$ ,  
no electric field  $\mathbf{E} = \mathbf{0}$  is required, illustrating dissipation-less flow. Using one of the  
Maxwell equations\*

$$\nabla \times \mathbf{E} = -\frac{1}{c} \frac{\partial \mathbf{B}}{\partial t} \quad (1.3)$$

we can express:

$$\nabla \times \left( \Lambda \frac{d\mathbf{j}}{dt} \right) = -\frac{1}{c} \frac{\partial \mathbf{B}}{\partial t}, \quad (1.4)$$

\*. Here and later in this Chapter, we use CGS units.

where  $\mathbf{B}$  represents a local magnetic induction.

Using another Maxwell equation

$$\nabla \times \mathbf{B} = \frac{4\pi}{c} \mathbf{j} \quad (1.5)$$

we can express it as an equation for magnetic induction:

$$\Lambda \frac{c}{4\pi} \frac{d}{dt} \nabla \times (\nabla \times \mathbf{B}) = -\frac{1}{c} \frac{\partial \mathbf{B}}{\partial t}. \quad (1.6)$$

Collecting everything on the left side and using the formula from vector calculus  $\nabla \times (\nabla \times \mathbf{B}) = \nabla(\nabla \cdot \mathbf{B}) - \Delta \mathbf{B}$ , we can rewrite it as:

$$\frac{d}{dt} \left( \Lambda \frac{c^2}{4\pi} \Delta \mathbf{B} - \mathbf{B} \right) = \mathbf{0}. \quad (1.7)$$

The general solution of this equation is:

$$\Lambda \frac{c^2}{4\pi} \Delta \mathbf{B} - \mathbf{B} = \mathbf{const}, \quad (1.8)$$

where the constant  $\mathbf{const}$  can be determined from the condition that far from the bulk superconductor's edges, both magnetic field and superconducting current are zero. In other words,  $\mathbf{const} = \mathbf{0}$  leads to the second London equation:

$$\Delta \mathbf{B} - \frac{1}{\lambda_L^2} \mathbf{B} = \mathbf{0} \quad (1.9)$$

where  $\lambda_L = \left( \frac{\Lambda c^2}{4\pi} \right)^{1/2} = \left( \frac{mc^2}{4\pi n_e e^2} \right)^{1/2}$  represents the London penetration depth. In this form, this equation is the Helmholtz equation for the magnetic induction  $\mathbf{B}$  with a solution of a decaying exponent.

In the considered effective 1D case, where  $x = 0$  is a superconductor-vacuum interface and the superconductor is at  $x > 0$ , and an external magnetic field  $\mathbf{B}_0$  is applied in the  $z$  direction, the problem becomes one-dimensional and depends solely on  $x$ :

$$\frac{d^2}{dx^2} B(x) - \frac{1}{\lambda_L^2} B(x) = 0. \quad (1.10)$$

With respect to the boundary conditions  $B(x = 0) = B_0$  and  $B(x \rightarrow \infty) = 0$ , the corresponding solution can be written as

$$B(x) = B_0 e^{-\frac{x}{\lambda_L}}. \quad (1.11)$$

Thus, the magnetic field penetrates the superconductor over a very short distance and exponentially decays on a scale of  $\lambda_L$ , justifying the name "penetration depth". Typically, in real samples, the London penetration depth is of the order of  $10^{-8} - 10^{-7}$  m. In our

considerations,  $\lambda_L$  does not depend on temperature, which contradicts the experimental results. This contradiction is addressed in the so-called two-fluid model.

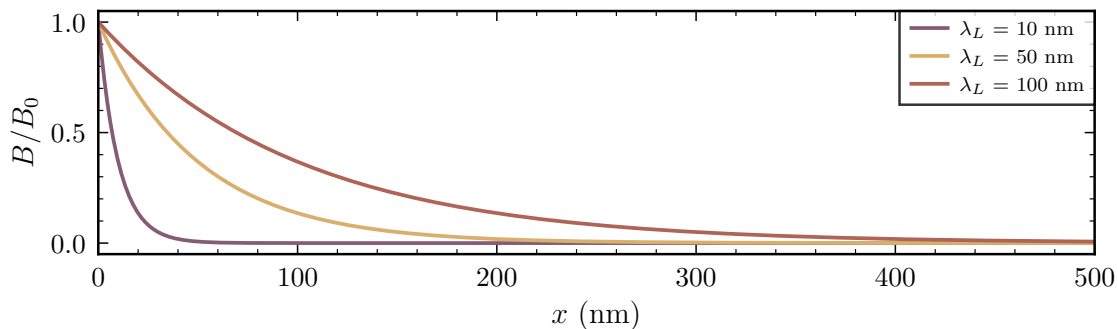


Figure 1.3 – The penetration of the magnetic field into the superconductor for different London penetration depth, according to the equation 1.11

In the two-fluid model, all electrons are divided into two electronic fluids: one is a fluid of normal electrons with density  $n_n$ , and the other is a fluid of superconducting electrons with density  $n_s$ . The latter depends on the temperature  $n_s(T)$  and equals zero at  $T = T_c$ . The empirical formula for the temperature dependence of the London penetration depth  $\lambda_L$  is given by:

$$\lambda_L(T) = \frac{\lambda_L(0)}{\left(1 - (T/T_c)^4\right)^{1/2}}. \quad (1.12)$$

where  $\lambda_L(0)$  is the London penetration depth at zero temperature.

The London model was the first theory that described key superconductor properties, including- zero resistance and the Meissner effect. Although lacking microscopic explanations, it provides a correct description of superconductor electrodynamics. Despite the complexity of contemporary theoretical instrumentation, this simple model can still be very efficient in some practically important limits.

## 3 Ginzburg-Landau theory

### 3.1 Ginzburg-Landau free energy

The next significant step towards understanding superconductivity was the development of the phenomenological theory, known as the [Ginzburg-Landau \(GL\) theory](#), by Landau and Ginzburg in 1950 [Ginzburg, 1950]. This theory builds upon the concept of second-order phase transitions, previously formulated by Landau in 1937 [Landau, 1937]. In second-order phase transitions, the state of matter changes continuously, but the symmetry undergoes a sharp jump. An illustrative example of such a transition is the ferromagnetic transition, where the rotational symmetry is lost, and the sample assumes a specific direction corresponding to the magnetisation vector. Applying this approach

to superconductivity involved defining the symmetry of the superconducting transition, which Landau and Ginzburg characterized as the appearance of the order parameter  $\psi$  — a macroscopic wave function describing the superconducting state. Once the symmetry is identified, the next step is to formulate the expansion of the free energy in powers of the order parameter. Since the wave function  $\psi$  is a complex function, the free energy takes the form:

$$F_s = F_n + a|\psi|^2 + (b/2)|\psi|^4 + \dots \quad (1.13)$$

Here,  $F_s$  and  $F_n$  represent the free energies of the superconducting and normal states, and  $a$  and  $b$  are the energy expansion parameters. At temperatures above  $T_c$ , where there is no superconducting phase, the minimum energy corresponds to  $F_n$ , resulting in  $\psi = 0$ . However, at temperatures  $T < T_c$ , the superconducting state is determined by the minimum of the free energy, leading to the following equation:

$$\frac{\partial F_s}{\partial |\psi|} = 2a|\psi| + 2b|\psi|^3 = 0. \quad (1.14)$$

There are two solutions to the Eq.1.14: one is  $|\psi| = 0$ , corresponding to the normal state, and the other is  $|\psi| = -a/b$ , corresponding to the superconducting state. To ensure the superconducting state, the square of the order parameter must be positive at  $T < T_c$ . This is possible if the parameter  $a < 0$  at  $T < T_c$ . Consequently,  $a > 0$  at  $T \geq T_c$  to satisfy the normal state condition above the critical temperature.

By defining the parameter  $a$  in this way, the parameter  $b$  must be positive both above and below the superconducting transition, allowing us to keep it constant ( $b > 0$ ). Since the total energy expansion is provided near the critical temperature of the superconducting transition  $T \approx T_c$ , we can approximately expand  $a$  in powers of  $(T - T_c)$  and keep only the first order of  $T$ :

$$a = \alpha(T - T_c), \quad (1.15)$$

where  $\alpha > 0$  is some positive function that depends on  $T$ .

### 3.2 Ginzburg-Landau equations

So far, we have considered only the coordinate-independent homogeneous case. However, when placing a superconductor in a magnetic field, London's equation predicts the appearance of a superconducting current along the edges. This current introduces inhomogeneity to the order parameter across the volume of the superconductor. Consequently, it becomes necessary to account for the proportional term  $|\nabla\psi|^2$ , which plays the role of the kinetic energy.

For a superconductor in a magnetic field, Landau and Ginzburg proposed expressing

the Gibbs free energy in the following form:

$$G_s = G_n + \int d^3r \left\{ a|\psi(\mathbf{r})|^2 + \frac{b}{2}|\psi(\mathbf{r})|^4 + \frac{1}{2m_s} \left| \left[ -i\hbar\nabla - \frac{e_s}{c}\mathbf{A}(\mathbf{r}) \right] \psi(\mathbf{r}) \right|^2 + \frac{1}{8\pi}(\nabla \times \mathbf{A})^2(\mathbf{r}) - \frac{1}{4\pi}\nabla \times \mathbf{A}(\mathbf{r}) \cdot \mathbf{H}_0(\mathbf{r}) \right\}, \quad (1.16)$$

where  $G_n$  is the free Gibbs energy of the normal state,  $\mathbf{H}_0(\mathbf{r})$  is the homogeneous external magnetic field,  $\mathbf{A}(\mathbf{r})$  is the vector potential associated with the magnetic field,  $e_s$ ,  $m_s$  are charge and mass of the superconducting electron, that according to the microscopic theory equals  $e_s = 2e$ ,  $m_s = 2m_e$ , where  $e$ ,  $m_e$  are charge and mass of the ordinary electron,  $\hbar$  is the reduced Plank constant and  $c$  is the speed of light in vacuum. Using variance calculus, we can minimize this functional with respect to  $\delta\mathbf{A}$  and  $\delta\psi$  consecutively. This process leads to the derivation of the famous [Ginzburg-Landau](#) equations:

$$\begin{cases} a\psi + b|\psi|^2\psi + \frac{1}{4m} \left( i\hbar\nabla + \frac{2e}{c}\mathbf{A} \right)^2 \psi = 0 \\ -\frac{i\hbar e}{2m} (\psi\nabla\psi^* - \psi^*\nabla\psi) - \frac{2e^2}{mc}|\psi|^2\mathbf{A} = \frac{c}{4\pi}\nabla \times (\nabla \times \mathbf{A}) \end{cases} \quad (1.17)$$

The [Ginzburg-Landau](#) equations need to be supplemented with appropriate boundary conditions to fully characterise the behaviour of the order parameter. Ginzburg and Landau originally considered the condition of the absence of superconducting current flow through the superconductor-vacuum boundary. This boundary condition is expressed as:

$$\mathbf{n} \cdot \left( i\hbar\nabla + \frac{2e}{c}\mathbf{A} \right) \psi = 0 \quad (1.18)$$

where  $\mathbf{n}$  is a normal vector to the superconductor-vacuum boundary.

Later de Gennes [De Gennes, 2018] suggested a generalised version of this condition suitable for the superconductor-normal metal interface

$$\mathbf{n} \cdot \left( i\hbar\nabla + \frac{2e}{c}\mathbf{A} \right) \psi = \nu\gamma_0\psi \quad (1.19)$$

where  $\gamma_0$  is a real constant that parameterizes the proximity effect: the extent to which the order parameter diffuses into normal metal.

The second equation is the Maxwell equation with the superconducting current that is defined as:

$$\mathbf{j}_s = -\frac{i\hbar e}{2m} (\psi\nabla\psi^* - \psi^*\nabla\psi) - \frac{2e^2}{mc}|\psi|^2\mathbf{A}. \quad (1.20)$$

### 3.3 Two characteristic lengths and two types of superconductors

[Ginzburg-Landau](#) equations 1.17 inherently contain two characteristic lengths.

One of this lengths is a coherence length  $\xi$ , which is defined as follows

$$\xi = \sqrt{\frac{\hbar^2}{4m|a|}}. \quad (1.21)$$

This length describes the scale over which the order parameter changes spatially. The microscopic interpretation of the coherence length, as later understood in terms of the BCS theory, relates to the size of the Cooper pairs.

The corresponding length scale for the vector field variable  $\mathbf{A}(\mathbf{r})$  is the penetration depth, and it is defined as:

$$\lambda = \sqrt{\frac{mc^2b}{8\pi e^2|a|}}. \quad (1.22)$$

Remarkably, the meaning of this penetration depth is completely the same as the one in the London equations as this length scale is associated with the spatial extent to which the magnetic field penetrates the superconductor. And indeed, it can be demonstrated that using the norm  $|\psi(\mathbf{r})|^2 = n_s/2$  this definition equals the London penetration depth  $\lambda_L$  defined in the Eq.1.12.

Both the coherence length  $\xi$  and the penetration depth  $\lambda$  depend on temperature, as they are influenced by the temperature-dependent parameter  $a(T)$ , which, near the critical temperature, varies as  $a(T) \propto (T_c - T)$ . Thus, both lengths approximately have an inverse square root temperature dependency  $\propto (T_c - T)^{-1/2}$ .

To establish a dimensionless parameter independent of temperature, the Ginzburg-Landau parameter  $\kappa$  is introduced:

$$\kappa = \frac{\lambda}{\xi}. \quad (1.23)$$

This parameter is crucial in the Ginzburg-Landau theory and defines the criteria for distinguishing between two qualitatively different types of superconductors: type I and type II. The exact criteria are given by:

$$\begin{aligned} \kappa &< \frac{1}{\sqrt{2}} \text{ Type I} \\ \kappa &> \frac{1}{\sqrt{2}} \text{ Type II} \end{aligned} \quad (1.24)$$

This criterion determines the sign of the surface energy at the superconductor-normal metal boundary, leading to important physical consequences. For superconductors of the second type (type II), the surface energy is negative and they possess two critical magnetic fields. Below the first critical field  $H_{c1}$ , the usual Meissner effect occurs and the magnetic field penetrates into the superconductor up to the penetration depth  $\lambda_L$ . Beyond this field, magnetic quantum filaments, called Abrikosov vortices, enter the superconductor, and the superconductor transitions to the so-called mixed state. In contrast, superconductors of the first type (type I) transition completely to the normal state upon reaching their only critical field.

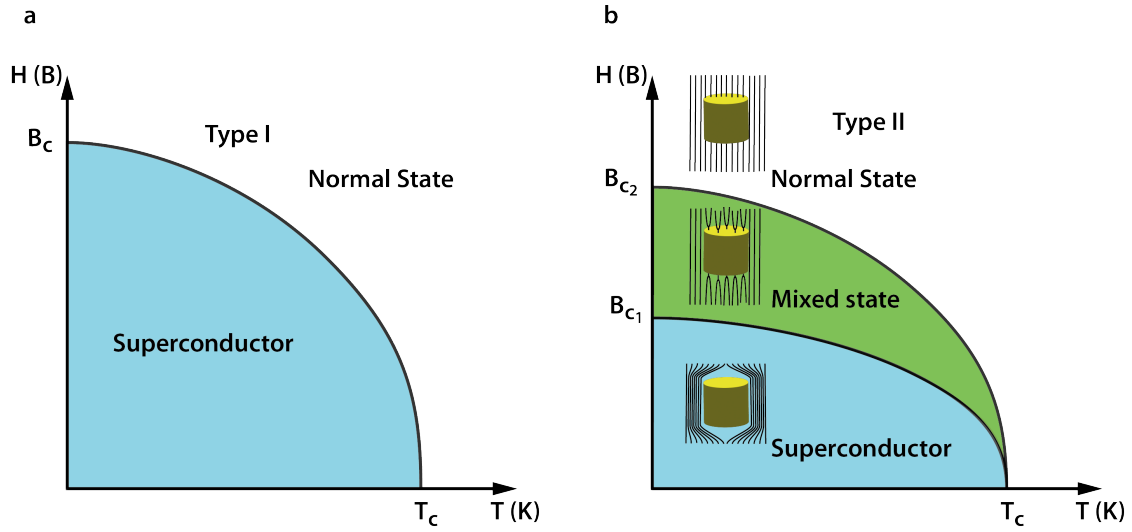


Figure 1.4 – Phase diagrams of a) the type-I and b) the type-II superconductors.

## 4 Abrikosov vortex

In 1957, Alexei Abrikosov, a student of Lev Landau, used the [Ginzburg-Landau](#) theory to demonstrate the entry of magnetic quantum vortices into a superconductor of the second kind and illustrated how they form a lattice structure\*. This discovery gave rise to a broad new direction in the field of superconductivity. The vortices discovered by Abrikosov are now commonly known as the Abrikosov vortices, and the lattice they form is referred to as the Abrikosov lattice. The existence of these vortices and their lattice arrangement has been substantiated by numerous experiments, including direct observations [Connolly, 2008; Stolyarov, 2018; Grigorieva, 2007; Ning, 2010; Vinnikov, 2003], making them integral to understanding superconductivity.

Consider a bulk superconductor with a cylindrical hollow with radius  $\sim \xi$  in the external magnetic field  $\mathbf{H}$ . Then, superconducting current will screen this magnetic field circulating around the hollow part on the length  $\lambda$ . Let us take a closed loop  $C$  around this hollow cylinder. If we place this loop at a distance larger than  $\lambda$  then there superconducting current is zero  $\mathbf{j}_s = 0$  and, according to Eq. 1.20 we can write an equation

$$-\frac{i\hbar e}{2m}(\psi\nabla\psi^* - \psi^*\nabla\psi) - \frac{2e^2}{mc}|\psi|^2\mathbf{A} = 0. \quad (1.25)$$

Far from the cylinder the amplitude of the order parameter is constant and we can express it as  $\psi = \psi_0 e^{i\theta}$ ,  $\theta$  being the phase of the order parameter. Rewriting the last equation using this expression and integrating it over the loop  $C$ , we obtain the following result

$$\oint \hbar\nabla\theta dl - \oint \frac{2e}{c}\mathbf{A}dl = 0. \quad (1.26)$$

---

\*. The original paper contained an error as it suggested a square lattice, the lattice is, in fact, triangular

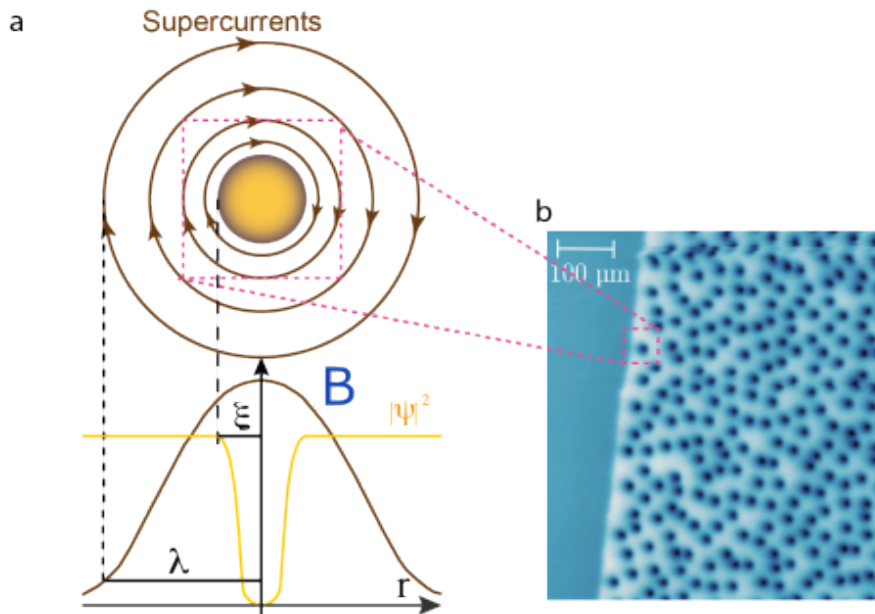


Figure 1.5 – a) The shape of the Abrikosov vortex and the two characteristic scales of a superconductor. b) Experimental observation of Abrikosov vortices by the scanning SQUID microscopy technique, adapted from [Wells, 2015a]

The second integral is just a magnetic flux through the hollow part  $\oint \mathbf{A} dl = \int \nabla \times \mathbf{A} d\mathbf{S} = \int \mathbf{H} d\mathbf{S} = \Phi$ . The first integral is defined by the condition that the function  $\psi$  must be single-valued. This condition means the phase integral equals  $2\pi n$ , where  $n$  is an integer. Combining these two results, we come to the quantisation of the magnetic flux:

$$\Phi = \Phi_0 n, \quad (1.27)$$

where  $\Phi_0 = \frac{\pi \hbar c}{e}$  is the magnetic flux quantum. This shows that in the superconductor the magnetic flux is quantised. In the superconductor of the second type Abrikosov vortices enter into the superconductor carrying exactly this magnetic flux quantum.

Now we will show the field distribution of one Abrikosov vortex. Consider a superconductor of the second type with  $\kappa \gg 1$  in the external magnetic field  $\mathbf{H}$ . In the centre of the vortex, at distance  $\xi$ , the order parameter is suppressed, but it recovers to its bulk value 1 at the penetration depth distance  $\lambda$ , as illustrated Fig 1.5. Using this assumption, we can express the order parameter as  $\psi = e^{i\theta}$ ,  $\theta$  being the phase of the order parameter ( $|\psi| = |e^{i\theta}| = 1$ ). Using this expression and the equality  $\nabla \times \mathbf{A} = \mathbf{H}$  we can write the second Ginzburg-Landau equation as

$$\nabla \times \mathbf{H} = \frac{1}{\lambda^2} \left( \frac{\Phi_0}{2\pi} \nabla \theta - \mathbf{A} \right). \quad (1.28)$$

Applying the operator  $\nabla \times$  to both sides, we get:

$$\lambda^2 \nabla \times (\nabla \times \mathbf{H}) = \frac{\Phi_0}{2\pi} \nabla \times (\nabla \theta) - \mathbf{H} \quad (1.29)$$

Note that we have  $\nabla \times (\nabla\theta) = 0$  everywhere because the curl of the gradient is zero, except at the zero point. The zero point is an exceptional point where the singularity is located. Let us take from this expression the integral over the circle of a surface much larger than  $\xi$  and apply to it Stokes' theorem:

$$\int \nabla \times (\nabla\theta) d\mathbf{S} = \oint \nabla\theta dl, \quad (1.30)$$

where the contour is the contour of our circle.

Since each vortex carries one quantum magnetic flux and the phase shifts by  $2\pi$  while the vortex is surrounded, we got the following expression:

$$\int \nabla \times (\nabla\theta) d\mathbf{S} = 2\pi, \quad (1.31)$$

or in a vector version

$$\nabla \times (\nabla\theta) = 2\pi\delta(\mathbf{r})\mathbf{e}_v, \quad (1.32)$$

where  $\mathbf{e}_v$  is the unit vector in the direction parallel to the vortex axis,  $\delta(\mathbf{r})$  is the Dirac delta function. Inserting this into Eq.1.29 we obtain the following equation

$$\mathbf{H} + \lambda^2 \nabla \times (\nabla \times \mathbf{H}) = \Phi_0 \delta(\mathbf{r}) \mathbf{e}_v. \quad (1.33)$$

Far away from the vortex, the magnetic field is zero, so with the boundary condition  $\mathbf{H}(\infty) = 0$ , the solution of the [Ginzburg-Landau](#) equation for the magnetic field can be written as:

$$\mathbf{H}(r) = \frac{\Phi_0}{2\pi\lambda^2} K_0(r/\lambda), \quad (1.34)$$

where  $K_0$  is a zeroth-order Bessel function and  $r$  is the radius in the plane perpendicular to the vortex line. This equation describes a magnetic field that the vortex created around itself. In the limit  $r \rightarrow 0$ , the function  $K_0(r)$  diverges, but the [Ginzburg-Landau](#) theory is irrelevant on a scale smaller than  $\xi$ . Thus, this function is typically truncated at a distance  $r \approx \xi$  as:

$$\mathbf{H}(0) = \frac{\Phi_0}{2\pi\lambda^2} \ln \kappa. \quad (1.35)$$

As the magnetic field increases, more and more vortices enter the superconducting sample, and these vortices interact with each other through the induced current distribution.

Let us consider the case of two vortices. If these vortices are at a distance greater than the penetration depth  $\lambda$  from each other, the currents created by each of them in their respective regions are small, and they do not significantly interact; they do not feel each other. When considering the condition  $\lambda \gg \xi$ , which allows us to work in the London approximation and neglect the term  $\nabla\psi$ , because the order parameter changes only on a small scale  $\sim \xi$ , the energy density of a single vortex per unit length can be expressed as follows:

$$\epsilon = \frac{1}{8\pi} \int [\mathbf{H}^2(\mathbf{r}) + \lambda^2 (\nabla \times \mathbf{H}(\mathbf{r}))^2] d^2r. \quad (1.36)$$

where  $\mathbf{H}^2(\mathbf{r})$  is the energy density of the normal state inside the core of the vortex, corresponding to the magnetic energy density, and  $\lambda^2(\nabla \times \mathbf{H}(\mathbf{r}))^2$  represents the kinetic energy density associated with the superconducting current. This expression captures the contributions of both the magnetic and the kinetic energy densities within the vortex core. Using the vector analysis identity

$$(\nabla \times \mathbf{H})^2 = [\mathbf{H}, \nabla \times \nabla \times \mathbf{H}] - \nabla \cdot [\nabla \times \mathbf{H}, \mathbf{H}] \quad (1.37)$$

we can rewrite the energy density per unit length as:

$$\begin{aligned} \epsilon &= \frac{1}{8\pi} \left( \int \mathbf{H} (\mathbf{H} + \lambda^2(\nabla \times \nabla \times \mathbf{H})) d^2r + \int \nabla \cdot [\nabla \times \mathbf{H}, \mathbf{H}] d^2r \right) = \\ &= \frac{1}{8\pi} \left( \int \mathbf{H} (\mathbf{H} + \lambda^2(\nabla \times \nabla \times \mathbf{H})) d^2r + \oint [\nabla \times \mathbf{H}, \mathbf{H}] d\mathbf{l} \right). \end{aligned} \quad (1.38)$$

The contour integral equals zero when integration is taken at the infinite distance because  $\mathbf{H} \rightarrow 0$  when  $\mathbf{r} \rightarrow \infty$ . The first term can be simplified using Eq.1.33. The final result is

$$\epsilon = \frac{1}{8\pi} \int \mathbf{H} \Phi_0 \delta(\mathbf{r}) \mathbf{e}_z = \frac{\Phi_0^2}{(4\pi\lambda)^2} \ln \kappa. \quad (1.39)$$

This energy density is positive, as expected. It indicates that a positive energy is required to introduce an Abrikosov vortex into the superconductor, consistent with the notion that a magnetic field must be applied to create the vortex

Now, let's consider the energy of a pair of vortices at a distance on the order of  $\lambda$ . When another vortex is added, the total energy density will consist of the energy density of each vortex separately and the energy density of their interaction with each other. The interaction energy will depend on the separation distance between the vortices and their relative positions. The latter, taking into account the equation Eq.1.33 with two sources, which must also be fulfilled, can be written as:

$$\begin{aligned} \epsilon &= \frac{1}{8\pi} \int \mathbf{H} \cdot [\mathbf{H} + \lambda^2 \nabla \times (\nabla \times \mathbf{H})] d^2\mathbf{r} \\ &= \frac{\Phi_0}{8\pi} \int [\mathbf{H} \delta(\mathbf{r} - \mathbf{r}_1) + \mathbf{H} \delta(\mathbf{r} - \mathbf{r}_2)] d^2\mathbf{r} \\ &= \frac{\Phi_0}{8\pi} (H(\mathbf{r}_1) + H(\mathbf{r}_2)), \end{aligned} \quad (1.40)$$

where  $H(\mathbf{r}_1)$  ( $H(\mathbf{r}_2)$ ) is the magnetic field in the centre of the first (second) vortex. It consists of a field created by the vortex itself and a magnetic field  $H_{12}(|\mathbf{r}_1 - \mathbf{r}_2|)$  created by another vortex in the centre of this one. The same applies to the other vortex. Otherwise, this energy density can be represented as:

$$\epsilon = 2\epsilon + \frac{\Phi_0}{4\pi} H_{12}(|\mathbf{r}_1 - \mathbf{r}_2|) \quad (1.41)$$

The last term can be considered as the interaction energy  $\epsilon_{12}$  and written as:

$$\epsilon_{12} = \frac{\Phi_0}{4\pi} H_{12}(|\mathbf{r}_1 - \mathbf{r}_2|) = \frac{\Phi_0^2}{8\pi^2\lambda^2} K_0(r/\lambda), \quad (1.42)$$

where  $r = (|\mathbf{r}_1 - \mathbf{r}_2|)$ . This energy is also positive, which means that the interaction between vortices of the same momentum is repulsive, while the interaction between vortices of different momentum is attractive.

In order to find the force acting on each vortex, we need to differentiate the interaction energy:

$$f_L = \frac{d\epsilon_{12}}{dr} = \frac{\Phi_0}{4\pi} \frac{dH_{12}}{dr} = \frac{\Phi_0}{c} j_{12}, \quad (1.43)$$

where  $j_{12}$  is the current density at the core of the first vortex created by another vortex. This formula is very general, and this force  $f_L$  is called the Lorentz force. Note that here the current density  $j_{12}$  can be created by various sources, including an external current source.

Each vortex carries a quantum of magnetic flux, resulting in the formation of a magnetic field according to the Faraday law of induction. The motion of vortices leads to the dissipation of energy. We can consider the motion of vortices in a viscous medium, and a frictional force can be introduced:

$$f_{friction} = -\eta v \quad (1.44)$$

where  $\eta$  is the friction coefficient and  $v$  is the vortex speed. In equilibrium, it is compensated with the Lorentz force. Then for a volume with a vortex density  $n$  we can write the following force balance equation

$$f_{friction} + f_L = -\frac{B}{\Phi_0} \eta v + \frac{1}{c} B j_{12} = 0 \quad (1.45)$$

Here,  $B = n\Phi_0$  is the magnetic field carried by vortices with the density  $n$ . Consequently, we obtain the resistance to the flow of vortices using Faraday's law of induction  $E = Bv/c$ :

$$\rho_{flow} = \frac{\Phi_0 B}{c^2 \eta}. \quad (1.46)$$

In real materials, vortices can stop and pin on the pinning centres, which are various defects. The description of the types and nature of pinning is a rather extensive field.

## 5 Time-dependent Ginzburg-Landau (TDGL)

Since the [Ginzburg-Landau](#) equations describe only stationary solutions, it is necessary to use other approaches, such as the solution of the Gorkov equations, to describe non-stationary processes. But the solution of the Gorkov equations is technically incredibly difficult and we would like some scheme like the [Ginzburg-Landau](#) equations. However, it

turned out to be extremely difficult to construct a general non-stationary system of the [Ginzburg-Landau](#) equations. The difficulty consists in taking into account in the time representation of the peculiarity in the density of states at the edge of the superconductor gap. The first time generalisation of the equations was proposed by Schmid [Schmid, 1966]. Then it was shown by Gorkov and Eliashberg [Eliashberg, 1969; GORKOV, 1968] that in the presence of a large number of scattering centres (impurities) the gap feature is weakened and the superconductor becomes gapless. In this case, one can strictly justify the form of the [Time-Dependent Ginzburg-Landau \(TDGL\)](#) equations proposed by Schmid [Schmid, 1966]. The TDGL equations can be written as [Gropp, 1996]

$$\begin{aligned} \frac{\hbar^2}{2m_s D} \left( \frac{\partial}{\partial t} + i \frac{e_s}{\hbar} \mu \right) \psi &= - \frac{\delta F}{\delta \psi^*} \\ \frac{\sigma}{c} \left( \frac{1}{c} \frac{\partial \mathbf{A}}{\partial t} + \nabla \mu \right) &= - \frac{\delta F}{\delta \mathbf{A}} - \frac{1}{4\pi} \nabla \times \nabla \times \mathbf{A} \end{aligned} \quad (1.47)$$

where  $\psi$  is the [Ginzburg-Landau](#) order parameter,  $\mathbf{A}$  is the vector potential,  $\mu$  is the electric (scalar) potential,  $F$  is the free-energy density functional,  $t$  is the time,  $\sigma$  is the conductivity in the normal state,  $D$  is the phenomenological diffusion constant,  $m_s$  and  $e_s$  are the mass and charge of the Cooper pair, correspondingly. The free energy density  $F$  is given by the same expression as in stationary [Ginzburg-Landau](#) theory:

$$F = a|\psi|^2 + \frac{b}{2}|\psi|^4 + \frac{1}{2m_s} \left| \left( \frac{\hbar}{i} \nabla - \frac{e_s}{c} \mathbf{A} \right) \psi \right|^2 \quad (1.48)$$

Taking the variational derivative, one rewrites these equations in a familiar way

$$\begin{aligned} \frac{\hbar^2}{2m_s D} \left( \partial_t + i \frac{e_s}{\hbar} \mu \right) \psi &= |a|\psi - b|\psi|^2\psi \\ &\quad - \frac{1}{2m_s} \left( \hbar \nabla + \frac{e_s}{ic} \mathbf{A} \right)^2 \psi \\ \nabla \times (\nabla \times \mathbf{A}) &= \frac{4\pi}{c} [\mathbf{J}_N + \mathbf{J}_S] \end{aligned} \quad (1.49)$$

where  $\mathbf{J}_N$  and  $\mathbf{J}_S$  are normal and superconducting current density correspondingly

$$\begin{aligned} \mathbf{J}_N &= -\sigma \left[ \frac{1}{c} \partial_t \mathbf{A} + \nabla \mu \right] \\ \mathbf{J}_S &= -\frac{e}{2m} \left[ \psi^* \left( i \hbar \nabla + \frac{2e}{c} \mathbf{A} \right) \psi + \text{c.c.} \right] \end{aligned} \quad (1.50)$$

here c.c. is a complex conjugated.

It is convenient to work with this system in dimensionless units. For this purpose, we need to choose a characteristic scale for each magnitude. We will denote the new coordinates with a dashed line. The order parameter, as known from the [Ginzburg-Landau](#) theory, effectively changes at length  $\xi$ , which is convenient to take as a characteristic dimensional scale. Then spatial differential operators in the new coordinates will be written

as

$$q = \xi q' \Rightarrow \frac{d}{dq} = \frac{d}{\xi dq'}, \quad q = \{x, y, z\} \quad (1.51)$$

The amplitude of the order parameter is normalised in the same way as in the [Ginzburg-Landau](#) theory:  $\psi = \psi_0 \psi'$ , where  $\psi_0 = \sqrt{|a|/b}$ . Time is normalised as  $t = \tau t'$ , where  $\tau = \frac{4\pi\sigma\lambda^2}{c^2}$ . The vector potential  $\mathbf{A}$  varies on the scale  $\lambda$ , but this value we will define through the [Ginzburg-Landau](#) parameter  $\kappa$  as  $\lambda = \kappa\xi$ . The [Ginzburg-Landau](#) parameter  $\kappa$  is itself an input parameter of the system. The amplitude of the potential vector is conveniently normalised by the magnetic field values and the distance characteristic of the system:  $\mathbf{A} = H_{c2}\xi\mathbf{A}'$ , where  $H_{c2}$  is the second critical field. The magnetic field itself is then measured in units of the second critical field. Then the scalar potential, according to the formula, will be written in the new coordinates as  $\mu = \mu_0, \mu'$ , where  $\mu_0 = \frac{\hbar}{2e\tau\xi}$ . And, consequently, the characteristic scale for the current  $\mathbf{J} = J_0\mathbf{J}'$ , where  $J_0 = \frac{\hbar\sigma}{2e\tau\xi}$ .

Finally, in the new normalised coordinates, the equations are written as

$$\begin{aligned} u(\partial_\tau + i\mu)\psi &= \epsilon(\mathbf{r})\psi - |\psi|^2\psi + (\nabla - i\mathbf{A})^2\psi \\ \varkappa^2\nabla \times (\nabla \times \mathbf{A}) &= \mathbf{J}_N + \mathbf{J}_S \end{aligned} \quad (1.52)$$

These equations as well as static [Ginzburg-Landau](#) equations are invariant under gauge transformations

$$\begin{aligned} \psi &\mapsto \psi e^{i\chi}, \\ \mathbf{A} &\mapsto \mathbf{A} + \nabla\chi \\ \mu &\mapsto \mu - \frac{\partial\chi}{\partial t}, \end{aligned} \quad (1.53)$$

The invariance has not only a fundamental physical meaning but also allows us to simplify the calculation in some cases. For example, by choosing the zero-scalar  $\mu = 0$  potential calibration, one can completely exclude the scalar potential from the equations:

$$\begin{aligned} u\partial_\tau\psi &= \epsilon(\mathbf{r})\psi - |\psi|^2\psi + (\nabla - i\mathbf{A})^2\psi, \\ \varkappa^2\nabla \times (\nabla \times \mathbf{A}) &= -\sigma(1/c)\partial_t\mathbf{A} - \frac{e}{2m} \left[ \psi^* \left( i\hbar\nabla + \frac{2e}{c}\mathbf{A} \right) \psi + \text{c.c.} \right] \end{aligned} \quad (1.54)$$

To solve the [TDGL](#) equations, it is also necessary to supplement them with boundary and initial conditions. Similarly to the [Ginzburg-Landau](#) equations, the boundary conditions for the order parameter at the superconductor-vacuum boundary will be written as follows:

$$\mathbf{n} \cdot (\nabla - i\mathbf{A})\psi = 0, \quad (1.55)$$

the boundary conditions for the potential vector are determined from the equality to the external magnetic field at the boundary

$$\nabla \times \mathbf{A} = \mathbf{H}_{ext}, \quad (1.56)$$

Let us finally discuss the applicability region of the [TDGL](#) approach. Formally, the [TDGL](#) equations are justified, like the stationary [Ginzburg-Landau](#) equations, only near the crit-

ical temperature and for slowly varying electromagnetic fields. In addition, they are valid only for gapless superconductors, based on the conclusion of Gorkov. Furthermore, this theory is local, relating the local field  $\mathbf{A}$  to the local superconducting current density  $j_s$ . Such an approximation is possible under the condition  $\lambda \geq \xi$ , satisfied by London superconductors. However, in most applications of interest, the TDGL equations qualitatively describe the behaviour of the Abrikosov vortices, even beyond the strict limits of applicability. This is partly due to the fact that, for example, in the limit of dirty superconductors, the effective coherence length is smaller and proportional to  $\sim \sqrt{\xi l}$ , where  $l$  is the free path length  $l \ll \xi$ . This effect extends the limits of applicability. The restriction to gapless superconductors can be addressed by the generalisation of the TDGL equations, known as the so-called generalised TDGL equation:

$$\frac{u}{\sqrt{1+\gamma^2|\Psi|^2}} \left( \frac{\partial}{\partial t} + i\mu + \frac{1}{2}\gamma^2 \frac{\partial |\Psi|^2}{\partial t} \right) \Psi = (\nabla - i\mathbf{A})^2 \Psi + (1 - T - |\Psi|^2) \Psi \quad (1.57)$$

where  $\gamma$  is a parameter describing inelastic electron-phonon collisions and  $T$  is the temperature. These equations were first obtained by Kramer and Watts-Tobin [Kramer, 1978] based on the linearised Eilenberger equations in the dirty superconductor approximation.

## 6 Conclusion

In this chapter, we have presented a brief history of the development of the field of superconductivity from the beginning of the discovery of the phenomenon to current issues and developments. We have highlighted separately those theoretical aspects and details that are important and will be used in the subsequent chapters of this work. Much attention is paid to the phenomenological Ginzburg-Landau theory, which due to its simplicity allows us to obtain a large number of physical results and to the phenomenon of Abrikosov vortices, because their influence on the properties of superconductors of the second kind can hardly be overestimated. We have also briefly described the apparatus of TDGL theory, which we will use in the future for numerical modelling of realistic experimental structures.

# Chapter 2

## High temperature superconductors

### Objectives

In this chapter we give the discovery and the main properties of High Temperature Superconductors with a focus on  $\text{YBa}_2\text{Cu}_3\text{O}_{7-\delta}$ .

### Contents

|   |  |    |
|---|--|----|
| 1 | High temperature superconductors: the short story of its discovery . . . . .             | 19 |
| 2 | Crystal structures . . . . .   | 20 |
| 3 | Properties of $\text{CuO}_2$ planes . . . . .  | 21 |
| 4 | Electronic properties of $\text{YBa}_2\text{Cu}_3\text{O}_{7-\delta}$ . . . . .          | 24 |
|   | 4.1 Phase Diagram . . . . .  | 24 |
|   | 4.2 Superconducting properties in $\text{YBa}_2\text{Cu}_3\text{O}_{7-\delta}$ . . . . . | 25 |
| 5 | Thin Film growth . . . . .   | 26 |
| 6 | Conclusion . . . . .   | 30 |

In the period following the discovery of superconductivity in mercury by Kammerlingh Ohnes in 1911, many groups explored a large number of metals and alloys for superconducting properties. The BCS shed light on the microscopic mechanism behind superconductivity in certain metals and alloys, they are the so-called conventional superconductors. This theory predicts two effects : the formation of Cooper pairs through electron pairing and the emergence of a gap in the spectrum of electronic excitations. The crystal lattice plays a role in this pairing mechanism by screening the coulomb interactions between the two electrons in a pair. This leads to the creation of new, more energetically favourable electronic states known as Cooper pairs. These pairs behave as bosons and can condense into the same macroscopic quantum state below a critical temperature denoted as  $T_c$ . The outcome is a state of zero electrical resistance. The presence of a gap in the spectrum of excitations at zero temperature reflects the energy required to break a pair in the condensate.

During that period, the BCS theory, along with Matthias' heuristic law from 1957, offered valuable criteria to assist experimentalists in their quest to identify new superconducting materials among metals and alloys. These criteria included high crystalline symmetry, high electron density, the absence of insulating, oxide, and magnetic properties. Consequently, researchers discovered hundreds of superconductors, while some materials did not exhibit these properties. The highest critical temperature  $T_c$  observed reached its peak at 23 K in Nb<sub>3</sub>Ge [Païdassi, 1979] in 1979. The BCS theory provided an explanation for this ceiling in critical temperature. Over nearly six decades, the critical temperature experienced an incremental increase of approximately 0.4 K per year. As a result, research into superconductivity experienced a commensurate slowdown.

## 1 High temperature superconductors: the short story of its discovery

In this context, the discovery by Bednorz and Müller \* of superconductivity at 30 K in 1986 [Bednorz, ] triggered the start of a wild race for superconducting materials in oxides and renewed interest in "unconventional" superconductivity, which broke the paradigm. In 1987, superconductivity in YBa<sub>2</sub>Cu<sub>3</sub>O<sub>7- $\delta$</sub>  [Wu, 1987a] was discovered with a  $T_c=93$  K above the temperature of liquid nitrogen. This opened up new horizons for the introduction of superconductors into applications.

Müller's experiment with oxides was decisive and led him, with the help of his colleague Bednorz, to go against the stream and look for materials in which a structural transition would cause a strong increase in the interaction between pairs of electrons. This interaction was different from the traditional Debye phonon responsible for the  $T_c$  cap in BCS theory. The Jahn-Teller structural transition in perovskite materials generated a much stronger electron-phonon coupling.

**High-Temperature Superconductors** can be classified into two broad classes : those

---

\*. he made a significant contribution to the understanding of SrTiO<sub>3</sub>-

based on copper oxides (or cuprates) and those based on iron (pnictures). Here, we will focus on  $\text{YBa}_2\text{Cu}_3\text{O}_{7-\delta}$ .

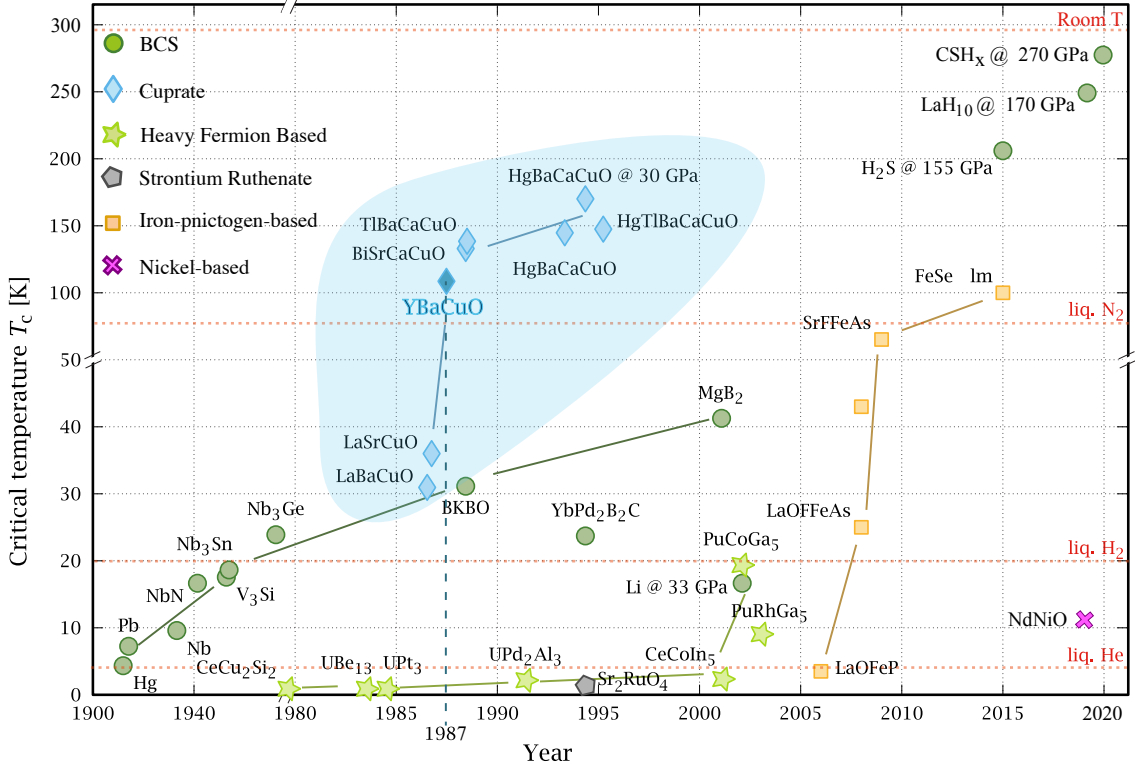


Figure 2.1 – Different classes of superconducting materials shown in colour adapted from wikipedia [Ray, 2015] : BCS (dark green circle), based on heavy fermions (green star), cuprates (blue diamond), based on iron-pnicture (orange square), strontium ruthenate (grey pentagon), nickel (pink cross).  $\text{YBa}_2\text{Cu}_3\text{O}_{7-\delta}$  compound has been outlined with its discovery in 1987.

## 2 Crystal structures

High-temperature superconductors have a generic crystal structure derived from a cubic perovskite structure of the  $\text{ABX}_3$  type shown in figure 2.11b, where X is an oxygen (O) atom. They are structured so that a stack of several  $\text{CuO}_2$  conductive planes (from 1 to 5 planes) separated by Yttrium (Y) or Calcium (Ca) atoms, alternating with blocks of BO/AO/BO type oxides which are themselves charge reservoirs (B being an alkaline-earth metal of the Barium (Ba) or Strontium (Sr) type, and A being, for example, Bismuth (Bi), Calcium (Ca), Lead (Pb), Thallium (Tl)).

The elementary cell of  $\text{YBa}_2\text{Cu}_3\text{O}_{7-\delta}$ , figure 2.11c, is composed of three oxygen-deficient perovskite meshes in which the Barium atom (Ba) and the Yttrium atom (Y) at the centre of a cube, are surrounded by Copper atoms (Cu) at the vertices of the cube, and Oxygen atoms (O) at the centre of the edges. The two conductive planes are separated by the Yttrium atom. The elementary lattice has very close  $a$  and  $b$  parameters, which is the

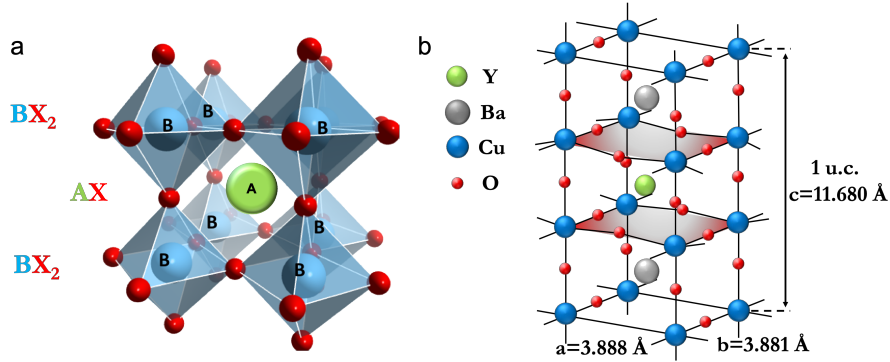


Figure 2.2 – a)  $\text{ABX}_3$ -type perovskite lattice, where A is an alkali metal, alkaline earth or rare earth cation, B is a transition metal cation and X is  $\text{O}^{-2}$  b)  $\text{YBa}_2\text{Cu}_3\text{O}_{7-\delta}$  unit cell.

reason for the quasi-systematic presence of macles in the films. Depending on the oxygen doping, the crystallographic structure of  $\text{YBa}_2\text{Cu}_3\text{O}_{7-\delta}$  can evolve from the tetragonal phase for  $\text{YBa}_2\text{Cu}_3\text{O}_{7-\delta}$  to an orthorhombic phase for the optimum doping, while passing through intermediate phases for the other dopings.

All cuprates have in common the presence of  $\text{CuO}_2$  planes separated from each other by other planes, acting as charge reservoirs and structural stabilisers. In the following section, we will provide a brief description of the properties of these planes upon which superconductivity is based.

### 3 Properties of $\text{CuO}_2$ planes

In the  $\text{CuO}_2$  planes shown in Figure 2.3b, the  $\text{Cu}^{2+}$  transition ions have a valence configuration of  $3d^9$  and are positioned at the centre of an octahedron formed by six oxygen atoms, as depicted in Figure 2.3a. The apical oxygen atom is not included in this arrangement. As a result, the Cu band is partially filled, leaving a single hole with a spin of  $1/2$ . In the presence of the crystalline field, similar to the case of the Ti atom in  $\text{SrTiO}_3$ , there is a lifting of degeneracy in the energy levels of the five 3d orbitals of Cu. This splitting results in  $e_g$  orbitals (for  $d_{xy}$ ,  $d_{yz}$ , and  $d_{xz}$ ) and  $t_{2g}$  orbitals (for  $d_{3z^2-r^2}$  and

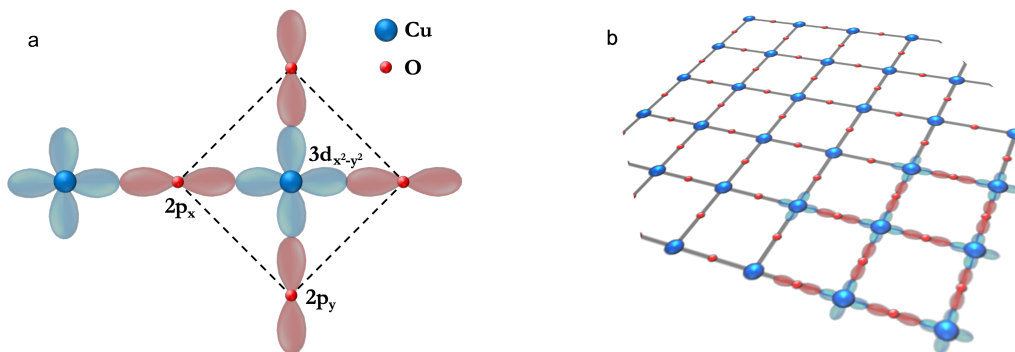


Figure 2.3 – a) Orbitals of the Cu and O atoms involved in  $\text{CuO}_2$  planes. b) Schematic arrangement of Cu-O-Cu bonds in  $\text{CuO}_2$  planes.

$d_{x^2-y^2}$ ), as shown in Figure 2.3c. Furthermore, the Jahn-Teller tetragonal deformation along the  $z$  axis further lifts the degeneracy of the  $e_g$  levels, with the highest energy level,  $d_{x^2-y^2}$ , being partially filled. The  $p$  orbitals of oxygen are also partially degenerate. The lowest energy level corresponds to the  $d_{xy}$ ,  $d_{yz}$ , and  $d_{xz}$  orbitals, which do not point toward oxygen atoms, and thus, are less affected by Coulombic repulsion.

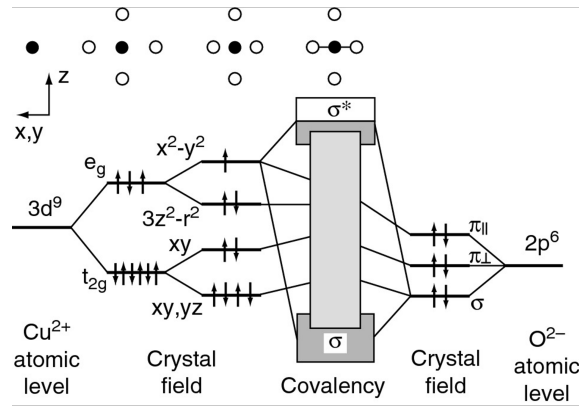


Figure 2.4 – Energy diagram of the 3d Cu and 2p O orbitals, and their hybridisation [Alloul, 2009]

The  $d_{x^2-y^2}$  orbital of copper aligns with the  $p_x$  or  $p_y$  orbitals of oxygen, resulting in strong hybridization and a very strong covalent Cu-O-Cu bond within the  $\text{CuO}_2$  planes, as schematically represented in Figure 2.5. The Coulombic repulsion ( $U$ ) between the  $1/2$  spins of  $\text{Cu}^{2+}$  is exceptionally high, in the order of tens of electronvolts (eV), and it dominates all other energy scales in the system. It's important to note that the electron jump term ( $t_{pd}$ ) between the Cu and O orbitals is relatively high, approximately 1.5 eV. The strong Coulombic repulsion ( $U$ ) between the Cu atoms in the planes, in the absence

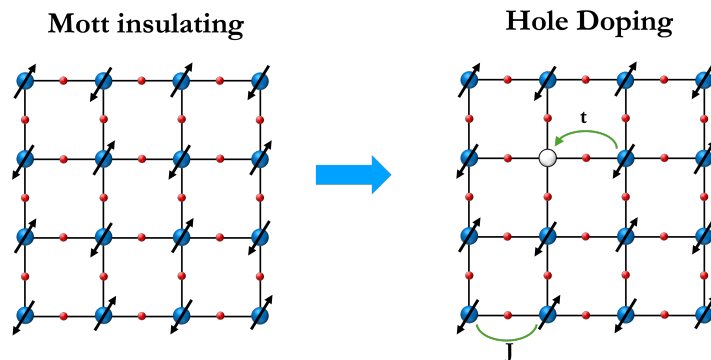


Figure 2.5 – Schematic of the  $\text{CuO}_2$  plane in its Mott insulator phase and in the case of hole doping.

of any doping, results in electrons being localized at each of the sites, as schematically represented in Figure 2.6. An uncorrelated band calculation for a partially filled  $d$  band would predict the material's metallicity. However, the parent compound of the cuprates is an insulator, more precisely, a Mott insulator. This is because the Coulombic repulsion

( $U$ ) between the high and low Hubbard bands on the Cu sites exceeds the bandwidth. These compounds can be classified as charge-transfer Mott insulators, as distinct from Mott-Hubbard insulators. This distinction arises from the energy values of the electronic levels ( $\epsilon_p$  for O and  $\epsilon_d$  for Cu), which are among the closest within the transition ions. The

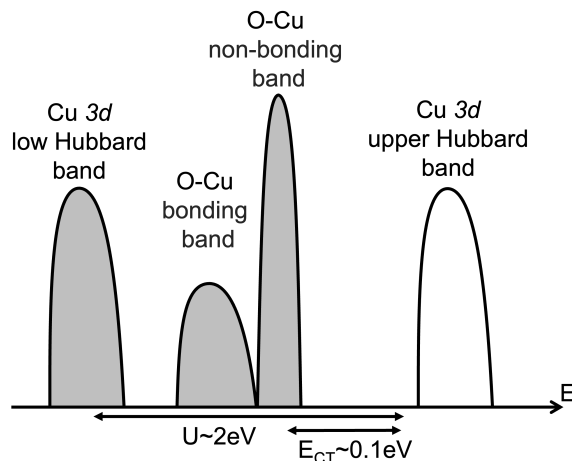


Figure 2.6 – Band structure of a  $\text{CuO}_2$  plane. The Hubbard bands of Cu, and the bonding and non-bonding bands of O-Cu are shown,  $U$  is the coulombic interaction energy on Cu.

lowest excitation energy in undoped cuprates remains weak compared to the Coulombic repulsion. Undoped cuprates can be described as a model system using the Heisenberg Hamiltonian with  $1/2$  spins in two dimensions, involving the  $t$  hopping term and the  $J$  site exchange coupling.

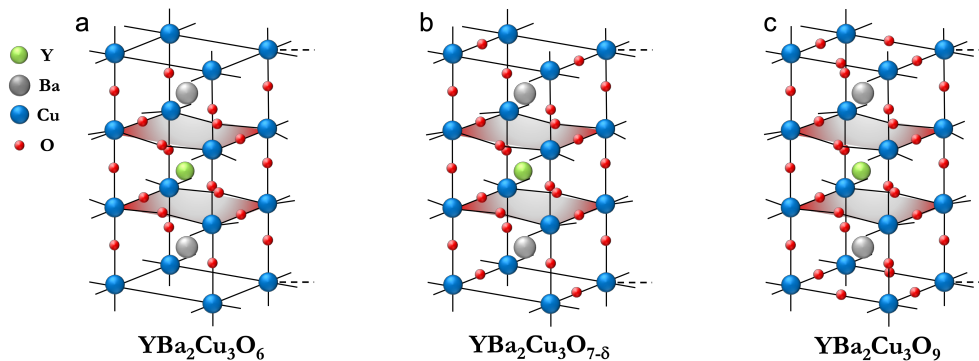


Figure 2.7 – YBCO Unit Cell for Different Doping Levels a) Insulating underdoped  $\text{YBa}_2\text{Cu}_3\text{O}_6$  where in the  $\text{CuO}$  chains there are no oxygen ions. b) Optimally doped  $\text{YBa}_2\text{Cu}_3\text{O}_{7-\delta}$  c) Overdoped  $\text{YBa}_2\text{Cu}_3\text{O}_9$ : in this case, the  $\text{CuO}$  chains are fully occupied by oxygen ions.

If undoped  $\text{CuO}_2$  planes are insulating, their properties can be modulated by controlling electron or hole doping. This modulation can be achieved through various means, such as substituting atoms with different valencies, creating oxygen vacancies, or incorporating oxygen. Hole doping is typically accomplished by substituting divalent atoms with trivalent atoms, as seen in the substitution of  $\text{Y}^{3+}$  with  $\text{Ca}^{2+}$  in  $\text{YBa}_2\text{Cu}_3\text{O}_{7-\delta}$  to obtain

$Y_{1-x}Ca_xBa_2Cu_3O_{6+y}$ . Another approach is to modify reservoir blocks, which, through charge transfer, introduce holes into the  $CuO_2$  planes.  $YBa_2Cu_3O_6$  is insulating, while  $YBa_2Cu_3O_{7-\delta}$  is superconducting due to hole doping.

In a more general sense, precise control over the doping of  $CuO_2$  planes allows for the exploration of a common phase diagram shared by all cuprates, as shown in Figure 2.8. Typically, this generic phase diagram is constructed based on various chemical dopings, which may involve multiple samples or different chemical and physical treatments of the same sample.

## 4 Electronic properties of $YBa_2Cu_3O_{7-\delta}$

### 4.1 Phase Diagram

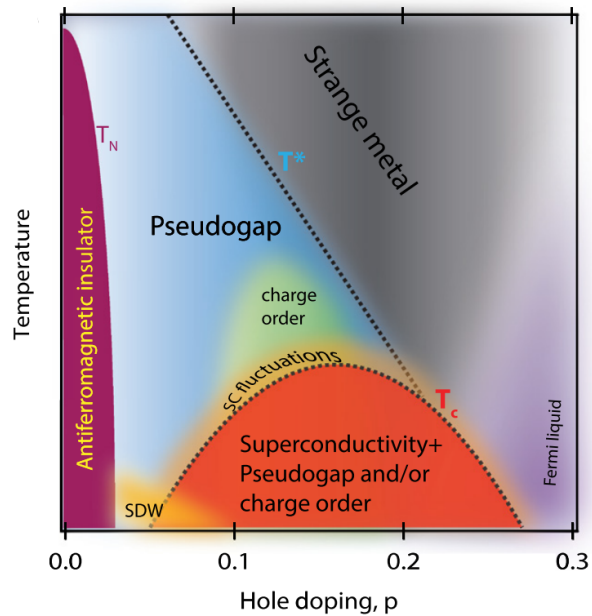


Figure 2.8 – Generic phase diagram of cuprates [Vishik, 2018].

Figure 2.8 shows the phase diagram for hole-doped cuprates, specifically the case of  $YBa_2Cu_3O_{7-\delta}$ . In this case, the mobile carriers are positive charges. The cuprate diagram illustrates different electronic phases. The parent compound of  $YBa_2Cu_3O_{7-\delta}$  is a Mott Insulator, see figure 2.6. In the absence of doping, there is antiferromagnetic order with a Neel temperature that decreases with hole doping. Conversely, there is a superconducting order with a specific doping value where the critical temperature is at its maximum, often referred to as the optimum doping point. In the overdoped regime and in the normal state, we observe metallic behaviour of the Fermi liquid type (characterized by a temperature dependence of  $T^2$ ) or of the anomalous metal type (linear resistance dependence on temperature) for lower doping levels. As doping decreases further, we reach a phase known as the pseudo-gap, marked by a gap in the spectrum of excitations, which seems to characterize a freezing of low-energy excitations. Each region of this diagram has been

studied using various experimental probes, both resonant and non-resonant, local and global, optical, electrical, thermoelectric, etc. [Tsuei, 1994; Tsuei, 2000; Bobroff, 2005; OMahony, 2022].

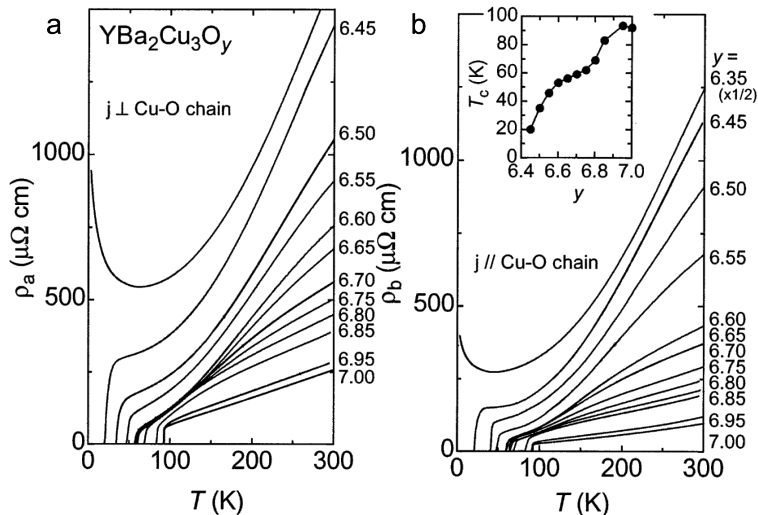


Figure 2.9 – Anisotropy of resistivity measured in-plane (a) and out-of-plane (b). [Segawa, 2003].

Electronic transport in cuprates exhibits high anisotropy. The conductivity perpendicular to  $\text{CuO}_2$  planes can be more than 1000 times lower than in-plane conductivity. If we consider the cuprates  $\text{YBa}_2\text{Cu}_3\text{O}_{7-\delta}$ , the conductivity anisotropy is of a factor of 30 [Segawa, 2003] at room temperature, see figure 2.9.

## 4.2 Superconducting properties in $\text{YBa}_2\text{Cu}_3\text{O}_{7-\delta}$

The  $\text{CuO}_2$  planes harbor superconductivity. Several experimental studies using different techniques [Ding, 1996; Tsuei, 1994; Wollman, 1993] [Wollman, 1993; Hilgenkamp, 2003; Tsuei, 2000; OMahony, 2022] have demonstrated the existence of a knot in the non-isotropic gap of superconductors at high critical temperature, as shown in Figure 2.10. This work has led to a consensus on the symmetry of the order parameter, which is of the  $d_{x^2-y^2}$  type. Quasi-particles can therefore exist down to absolute zero, along nodal lines at  $45^\circ$  to the lobe direction. The superconducting characteristic lengths are different in the  $ab$  plane and along the  $c$  axis, resulting in significant anisotropy in critical fields in these two directions.

The d-type wave symmetry of the superconducting order parameter in  $\text{YBa}_2\text{Cu}_3\text{O}_{7-\delta}$  enhances its sensitivity to defects. Each defect acts as a depairing centre for the Cooper pairs. By controlling the amount of disorder introduced, the superconducting properties of a thin film of  $\text{YBa}_2\text{Cu}_3\text{O}_{7-\delta}$  can be finely tuned. This effect has been demonstrated using different types of sources (electrons [Rullier-Albenque, 2001],  $\text{Ga}^+$  [Chen, 1989],  $\text{He}^+$  [Lesueur, 1993],  $\text{O}^+$  ions [Bergeal, 2005]). This is the technique we have used, and will describe in the next chapter, to fabricate  $\text{YBa}_2\text{Cu}_3\text{O}_{7-\delta}$ -based superconducting nanowires.

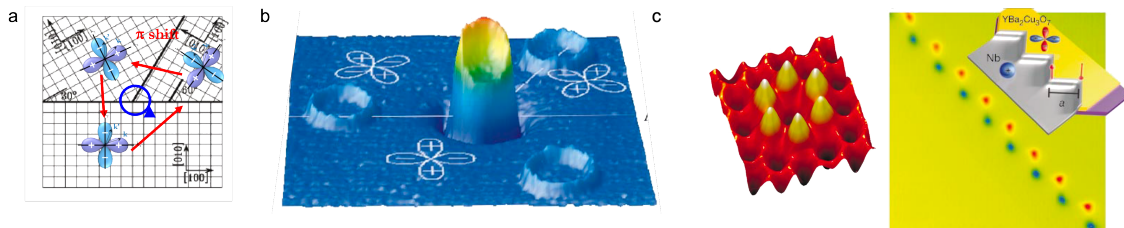


Figure 2.10 – a) Schematic diagram of the tri-crystalline substrate of  $\text{SrTiO}_3$  (100), with four epitaxial  $\text{YBa}_2\text{Cu}_3\text{O}_{7-\delta}$  rings. b) Scanning SQUID microscope image of the four superconducting rings, cooled under a magnetic field of approximately 5 mG [Tsuei, 1994]. c) Ordered antiferromagnetic lattice of half-flow quanta spontaneously generated in a zigzag lattice ( $\text{YBa}_2\text{Cu}_3\text{O}_{7-\delta}$ -Au-Nb) [Hilgenkamp, 2003].

In bulk cuprates, the coherence length is approximately  $\xi_0 = 2$  nm, and the mean free path is on the order of  $l_e = 15$  nm [Krishana, 1995; Tang, 2000; Wells, 2015b]. Therefore, superconductivity in the  $\text{CuO}_2$  planes is in the so-called clean limit. This type of superconductivity is of type II, and the Ginzburg-Landau parameter satisfies  $\kappa = \lambda/\xi \gg 1$ . Transport properties are dominated by vortex dynamics.

The closing section of this chapter will detail the primary technique employed for thin film growth. Additionally, it will provide an overview of the original samples that have been the focus of investigation throughout our work.

## 5 Thin Film growth

Typically,  $\text{YBa}_2\text{Cu}_3\text{O}_{7-\delta}$  deposition is performed on a mono-crystalline substrate, often an oxide like sapphire,  $\text{LaAlO}_3$ , or  $\text{MgO}$ . A suitable buffer layer, such as  $\text{CeO}_2$  (with a lattice parameter adapted to  $\text{YBa}_2\text{Cu}_3\text{O}_{7-\delta}$  growth) or  $\text{SrTiO}_3$  (with a lattice parameter close to  $\text{YBa}_2\text{Cu}_3\text{O}_{7-\delta}$ ), is employed. In the case of a silicon substrate, a multilayer approach like  $\text{Si}/\text{SrTiO}_3/\text{YBa}_2\text{Cu}_3\text{O}_{7-\delta}$  or  $\text{Si}/\text{YSZ}/\text{CeO}_2/\text{YBa}_2\text{Cu}_3\text{O}_{7-\delta}$  (YSZ for Yttrium Stabilized Zirconia) can be utilized. Various techniques are available for  $\text{YBa}_2\text{Cu}_3\text{O}_{7-\delta}$  thin film growth, with sputtering, evaporation, molecular beam epitaxy, and pulsed laser ablation being the main methods. The thin films utilized in our work are primarily produced using the latter two techniques.

Molecular jet evaporation and epitaxy necessitate a partial oxygen vacuum of approximately  $10^{-4}$  mbar, a rotating substrate heated to temperatures between  $650^\circ\text{C}$  and  $800^\circ\text{C}$ , and crucibles made of materials like Y, Ba, and Cu. These crucibles are heated through the joule effect or by an electron gun, enabling the materials to evaporate onto the hot, rotating target substrate.

In the Pulsed Laser Ablation (PLD) growth technique, Ultraviolet (UV) light from a class IV laser is focused through a lens onto a target inside a chamber. The chamber is kept at a low gas pressure (in our case, Oxygen), so that the atoms extracted by the laser beam can reach the substrate, which faces the target. The substrate is heated, in our case by a heating element fig 2.11, so as to give energy to the atoms and thus obtain an ordered

structure. The parameters that need to be controlled are:

1. Pressure in the chamber during growth;
2. Substrate temperature
3. Laser energy on the target
4. Target-substrate distance

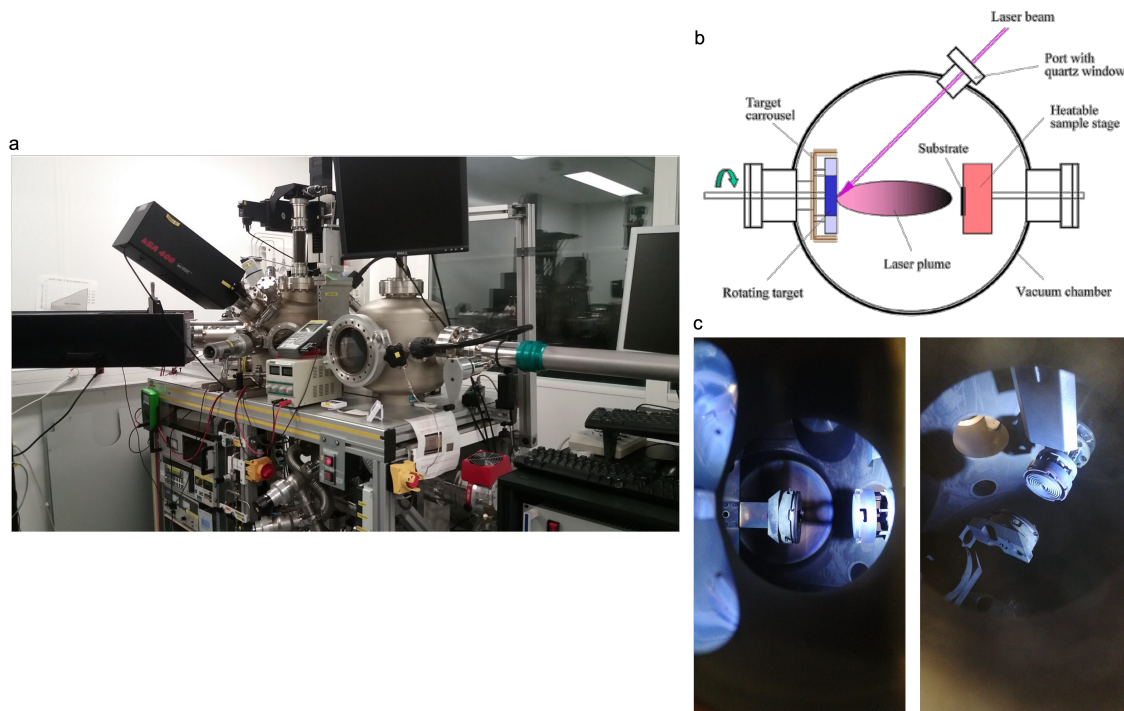


Figure 2.11 – a) Pulsed Laser Ablation in Thalès. b) Scheme of the process showing the laser, the target and the heated samples. c) Photos of the interior of the PLD chamber with the target and heated sample holder, courtesy to J. Briatico

For the production of thin films we collaborated with German company Ceraco and J. Briatico of UMR CNRS/Thalès . In collaboration with Robert Semerad from Ceraco and Javier Briatico from Thales, the group has developed an original sample growth technique to ensure the stability of thin layers of  $\text{YBa}_2\text{Cu}_3\text{O}_{7-\delta}$  during the nanowire fabrication processes. The detailed steps of this process are described in Chapter 3.

This fabrication process involves the addition of an extra protective surface layer of  $\text{YBa}_2\text{Cu}_3\text{O}_{7-\delta}$  on top of the  $\text{YBa}_2\text{Cu}_3\text{O}_{7-\delta}$  only in the center of the sample. Additionally, a layer of gold is deposited *in situ*, directly in contact with the  $\text{YBa}_2\text{Cu}_3\text{O}_{7-\delta}$  at the periphery of the sample. For further details on the process, refer to Fig. 2.12.

The morphology of the resulting  $\text{YBa}_2\text{Cu}_3\text{O}_{7-\delta}$  films is very complex due to complex crystalline structure of  $\text{YBa}_2\text{Cu}_3\text{O}_{7-\delta}$ . Different kind of structural disorders are present in films. The main one is grain boundaries, which strongly influence the transport properties of the resulting samples. Fig.2.13 shows an example of how a film can be formed and how a typical grain boundary looks like.

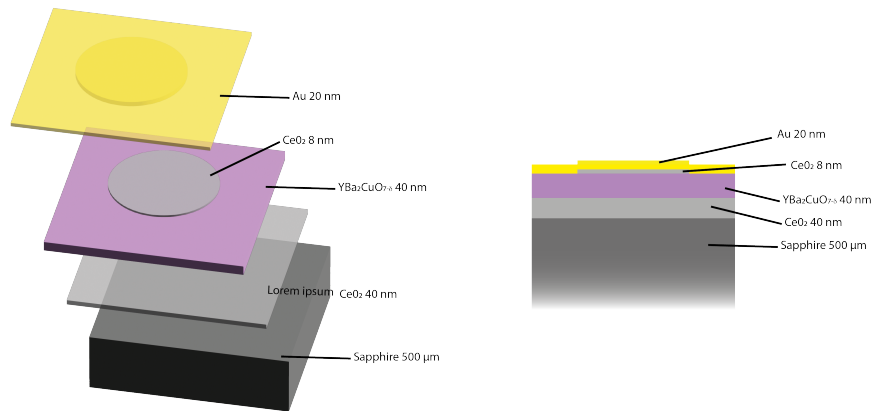


Figure 2.12 – Layers of the special samples: on a sapphire substrate, a 40 nm  $\text{CuO}_2$  buffer layer allows the deposition of a 30 nm thick  $\text{YBa}_2\text{Cu}_3\text{O}_{7-\delta}$  thin film under a partial oxygen vacuum of approximately  $10^{-4}$  mbar, on a rotating substrate heated between  $650^\circ\text{C}$  and  $800^\circ\text{C}$ . The sample is then cooled to room temperature. A mechanical mask is aligned with the sample and heated under a  $\sim 10^{-4}$  mbar partial oxygen vacuum, reaching temperatures between  $650^\circ\text{C}$  and  $800^\circ\text{C}$  to ensure optimal doping of the  $\text{YBa}_2\text{Cu}_3\text{O}_{7-\delta}$  layer. Subsequently, a 4 nm capping  $\text{CuO}_2$  layer, through this circular stencil mask, is deposited under the same conditions to ensure full stoichiometry of the capping layer.  $\text{CuO}_2$  is known to be highly stoichiometric and prevents grabbing oxygen from  $\text{YBa}_2\text{Cu}_3\text{O}_{7-\delta}$ , requiring deposition under partial oxygen vacuum. In the last step, the sample is cooled down to room temperature, the mechanical mask removed. In the last step the sample is heated around  $650^\circ\text{C}$  under the same partial oxygen vacuum ( $\sim 10^{-4}$  mbar), on a rotating substrate heated between  $650^\circ\text{C}$  and  $800^\circ\text{C}$  to ensure optimal doping of the uncapped  $\text{YBa}_2\text{Cu}_3\text{O}_{7-\delta}$  layer. The sample is cooled down under this partial oxygen pressure. Then 20 nm thick Au thin film is deposited in situ on all the sample in this last step, ensuring ohmic contact with the unprotected  $\text{YBa}_2\text{Cu}_3\text{O}_{7-\delta}$  layer around the  $\text{CuO}_2$  capping layer.

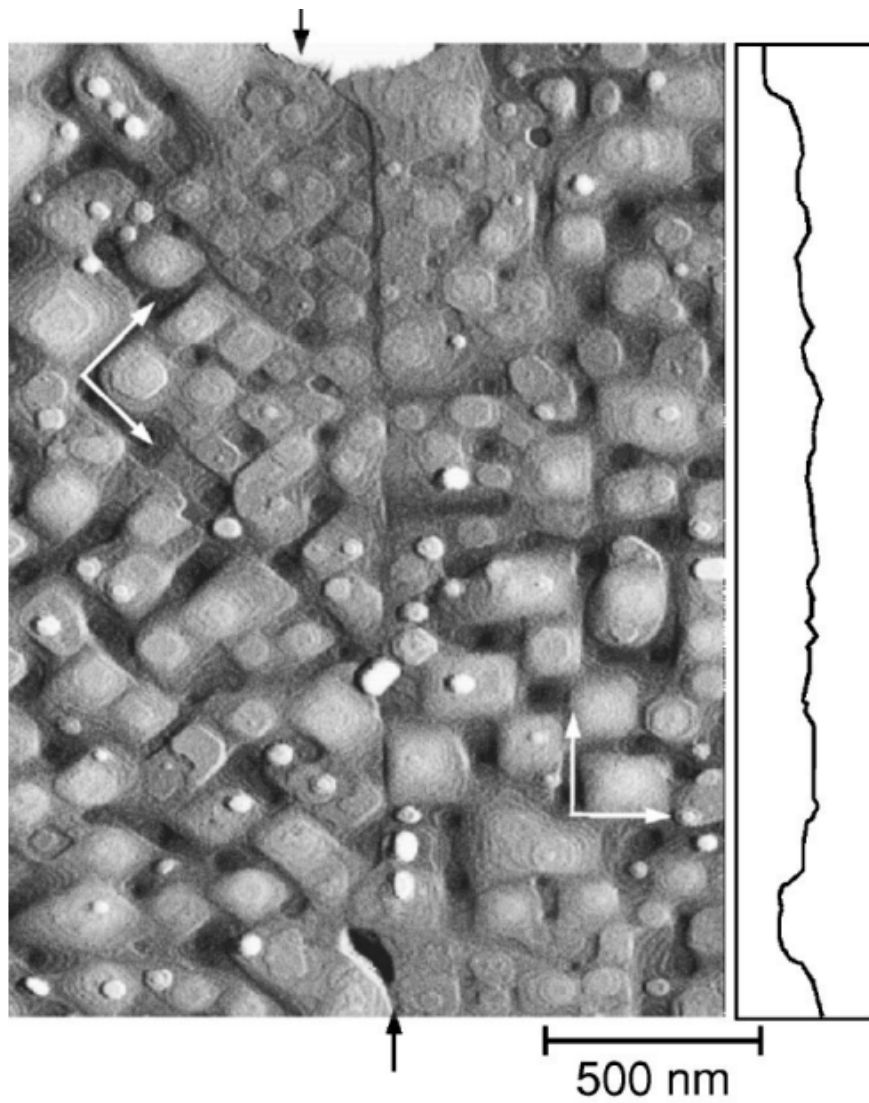


Figure 2.13 – Atomic Force Microscopy (AFM) image of the surface of a  $\approx 150$ -nm-thick  $\text{YBa}_2\text{Cu}_3\text{O}_{7-\delta}$  film with an asymmetric  $45^\circ$  [001]-tilt grain boundary. Adapted from [Hilgenkamp, 2002]

## 6 Conclusion

In this chapter, we have provided a concise overview of the discovery of cuprates and their Perovskite-type crystalline structures. We delved into the significance of  $\text{CuO}_2$  planes and the impact of strong electronic correlations, giving rise to a complex phase diagram modulated by hole doping. The main features of the superconducting phase, belonging to the broad category of superconductors of the second type with a symmetry order parameter  $d$ , were outlined. Despite the potential applications linked to superconductivity at temperatures above nitrogen's,  $\text{YBa}_2\text{Cu}_3\text{O}_{7-\delta}$  still present numerous challenges. These include technological hurdles in terms of nanoscale structuring, as discussed in the upcoming chapter on 6, and fundamental issues surrounding the mechanism driving superconductivity—a topic subject to ongoing debates within the scientific community.

# Chapter 3

## YBa<sub>2</sub>Cu<sub>3</sub>O<sub>7- $\delta$</sub> nanowires

### Objectives

In this section, we explain why high-temperature superconductor nanowires are an issue from both a fundamental and an applied point of view. We then give an overview of the various projects for producing superconducting nanowires. Finally, we describe the overall process for fabricating YBa<sub>2</sub>Cu<sub>3</sub>O<sub>7- $\delta$</sub>  nanowires using a high-energy oxygen ion irradiation technique combined with electron lithography implemented in this thesis. We start with the general idea of using ion implantation and then describe the whole technical process of fabricating a device using two types of lithography (laser lithography and electron-beam lithography).

### Contents

|   |  |           |
|---|--|-----------|
| 1 | Motivation . . . . .                     | <b>32</b> |
| 2 | State of the art . . . . .               | <b>33</b> |
| 3 | Fabrication by ion irradiation . . . . . | <b>36</b> |
|   | 3.1 Disorder effect . . . . .            | 36        |
|   | 3.2 Ion implantation . . . . .           | 37        |
|   | 3.3 SRIM Simulations . . . . .           | 38        |
| 4 | Fabrication workflow . . . . .           | <b>39</b> |
| 5 | Conclusion . . . . .                     | <b>43</b> |

## 1 Motivation

In the last two decades, a novel class of detectors has emerged, operating on a specific detection principle. Their operating mechanism was first proposed by Golt'sman *et al.* in 2001 [Goltsman, 2001]. These detectors are made of a superconducting nanowire giving rise to what is known as **Superconducting Nanowire Single Photon Detector (SNSPD)**. The operational mechanism is illustrated Fig.3.1a along with the electrical circuit necessary to be able to detect the fast voltage pulse upon absorption of the photon, see Fig. 3.1b.

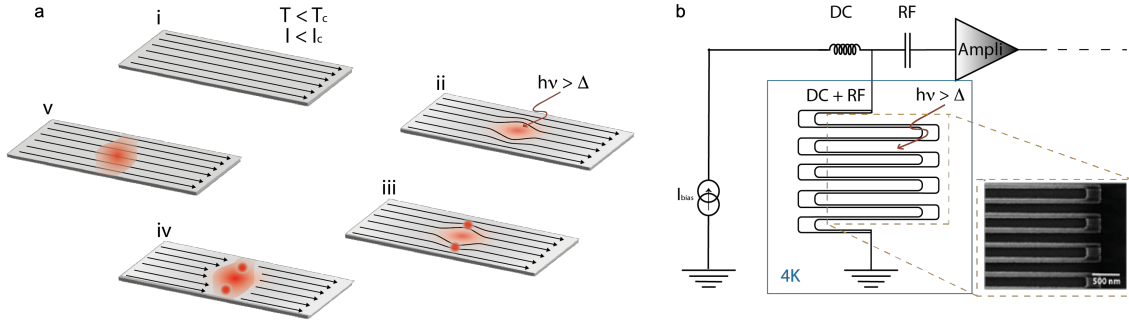


Figure 3.1 – a) Operational mechanism originally proposed by Golt'sman *et al.* [Goltsman, 2001]. The superconducting nanowire is biased just below its critical current (i). When a photon with energy  $h\nu$  surpassing the superconducting gap  $\Delta$  is absorbed, it disrupts the Cooper pairs and forms a normal region (ii), termed a hot spot. This normal region deflects the supercurrents (iii), which propagate along the wire's edges until they exceed the critical current density. Consequently, the nanowire undergoes a local transition to a resistive state (iv), generating a measurable voltage pulse. To be able to detect such a fast voltage pulse, the superconducting nanowire is in an electrical circuit allowing to separate the **Direct Current (DC)** and **Radio-Frequency (RF)** part of the signal. b) Electrical circuit involving a Bias Tee to be able to bias with a **DC** current and detect the fast voltage pulse through an amplifier towards a counter or an oscilloscope.

To obtain the best yields, the nanowire must be thin, typically a few nanometres to a few tens of nanometres thick. Its width should be on the order of the magnetic penetration length in superconducting materials (typically 100 nm). To optimise the detection area, the nanowire is generally long (10  $\mu\text{m}$ ) and folded on itself, typically in the area of a pixel, figure 3.1b. These detectors are broadband since the detection mechanism is not based on a specific energy. In addition, they have a low dark count rate because no ionisation process is involved in the detection event. Nowadays, **SNSPDs** based on conventional low  $T_c$  materials such as NbN, NbTi or WSi [Goltsman, 2001; Natarajan, 2012; Hadfield, 2009; Dauler, 2014] outperform their semiconductor-based counterparts in many respects [Hadfield, 2009] and are commercially available throughout the world [httpwwwcontelru, 2022]. Some remarkable properties include high quantum efficiency ( $\sim 94\%$  at  $\lambda \sim 1.31 \mu\text{m}$  [Smirnov, 2018],  $93\%$  at  $\lambda \sim 1.55 \mu\text{m}$  [Marsili, 2013]), high operating frequency ( $\sim 1.2 \text{ GHz}$  [Vetter, 2016]), low intrinsic dark count rate ( $6 \cdot 10^{-6}$  count/s) [Chiles, 2022]), low jitter ( $\sim 4.6 \text{ ps}$  full width at half height  $\lambda \sim 1.55 \mu\text{m}$  [Korz, 2020]) and a wide spectral range (from visible to mid-infrared [Marsili, 2012; Korneev,

2012]) up to 10  $\mu\text{m}$  wavelength [Verma, 2021]). [Protte, 2022]. Very recently, this width constraint has been largely relaxed : single-photon detectors based on thin wires of the order of a micron in width have been produced [Protte, 2022].

However, these devices operate at ultra-low temperatures, below 1 K, which requires heavy and energy-intensive cryogenics, preventing large-scale applications.

In this context, the manufacture of SNSPDs using high critical temperature superconductors (HTS SNSPDs) would offer two main advantages : the ability to work at a higher temperature (around 40 K) with simplified cryogenics and the possibility of operating at a higher frequency, thanks to an electron-phonon relaxation time that is two orders of magnitude shorter [Lindgren, 1999].

## 2 State of the art

For these reasons, the development of an SNSPD from a high-temperature superconductor is at the heart of intense research worldwide [Santavicca, 2018] based on doped high-temperature superconductors such as:

1.  $\text{Pr}_{2-x}\text{Ce}_x\text{CuO}_{4-\delta}$  [Charpentier, 2016],
2.  $\text{Nd}_{2-x}\text{Ce}_x\text{CuO}_{4\pm\delta}$  [Romano, 2018],
3.  $\text{YBa}_2\text{Cu}_3\text{O}_{7-\delta}$  [Arpaia, 2015b; Ejrnaes, 2017b; Arpaia, 2017; Amari, 2017b; Lyatti, 2018; Trbaldo, 2019; Andersson, 2020], see figure 3.2a ,
4.  $\text{La}_{1.85}\text{Ce}_{0.15}\text{CuO}_4$  [Shibata, 2017], see figure 3.2b-,  $\text{La}_{1.85}\text{Ce}_{0.15}\text{CuO}_4$  [Charaev, 2023], see figure 3.2d-,
5.  $\text{YBa}_2\text{Cu}_3\text{O}_{7-\delta}/\text{La}_{0.7}\text{Sr}_{0.3}\text{MnO}_3$  [Arpaia, 2014a],
6.  $\text{Bi}_2\text{Sr}_2\text{CaCu}_2\text{O}_{8+\delta}$  [Charaev, 2023], see figure 3.2d -

High-temperature superconductors fulfil all the conditions required for detection, such as, for example, a short coherence length  $\xi_{YBCO} \sim 2$  nm (comparable to the low-temperature superconducting materials used for SNSPD :  $\xi_{NbN} \sim 5$  nm [Annunziata, 2010]), an intrinsically fast quasiparticle recombination time ( $\sim 1$ ps [Sobolewski, 1998]), hysteretic Current versus Voltage (IV) curves [Sobolewski, 1998; Arpaia, 2017] and, at the same time, a high critical temperature  $T_c \sim 87$  K. For more than a decade, efforts failed to demonstrate the sensitivity of nanowires to the single photon. And it was only very recently that a first proof of principle was achieved [Charaev, 2022] in cuprate nanowires on ultrathin layers below 25 K from a high-temperature superconducting nanowire, re-launching the race to achieve a single-photon detector operating at around 40K, figure 3.2.

The main problems in making such thin nanowires arise from the growth of ultra-thin high-temperature superconducting films and their shaping on a nanometric scale [Assink, 1993; Nawaz, 2013a; Larsson, 2000]. Approaching the typical length scale required for SNSPD operation and known for low  $T_c$  (typically 100 nm wide, 5 nm thick, several  $\mu\text{m}$  long for nanowires) is a major challenge. The other problem relates to the generation of self-stabilising hot spots when photons are absorbed. This requires a homogeneous

nanowire carrying a current density approaching the theoretical Ginzburg-Landau depairing limit of  $J_d = 5.10^8 \text{ A.cm}^{-2}$  [Vodolazov, 2017], with hysteretic  $IV$  curves [Arpaia, 2017], the signature of a runaway effect.

Manufacturing steps very often lead to the degradation of superconducting properties. Thin films exposed to air easily lose their optimum oxygen doping, mainly because of the ease with which oxygen atoms migrate along Cu-O [Gupta, 1991] chains, and their high sensitivity to introduced defects [Lesueur, 1990]. Various techniques have been proposed to overcome these difficulties, including standard argon ion etching with very careful adjustment of the etching parameters to avoid overheating effects and limit interaction with the corresponding ions [Arpaia, 2017], the edges of etched wires are favourable zones for the escape of oxygen atoms along Cu-O chains, a phenomenon that is amplified for ultra-thin films. The thin film is protected by a layer of gold [Papari, 2012; Papari, 2014; Lam, 2019] or a mask of carbon 100 nm thick [Arpaia, 2013; Arpaia, 2014b] improves both manufacturing reliability and homogeneity of superconducting properties. However, photon detection requires the removal of this protective layer, an additional step that generally damages the superconducting properties. An alternative approach to argon etching is based on direct etching of the film by a focused  $\text{Ga}^{3+}$  ion beam [Curtz, 2010; Lyatti, 2016; Lam, 2019]. This method offers higher resolution than the usual electron lithography process. The doses used are lower than in conventional Ar etching, thus limiting the introduction of disorder. However,  $\text{Ga}^{3+}$  ions poison  $\text{YBa}_2\text{Cu}_3\text{O}_{7-\delta}$ , damaging the superconducting properties.

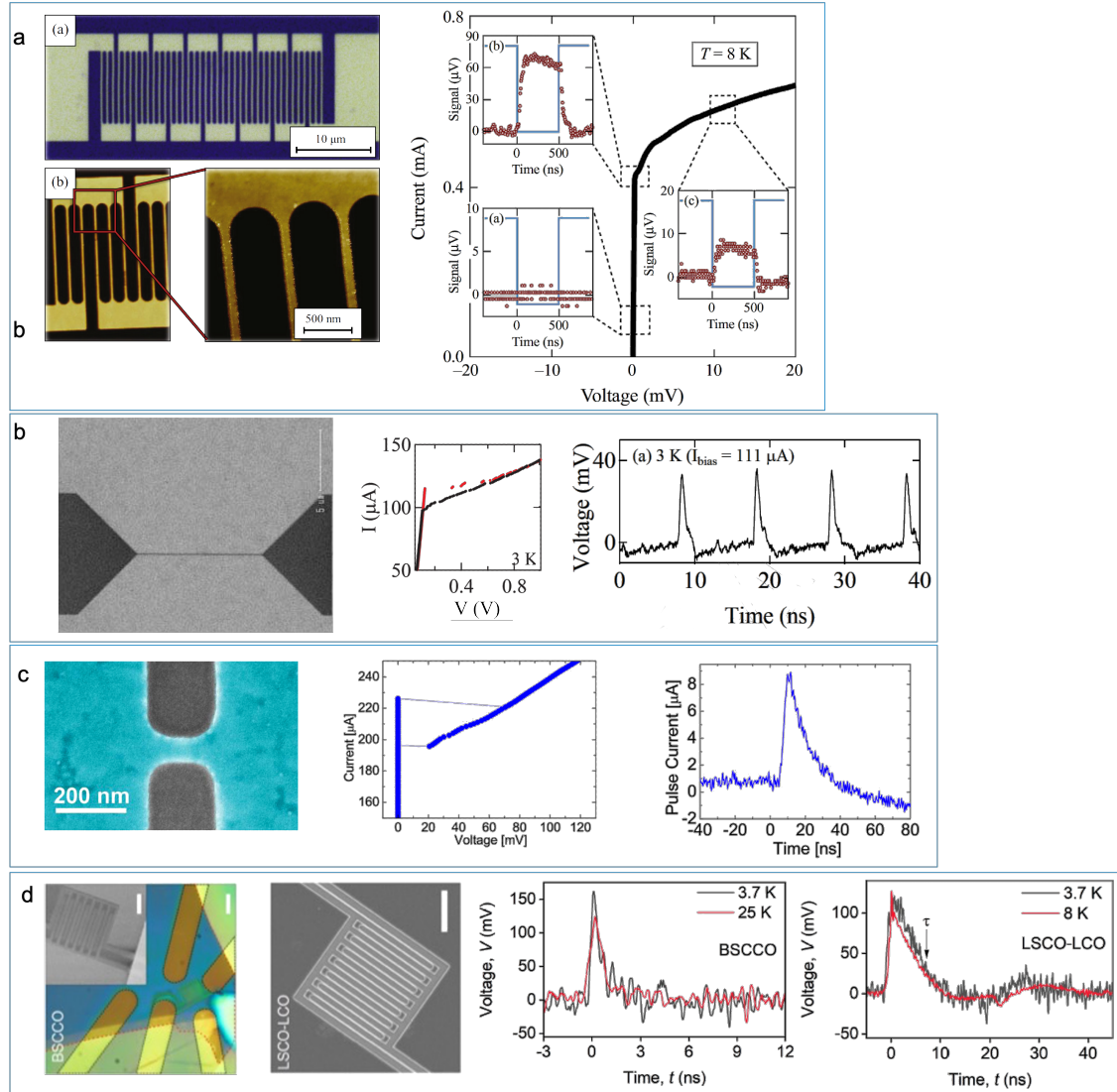


Figure 3.2 – a) Top : optical microscope image of 300 nm wide parallel  $\text{YBa}_2\text{Cu}_3\text{O}_{7-\delta}$  nanowires and AFM image of several 130 nm wide YBCO nanowires. Bottom : photoresponse under pulsed optical illumination at 1550 nm wavelength at 8 K.  $I(V)$  characteristics at  $T = 8\text{ K}$ . The three insets show the time-resolved photoresponse signal (red circles) measured at three polarisation currents, adapted from [Arpaia, 2015a]. b) Top : Scanning Electron Microscope (SEM) image of the mask before etching to produce  $\text{La}_{1.85}\text{Ce}_{0.15}\text{CuO}_4$  wires 100 nm wide, 10  $\mu\text{m}$  long, 5 nm thick. And  $I(V)$  hysteresis at 3 K. Bottom : Transient photoresponse of a 100 nm wide, 10  $\mu\text{m}$  long, 5 nm thick  $\text{La}_{1.85}\text{Ce}_{0.15}\text{CuO}_4$  wire at different laser pulse powers. The wire is illuminated by a femtosecond laser pulse of 1.56  $\mu\text{m}$  wavelength at a repetition rate of 100 MHz, and measured at 3 K with  $I_{bias} = 111\ \mu\text{A}$ , adapted from [Shibata, 2016]. c) Ultra-thin nanowires (10-20 nm thick, 65 nm wide, 200 nm long) of optimally doped unprotected YBCO, taken from [Ejrnaes, 2017a].  $I(V)$  hysteresis at 4.9 K and pulse associated with a black shot. d) Nanowires made of  $\text{Bi}_2\text{Sr}_2\text{CaCu}_2\text{O}_{8+\delta}$  cuprates on the left and LSMO on the right. Detection pulse with single-photon sensitivity in each of the two cuprates [Charaev, 2023].

### 3 Fabrication by ion irradiation

#### 3.1 Disorder effect

Due to the d-wave nature of superconductivity in  $\text{YBa}_2\text{Cu}_3\text{O}_{7-\delta}$ , it is highly sensitive to crystal defects. Each electron collision with a crystalline defect can lead to a loss of Cooper pair coherence, effectively acting as a depairing center for the Cooper pairs. The work by [Lesueur, 1993] demonstrated that when irradiated with a beam of  $\text{He}^+$  ions, the  $\text{YBa}_2\text{Cu}_3\text{O}_{7-\delta}$  film undergoes a continuous transition from a superconducting to an insulating state. The authors observed that an increase in displacement per atom ( $dpa$ ) correlates with a decrease in the critical temperature. After reaching a certain value of  $dpa$  (approximately 0.04), the critical temperature reduces to zero, rendering the  $\text{YBa}_2\text{Cu}_3\text{O}_{7-\delta}$  thin film insulating. This effect has been described based on the Abrikosov-Gorkov model of depairing in s-wave superconductors due to magnetic impurities, assuming that defects play a similar depairing role for d-wave superconductors.

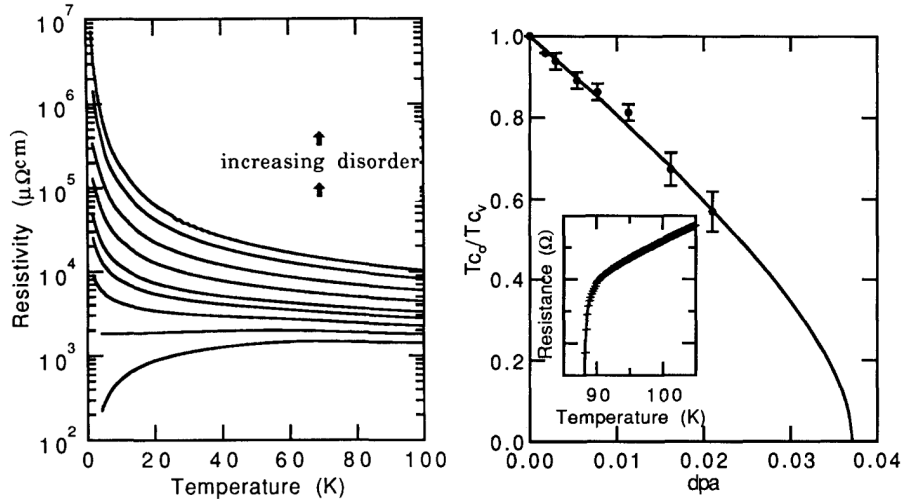


Figure 3.3 – Normalized critical temperature as a function of  $dpa$ . Adapted from [Lesueur, 1993].

Using this approach, following Abrikosov-Gorkov model [Abrikosov, 1969], one can write the relationship as:

$$\ln\left(\frac{T_c}{T_{ci}}\right) = F\left(\frac{1}{2}\right) - F\left(\frac{1}{2} + 0.14\frac{dpa}{dpa_c}\frac{T_{ci}}{T_c}\right), \quad (3.1)$$

where  $F$  - is a digamma function,  $T_{ci}$  is the initial critical temperature before irradiation. This formula is in a good agreement with Lesueur's *et al.* [Lesueur, 1993] experimental results. Using this method, it is possible to pattern different mesoscopic superconducting devices inside an insulating  $\text{YBa}_2\text{Cu}_3\text{O}_{7-\delta}$  matrix through ion beam irradiation, thereby controlling local critical temperature [Bergeal, 2005; Bergeal, 2006; Lesueur, 2007; Sirena, 2007b; Sirena, 2007a; Sharafiev, 2016; Ouanani, 2016a; Couëdo, 2019; Couëdo, 2020; Pawlowski, 2018]. The next sections provide a detailed description of this approach.

### 3.2 Ion implantation

Ion irradiation (or implantation) is a wide use technique in the semiconductor industry and nanotechnology.

Various techniques exist for ion implantation into solid materials. These include wide-beam ion implantation, commonly used for n- or p-doping in the semiconductor industry [Jaeger, 2002], as well as focused ion beams using gallium [Curtz, 2010] or helium [Cybart, 2015; Couëdo, 2020]. Depending on the chosen technique, specific ions are extracted from the source and then accelerated by a voltage ranging from 10 kV to 200 kV (with a maximum of 30 kV for **Focused Ion Beam (FIB)**) toward the thin film. These high-energy ions penetrate the material over a typical length of a few tens to a few hundreds of nanometers. As a result, the ions can dope, create defects, or even modify the material, depending on the chosen dose.

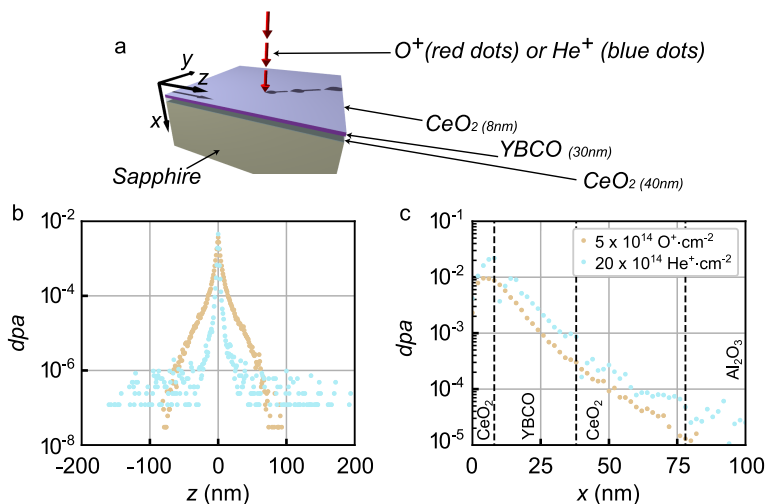


Figure 3.4 – Simulation of the  $dpa$  generated by punctual source of  $\text{He}^+$  and  $\text{O}^+$  ions with an energy of 30 keV into a stack of  $\text{CeO}_2$  (8 nm)/ $\text{YBa}_2\text{Cu}_3\text{O}_{7-\delta}$  (30 nm)/ $\text{CeO}_2$  (40 nm)/ $\text{Al}_2\text{O}_3$  ( $10^5$  ions simulation). a) Scheme of the irradiated sample with the axes ( $x$ ,  $y$ ,  $z$ ), the different layers and their thicknesses. Nota Bene: the scales are not respected. b)  $Dpa$  averaged along the depth  $x$  in the  $\text{YBa}_2\text{Cu}_3\text{O}_{7-\delta}$  layer at  $y = 0$  as a function of the lateral dimension  $z$ . c)  $dpa$  at  $y = 0$  and  $z = 0$  as a function of the depth  $x$ . The dose is adjusted such that the maximum  $dpa$  in a) are equals for the  $\text{He}^+$  ions and the  $\text{O}^+$  ions. The black dashed lines separate the different material layers.

The working principle of ion irradiation involves accelerating ions of a chosen element to high energy (ranging from 1 keV to 10 MeV) using an electric field. These accelerated ions are then directed towards a target substrate. As the ions penetrate the target, they displace atoms from their original crystallographic positions, potentially causing successive displacements of other atoms. This ion beam induces defects along the trajectories of the implanted ions, as illustrated in Figure 3.4.

The control of the critical temperature ( $T_c$ ) of the film depends significantly on the amount of disorder introduced locally into the thin film. This dependence is directly re-

lated to the type of ions, their energy, and the dose used. By using Monte Carlo **SRIM** (The Stopping and Range of Ions in Matter) [Ziegler, 2004] numerical simulations, it becomes possible to determine the appropriate range of parameters necessary to control the superconducting properties of the irradiated film. This simulation tool enables the estimation of the interaction zone of implanted ions and the resulting defect rate created by a large number of ions, typically on the order of  $10^5$  ions.

After the first collision with the substrate surface, ions travel inside the substrate to a certain depth, which depends on factors such as the ion's energy, size, mass, and the composition of the substrate. The number of ions implanted into the substrate is proportional to the implantation time and ion current. An important characteristic used to quantify the amount of implanted ions per unit area is called the dose, denoted by  $D$ , and defined as follows:

$$D = \frac{I\Delta t}{eS}, \quad (3.2)$$

where  $I$  is a using ion current,  $\Delta t$  is the implantation time,  $e$  is the elementary charge, and  $S$  is the target surface. By varying the dose  $D$ , it is possible to introduce different atoms into the substrate or even etch the substrate at sufficiently high dosages.

### 3.3 SRIM Simulations

For preliminary estimation of ion implantation parameters for the desired sample, we simulate the ion implantation process using **SRIM** software. **SRIM** is based on Monte Carlo simulation of collisions that an accelerated ion introduces into the target material. Starting from the first collision with a surface atom, the ion transfers part of its energy to the target atom. If this energy exceeds the displacement energy of the atom, it shifts from its position and launches another series of subsequent collisions, while the ion maintains its motion through the target until it loses all its energy (or reaches the edge of the target) and stops. This process repeats for a statistically meaningful number of ions. At the end of the simulation, the program provides information about all collisions in all cascades. To estimate the introduced disorder, we keep information only about coordinates  $(x, y, z)$  of each vacancy. The overall simulation volume  $V = x_{max}y_{max}z_{max}$ , where  $x_{max}, y_{max}, z_{max}$  are the maximum coordinate values through all vacancies. This volume is divided into cubic elementary volumes  $\delta V = \delta x\delta y\delta z$ . For each elementary volume we compute number of vacancies inside  $C(x,y,z)$ . Using this information we can estimate  $dpa$  as follows:

$$dpa(x, y, z) = \frac{C(x, y, z)D}{n\delta xN_{ions}}, \quad (3.3)$$

where  $D$  - is an ion dose,  $n$  - is a target material density ( $n_{YBCO} = 7.53 \times 10 \text{ atoms.cm}^{-3}$ ),  $N_{ions}$  - is a number of ions ( $\approx 10^5$ ).

In **SRIM** simulation, each ion hits the target surface at the origin  $(0, 0, 0)$ . To simulate **FIB** pattern or irradiation through a mask we introduce a  $dpa_P$  for a whole pattern as a convolution of the punctual effect of a beam irradiation  $dpa_B$  with a binary matrix  $M(y,z)$

represents sample pattern:

$$dpa_P(x, y, z) = \sum_i^{N_x} \sum_j^{N_z} dpa_B(x, y - y_i, z - z_j) M(y_i, z_j). \quad (3.4)$$

## 4 Fabrication workflow

**Step 0. Bare  $\text{YBa}_2\text{Cu}_3\text{O}_{7-\delta}$  film** Starting point of our nanowire fabrication workflow is the unpatterned bare  $\text{YBa}_2\text{Cu}_3\text{O}_{7-\delta}$  film. All samples in this work are made from thin  $\text{YBa}_2\text{Cu}_3\text{O}_{7-\delta}$  films from two origins as already pointed out in Chapter 2: commercial films from Ceraco GmbH (marked as "CS") and other from collaboration with Javier Briatico at the UMR CNRS-Thales (marked as "JS"). After deposition  $\text{YBa}_2\text{Cu}_3\text{O}_{7-\delta}$  film of desired thickness the central part of the film is covered with 5 mm diameter 8 nm thick  $\text{CeO}_2$  disc, see Fig. 3.5. Then all film is covered with 20 nm thick gold layer. This capping  $\text{CeO}_2$  disc is important part of our fabrication workflow. This material keeps its stoichiometry during the following deposition procedure and protect underneath  $\text{YBa}_2\text{Cu}_3\text{O}_{7-\delta}$  part from change in oxygen doping. As it was mentioned before  $\text{YBa}_2\text{Cu}_3\text{O}_{7-\delta}$  superconducting properties is very sensitive to oxygen concentration thus it is important to preserve optimal doping during the whole fabrication process.

**Step 1. Current and voltage probes** The next step involves the fabrication of gold current and voltage probes for the future nanowires. These gold electrodes are designed to reach the superconducting central part of the sample, protected by the  $\text{CuO}_2$  layer, ensuring excellent electrical contact. The dimensions of the probes are larger than 10  $\mu\text{m}$ , so laser lithography is employed. A first layer of LOR05B is deposited and baked at 110°C. Following this, a 500 nm thick layer of S1805 photoresist is deposited and baked at 110°C. This bilayer is chosen to ensure a good lift-off with an undercut. It's noteworthy that the annealing temperature of the resist never exceeds 110°C. All resist deposition and lithography processes are adapted to allow the production of resist contacts and microbridges under these conditions. The sample is then patterned with a PhotonSteer LW450C laser lithography system. During this step, the exposed areas are developed and define the gold layer of the contact electrodes. The entire laser lithography process is carried out at the College de France clean room facility.

After preparing the lithography mask, a 0.5 nm thick Ti layer is deposited for good adhesion, followed by a 200 nm thick Au layer using e-beam evaporation in a Plassys SEM 550S. Subsequently, a lift-off and etching process is performed to remove the thin gold layer deposited *in situ*. During the etching process, the sample holder is continuously cooled to avoid heating the sample.

After this step, the superconducting properties of the sample are checked to ensure that they have not been damaged during the probe fabrication. For this purpose, bonding is performed on some gold probes, and the critical temperature  $T_c$  is measured before proceeding further.

**Step 2. Nanowire patterning** If the sample passes the critical temperature check, we proceed to pattern nanowires using electron lithography and ion irradiation. For electron lithography, the sample is covered with a 500 nm thick ma-N 2405 electronic resist [wwwmicroresistde, 2022]. Exposure is carried out using the FEI Magellan SEM in two steps: the first for the finest parts with low current (11 pA) in ultra-high-resolution mode, and the second for the rest with a current of 23 nA in standard resolution. After developing the unexposed resist before ion irradiation, we inspect the mask and nanowire alignment to the gold electrodes using an optical microscope. The next stage involves ion irradiation to form an insulating matrix around superconducting nanowires. This is performed at the ICUBE laboratory in Strasbourg in collaboration with Y. Legall. The samples are fixed with carbon tape on a metallic sample holder to ensure good thermalization during the irradiation process. To discharge the sample, metallic clips are placed on the gold pads of the current probe. The samples are irradiated with an adjusted beam that is homogeneous on the scale of the sample surface. For ion beam parameters, we use a dose of  $3 \times 10^{14}$  ions/cm<sup>-2</sup> with current values set between 10  $\mu\text{A}$  and 15  $\mu\text{A}$  to prevent overheating of the samples.

All the samples geometries designed on sample CS15 are presented in Fig.3.5.

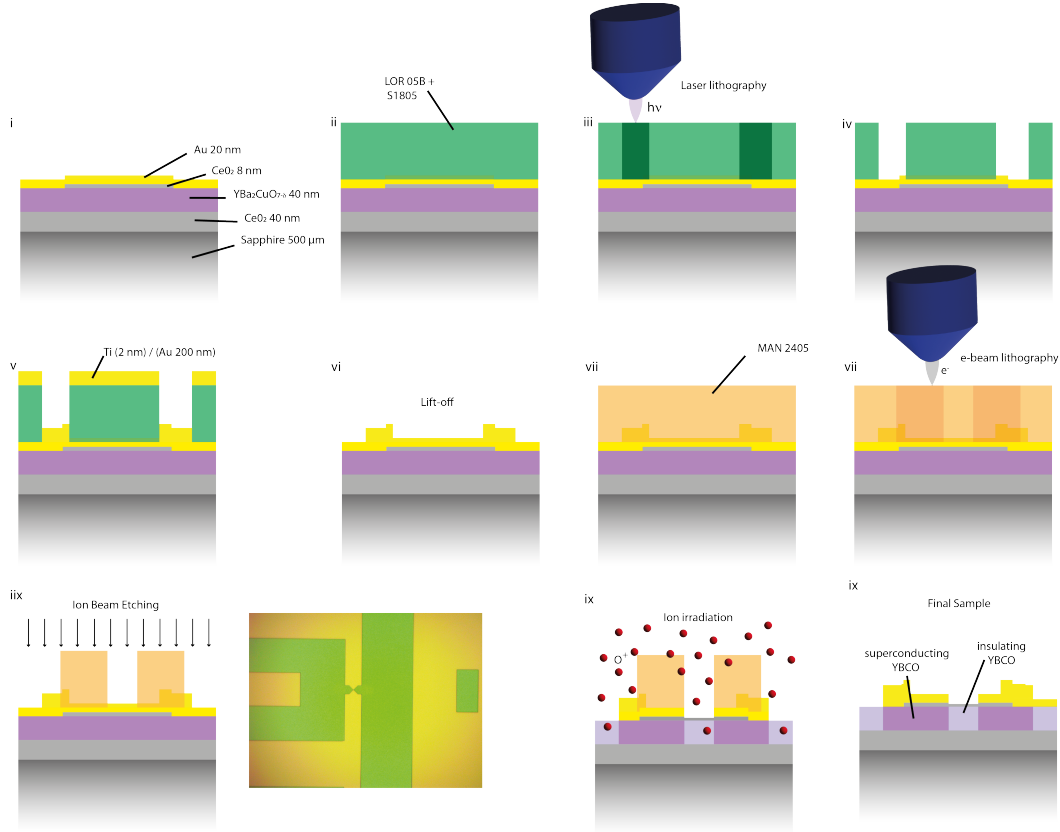
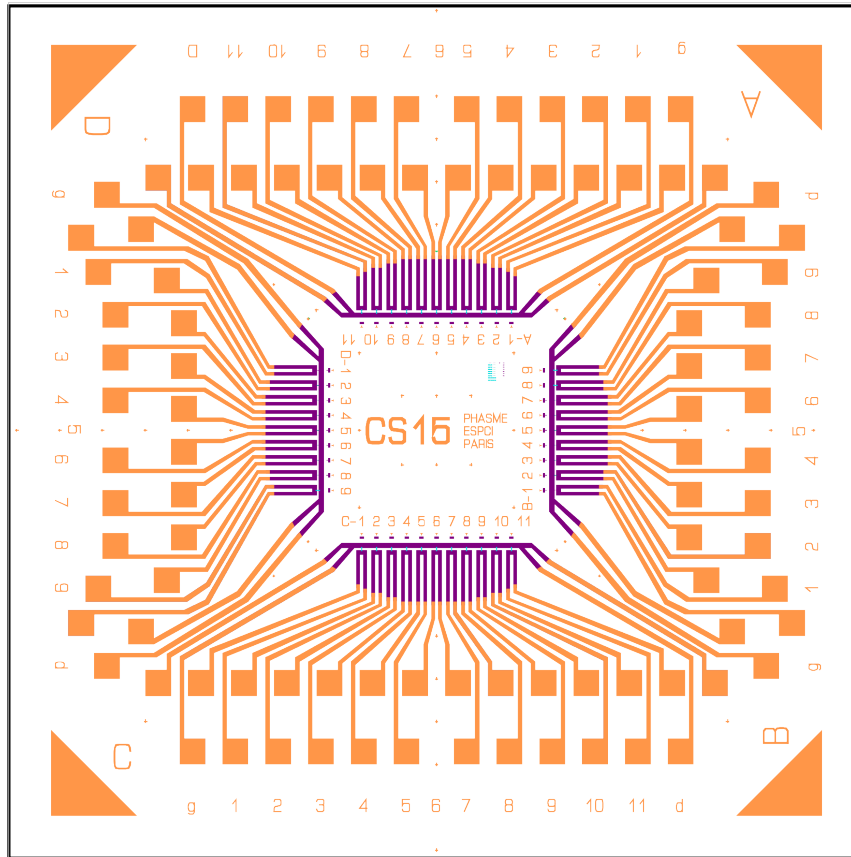


Figure 3.5 – i) Main structure of the initial samples. ii) Spin coating of a 500-nm thick S1805 photoresist with a first layer of LOR05B to achieve an undercut. iii) Laser lithography to pattern the pre-contact. iv) Development of the photoresist. v) Deposition of a Ti(2nm)/Au(200nm) thin film in a Plassys ultra-high vacuum thin film deposition system. vi) Lift-off. vii) Spin coating of a 500-nm thick MAN 2405 negative electron-sensitive resist. viii) Electron beam lithography to design nanowires and contacts, particularly under the CeO<sub>2</sub> capping layer. ix) **Ion Beam Etching (IBE)** with Argon ions accelerated at 500 eV at a rate of 25 nm of gold per minute. An optical picture of one of the devices on CS15 after the development of the lithography and before the **IBE** effect is shown. x) Ion irradiation of all the samples at an energy of 30 keV, a dose of  $3 \times 10^{14}$  ions/cm<sup>2</sup>. The parts protected either by the gold layer or the MAN resist are not irradiated and remain superconducting, while in the other non-protected areas, YBa<sub>2</sub>Cu<sub>3</sub>O<sub>7- $\delta$</sub>  becomes insulating. This entire process prevents the out-diffusion of oxygen from YBa<sub>2</sub>Cu<sub>3</sub>O<sub>7- $\delta$</sub> , as the thin film remains embedded in the insulating YBa<sub>2</sub>Cu<sub>3</sub>O<sub>7- $\delta$</sub>  and between two highly stable and stoichiometric CeO<sub>2</sub> layers (buffer layer and capping layer).



| A            |  | B            |                                      | C            |  | D            |                                      |
|--------------|--|--------------|--------------------------------------|--------------|--|--------------|--------------------------------------|
| 10x10mm_A_DC |  | 10x10mm_B_DC |                                      | 10x10mm_C_DC |  | 10x10mm_D_DC |                                      |
| 0            | 1980 $\mu\text{m}$ x57,5 $\mu\text{m}$ | 0            | 1660 $\mu\text{m}$ x60 $\mu\text{m}$ | 0            | 1980 $\mu\text{m}$ x57,5 $\mu\text{m}$ | 0            | 1660 $\mu\text{m}$ x60 $\mu\text{m}$ |
| 1            | Bi0.5 $\mu\text{m}$ x150nm             | 1            | 20 $\mu\text{m}$ x2 $\mu\text{m}$    | 1            | 0.5 $\mu\text{m}$ x126nm               | 1            | 20 $\mu\text{m}$ x2 $\mu\text{m}$    |
| 2            | Bi0.5 $\mu\text{m}$ x150nm             | 2            | 20 $\mu\text{m}$ x500nm              | 2            | Bi0.5 $\mu\text{m}$ x150nm             | 2            | 20 $\mu\text{m}$ x500nm              |
| 3            | 0.5 $\mu\text{m}$ x150nm               | 3            | 20 $\mu\text{m}$ x300nm              | 3            | 0.5 $\mu\text{m}$ x150nm               | 3            | 20 $\mu\text{m}$ x300nm              |
| 4            | 0.5 $\mu\text{m}$ x176nm               | 4            | 20 $\mu\text{m}$ x200nm              | 4            | 0.5 $\mu\text{m}$ x150nm               | 4            | 20 $\mu\text{m}$ x200nm              |
| 5            | Bi0.5 $\mu\text{m}$ x200nm             | 5            | 20 $\mu\text{m}$ x176nm              | 5            | 0.5 $\mu\text{m}$ x176nm               | 5            | 20 $\mu\text{m}$ x200nm              |
| 6            | Bi0.5 $\mu\text{m}$ x200nm             | 6            | 20 $\mu\text{m}$ x150nm              | 6            | 0.5 $\mu\text{m}$ x176nm               | 6            | 20 $\mu\text{m}$ x176nm              |
| 7            | 0.5 $\mu\text{m}$ x200nm               | 7            | 20 $\mu\text{m}$ x126nm              | 7            | Bi0.5 $\mu\text{m}$ x200nm             | 7            | 20 $\mu\text{m}$ x150nm              |
| 8            | 0.5 $\mu\text{m}$ x200nm               | 8            | 0.5 $\mu\text{m}$ x126nm             | 8            | 0.5 $\mu\text{m}$ x200nm               | 8            | 20 $\mu\text{m}$ x126nm              |
| 9            | Bi0.5 $\mu\text{m}$ x300nm             | 9            | 0.5 $\mu\text{m}$ x126nm             | 9            | Bi0.5 $\mu\text{m}$ x300nm             | 9            | 0.5 $\mu\text{m}$ x126nm             |
| 10           | 0.5 $\mu\text{m}$ x300nm               |              |                                      | 10           | 0.5 $\mu\text{m}$ x300nm               |              |                                      |
| 11           | 0.5 $\mu\text{m}$ x500nm               |              |                                      | 11           | Bi0.5 $\mu\text{m}$ x300nm             |              |                                      |

Figure 3.6 – Map of a typical sample with all the nanowire geometries patterned by ion irradiation onto a 30 nm thick  $\text{YBa}_2\text{Cu}_3\text{O}_{7-\delta}$  thin film on a single  $10 \times 10 \text{ mm}^2$  chip. The region delimited by the purple contact, made by e-beam lithography on negative resist, outlines the  $\text{CeO}_2$  capping layer. Orange areas represent the gold contact.

## 5 Conclusion

This chapter was devoted to the fabrication of HTS nanowires. Ideally, it is divided into two parts. In the first part, we described the current fundamental and technological problems and challenges that scientists and engineers face in order to create complete devices based on HTS nanowires. However, the advantages that HTS devices promise are attracting multiple groups of scientists around the world. We have also presented the advances that have been made in this topic by the scientific community in recent years.

The second part is devoted to the  $\text{YBa}_2\text{Cu}_3\text{O}_{7-\delta}$  nanowire fabrication method used in this work. This method uses such a feature of the  $\text{YBa}_2\text{Cu}_3\text{O}_{7-\delta}$  superconductor as d-wave symmetry, which makes the superconductivity in this material extremely sensitive to disorder. Because of this and the fact that disorder can be introduced pointwise using an ion beam, we are able to draw superconducting structures in the  $\text{YBa}_2\text{Cu}_3\text{O}_{7-\delta}$  thin film. Beyond this simple idea, there are a number of technological features that are necessary to obtain a good quality sample and have also been described in the second part of this chapter.

# Chapter 4

## Transport measurements

### Objectives

In this chapter, we present our transport measurements of  $\text{YBa}_2\text{Cu}_3\text{O}_{7-\delta}$  nanowires at zero magnetic field. First, we describe our different measurements setups for various type of measurements. Then, we present resistance versus temperature dependence, that we analyze using different existing models. We then show the current-voltage characteristics measured over a wide temperature range and analyze their shape in the framework of vortex motion. In the last section, we present our results on the Shapiro experiment on the fabricated nanowires. Within this experiment, we obtain a number of interesting results that require further analysis.

### Contents

|   |  |    |
|---|--|----|
| 1 | Measurement setup . . . . .                              | 45 |
| 2 | RT measurements . . . . .                                | 46 |
| 3 | IV characteristics . . . . .                             | 50 |
|   | 3.1 Switching, returning and critical currents . . . . . | 50 |
|   | 3.2 Flux Creep behavior . . . . .                        | 60 |
|   | 3.3 Shapiro steps . . . . .                              | 65 |
| 4 | Conclusion . . . . .                                     | 78 |

## 1 Measurement setup

All transport measurements were provided in an OptiDry pulsed tube cryostat with a base temperature equals to 3.4 K. Samples were glued with silver paste to the homemade sample holder and then bonded with Al wires to contact pads. To control the temperature over a wide range, we utilized a calibrated CX-1030 resistor as a thermometer and an Arcol HS10 100  $\Omega$  resistor as a heater. Both the thermometer and the heater were affixed to the back of the sample holder. The sample holder was thermally decoupled from the optical plate of the cryostat using Duralumin pillars, resulting in a base temperature increase up to 4.2 K. Electrical measurements were conducted using twisted pairs passing through low-pass RC filters inside the cryostat. Outside the cryostat, the wires were connected to a distribution box where the connection to the selected sample occurred. Each connector on this box was equipped with a three-position toggle switch that connects the contact to the ground, protecting the sample from electrostatic discharges, as the samples demonstrated high sensitivity to electrostatic voltage.

Resistance measurements were conducted using two Signal Recovery 7265 DSP lock-in amplifiers in a four-probe measurement scheme to eliminate the influence of contact resistance, which can be relatively high and non-ohmic for certain samples. The lock-in technique was chosen for its exceptional sensitivity and capability to measure complex impedance. This feature is particularly valuable for analysing the sample and contact quality even at room temperature. Samples with a significant imaginary impedance component are considered suboptimal because of internal defects or contact issues, allowing their identification before the cryostat cools down. Another notable advantage of the lock-in technique is its capacity to simultaneously measure multiple samples, thanks to the frequency sensitivity of the lock-in amplifier.

The temperature is regulated by a PID controller throughout the experiment, allowing control over not only the specific temperature but also over the rate of temperature change. Current-voltage characteristics (IV) were measured using a Yokogawa GS200 as a DC current source and a Keithley 2200 as a voltmeter. Both devices were equipped with low-pass filters with a characteristic frequency of 50 kHz. Prior to reaching the input of the voltmeter, the signal passes through a low-noise voltage preamplifier, the Stanford Research Systems SR560. All devices are controlled and monitored from a single computer using custom LabVIEW programs.

## 2 RT measurements

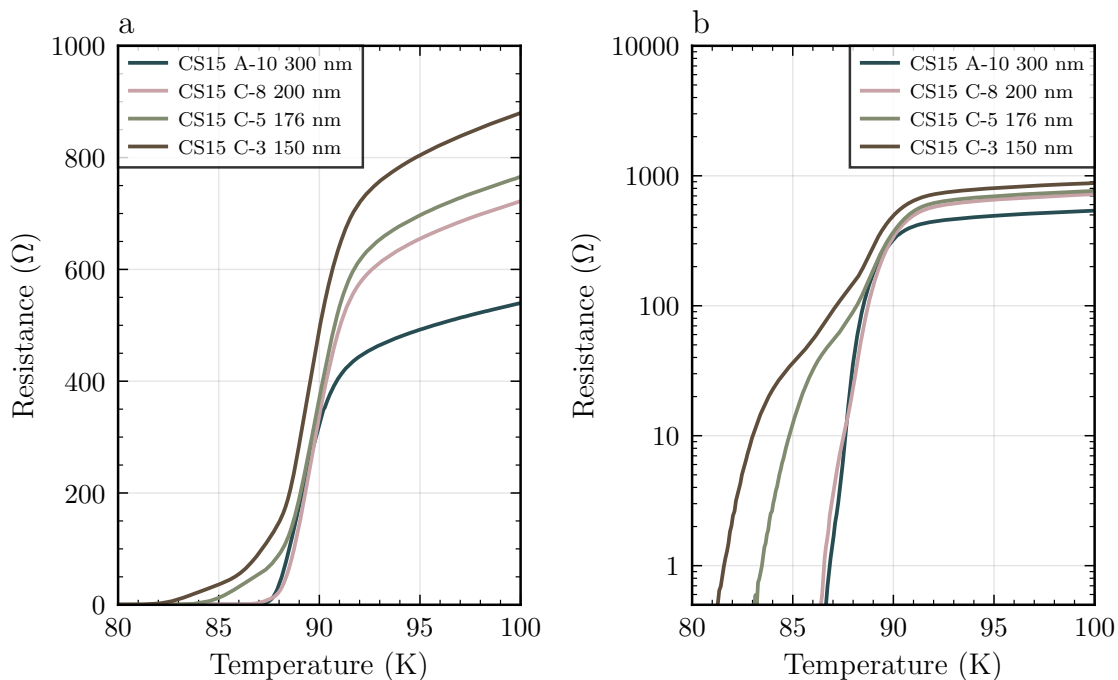


Figure 4.1 – Resistance versus temperature curves for different nanowires from the sample CS15 (see Fig.3.6). The exact dimensions of each nanowire are presented in table 4.1 or in Fig.3.6. a) in linear scale, b) in log scale.

In Fig.4.1, we present resistance versus temperature dependence for different nanowires from the sample CS15. One can observe that the resistance of all samples drops to zero below 90 K. The exact value of the critical temperature  $T_c$  varies with the width of the sample (see table 4.1). This can be explained in different ways: reducing the width increases the role of structural defects that can lead to a broadening of the superconducting transition (in the case of [Berezinskii–Kosterlitz–Thouless \(BKT\)](#) transition [Benfatto, 2009], for example), another argument suggests that decreasing the wire’s width changes the energy barrier for vortex to enter the nanowire [Bulaevskii, 2011; Gurevich, 2008; Vodolazov, 2012], and broaden the transition. The validity of these arguments depends on the specific mechanism causing the drop in resistance, and it is essential to determine which one is more probable.

The first scenario is the [BKT](#) transition experienced by [2D](#) superconducting systems. For this, our system must be two-dimensional with respect to the characteristic correlation length, which is the coherence length  $\xi$  in the superconducting case. The thickness of the sample CS15 is  $d = 30$  nm, while the bulk literature coherence length of  $\text{YBa}_2\text{Cu}_3\text{O}_{7-\delta}$  is  $\sim 2$  nm, which is one order of magnitude smaller. However, in the vicinity of the superconducting transition coherence length diverges. Thus, there can be a temperature region close to the critical temperature  $T \sim T_c$  where our sample becomes effectively two-dimensional. We can attempt to estimate the dimensionality via the fluctuation con-

| Nanowire | Width (nm) | Length (nm) |
|----------|------------|-------------|
| A-10     | 300        | 500         |
| C-8      | 200        | 500         |
| C-5      | 176        | 500         |
| C-3      | 150        | 500         |

Table 4.1 – Geometrical parameters for the nanowire’s RT curves plotted in Fig.4.1

ductivity. Above but close to  $T_c$ , there is some distribution of Cooper pairs created by thermal fluctuations that enhances conductivity. This effect is called paraconductivity and is stronger with a higher critical temperature  $T_c$  because thermal fluctuations are proportional to  $\sim k_B T$ .

Based on the microscopic theory, Aslamazov and Larkin [Aslamazov, 1968] calculated the impact of fluctuation on conductivity for different dimensions:

$$\begin{aligned}
\Delta\sigma_{1D}(T) &= \pi \cdot \frac{e^2 \xi_0}{16 \hbar w d} \cdot \left( \frac{T_c}{T - T_c} \right)^{\frac{3}{2}} \\
\Delta\sigma_{2D}(T) &= \frac{1}{16} \cdot \frac{e^2}{\hbar d} \cdot \left( \frac{T_c}{T - T_c} \right) \\
\Delta\sigma_{3D}(T) &= \frac{1}{32} \cdot \frac{e^2}{\hbar \xi_0} \cdot \left( \frac{T_c}{T - T_c} \right)^{\frac{1}{2}},
\end{aligned} \tag{4.1}$$

where  $\xi_0$  is a coherence length at zero temperature  $T = 0$ ,  $d$  is the thickness of the sample,  $w$  is the width of the sample,  $T$  is the temperature and  $T_c$  is the critical temperature. This paraconductivity is a part of a full conductivity, which can be written as  $\sigma(T) = \sigma_n + \Delta\sigma(T)$ , where  $\sigma_n$  is a normal part of the full conductivity and  $\Delta\sigma(T)$  is a fluctuations component. We can express it in terms of resistivity, which is easier to compare with our experiment:

$$\rho(T) = \frac{1}{\sigma(T)} = \frac{1}{\sigma_n + \Delta\sigma(T)} = \frac{1}{\frac{1}{\rho_n} + \Delta\sigma(T)}, \tag{4.2}$$

where  $\rho_n$  is a normal resistivity in the vicinity of the critical temperature  $T_c$ . The resulting resistance can be calculated as  $R(T) = \frac{\rho(T)l}{wd}$ , where  $l$  is the length of the sample.

In Fig.4.2, the resulting fit with this fluctuation model is presented for the nanowire A-10. Both 3D and 2D fits look well only in a very small region, but the 2D case seems to be in better agreement and with reasonable parameters (see Tab.4.2). In fact, this expression for 2D paraconductivity is valid for quasi-bidimensional systems. In real 2D systems, the phase transition occurs at the BKT temperature  $T_{BKT}$ , which is lower than the critical temperature  $T_c$ , where the Aslamazov-Larkin theory no longer holds. At the same time, the BKT theory works only close to the BKT temperature  $T_{BKT}$ . Halperin and Nelson [Halperin, 1979] proposed an interpolation formula to connect these two temperature regions. In reduced variables, it can be written as

$$\Delta\sigma_{HN} = a_{HN} \sigma_n \sinh^2 \left( \sqrt{b_{HN} t_c / t} \right), \tag{4.3}$$

| Model        | $R_N$ ( $\Omega$ ) | $d$ (nm) | $T_c$ (K) | $\xi_0$ (nm) | $b$ | $T_{BKT}$ (K) | $w$ (nm) | $\lambda_L$ (nm) |
|--------------|--------------------|----------|-----------|--------------|-----|---------------|----------|------------------|
| 2D           | 554                | 17       | 88.9      | -            | -   | -             | -        | -                |
| 3D           | 592                | -        | 89.8      | 1.7          | -   | -             | -        | -                |
| HN           | 517                | -        | 89.9      | -            | 2.7 | 87.2          | -        | -                |
| Vortex entry | 750                | 30       | 88.9      | 2            | -   | -             | 300      | 300              |

Table 4.2 – RT fit parameters

where  $a_{HN}, b_{HN}$  are dimensionless constants ( $b_{HN} \sim 1$  and  $a_{HN} = 0.37/b_{HN}$ ),  $t_c = \frac{T_c - T_{BKT}}{T_{BKT}}$ ,  $t = \frac{T - T_{BKT}}{T_{BKT}}$ .

We can see that at higher temperatures, close to  $T_c$ , it overlaps with Aslamazov-Larkin 2D fluctuations  $\Delta\sigma_{2D}$  and at lower temperatures it fits better in a wider range (see Fig.4.2). Despite the fact that the fit describes part of the curve well, as the temperature decreases, there remains a tail of resistance that is not captured by any of the models considered. Comparing such a slow decline in resistance with other samples (see Fig.4.1), one can see a tendency that the width of the superconducting transition is inversely proportional to the width of the sample. This may indicate an increase in the contribution of inhomogeneities because a decrease in the effective volume leads to a greater impact of any morphological defects in transport measurements. For example, Benfatto *et al.* [Benfatto, 2009] have shown that accounting for sample inhomogeneities at the BKT transition effectively broadens the superconducting phase transition.

The second scenario is the vortex entry. According to [Qiu, 2008; Bartolf, 2010; Bulaevskii, 2011] the most favorable dissipation route in 2D superconducting strips is the vortex entrance. There is a barrier for a vortex to enter that can be overcome in the vicinity of  $T_c$  due to thermal fluctuations. Once the vortex enters the sample, it drags by the Lorenz force of the bias current  $I_b$  and thus dissipates energy. Based on the Langevin equation for the vortex motion, Bulaevskii *et al.* [Bulaevskii, 2011] showed that the resistance corresponding to vortex motion can be written as

$$R_v(T) = 7.1R_N \frac{\xi(T)}{w} \left( \frac{\epsilon_0(T)}{k_B T} \right)^{3/2} \exp \left( -\frac{\epsilon_0(T)}{k_B T} \ln \frac{1.47w}{\pi\xi(T)} \right) \quad (4.4)$$

where  $\epsilon_0(T) = \Phi_0^2 d / 4\pi\mu_0\lambda_L^2(T)$  is the vortex energy inside the superconductor,  $\mu_0$  is the vacuum permeability, and  $R_N$  is the resistance in the normal state. For the temperature dependence of the London penetration depth we use the Gorter-Casimir phenomenological law [Ouanani, 2016b; Rauch, 1993; Wolf, 2013; Johansson, 2009]

$$\lambda_L(T) = \frac{\lambda_0}{\sqrt{1-t^2}}, \quad (4.5)$$

where  $t = T/T_c$  and  $\lambda_0$  is the London penetration depth at zero temperature. And for the coherence length temperature dependence we use the usual expression  $\xi(T) = \xi_0 \frac{1}{\sqrt{1-t}}$  from the Ginzburg-Landau theory. The resulting fit is shown in Fig.4.2. We can see that it

visually smoothly continues the 2D fit from the Aslamazov-Larkin model and fits our data well in this region. However, parameters such as normal state resistance  $R_N$  and London penetration depth  $\lambda_L$  are significantly overestimated (see Tab.4.2). For  $\text{YBa}_2\text{Cu}_3\text{O}_{7-\delta}$  thin film, London penetration depth is around  $\lambda_L \approx 150 - 180$  nm [Amari, 2017a; De Nivelles, 1993], while in our case it approximately equals the width of the sample  $\lambda_L \approx w$ . Perhaps this overestimation is due to the way the integral is trimmed when deriving this equation. Indeed, the region near the edge of the sample on the length of the coherence length  $\xi$  is beyond the limits of the approximation used and must be truncated in some way. This point is a matter of debate [Gurevich, 2012; Bulaevskii, 2012]. Also, this model does not fit well the resistance "tail" well before the resistance drops to zero.

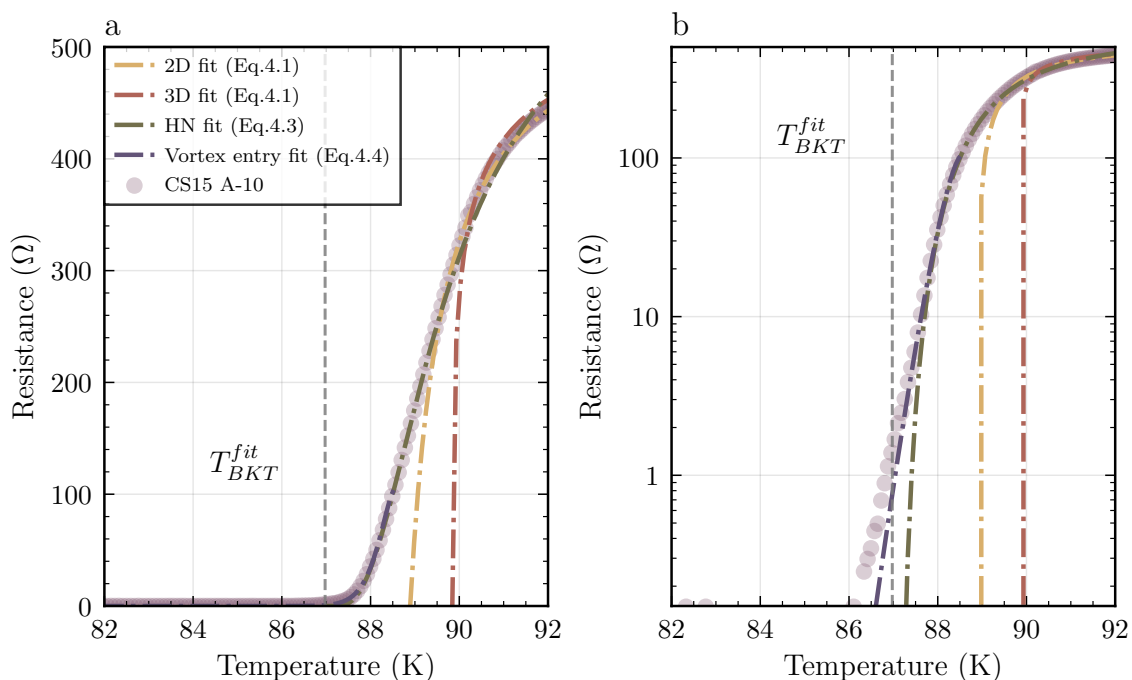


Figure 4.2 – Fit of the resistance versus temperature dependence for the nanowire A-10 based on the different models: 3D and 2D fluctuations models (Eq.4.1), the Halperin-Nelson model (Eq.4.3) and the vortex entry model (Eq.4.4). a - linear scale, b - log scale.

As we can see both models offer a partial description of our data, and both fall short in fitting the resistance "tail". According to arguments presented in [Arpaia, 2014c], the vortex entry model explicitly incorporates the effect of the broadening of the transition with decreasing width of the nanowire (Eq.4.4). In contrast, the simple BKT model we employed lacks explicit geometric dependencies. In real samples, it becomes essential to consider morphological imperfections that could contribute to the broadening of the superconducting transition, as mentioned earlier and also a finite size of the sample. Despite weighing the pros and cons of both scenarios, definitively distinguishing between them is challenging. Further investigation involving comparisons with other dimensions is necessary for a more comprehensive understanding. In the subsequent analysis, we will

explore additional measurements such as current-voltage characteristics and Shapiro step measurements, delving back into the discussion of vortex and BKT mechanisms.

### 3 IV characteristics

A large amount of information about the physical nature of the processes taking place can be provided by the current-voltage characteristic or **Current versus Voltage (IV)** curves. Fig.4.3 shows a typical IV curve for the nanowire D-4 from the sample CS15 with length  $l = 20 \mu\text{m}$ , width  $w = 200 \text{ nm}$ , and thickness  $d = 30 \text{ nm}$  at temperature  $T = 7 \text{ K}$ . The voltage changes by seven orders of magnitude as the current increases, so the plot on the left is shown on a logarithmic scale. The IV curve itself is divided into two parts: "up" with a positive current sweep from zero current to the maximum current  $I_{max}$  with the step  $I_{step}$ , and part "down" with a negative current sweep from the maximum current  $I_{max}$  to zero current with the same step. These two parts partially overlap, exposing a strong hysteresis.

#### 3.1 Switching, returning and critical currents

Furthermore, we can define a number of important points on the plot that provide significant information about the physical properties of the system. The first one is the critical current  $I_c$ , which defines the maximum current that the system can provide without dissipation. There are several ways to determine critical current. We use the threshold algorithm: the critical current is defined as the current where voltage exceeds threshold value  $V_{thr} = 6 \text{ mV}$ , which is slightly above the level of noise. Further increase of current leads to increase of voltage on the sample. This growth is very nonlinear, depends on many parameters, and is the subject of separate studies.

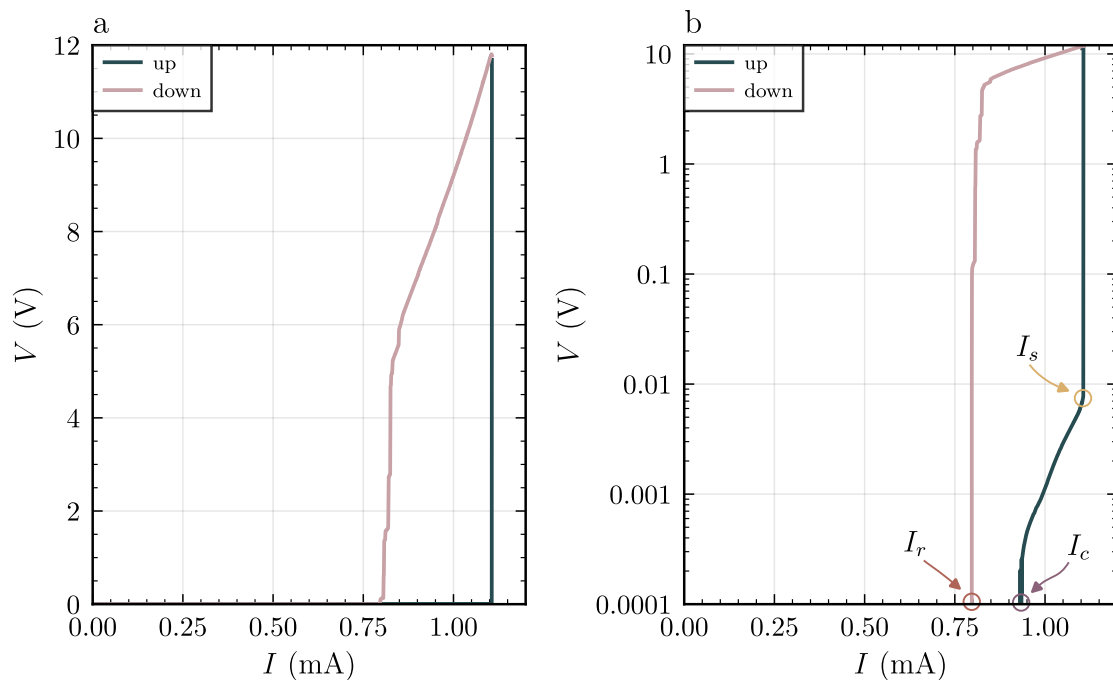


Figure 4.3 – IV curve of the nanowire D-4 from the sample CS15. a - linear scale, b - log scale.

After the current reaches a value called the switching current, the voltage jumps sharply and then grows linearly. The switching current is the maximum current before the system jumps to the normal state. By normal state, we mean the moment when the sample or a part of the sample transitions to the normal state so that the superconducting phase region loses cohesion along the current path. In this case, there is a large dissipation of energy associated with Joule heating, which leads to a cascade process of superconductivity destruction in a larger and larger part of the sample and, as a consequence, to a large increase in voltage.

When reversing the current, the sample does not go into the superconducting state at the switching current. Instead, the voltage decreases almost linearly with decreasing current. The sample is said to be overheated and in a metastable state, which describes the hysteresis of this curve. The sample enters the superconducting state only at the return current, experiencing a series of successive jumps. We estimate the switching and the return current by the same method using thresholds  $V_{thr}^s = 1$  V and  $V_{thr}^r = 10$  mV for the switching current and the return current, respectively.

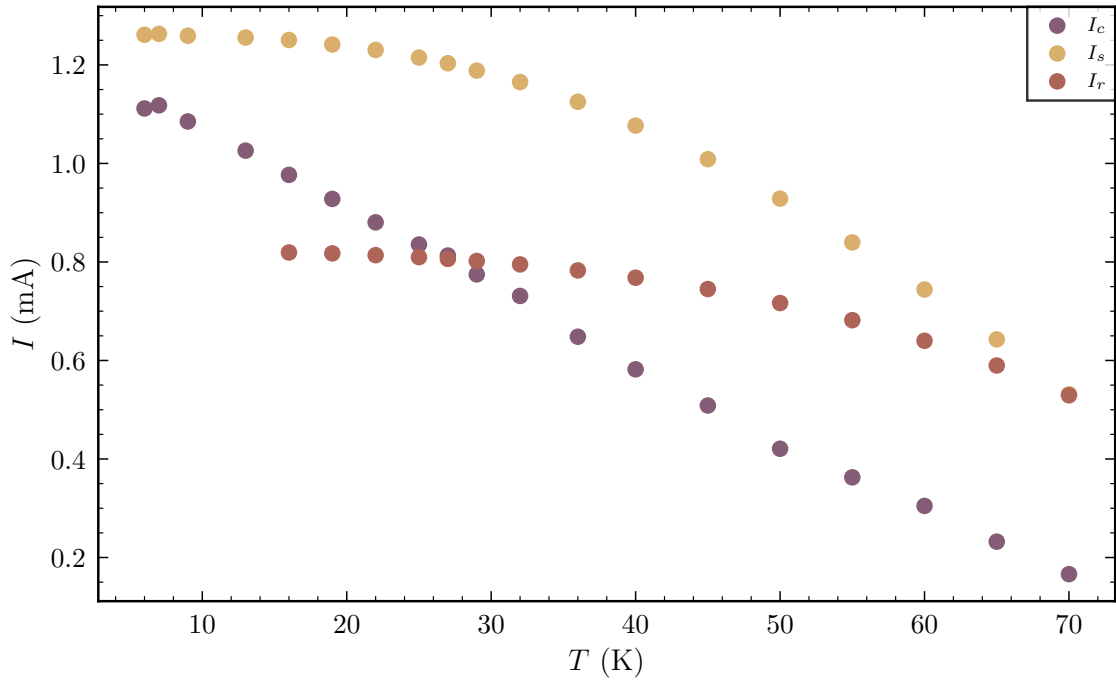


Figure 4.4 – Temperature dependencies of the switching current  $I_s$ , the critical current  $I_c$  and the returning current  $I_d$  for the nanowire B-6 of the sample CS16.

**Temperature dependence** A great deal of information can be obtained by studying the temperature dependence of the  $IV$  curves. We have already marked three special points on these curves and now we will analyse their temperature dependence. Fig.4.4 shows the temperature dependencies of the switching current, the critical current and the returning current for the nanowire B-6 of the sample CS16 with length  $l = 500$  nm, width  $w = 200$  nm, and thickness  $d = 30$  nm. We will consider switching, return and critical currents separately because their nature is different.

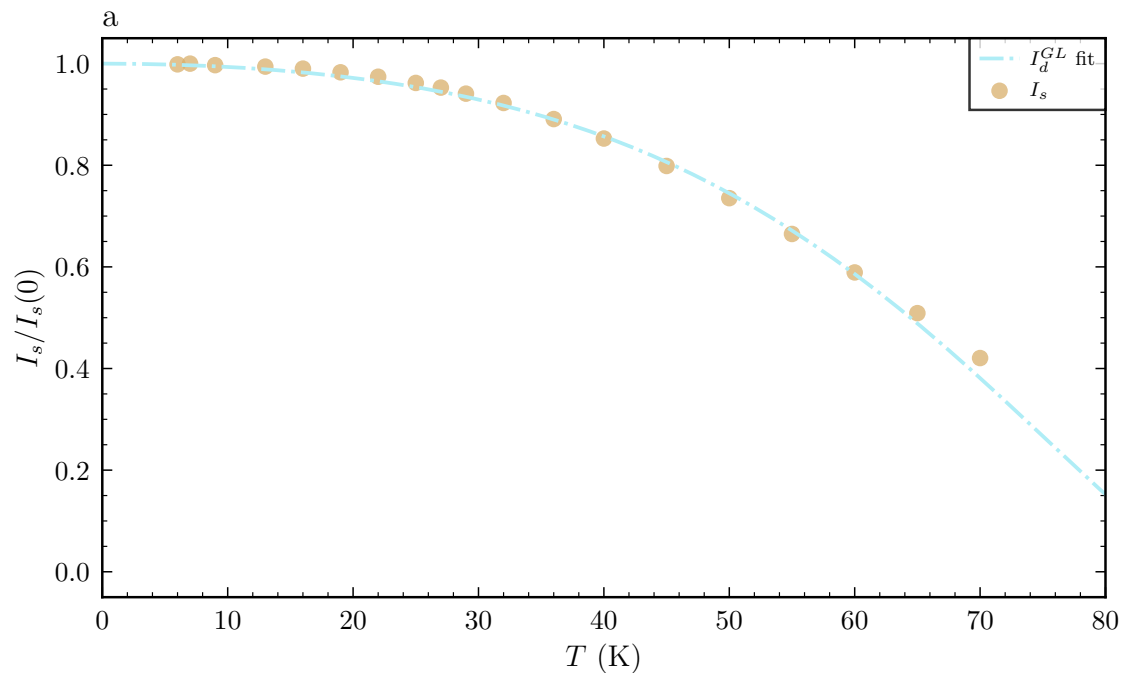


Figure 4.5 – Fit of the switching current versus temperature dependence based on the depairing current from the Ginzburg-Landau model (Eq.4.7) for the nanowire B-6 from the sample CS16.

We start with the switching current. The switching current is related to the full depletion of the order parameter that brings the system to the normal state through a non-equilibrium process. In other words, it is the maximum possible current of the system before it fully returns to the normal state. In superconducting samples, such a current is the depairing current, a current whose strength destroys Cooper pairs. In terms of the Ginzburg-Landau theory, the depairing current density can be expressed as:

$$j_d^{GL}(T) = 0.385 \frac{\Phi_0}{2\pi\mu_0\lambda_L^2(T)\xi(T)} \quad (4.6)$$

where  $\mu_0$  is the vacuum permeability,  $\Phi_0$  is the magnetic flux quantum,  $\lambda_L(T)$  is the London penetration depth, and  $\xi(T)$  is the coherence length of the Ginzburg-Landau theory. The temperature dependence is given by temperature dependencies of  $\lambda_L(T)$  and  $\xi(T)$ . Multiply the depairing current density by the nanowire cross-section  $wd$  ( $w$  is the width and  $d$  is the thickness of the sample), we obtain the expression for the depairing current:

$$I_d^{GL}(T) = j_d^{GL}(T)dw = 0.385 \frac{\Phi_0 wd}{2\pi\mu_0\lambda_L^2(T)\xi(T)} \quad (4.7)$$

Estimating the value of the current by formula from the Eq.4.7 at zero temperature, we obtain a value of the switching  $I_s$ , six times the value of the experimental one. However, if we plot the graphs normalised to the maximum value, we find a complete coincidence of the shape of the curves (see Fig.4.5). Here, we use the temperature dependencies for the

coherence length in the a-b planes of the  $\text{YBa}_2\text{Cu}_3\text{O}_{7-\delta}$  and for the London penetration depths from the two-fluid phenomenological formula [De Nivelles, 1993; Kunchur, 2019], as follows:

$$\begin{aligned}\xi(T) &= \xi_0 \left(1 - \left(\frac{T}{T_c}\right)^2\right)^{-1/2} \\ \lambda(T) &= \lambda_0 \left(1 - \left(\frac{T}{T_c}\right)^4\right)^{-1/2}\end{aligned}\tag{4.8}$$

The used zero temperature values are  $\xi_0 = 2$  nm and  $\lambda_0 = 200$  nm. The good shape fit and the discrepancy in its amplitude can be explained in terms of the *phase slip lines* [Berdiyrov, 2009b; Weber, 1991; Dmitriev, 2005] or the *kinematic vortices* [Andronov, 1993; Berdiyrov, 2009a] induced by edge defects [Souto, 2021]. Before reaching the switching current, there are already many vortices in the sample that are travelling at high speed. Their motion causes dissipation of energy, which must be effectively dissipated by the sample and its environment. If this cannot be done, the sample avalanches into a normal state. But this requires a nucleus. Such a nucleus can be a kinematic vortex. At high velocities, the shape of the vortex is distorted, stretching along the direction of motion. At the same time, under these conditions, one vortex is followed by a second one and so on, forming so-called *vortex rivers* or *rivers of flux* [Olson, 1998; Silhanek, 2010a; Dobrovolskiy, 2020b]. Further, they merge into two-dimensional phase slips, forming lines where the order parameter is strongly suppressed. Such mechanism can lead to the subsequent vortex instability [Larkin, 1975; Vodolazov, 2007] and transition to the normal state. And, as it was shown in [Kramer, 1977; Kramer, 1978], these phase slips lines can occur at lower currents than the depairing one.

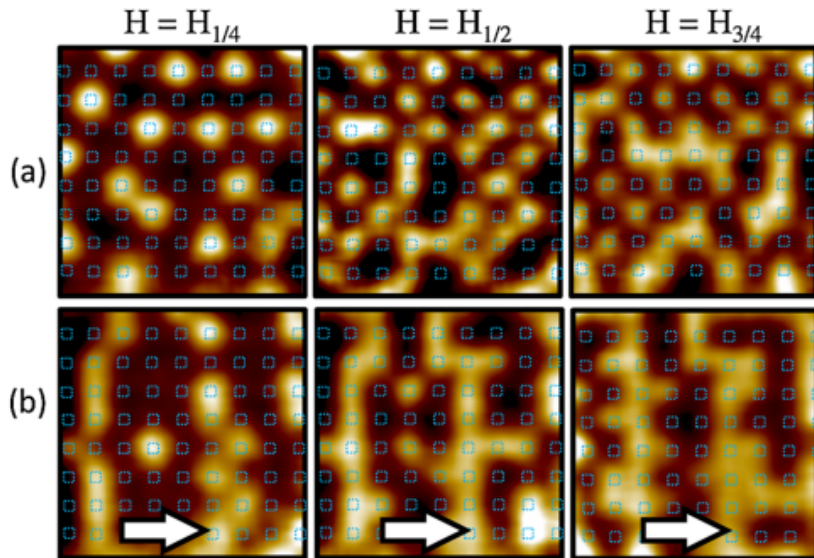


Figure 4.6 – *Frozen vortex rivers* adapted from [Silhanek, 2010b]. Vortex configurations, imaged by scanning Hall probe microscopy at  $T = 4.2$  K in a superconducting Pb film with a periodic array of pinning sites: (a) field cooled without applied current and (b) field cooled with applied current of 36 mA. The arrows indicate the direction of the applied current.

On the inverse branch of the IV curve, the switching current is equivalent to the returning current  $I_r$  - the current at which the sample returns to the superconducting state. As we have already mentioned, the returning current is determined by the effect of overheating during the switching. It is a thermal multifactorial process involving not only the sample but also the substrate, which dissipates heat. The returning process to the superconducting (at least partially) state can be described through the hot-spot model by Skocpol, Beasley, and Tinkham (SBT) [Skocpol, 1974]. This model considers heat propagation in a one-dimensional superconducting filament of thickness  $d$ , width  $w$ , and length  $l$ . Under the action of current  $I$ , a hot region of the normal phase (hot-spot) appears, the Joule heat from which propagates along the filament and the substrate. According to this model, the balance equation for such a system is written as

$$\begin{aligned}
 -\kappa_n \frac{d^2 T}{dy^2} + \frac{\alpha}{d}(T - T_b) &= \left(\frac{I}{wd}\right)^2 \rho \quad (|y| < y_0) \\
 -\kappa_s \frac{d^2 T}{dy^2} + \frac{\alpha}{d}(T - T_b) &= 0 \quad (|y| > y_0)
 \end{aligned}
 \tag{4.9}$$

where  $\kappa_n$  and  $\kappa_s$  are the thermal conductivity in the normal and in the superconducting states respectively,  $\rho$  is the film resistivity,  $T_b$  is the bath temperature,  $y_0$  is the half size of the normal hot-spot (see Fig.4.7), and  $\alpha$  is the thermal conductance per unit area.

For the normal region, the right-hand term of the first equation in Eq.4.9 is the Joule heating. In the left-hand side of the first equation in the Eq.4.9 the first term corresponds to the thermal conduction of the nanowire in the normal and superconducting phase

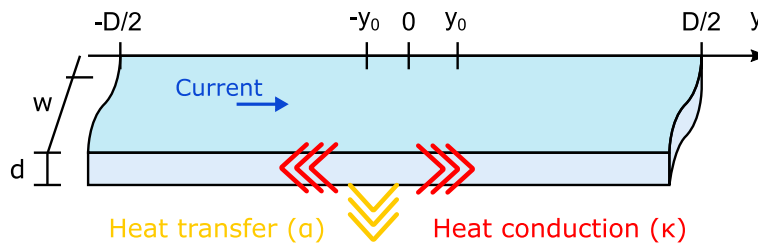


Figure 4.7 – Schematics of a biased current wire in the framework of the SBT thermal model. A normal hot region of length  $2y_0$  along the  $y$ -axis in red transfers thermal energy laterally to the superconducting wire via heat conduction  $\kappa$ , and through the substrate due to the heat transfer  $\alpha$ . Depending on the values of  $\alpha$  and  $\kappa$ , the hot region either expands or self-heals.

respectively, while the second term represents the thermal transfers through the substrate.

As a first approach, assuming that the conductivities are identical, i.e.  $\kappa = \kappa_s = \kappa_n$ , the equilibrium between these terms naturally leads to a characteristic thermal length  $\eta_h$ , called the healing length, and expressed as:

$$\eta_h = \sqrt{\frac{\kappa d}{\alpha}} \quad (4.10)$$

Depending on the length  $l$  of the nanowire compared to the healing length  $\eta_h$ , there are two types of behaviour. Either for  $l > \eta_h$ , heat is dissipated mainly through the substrate, preventing the hot spot from extending across the entire width of the nanowire, which remains in the superconducting state. For  $l < \eta_h$ , heat exchange within the superconducting nanowire dominates, and the hot spot propagates throughout the nanowire. The result is a superconducting transition to the normal state, the signature of which is both hysteresis and switching in the  $IV$ 's curve. To estimate  $\eta_h$  in our  $\text{YBa}_2\text{Cu}_3\text{O}_{7-\delta}$  nanowires on a sapphire substrate, we use  $\alpha \approx 1 \times 10^7 \text{ W} \cdot \text{K}^{-1} \cdot \text{m}^{-2}$  [Sergeev, 1994] and  $\kappa_n \approx 0.8 - 3 \text{ W} \cdot \text{K}^{-1} \cdot \text{m}^{-1}$  [Nahum, 1991]. Using these two limiting values for thermal conductivity, the healing length of a 30 nm thick  $\text{YBa}_2\text{Cu}_3\text{O}_{7-\delta}$  film can be estimated to be  $\eta_h \approx 50 - 100 \text{ nm}$ . In our case, the nanowires are always longer than the estimated healing length, while their width is of the same order of magnitude or greater than the healing length.

For long bridges  $l \gg \eta_h$ , we have the following approximation for the healing current:

$$I_h \approx w \sqrt{\alpha d \frac{T_c}{\rho}} \sqrt{1 - T/T_c} \quad (4.11)$$

In terms of the  $IV$  curve, the healing current equals the returning current  $I_h \equiv I_r$ . Calculation according to the formula Eq.4.11 gives  $I_r(T = 0) \approx 0.5 \text{ mA}$  that nearly twice smaller than in our experimental data. The source of this discrepancy can be in possible variations of material parameters such as  $\rho, \alpha, T_c$  or in our estimation of the sample geometry  $w, d$ , but due to the square root dependence on most of the parameters, such errors

must peak summarily by a factor of 4, which raises the question of the applicability of the original model as such in our case.

Last, we consider the third special point on the IV curve - the critical current  $I_c$ . The critical current is defined by the current at which a voltage greater than the noise level appears on the sample. This current is different in nature from the switching current and is related to the movement of vortices in the sample. For this to happen, the vortices must first enter the sample and secondly start to move. But, in real samples, their movement is hampered by the pinning effect. The critical current is reached when the applied current exceeds the pinning force at a given temperature. The pinning phenomenon is very comprehensive (especially in HTS, where the coherence length is very small), so we will consider only the partial results of some models describing the temperature dependence of the critical current.

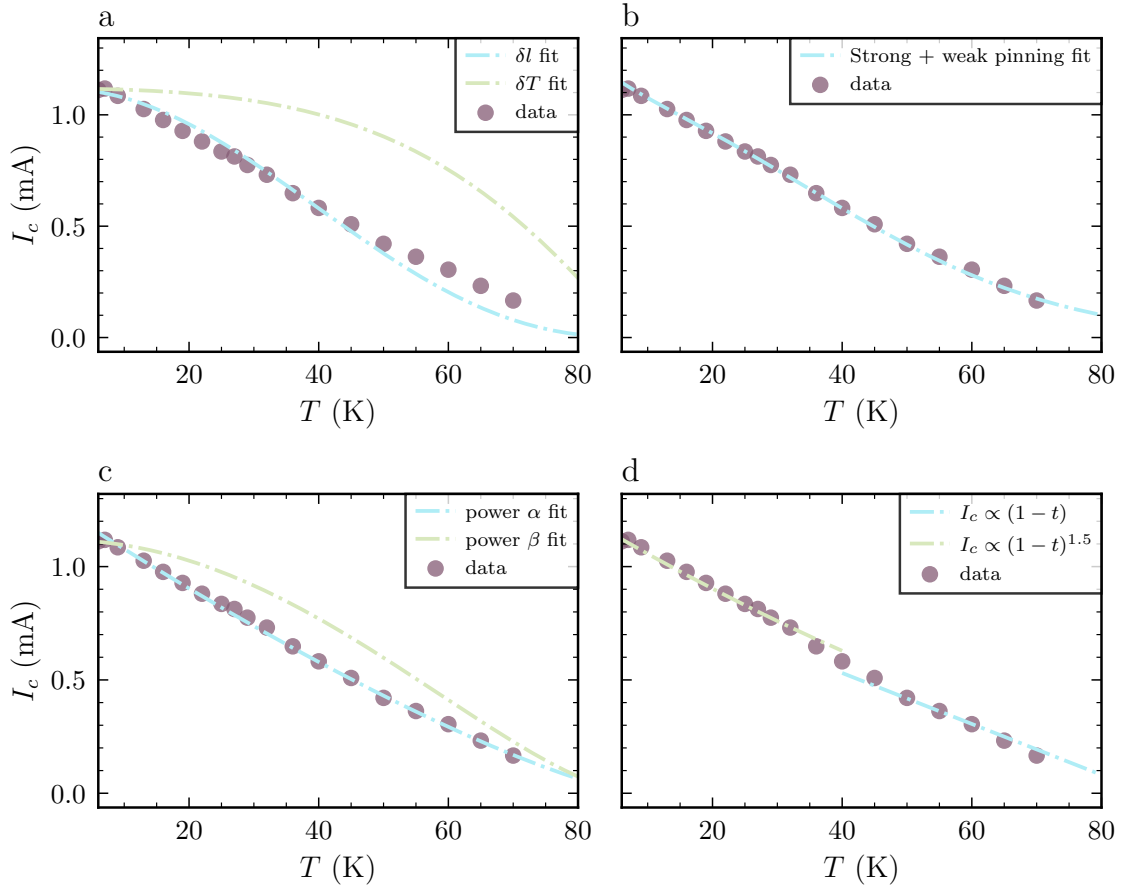


Figure 4.8 – Fit of the critical currents versus temperature dependence for the nanowire B-6 from the sample CS16, based on the different models described in the main text. a) Model from Griessen *et al.*[Griessen, 1994] implementing the fluctuations of the critical temperature  $\delta T$  or fluctuations of the mean free path length  $\delta l$  to the critical current evolution in temperature (Eq.4.12). b) Model from Plain *et al.*[Plain, 2002] with the contributions of both strong and weak pinning types to the critical current evolution in temperature (Eq.4.13). c) Power  $\alpha$  and  $\beta$  fits (Eq.4.14) d) Albrecht *et al.*[Albrecht, 2007] model with two regimes below 40K (vortex pinned on specific pinning shape and morphology) and above 40 K (depinning is thermally activated) .

One way of treating the pinning effect is in terms of fluctuations in the critical temperature or fluctuations of the mean free path length in the sample volume. In the Ref.[Griessen, 1994], it was shown that for these two types of pinning critical current can be written as

$$\begin{aligned}
 I_c(t) &= I_c(0)(1 - t^2)^{\frac{5}{2}}(1 + t^2)^{-\frac{1}{2}}, \text{ for } \delta l \text{ pinning} \\
 I_c(t) &= I_c(0)(1 - t^2)^{\frac{7}{6}}(1 + t^2)^{\frac{5}{6}}, \text{ for } \delta T_c \text{ pinning}
 \end{aligned}
 \tag{4.12}$$

where  $t = \frac{T}{T_c}$  is a reduced temperature and  $I_c(0)$  is a critical current at zero temperature. The corresponding fit is shown in Fig.4.8a. As previously mentioned, our experimental critical current versus temperature data  $I_c(T)$  exhibits a rather linear behaviour. This

contradicts the  $\delta T$  pinning law but aligns better with the  $\delta l$  pinning model, albeit with some slight deviations. This observation supports the notion that pinning likely governs the critical current in our sample.

However, the pinning can vary significantly in nature, and different types of pinning exert distinct influences on the critical current across various temperature ranges. For example, weak point-like pinning sites, such as oxygen vacancies in  $\text{YBa}_2\text{Cu}_3\text{O}_{7-\delta}$ , have a strong impact at low temperatures. At higher temperatures, the so-called strong pinning becomes more significant, attributed to morphological and structural defects in the crystal, such as dislocations, twin boundaries, and inclusions. The study by Plain *et al.* [Plain, 2002] demonstrated the presence of both types of pinning in  $\text{YBa}_2\text{Cu}_3\text{O}_{7-\delta}$ . They also proposed an approximation formula combining the contributions of both pinning types to the critical current:

$$I_c(t) = I_w e^{-\frac{T}{T_w}} + I_{str} e^{-3\left(\frac{T}{T_{str}}\right)^2} \quad (4.13)$$

where the first term on the right side is the weak pinning contribution [Senoussi, 1988; Christen, 1993; Blatter, 1994], with  $I_w$  as the weak pinning critical current component and  $T_w$  as the characteristic weak pinning energy in terms of temperature and typically in a range of 8 – 13 K. The second term on the right side represents the strong pinning contribution [Nelson, 1993; Hwa, 1993], with  $I_{str}$  as the strong pinning critical current component and  $T_{str}$  as the characteristic strong pinning energy in terms of temperature, typically in the range of 78 – 93 K for  $\text{YBa}_2\text{Cu}_3\text{O}_{7-\delta}$  [Gutiérrez, 2007; Polat, 2011]. In Fig.4.8b, the resulting fit is presented with temperature parameters  $T_w = 9$  K and  $T_{str} = 91$  K and current parameters  $I_w = 0.25$  mA and  $I_{str} = 1.03$  mA. One can see that this model works very well with reasonable fit parameters, and these parameters indicate a significant contribution of the strong pinning component. This is an important result for our subsequent analysis of the other results. Despite the fact that this model satisfies us in many respects, technically it cannot describe the dependence of the critical current on temperature in the whole temperature range. In fact, at a temperature equal to the critical temperature, the critical current according to the formula 4.13 is not equal to zero. But this property is possessed by the power dependencies used in the works [Fedotov, 2002; Ijaduola, 2006; Miura, 2011; Albrecht, 2007]. They propose the following formula for the critical current:

$$\begin{aligned} I_c(t) &= I_c(0)(1-t)^\alpha \\ I_c(t) &= I_c(0)(1-t^2)^\beta, \end{aligned} \quad (4.14)$$

where  $t = \frac{T}{T_c}$  is a reduced temperature and typical values of  $\alpha = 0.9-2$  and of  $\beta = 1.2-1.5$  were found in literature [Kuznetsov, 2017]. In the Fig.4.8c, we present the corresponding fit with parameters  $\alpha = 1.3$  and  $\beta = 1.65$ . The power  $\alpha$  fit with the first formula in the Eq.4.14 is nearly as good as the previous fit with the strong and weak pinning model using the formula in the Eq.4.13. Now it satisfies the condition that the critical current is zero when the critical temperature is reached. We found that  $\alpha = 1.3$  fits the experimental curve well with the power law  $\propto (1-t)^\alpha$  in all temperature ranges, which is quite expected,

since behaviour of the experimental data is linear.

A last model we want to present accounting for pinning contribution to critical current deals with two main contributions of pinning in different ranges of temperature. According to analysis by Albrecht *et al.* [Albrecht, 2007], the whole temperature range can be divided into two parts: a low-temperature regime, below  $T \approx 40$  K and a high-temperature regime, above  $T \approx 40$  K. In the high-temperature regime, the critical current should be linear with temperature  $I_c \propto (1 - t)$ , consistent with the linear dependence of the vortex energy  $\epsilon(T) \sim \frac{1}{\lambda_L^2} \sim (T_c - T)$  on temperature in the Ginzburg-Landau theory (see Eq.1.39). In this case, depinning is thermally activated, and the pinning energy is proportional to the vortex energy at a particular temperature  $\epsilon(T)$ . As the temperature decreases, the probability of thermal depinning decreases, and we move into the low-temperature regime. Now, the specific pinning shape and morphology come into play. In the work [Albrecht, 2007], the authors found that in this case, the critical current can be estimated as  $I_c \propto (1 - t)^s$ , where the power  $s$  depends on the particular pinning landscape and can vary from  $s = 1.5$  to  $s = 2.5$ .

In Fig.4.8d, we present our results of the described analysis. For the fit, we use these power laws in the form  $I_c = a(1 - t) + b$  or  $I_c = I_c^0(1 - t)^s + I^0$  for the corresponding fit. Here,  $a$  is the coefficient proportional to the critical current at zero temperature, and  $b$  simulates the depth of the pinning potential. Fitting parameters were obtained by the least squares method. One can see that at high temperatures, the suggested model works well and deviations from it start exactly around  $T \approx 40$  K. At low temperature, we switched to the other suggested power law and found that with  $s = 1.5$ , we are able to fit our data correctly. At the intermediate temperature regimes, change occurs, and our simple models fail. This range is very complex since one cannot work within the limits of high or low  $k_B T$ , and contributions from many processes must be taken into account.

Based on this analysis, we can conclude that models based on the pinning mechanism can adequately describe the temperature dependence of the critical current. Further details can be clarified, but the general conclusion remains the same: pinning plays a crucial role in the transport properties of our samples.

### 3.2 Flux Creep behavior

In this part, we will focus on the shape for the **IV** curves in the normal state near the critical current and before the switching current. In Fig.4.9a and Fig.4.9b, a typical set of **IVs** are plotted in linear scale and log scale, respectively, for temperatures ranging from 6 K to 70 K.

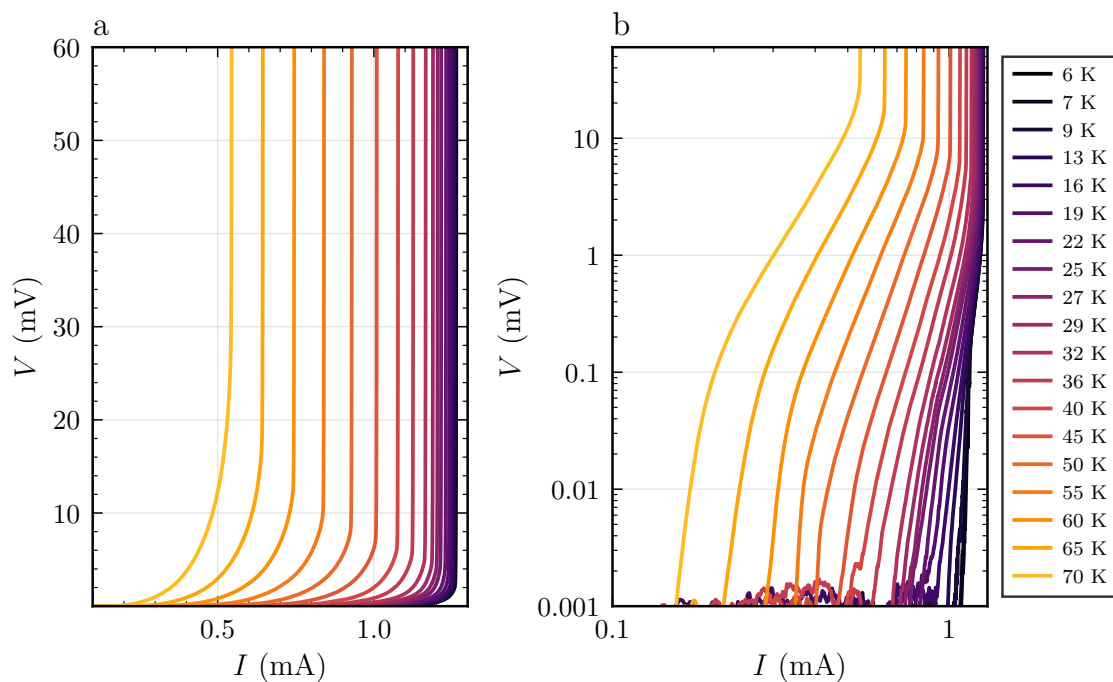


Figure 4.9 – IV curves for different temperatures in linear scale a) and log scale b) for the nanowire C-5 from the sample CS15.

At small currents relative to the critical current  $I \gtrsim I_c$ , the model associated with vortex creep is realised. In this regime, the mobility of vortices is low, and their motion is carried out by jumps from one pinning point to another. This vortex motion is a result of the Lorentz force of the transport current and thermal fluctuations. In this picture, the pinning centres represent a potential well of some depth, which in the simplest case captures one vortex. The creep flux model was proposed by Anderson and Kim [Anderson, 1964], and applied specifically to  $\text{YBa}_2\text{Cu}_3\text{O}_{7-\delta}$  by Bernstein *et al.* [Bernstein, 1995; Bernstein, 1997; Pannetier, 2000]. We will follow this approach in analysing our data.

Consider a nanowire of length  $l$  and width  $w$  under the action of a transport current  $I$ . We assume that vortices (created by an external magnetic field or by a current itself) of density  $n_\phi$  are present in the nanowire. Then, under the action of the Lorentz force, they will come into motion, creating a voltage drop at the ends of the nanowire equal to

$$V = lv_\phi n_\phi \Phi_0 \quad (4.15)$$

where  $v_\phi$  is the average velocity of the vortices,  $\Phi_0$  is, as usual, the flux quantum.

Considering vortex motion as a diffusion process from the nanowire edges to its centre, we can write the following expression for the vortex density along the edges at zero external magnetic field [Pannetier, 2000]

$$n_\phi(w/2) = \frac{\mu_0(I - I_c)}{2\Phi_0 d}, \quad (4.16)$$

where  $I_c$  is the critical current, and the condition  $I > I_c$  is assumed. According to the description in the original model [Anderson, 1964], the vortex velocity can be written as

$$v_\phi = 2v_0 \exp\left(-\frac{E_p}{k_B T}\right) \sinh\left(\frac{W}{k_B T}\right), \quad (4.17)$$

where  $T$  is the temperature,  $v_0$  is the maximum vortex velocity along the edges,  $E_p$  is the pinning energy,  $W$  is the work done by the Lorentz force. Maximum velocity can be expressed as

$$v_0 = \omega \delta_p, \quad (4.18)$$

where  $\omega$  is the thermal activation attempt frequency and  $\delta_p$  is the jump width between pinning sites. The Lorentz force work can be written as

$$W = \frac{I \delta_p \Phi_0}{w}. \quad (4.19)$$

Combining these all equations Eqs.4.15-4.18, we can finally retrieve voltage versus current dependence:

$$V = (I - I_c) \frac{\mu_0 l \omega \delta_p}{d} \exp\left(-\frac{E_p}{k_B T}\right) \sinh\left(\frac{I \delta_p \Phi_0}{k_B T w}\right). \quad (4.20)$$

Before fitting our data, we need to decide on a set of parameters. Geometrical parameters, critical current and temperature are known from the experiment with good accuracy. The internal parameters of the model include the thermal activation attempt frequency  $\omega$ , the jump width  $\delta_p$  and the pinning energy  $E_p$ . From literature data [De Nivelles, 1993] at zero magnetic field, the frequency can be limited within a range  $2 \times 10^{12} - 2 \times 10^{13}$  Hz. An estimation from the Heisenberg uncertainty principle  $k_B T \sim \hbar \omega$  gives a value of the same order for temperatures  $T \approx 50 - 100$  K. We fix the value of the frequency to  $\omega = 1 \times 10^{13}$  Hz. The remaining two parameters: jump length and pinning energy will be the fit parameters.

Since this model describes only the initial part of the **IV** curve after the critical current, it is necessary to manually determine the final boundary. This freedom of choice is a separate problem when working with this kind of models because different fit algorithms, such as the least squares method, are sensitive to the data set. This makes it much more difficult to find the optimal fit. In our work, we will use the Akaike criterion to compare fits with different current bounds. The general procedure can be described as follows: a minimum current equal to the critical current is selected, then a fit with different boundary currents starting from the critical current and ending with the switching current is made. For each fit, the Akaike criterion is calculated and the fit with the lowest criterion value is considered the most satisfactory. The procedure is repeated for each temperature. This way we reduce the uncertainty in the choice of data for the fit, and the overall procedure increases the self-consistency of the results.

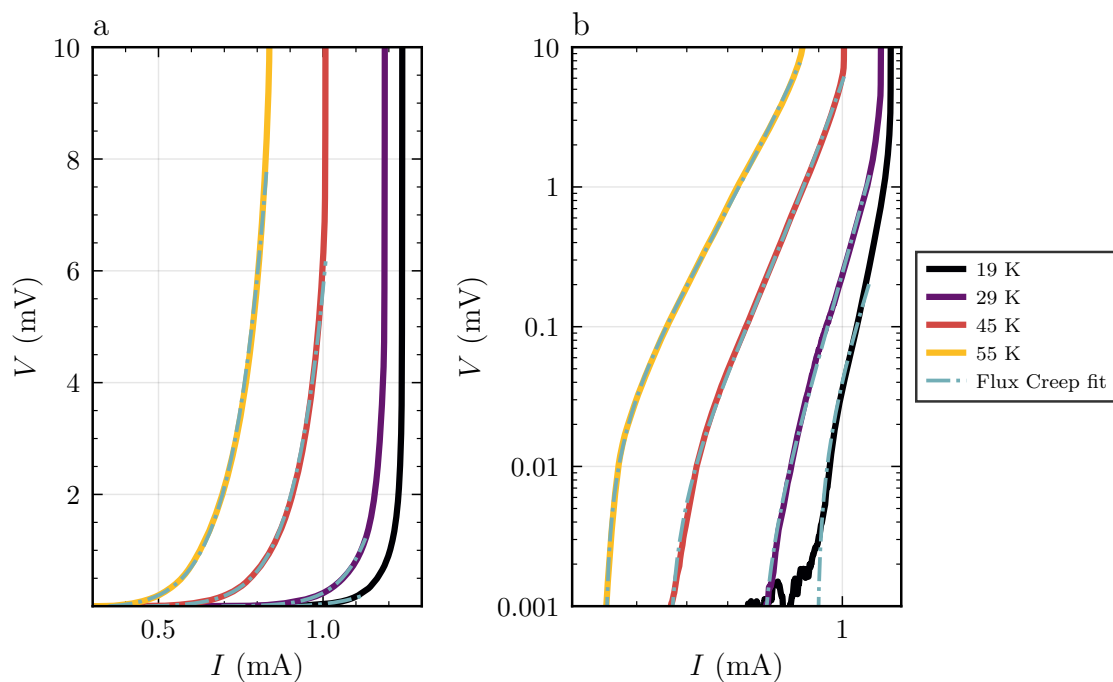


Figure 4.10 – Fit of IV curves based on the flux creep model (Eq.4.20) for the nanowire B-6 from the sample CS16.

Fig.4.10 shows a selected set of the experimental curves from 4.9 for the sample B-6 from sample CS16 and the fit by the described model. As can be seen, the model well describes the initial growth of IV curves in a wide range of temperatures. At high temperatures, the same coincidence of experiment and theory also occurs at large values of current close to the switching current. This is unexpected because, formally, the applicability conditions in this current region are not fulfilled. Indeed, this model works in the single vortex approximation, meaning it is restricted to the region where the mutual interaction of the vortices starts to play a role. We can estimate this current region from the equation that gives the current difference. However, in thin films, the vortices start to sense each other already at the Pearl length  $\lambda_P$ , which in our case is of order and larger than the nanowire length. In this sense, we initially do not fulfil the conditions of the model. But such a good match between our data and the flux creep theory may be due to the fact that the mutual interaction of the vortices is still weak compared to the Lorentz force and the pinning force. It has already been discussed in the section that there is good reason to believe in the presence of strong pinning centres such as twin boundaries in this sample. For the same reason, the fit can also work at high currents when part of the vortices are still trapped in the strong pinning centres.

From the resulting fit, we can also extract the model parameters: the pinning energy and the jump length, whose dependence on  $(1 - t)$  is depicted ( $t = T/T_c$ ). We have chosen such coordinates for a simpler comparison with the Goupil work [Cristophe, 1997]. According to this work, at small magnetic fields, taking into account the presence of twin

boundaries, the pinning energy can be written as [Kramer, 1973]:

$$E_p = \frac{\Phi_0^2 l}{4\pi\mu_0\lambda_L^2\gamma} \ln\left(\frac{l}{\xi}\right), \quad (4.21)$$

where  $\gamma$  is the electronic anisotropy factor for  $\text{YBa}_2\text{Cu}_3\text{O}_{7-\delta}$ . Using classical temperature dependencies from the Ginzburg-Landau theory, we obtain that the energy is proportional  $(1 - t)$ . As can be seen from Fig. 4.11a, our case is quite close to this simple estimate. This indirectly further confirms our idea about the influence of twin boundaries on the flux creep.

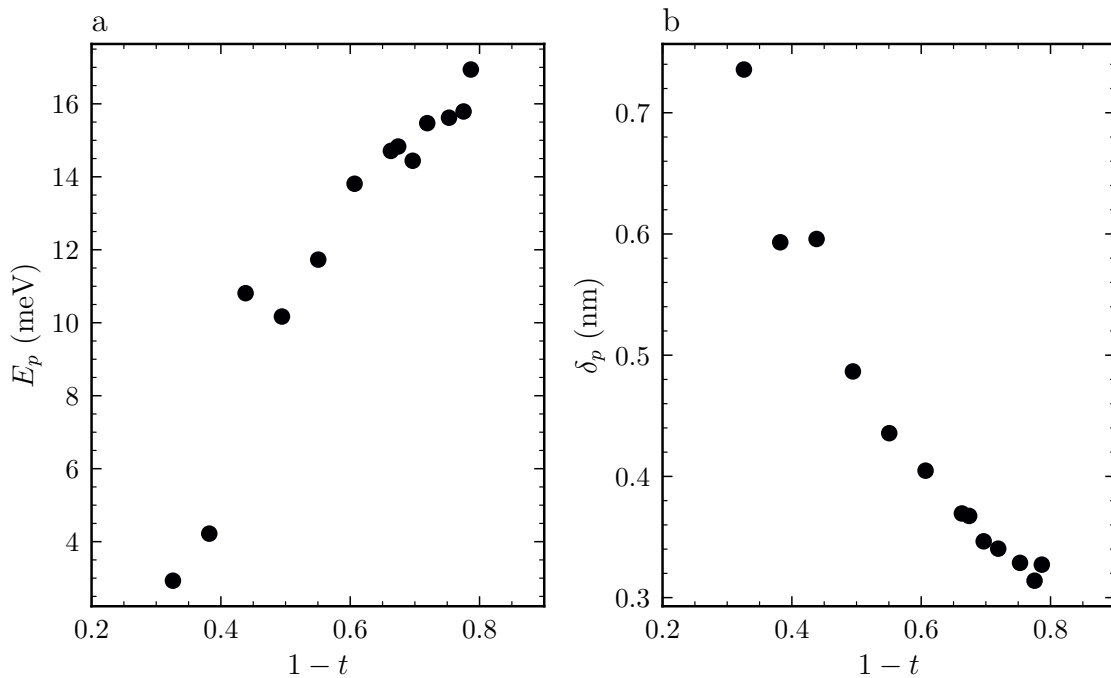


Figure 4.11 – The pinning energy  $E_p$  and the jump width between pinning sites  $\delta_p$  resulting from the flux creep model fit for the nanowire B-6 from the sample CS16.

Fig. 4.11 b shows the dependence of the jump length. Its behaviour seems intuitive: An increase in temperature leads to larger jumps due to a larger contribution of thermal fluctuations, which may lead to overshooting of several pinning centres and effectively increasing the jump length. However, comparison with literature data [Bernstein, 1997] shows that our lengths are two orders of magnitude smaller in amplitude.

We have analysed the initial part of the  $IV$  curve within the framework of the flux creep theory. A satisfactory fit of the experimental data was obtained and the physical parameters of the model were extracted. The summary analysis shows that the vortex creep may be the mechanism of the onset of pinning when the critical current is exceeded. The temperature dependence of the pinning energy is an argument for the large role of possible strong pinning centres in our sample. This argument agrees with the analysis

of the temperature dependence of the critical current given in Sect. 3. The temperature dependence of the jump length, on the other hand, agrees qualitatively with the literature data, but is quantitatively two orders of magnitude smaller. Characteristically, the length in the whole temperature range remains less than 1 nm. Perhaps such short jumps are performed within twin boundaries, which leads to such an effective underestimation of the jump length at the overall small sample size, when the contribution of each large defect can be enormous. The strength of such a defect was also showed in a direct measurement done by means of [Scanning Tunneling Microscope \(STM\)](#). Alternatively, it raises the question of the applicability of the model at all in our case. Direct measurements and transport measurements done simultaneously could probably provide a definitive answer.

### 3.3 Shapiro steps

#### 3.3.1 RF-illumination setup

One possible method of studying vortex motion can be the perturbation of vortices by [Radio-Frequency \(RF\)](#) radiation.

To do that, we placed a broad-band RF antenna several centimetres above our sample. The antenna was supplied by Anritsu MG3692C RF signal generator which provides a frequency range from 0.1 GHz to 20 GHz. In this setup, we cannot supply our sample with a specific frequency due to the fixed unknown absorption spectrum of a sample holder and wirings. Because of this, measurements of each new sample start from a scan with a range of frequencies 1 GHz - 10 GHz searching for the best absorption of the incident microwave.

To determine the best absorption, we use the frequency at which the critical current is most significantly suppressed. We determine this criterion by the following procedure: First, we measure the [IV](#) curve without any microwaves to estimate the critical current  $I_c$  in the absence of radio-frequency radiation. Then, we choose a somewhat arbitrary power level at the generator. It must be high enough to detect its impact on the critical current but not too high to completely destroy the superconductivity in the sample. We set the selected power and apply a current to the sample equals to the critical current. Following this, we vary the frequency while measuring the voltage. The frequencies at which the voltage is highest correspond to those frequencies where the critical current is most suppressed - the [IV](#) characteristic is monotonic in most cases - indicating optimal absorption by the sample. Thus, we identify a set of well-absorbed frequencies for further investigation, starting with the highest frequency to enhance the signal-to-noise ratio as the Shapiro steps appear at higher voltages.

In this type of measurement, we should note that the absolute value of the power effectively supplied to the sample can not be precisely determined. Indeed, in our setup, we only control the power supplied to the antenna. Due to the impedance mismatches between the antenna and vacuum, as well as between the vacuum and instrumentation, a portion

of this power is reflected, while the rest is absorbed and dissipated by various components, including the sample, the sample holder, wires, contacts, and the cryostat itself. Moreover, the temperature and frequency dependence introduces additional complexities, making it challenging to achieve quantitative calibration. Thus, the power values obtained in this experiment are relative.

On the contrary, the frequency is a well-defined parameter entirely set by us through the oscillator. Despite potential distortions, the very quantum nature of the Shapiro steps allows us to produce a well-measured relationship between voltage and frequency.

Returning to power, we note that the very nature of the effect gives us a number of reference points for power through the values of the critical current. The first reference point is the critical current when the radio-frequency generator is switched off: this is the zero point. The second reference point is the power level at which the critical current is maximally suppressed, often falling to zero. We mean the first minimum of the critical current because then it can oscillate with increasing power. These two reference points allow us to build a power scale for comparison with measurements under varying conditions such as temperature or frequency.

### 3.3.2 Shapiro-like steps

Once a frequency is fixed, we measure IV curves under applied RF illumination at different temperatures.

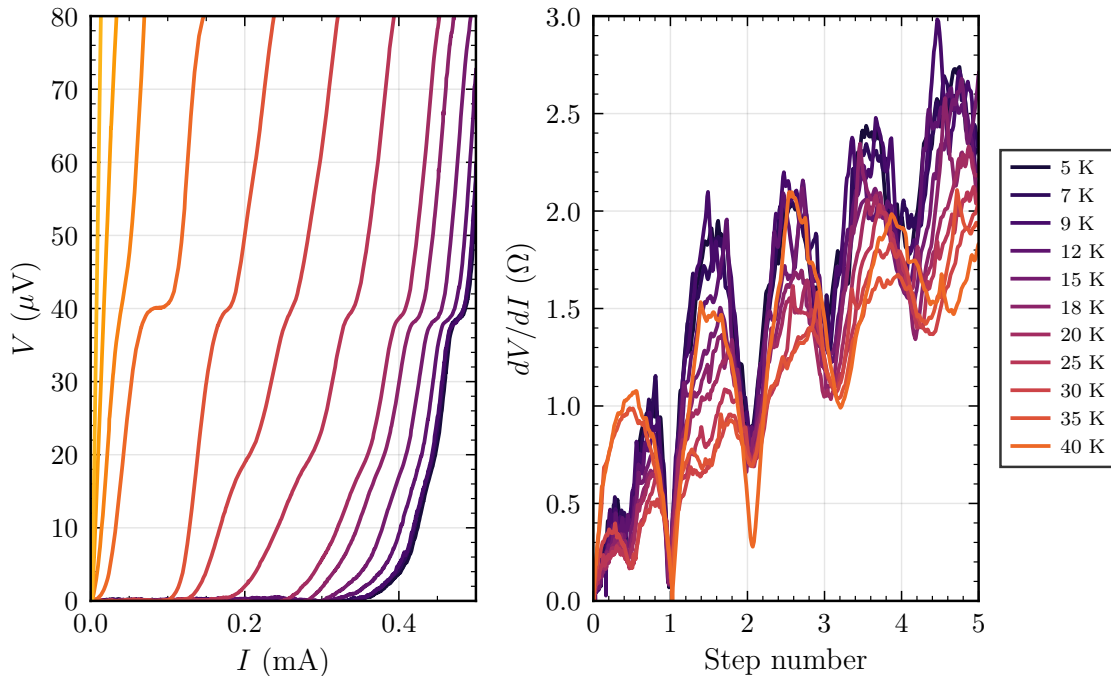


Figure 4.12 – a) IV curves under RF illumination at different temperatures. b) Dynamical resistance  $dV/dI$  versus the number of the Shapiro step for different temperatures for the nanowire B-6 of the sample CS16.

In Fig.4.12a, a set of IV curves for the nanowire B-6 of the sample CS16 is shown, measured under fixed-frequency microwave illumination at  $f = 18.9402$  GHz and fixed source power of  $P_{RF} = 10$  dBm. Each curve in the set corresponds to a sample temperature. Several constant voltage plateaus or steps can be seen at different voltage values. This voltage value is correlated to the applied frequency via the second Josephson relation:

$$hf = n \cdot 2eV \quad (4.22)$$

where  $V$  is the voltage value at which constant voltage step appears at frequency  $f$ , and  $n$  is the number of steps. In our case, the first step appears at voltage  $V_1 \approx 40 \mu V$ .

The effect becomes more pronounced in the derivative  $dV/dI$ . We normalise the voltage in terms of the number of the Shapiro steps using the Josephson relation, as presented in Fig.4.12b. We can detect up to the first five Shapiro steps over a wide temperature range from 5 K to 50 K. Additionally, at moderate temperatures, we can distinguish a fractional step of one-half and fractional steps of one-third and two-thirds at sufficiently low temperatures.

**Nanobriges as weak links in the framework of Aslamazov Larkin and Likharev models.** It should be noted that, although there are no explicit Josephson junctions, these phenomena are well described by the second Josephson relation. Aslamazov and Larkin [Aslamazov, 1975a] initially demonstrated this, and Likharev [Likharev, 1975] later generalized their findings, showing that signatures typically attributed to Josephson junctions can be observed in various superconducting weak links.

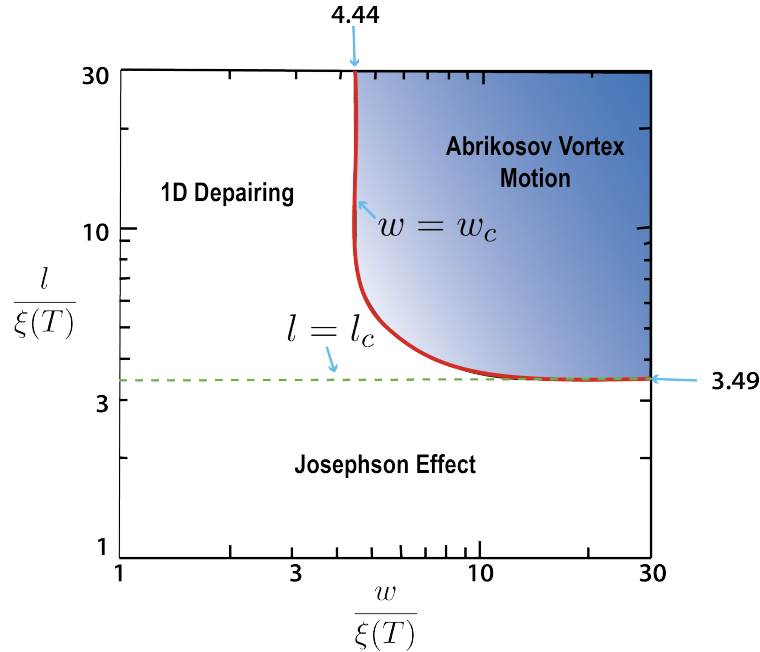


Figure 4.13 – Phase diagram of different effects in superconducting nanobridges depicting different cases depending on lateral sizes (length  $l$  and width  $w$ ) of a weak link. Adapted from [Likharev, 1979].

Fig.4.13 illustrates a phase diagram describing different cases responsible for the appearance of the Shapiro steps as a function of lateral sizes of a weak link. Although all effects exhibit the Shapiro steps, there are significant microscopic differences.

The first case, referred to as the [Aslamazov-Larkin \(AL\)](#) case, is at the lowest part of the phase diagram 4.13. In this case, the length  $l$  of the weak link is less than the critical length  $l_c$ , and the Abrikosov vortex cannot exist. It has been shown [Aslamazov, 1969] that, in this case, at temperatures close to the critical one  $T \sim T_c$  the pure Josephson effect is pronounced with a sinusoidal [Current Phase Relationship \(CPR\)](#). With sufficient width, the nanobridge behaves like a long Josephson junction, with Josephson vortices entering the nanobridge.

The upper part of the phase diagram ( $l > l_c$ ) is divided into two parts depending on the width  $w$  of the nanobridge.

If the width is less than the critical width ( $w < w_c$ ), there is not enough room for the Abrikosov vortex in the width, and a one-dimensional phase slip occurs when the current reaches the critical current. This case has been extensively studied in low-temperature superconducting nanowires both experimentally [Lau, 2001; Bezryadin, 2008; Arutyunov, 2008; Lehtinen, 2012; Arutyunov, 2012] and theoretically [Golubev, 2001; Tinkham, 2002; Matveev, 2002; Oreg, 1999; Golubev, 2008; Mooij, 2006]. Once the width of the weak link exceeds the critical width ( $w > w_c$ ), the Abrikosov vortex can enter the nanobridge at a certain critical current. This vortex then moves under the effect of the Lorentz force due to the transport current, resulting in vortex motion ( $\phi(t) \neq const$ ) and, consequently, a

finite voltage  $\langle V \rangle \neq 0$ , causing the nanobridge to enter the resistive state.

In our case, where the length  $l$  and width  $w$  are much larger than the coherence length  $\xi(T)$ , the Shapiro steps can be explained in terms of Abrikosov vortex motion synchronized by an externally applied microwave signal. The motion of the Abrikosov vortex is the motion of magnetic flux quanta, leading to a voltage drop  $V = \frac{d\Phi}{dt}$  according to Maxwell's equations, where  $\Phi$  is a magnetic flux through a superconducting surface. This voltage drop is equivalent to the rate of change of the magnetic flux, which corresponds directly to the speed of the vortex. Experimental observations of voltage steps in IV curve due to vortex motion were reported by Fiory [Fiory, 1971] and Gubankov *et al.* [Gubankov, 1976] in conventional superconductors. Similar observations were made by Early *et al.* [Early, 1994] and Nawaz *et al.* [Nawaz, 2013b] in  $\text{YBa}_2\text{Cu}_3\text{O}_{7-\delta}$ .

Our case ( $l, w \gg \xi$ ) corresponds to the Abrikosov vortex motion on this diagram. However, this diagram changes scale with temperature because of the temperature dependence of the coherence length. In the limit of  $T \rightarrow T_c$ , all weak links exhibit a pure Josephson effect behaviour. For the case  $l, w \gg \xi$  in one dimension, Larkin and Aslamazov [Aslamazov, 1975a] showed, based on the Ginzburg-Landau theory, how vortex motion under the application of an alternating electromagnetic field leads to the Shapiro steps on IV curves. Later, Likharev generalised this theory and calculated an approximation of CPR for a superconducting bridge (Fig. 4.14).

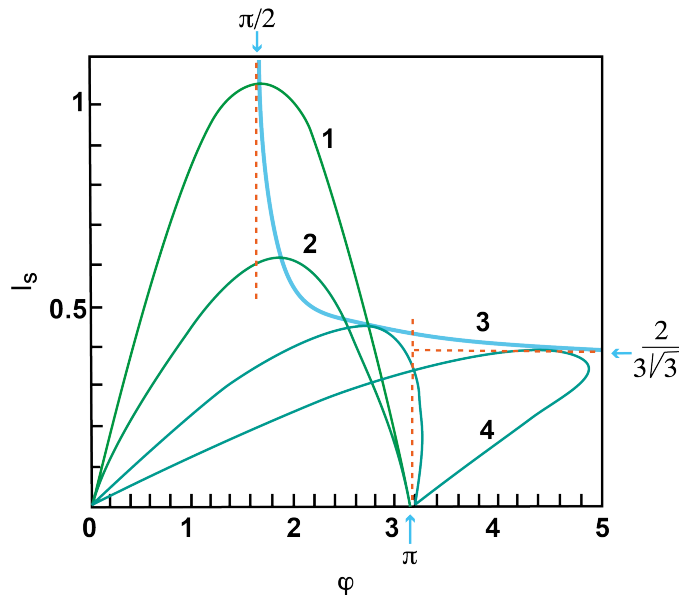


Figure 4.14 – CPR for various lengths of the superconducting bridge. Adapted from [Likharev, 1975].

From a sinusoidal Josephson CPR, with increasing bridge length  $l$ , the CPR becomes

asymmetric, and at a certain point, it becomes multi-valued:

$$I_S = I_C \frac{3\sqrt{3}}{2} \left( \frac{\varphi}{l/\xi(T)} - \left( \frac{\varphi}{l/\xi(T)} \right)^3 \right), \quad (4.23)$$

where  $I_C$  is the critical current in the case  $l = \xi(T)$ . This approach has been applied to the **One-Dimensional (1D)** nanowire and is described in [Dinsmore, 2008]. We implement this **CPR** within the framework of the **Resistive Shunted Junction (RSJ)** model to describe our nanowires:

$$\frac{d\phi}{dt} + I_S = I_{DC} + I_{RF} \sin \omega t + I_{\text{Noise}} \quad (4.24)$$

where  $I_{DC}, I_{RF}$  are the values of the corresponding **Direct Current (DC)** and **RF** current,  $\omega$  is the frequency of the **RF** current, and  $I_{\text{Noise}}$  is the noise current due to thermal fluctuations.

Solving this equation numerically gives the phase versus time  $\phi(t)$  dependency; then, using the second Josephson relation, we calculate the instantaneous voltage  $V(t)$ . Averaging it over time, we obtain the average voltage  $\langle V \rangle$ , which corresponds to the **DC** voltage measured during an experiment. By repeating this procedure, we calculate the **IV** curve for fixed values of  $I_{RF}$  and  $\omega$ . In Fig.4.15, we take a derivative of the simulated **IV** curve to compare it with the experimental curve. Fractional steps similar to the experimental ones are pronounced.

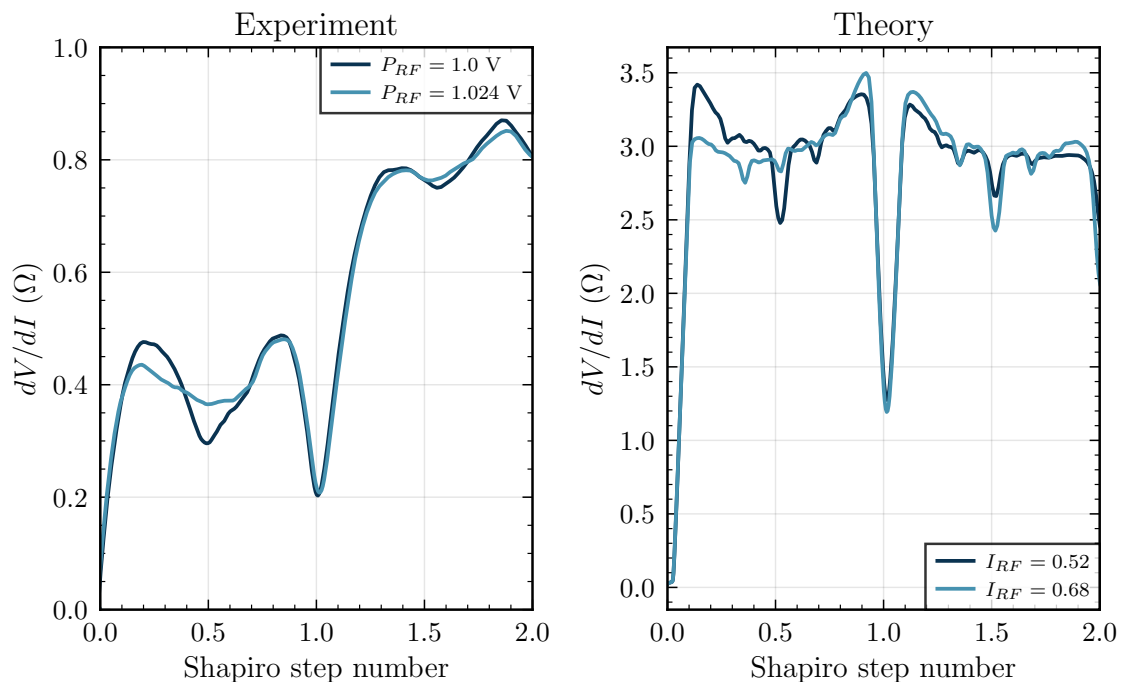


Figure 4.15 – Dynamical resistance  $dV/dI$  versus the number of Shapiro step a) Experimental measurements of the sample C-8 from CS15 measured at  $T = 6$  K at  $f = 18.32$  GHz. b) Simulations from **RSJ** model with Likharev’s **CPR** (Eq.4.23).

Although this approach qualitatively reproduces experimental **IV** curves, it is more of

a mathematical approach than a physical one. Any additional harmonics in CPR will lead to the fractional Shapiro steps on an IV curve. In general, we can consider the CPR in the following Fourier series:

$$I_s = i_1 \sin(\phi) + i_2 \sin(2\phi) + i_3 \sin(3\phi) + \dots \quad (4.25)$$

where  $i_1, i_2, \dots$  are the corresponding coefficients to be defined.

However, this does little to clarify the physical picture of this phenomenon. Even if we admit that vortex synchronisation is at the origin of Shapiro steps in nanowires, all the models described are 1D approximations of the vortex motion. For the measured geometry, the vortex motion is 2D up to very high temperatures ( $T \approx T_c$ ), and an efficient 2D model should be considered.

### 3.3.3 Shapiro steps width

Another useful information that can be easily extracted from the experiment is the width of the Shapiro steps.

We measured IV curves by sweeping RF power from zero to the maximum possible power at the RF source. The resulting data can be plotted as 2D heatmaps, as shown in Fig.4.16. Starting from zero power and monotonically increasing power, we can observe that the critical current decreases and the Shapiro steps appear. At some point, the critical current is fully suppressed. Further increasing the power leads to an increase in the critical current up to a lower maximum, and then it decreases again.

The width of the Shapiro steps follows the same oscillatory behaviour but starts from zero width at zero power. Apart from integer steps at low power, we can also observe the power evolution of fractional steps. At some value of RF power, they transit into integer steps and do not reappear with increasing power.

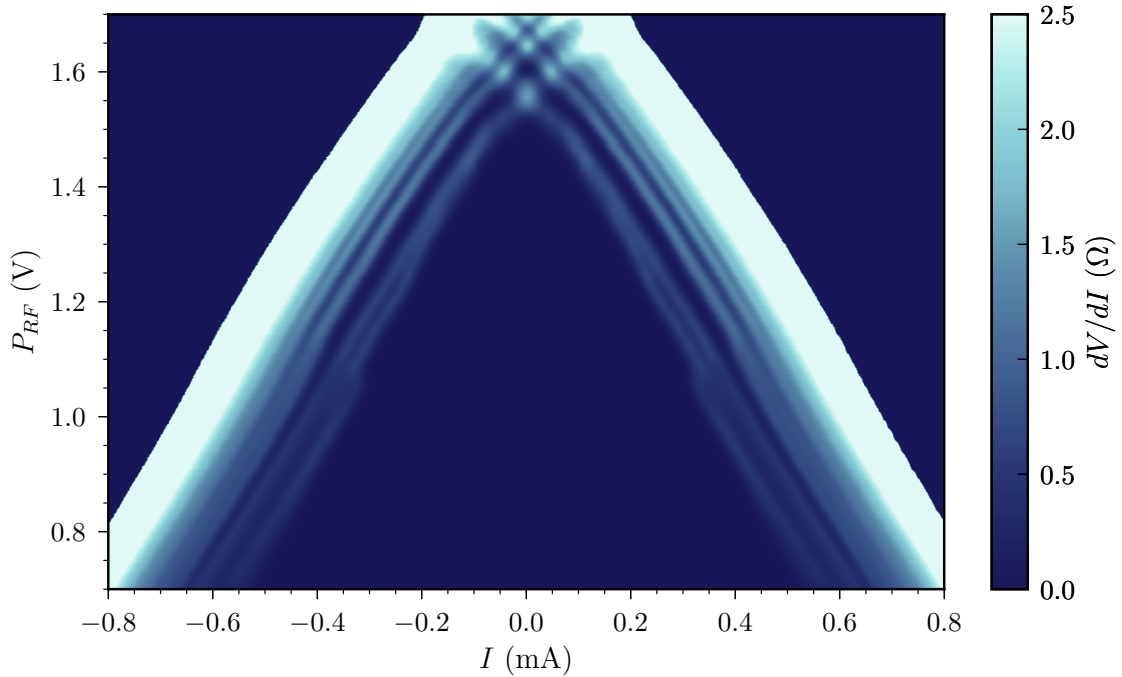


Figure 4.16 – Color-maps of the dynamic resistance under an RF illumination at  $f = 18.32$  GHz as a function of bias current and the RF power for the of the nanowire C-8 from the sample CS15 at  $T = 6$  K.

This behaviour in general is typical for the Shapiro steps in the Josephson junctions but has several peculiar features.

The first feature is the almost linear decrease of the critical current with increasing RF power. This is more easily seen in Fig.4.17a, which shows the dependence of the width of each Shapiro step (the critical current is numbered as the Shapiro step number 0) on the irradiated power. In some sense, this almost linear dependence is similar to the temperature dependence of the critical current. Taking into account the pinning model as an explanation of the temperature dependence, we can describe this behaviour by replacing the thermal energy  $k_B T$  by the energy of the quantum of electromagnetic radiation  $hf$ . The greater the power, the more quanta that allow the vortices to escape from the potential pinning hole. We will resort to the replacement of thermal energy by electromagnetic energy again later to explain another effect.

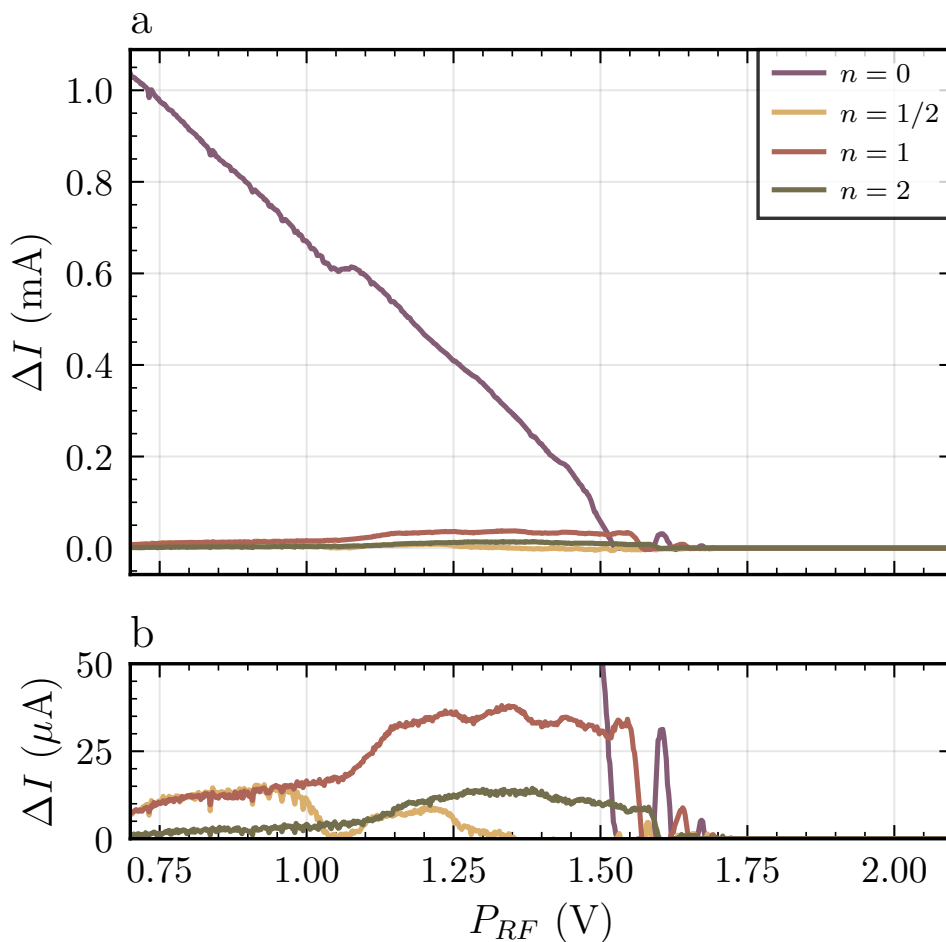


Figure 4.17 – a) RF power evolution of the critical current (step 0) and width of the Shapiro steps (step number  $> 0$ ) of the nanowire C-8 from the sample CS15 at  $T = 6$  K. b) Zoom in  $\mu$ A range showing the evolution of the Shapiro steps width with RF power

The second notable feature is the observed enhancement of the critical current  $I_c$  increases with increasing RF power in some region. This effect was observed by Gubankov *et al.* [Gubankov, 1976] in Sn nanobridges and by Rudenko *et al.* [Rudenko, 1991] in  $\text{YBa}_2\text{Cu}_3\text{O}_{7-\delta}$  microbridges. The first theoretical explanations were made by Eliashberg [Eliashberg, 1970] and then by Aslamazov *et al.* [Aslamazov, 1978]. According to their models RF illumination acts as a rescale of the quasiparticle spectrum that leads to a larger effective superconducting gap. But this explanation as well as the observed effect are restricted to a very narrow range of the RF power close to zero microwave power. Conditions of Aslamazov's model are hardly fulfilled in our sample and increasing of the critical current with RF power appears rather at sufficient powers in contrast to other experimental observations in microbridges of a conventional superconductor [Gubankov, 1976] or in  $\text{YBa}_2\text{Cu}_3\text{O}_{7-\delta}$  microbridges [Rudenko, 1991]. Perhaps a potential explanation lies also in the behaviour of Abrikosov vortices as it was also suggested [Rudenko, 1991]. Possibly there is a kind of analogue of the peak effect. But this requires further research.

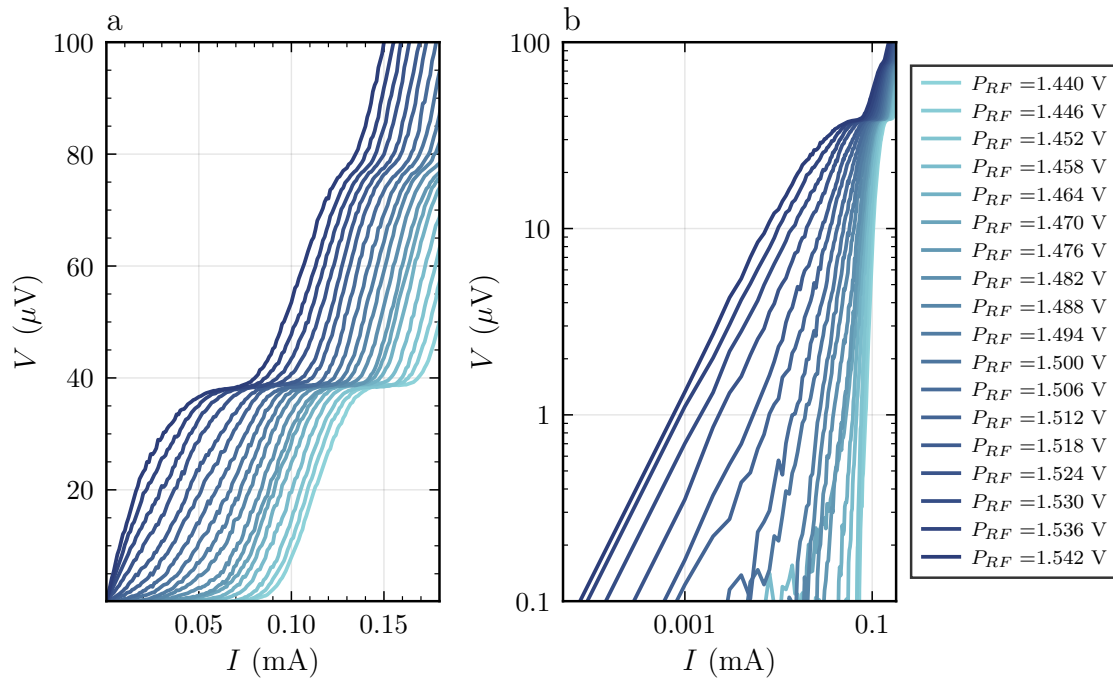


Figure 4.18 – Series of IV curves at different RF powers of the nanowire C-8 from the sample CS15 at  $T = 6 \text{ K}$ . a) Uniform scale, b) log-log scale.

Fig.4.17 shows the evolution of the Shapiro step width with increasing electromagnetic radiation power. It can be seen that the steps experience the same oscillatory behaviour as the Shapiro steps in the Josephson tunnel contact, but the shape is very different. The fractional Shapiro steps also oscillate. It can be seen that the above-described effect of the increasing the critical current occurs at the same power at which the first step minimum  $1/2$  is observed.

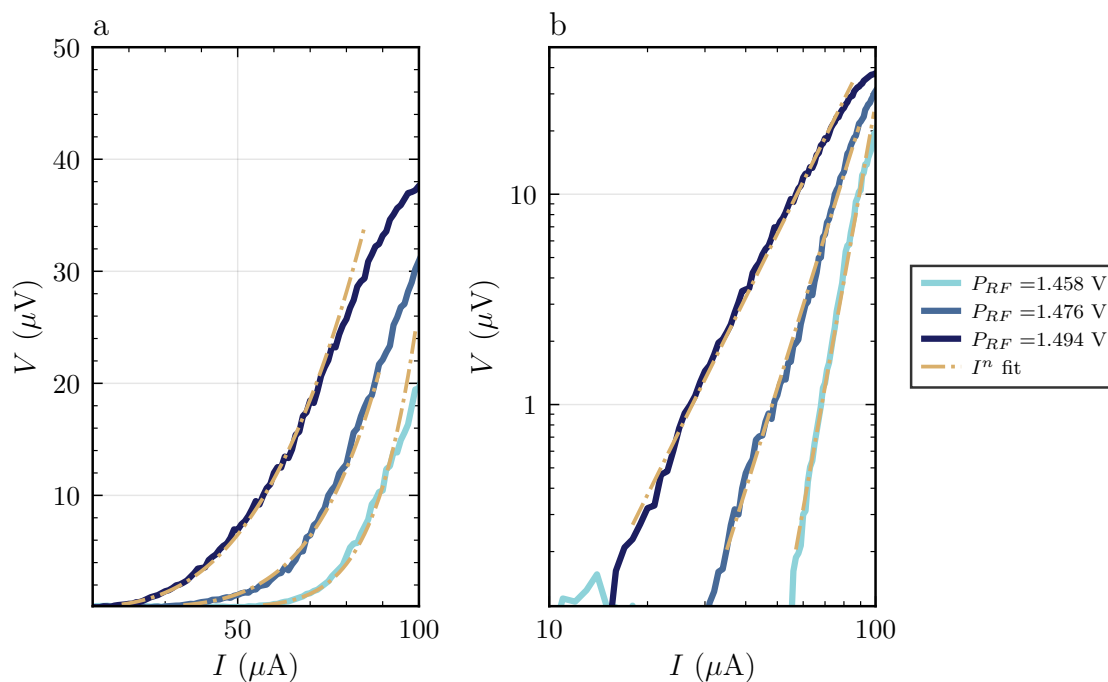


Figure 4.19 – Series of IV curves at different RF powers with the corresponding power law fits. a) Linear scale, b) log-log scale.

We have considered what happens at different power with Shapiro steps, now let us consider the evolution of IV curves with changing power.

Fig.4.18 shows a series of IV curves at different powers near the first minimum of the critical current. It can be seen that not only the critical current but also the curvature of the IV curves changes with increasing power. Plotting the same graph on a logarithmic scale (see Fig.4.18b), we can see that on this scale the curves are straight lines, which means the dependency is of power law type  $V \propto I^n$ . This kind of a power law dependence appears in various models, for example, collective flux creep [Vinokur, 1995], flux creep model proposed by Zeldov *et al.*[Zeldov, 1990; Zeldov, 1994], Thermally Activated Vortex Motion (TAVM) [Tafari, 2006; Repaci, 1996], BKT systems [Halperin, 1979] and others.

Without reference to any particular model, we, following the previous considerations, will consider an array of vortices moving in the pinning potential under the action of the Lorentz force from the sum of DC bias current and RF current, considering the antenna as a current source.

In general, the power law IV curve can be defined as

$$V = \left( \frac{I}{I_d} \right)^n, \quad (4.26)$$

where  $I_d$  is some characteristic current,  $n$  is some critical exponent. By applying our fit procedure described in Section 3.2, we can obtain the dependencies of these parameters on the power of the signal fed to the antenna.

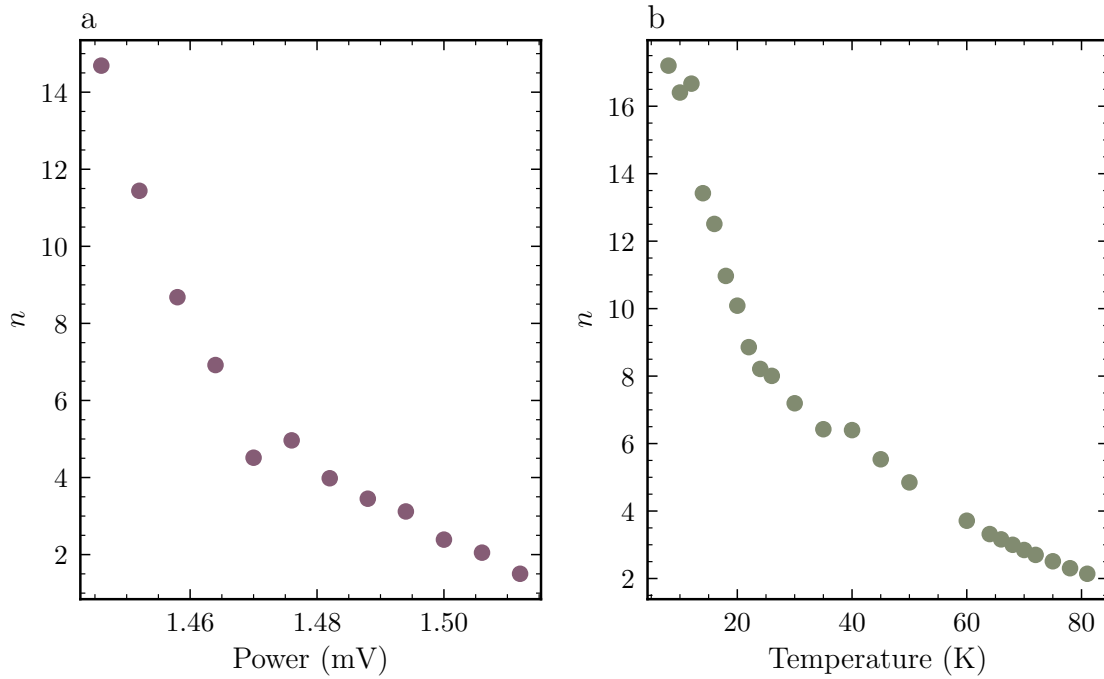


Figure 4.20 – Extracted the power  $n$  from the power law fitting of the series of **IV** curves for a) different **RF** powers, b) different temperatures  $T$ .

Fig.4.19 shows the fit using the formula for several power values. It can be seen that such a simple formula gives a satisfactory match with the experimental curves. The dependencies for the parameters obtained from the fit are shown in Fig.4.20a. The behaviour of power  $n$  qualitatively and quantitatively resembles the similar dependence in the work where the **TAVM** model was applied. In this model, the thermal activation of the vortex is considered and the corresponding degree is given by formula [Tafari, 2006].

$$n(T) = 1 + \frac{\Phi_0^2}{8\pi^2\lambda_P(T)k_B T} \quad (4.27)$$

where  $\Phi_0$  is the magnetic flux quantum,  $T$  is the temperature,  $\lambda_P(T)$  is the Pearl length. However, the corresponding estimate of the Pearl length in this case gives the value  $\lambda_P(0) \approx 200 \mu\text{m}$  that is much larger than the expected value for a thin film 30 nm thick  $\text{YBa}_2\text{Cu}_3\text{O}_{7-\delta}$  thin film of  $\lambda_P = \frac{2\lambda_L^2}{d} \approx 3 \mu\text{m}$ .

It should also be noted that the original model considers thermal activation and temperature dependence, while we study the microwave power dependence. The good numerical agreement of these different results may indicate the heating of the sample by microwave absorption. A complete analogy with the operation of a microwave oven is possible. To test this analogy, we provide the same fitting procedure for **IV** curves at different temperatures without **RF** illumination. The resulting dependency of the parameter  $n$  versus the temperature  $T$  is shown in Fig.4.20b. One can see qualitative and quantitative agreement between two plots. This can be an additional argument that in this case **RF** source acts as a heat source locally heating the sample while all surrounding stays at a

base temperature.

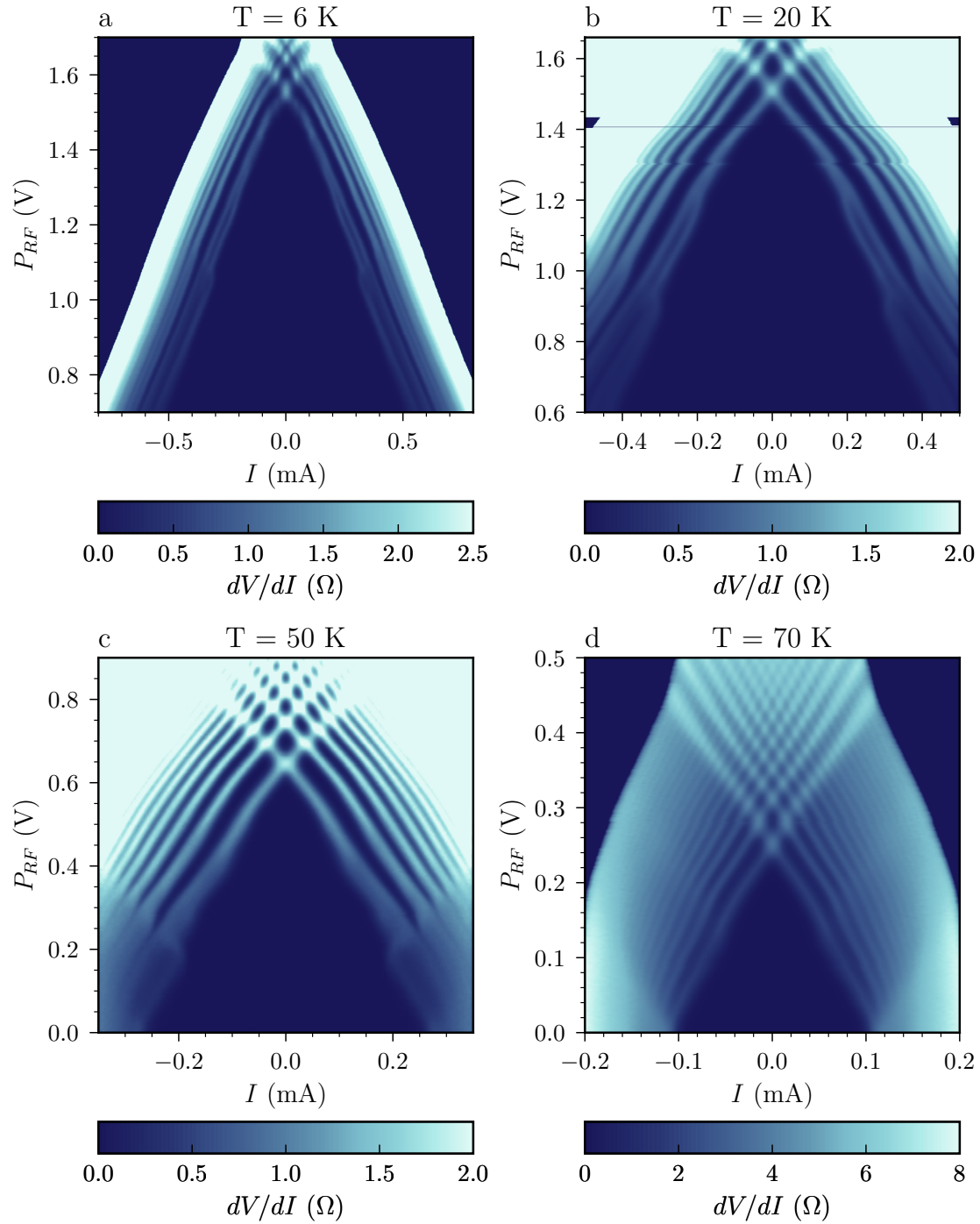


Figure 4.21 – Color-maps of the dynamic resistance under an RF illumination at  $f = 18.32$  GHz as a function of bias current and the RF power for the nanowire C=8 of the sample CS15 at a) 6 K, b) 20 K, c) 50 K, and d) 70 K.

### 3.3.4 Shapiro steps temperature dependence

High critical temperature allows us to study this coherent vortex motion induced by microwave irradiation over a wide temperature range. We measured color-maps like in Fig.4.16 at different temperatures and resulting plots are presented in Fig.4.21. The general trend is a smoothening of all effects with increasing temperature due to increasing thermal fluctuations. These fluctuations help vortices escape pinning sites and provide continuous vortex flow.

With increasing temperature, the color-map region where the critical current and Shapiro steps oscillate also increased. At high temperature, the analogy with the Josephson effect is now even more complete. Fractional Shapiro-like steps preserve up to 50 K that somehow define a pinning force of defects inside the sample. And up to temperature 50 K the region where fractional steps should be widens, and these regions are now also manifested at higher-order steps.

As we will show in Chapter 6, the motion of even one vortex can lead to fractional Shapiro steps, so the appearance of their hints with increasing temperature can speak about the increase of the general mobility of vortices and about the nature of this mobility.

## 4 Conclusion

This chapter presents the results of our transport measurements. Analysing our results using existing models, we tried to find a consistent and self-consistent explanation for the maximum number of effects and observations. Such an explanation seems to be the explanation through the motion of Abrikosov vortices. It is widely known that Abrikosov vortices play an enormous role in the transport properties of the superconductor of the second kind, which is  $\text{YBa}_2\text{Cu}_3\text{O}_{7-\delta}$ . For example, the broadening of RT curves can be explained by the peculiarities of the surface barrier of vortex entry. This barrier may significantly depend on morphological defects and inhomogeneities of the film. Penetrating inside, the vortex moves under the action of the Lorentz force and thermal fluctuations in the pinning landscape, getting stuck in deep minima. Such a picture of the vortex creep allows us to fit well the temperature dependence of the critical current and the initial part of the  $IV$  curves. The behaviour of the switching current and the return current is much more complicated because thermal processes in the sample and substrate are actively involved.

The effects associated with irradiation can also be explained as a synchronised vortex motion. Such synchronisation was previously predicted and observed as Shapiro steps in various samples. Here, in addition to integer steps we also observed fractional Shapiro steps. The evolution of these steps from the RF power was measured at different temperatures, allowing us to trace the thermal evolution. The effect of increasing critical current with increasing RF power in a narrow power range was also found.

Despite self-consistency, there are some inconsistencies in the explanation through the vortex motion, such as the large value of  $\lambda$  obtained at the resistance versus temperature

curve fit. Such a problem can, for example, be removed in the model of Josephson vortices. In the work by Sonin *et al.*[Sonin, 1989], it was shown that the effective length  $\lambda$  in the grid of Josephson vortices can exceed the Pearl length  $\lambda_P$ . The Josephson mesh is another possible explanation of the transport properties in such samples. It is known that twin boundaries are a frequent phenomenon in the growth of  $\text{YBa}_2\text{Cu}_3\text{O}_{7-\delta}$  films and at the same time they are natural Josephson contacts. It is very difficult to separate one type of vortices from another in our case, because the consequences of their motion measured in the experiment are very similar. Under some conditions they can even transform into each other.

# Chapter 5

## Simulation of vortex dynamics

### Objectives

The aim of this chapter is to provide a comprehensive description of the numerical simulation of vortex dynamics using the Time-Dependant Ginzburg-Landau (TDGL) framework. The discretization scheme, as well as the solving algorithm, is described.

### Contents

---

|   |                                   |           |
|---|-----------------------------------|-----------|
| 1 | System of equations . . . . .     | <b>81</b> |
| 2 | Discretization scheme . . . . .   | <b>83</b> |
|   | 2.1 Link-variables . . . . .      | 83        |
|   | 2.2 Computational grid . . . . .  | 84        |
|   | 2.3 Boundary conditions . . . . . | 86        |
| 3 | Conclusion . . . . .              | <b>87</b> |

---

## 1 System of equations

In chapter 1, we have introduced TDGL equations that provide an appropriate and well-known approach for modeling the dynamics of Abrikosov vortices. As these partial differential equations cannot be solved analytically in most interesting cases, we present a numerical solution procedure.

To facilitate the analysis, it is convenient to work in a dimensionless form, requiring the selection of appropriate units and scales. Following the approach by Sadovskyy *et al.*[Sadovskyy, 2015], the TDGL equations in dimensionless form can be written as follows:

$$\begin{aligned} u (\partial_\tau + i\mu) \psi &= \epsilon(\mathbf{r})\psi - |\psi|^2\psi + (\nabla - i\mathbf{A})^2\psi \\ \kappa^2 \nabla \times (\nabla \times \mathbf{A}) &= \mathbf{J}_N + \mathbf{J}_S \end{aligned} \quad (5.1)$$

where

- $u$  is a dimensionless parameter that defines diffusion of the order parameter, and it varies on a specific superconductor material (in all our simulations it is set to  $u = 1$  as we are not interested in times of creation and destruction of vortices)
- $\psi$  - is an order parameter in units of  $\psi_0 = \sqrt{|a|/b}$
- $\mu$  is the scalar potential in units of  $\mu_0 = \frac{\hbar}{2e\tau_{GL}}$ , where  $\tau_{GL} = 4\pi\sigma\lambda_L^2/c^2$  is a unit of time and  $\sigma$  is a normal conductivity.
- $\mathbf{A}$  is the vector potential and is measured in units of  $H_{c_2}\xi$ , where  $H_{c_2} = \frac{\hbar c}{2e\xi^2}$  is the second critical field,  $\kappa = \lambda_L/\xi$  is a Ginzburg-Landau parameter.
- lengths are in units of the coherent length  $\xi$ .

The normal and superconductor current density in these dimensionless units is written as:

$$\begin{aligned} \mathbf{J} &= \mathbf{J}_S + \mathbf{J}_N \\ &= \text{Im} [\psi^*(\nabla - i\mathbf{A})\psi] - (\nabla\mu + \partial_\tau\mathbf{A}) \end{aligned} \quad (5.2)$$

where the current density is in a unit of  $J_0 = \frac{e\hbar\psi_0^2}{m\xi}$ .

The disorder and pinning sites are introduced via the dimensionless function

$$\epsilon(\mathbf{r}) = \frac{T_c(\mathbf{r}) - T}{T}. \quad (5.3)$$

That allows us to vary the critical temperature over the sample volume, modeling  $\delta T$ -pinning [Kwok, 2016]. In superconducting regions,  $\epsilon(\mathbf{r}) = 1$ , while in regions where local critical temperature  $T_c(\mathbf{r})$  is suppressed,  $\epsilon(\mathbf{r}) < 1$ .

Metallic inclusions can be simulated by values  $\epsilon(\mathbf{r}) < 1$ .

The important property of this system of equations is invariance to the following gauge

transformation:

$$\begin{aligned}\psi &\mapsto \psi e^{i\chi} \\ \mathbf{A} &\mapsto \mathbf{A} + \nabla\chi \\ \mu &\mapsto \mu - \frac{\partial\chi}{\partial t}\end{aligned}\tag{5.4}$$

where  $\chi(t, \mathbf{r})$  is a scalar twice continuously differentiable function. The arbitrariness in the choice of the function  $\chi(t, \mathbf{r})$  can be used to efficiently simplify the system. In our work, we use the so-called *zero scalar potential* gauge setting  $\mu = 0$ . Thus, we eliminate the scalar potential from both equations of our system.

Finally, in this gauge our system is written as

$$\begin{aligned}\partial_\tau\psi &= \epsilon(\mathbf{r})\psi - |\psi|^2\psi + (\nabla - i\mathbf{A})^2\psi \\ \partial_\tau\mathbf{A} &= \text{Im}[\psi^*(\nabla - i\mathbf{A})\psi] - \varkappa^2\nabla \times (\nabla \times \mathbf{A})\end{aligned}\tag{5.5}$$

Here, the value  $u = 1$  is already taken into account.

**Boundary and initial conditions** To get a unique solution for the defined partial differential equation, we must satisfy it with appropriate boundary and initial conditions. Here, we use two types of boundary conditions: the superconductor-vacuum condition and the superconductor-metal condition.

For the first one we set:

$$\mathbf{n} \cdot (\nabla - i\mathbf{A})\psi = 0\tag{5.6}$$

where  $\mathbf{n}$  is a normal vector to the superconductor-vacuum boundary. This condition means that superconducting current cannot flow to the vacuum.

The superconductor-metal boundary situation is a bit more complicated because Cooper pairs, and so the order parameter can diffuse inside normal metal as well as normal electrons into a superconductor. The last process happens on some length where normal electrons transform into Cooper pairs. De Gennes [De Gennes, 2018] suggested superconductor-metal boundary conditions in a form

$$\mathbf{n} \cdot (\nabla - i\mathbf{A})\psi = i\gamma_0\psi\tag{5.7}$$

where  $\gamma_0$  is a real constant that measures the characteristic length of this proximity effect.

In our work, we use a simplified approach by setting  $\gamma_0 = 0$  and applying the following condition for metal-superconductor interface:

$$\mathbf{n} \cdot (\nabla - i\mathbf{A})\psi = 0\tag{5.8}$$

This choice has negligible impact on our results, since the region of interest is located far from the superconductor-metal boundaries where the order parameter is suppressed.

For vector potential, boundary conditions are based on the requirement that, at the superconductor's boundary, the magnetic field equals the external magnetic field:

$$\nabla \times \mathbf{A} = \mathbf{H}_{ext} \quad (5.9)$$

where  $\mathbf{H}_{ext}$  is the externally applied magnetic field.

Initial conditions are defined based on two widespread experimental techniques: zero-field cooling (ZFC) and field-cooling (FC). For the ZFC case, the initial value of the order parameter is set  $\psi \approx 1$  everywhere inside superconducting regions, while for the FC case, the order parameter is initially set randomly.

## 2 Discretization scheme

### 2.1 Link-variables

An important property of the TDGL equations is their invariance under the gauge transformation. It is crucial to preserve this invariance in the numerical scheme.

This can be done by the so-called link-variables approach, which was developed for gauge fields in lattice theories. Hereinafter, we describe only the 2D case, because it is used in our work, but this scheme can be easily upscaled into 3D.

We introduce link-variables  $U^x, U^y$  as

$$\begin{aligned} U^x(x, y) &= \exp\left(-i \int_{x_0}^x A^x(x', y) dx'\right) \\ U^y(x, y) &= \exp\left(-i \int_{y_0}^y A^y(x, y') dy'\right) \end{aligned} \quad (5.10)$$

where  $x_0, y_0$  are coordinates of the arbitrary point on the computational grid,  $A^x, A^y$  are corresponding components of the vector potential.

These link-variables are complex-valued and unimodular,  $U^{\mu*} = [U^\mu]^{-1}$ , and can be defined by the vector potential components  $A^x$  and  $A^y$ :

$$\begin{aligned} A^x &= -\frac{i}{2} \left( U^{x*} \frac{\partial U^x}{\partial x} - U^x \frac{\partial U^{x*}}{\partial x} \right) \\ A^y &= -\frac{i}{2} \left( U^{y*} \frac{\partial U^y}{\partial y} - U^y \frac{\partial U^{y*}}{\partial y} \right) \end{aligned} \quad (5.11)$$

With this definition of link-variables, we can rewrite TDGL equations in a covariant way that preserves the gauge invariance.

The second-order differential operator in the first TDGL equation (Eq.5.5) can be written with link-variables as follows:

$$(\nabla - i\mathbf{A})^2 \psi = U^{x*} \frac{\partial^2 (U^x \psi)}{\partial x^2} + U^{y*} \frac{\partial^2 (U^y \psi)}{\partial y^2} \quad (5.12)$$

The first-order differential operator in the second TDGL equation with link-variables can be rewritten as follows:

$$\begin{aligned} \left(\frac{\partial}{\partial x} - iA^x\right)\psi &= U^{x*} \frac{\partial(U^x\Psi)}{\partial x} \\ \left(\frac{\partial}{\partial y} - iA^y\right)\psi &= U^{y*} \frac{\partial(U^y\Psi)}{\partial y} \end{aligned} \quad (5.13)$$

## 2.2 Computational grid

We solve TDGL equations using the finite-difference method on a 2D rectangular grid.

We consider a uniform grid with spacing  $dx = dy$ , and the total number of grid points is  $(N_x + 1) \times (N_y + 1)$ , where  $N_{x,y}$  is a number of grid points in  $x$  or  $y$  direction correspondingly. The discrete version of the order parameter can be written in a following form  $\psi_{i,j}$ , where  $i = 1, \dots, N_x + 1$  and  $j = 1, \dots, N_y + 1$  are grid points.

In discrete form, the link-variables are defined on cell edges (halfway between grid points, see Fig. 5.1). Due to this displacement in the grid, the link-variables are discretized as

$$\begin{aligned} U_{i,j}^x &\text{ where } i = 1, \dots, N_x \text{ and } j = 1, \dots, N_y + 1, \\ U_{i,j}^y &\text{ where } i = 1, \dots, N_x + 1 \text{ and } j = 1, \dots, N_y \end{aligned} \quad (5.14)$$

To reduce operating memory consumption Winecki and Adams [Winecki, 2002] suggested using real valued variables  $\phi_{i,j}^x, \phi_{i,j}^y$  introduced as  $U_{i,j}^x = \exp(-i\phi_{i,j}^x)$  and  $U_{i,j}^y = \exp(-i\phi_{i,j}^y)$  correspondingly. This is possible because the original link-variables are unimodular  $|U_{i,j}^x| = |U_{i,j}^y| = 1$ .

The second order derivative with respect to  $x$  and  $y$  can be approximated using central difference as follows:

$$(\nabla - i\mathbf{A})^2\psi = U^{x*} \frac{\partial^2(U^x\psi)}{\partial x^2} + U^{y*} \frac{\partial^2(U^y\psi)}{\partial y^2} \quad (5.15)$$

For a discrete form of the TDGL equations, we use second order derivative approximation for spatial derivatives and first order derivative approximation for time derivatives. An integral in the link-variables definition is approximated by second order approximation as

$$\begin{aligned} U_{i,j}^x &= \exp(-iA_{i,j}^x dx) \\ U_{i,j}^y &= \exp(-iA_{i,j}^y dy) \end{aligned} \quad (5.16)$$

where  $A_{i,j}^x, A_{i,j}^y$  are discrete versions of vector potential which are defined on cell edges.

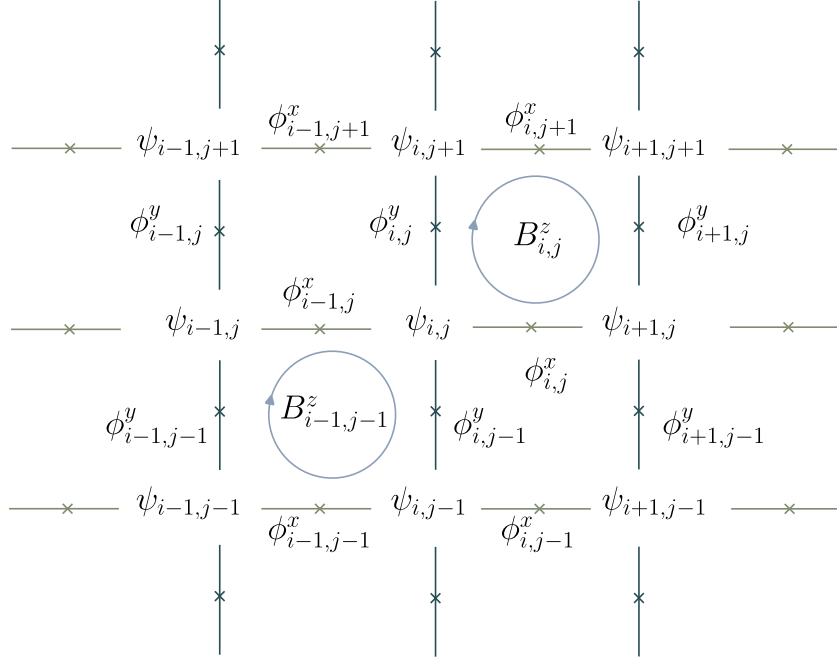


Figure 5.1 – Computational grid for the finite-difference method using link variables approach.

The first order differential operator is discretized as

$$\begin{aligned} \left( \frac{\partial}{\partial x} - iA^x \right) \psi &\rightarrow \frac{U_{i,j}^x \psi_{i+1,j} - \psi_{i,j}}{dx} = \frac{\exp(-i\phi_{i,j}^x) \psi_{i+1,j} - \psi_{i,j}}{dx} \\ \left( \frac{\partial}{\partial y} - iA^y \right) \psi &\rightarrow \frac{U_{i,j}^y \psi_{i,j+1} - \psi_{i,j}}{dy} = \frac{\exp(-i\phi_{i,j}^y) \psi_{i,j+1} - \psi_{i,j}}{dy} \end{aligned} \quad (5.17)$$

The Laplacian differential operator is discretized as

$$(\nabla - i\mathbf{A})^2 \psi \rightarrow \frac{U_{i,j}^x \psi_{i+1,j} - 2\psi_{i,j} + U_{i-1,j}^x \psi_{i-1,j}}{dx^2} + \frac{U_{i,j}^y \psi_{i,j+1} - 2\psi_{i,j} + U_{i,j-1}^y \psi_{i,j-1}}{dy^2}. \quad (5.18)$$

Using the discretization defined above, the first TDGL equation in discrete form can be written as:

$$\begin{aligned} \partial_\tau \psi_{i,j} &= \frac{\exp(i\phi_{i-1,j}^x) \psi_{i-1,j} - 2\psi_{i,j} + \exp(-i\phi_{i,j}^x) \psi_{i+1,j}}{dx^2} + \\ &+ \frac{\exp(i\phi_{i,j-1}^y) \psi_{i,j-1} - 2\psi_{i,j} + \exp(-i\phi_{i,j}^y) \psi_{i,j+1}}{dy^2} \\ &+ (1 - |\psi_{i,j}|^2) \psi_{i,j} \end{aligned} \quad (5.19)$$

Using the vector relation  $\nabla \times (\nabla \times \mathbf{A}) = \nabla^2 \mathbf{A} - \nabla(\nabla \cdot \mathbf{A})$ , we can write the second

TDGL equation in the following discrete form:

$$\begin{aligned}
\partial_\tau \phi_{i,j}^x &= \frac{\kappa^2}{h_y^2} (\phi_{i,j+1}^x - 2\phi_{i,j}^x + \phi_{i,j-1}^x) + \frac{\kappa^2}{h_y^2} (-\phi_{i+1,j}^y + \phi_{i,j}^y + \phi_{i+1,j-1}^y - \phi_{i,j-1}^y) \\
&\quad + \text{Im} \left( \exp(-i\phi_{i,j}^x) \psi_{i,j}^* \psi_{i+1,j} \right) \\
\partial_\tau \phi_{i,j}^y &= \frac{\kappa^2}{h_x^2} (\phi_{i+1,j}^y - 2\phi_{i,j}^y + \phi_{i-1,j}^y) + \frac{\kappa^2}{h_x^2} (-\phi_{i,j+1}^x + \phi_{i,j}^x + \phi_{i-1,j+1}^x - \phi_{i-1,j}^x) \\
&\quad + \text{Im} \left( \exp(-i\phi_{i,j}^y) \psi_{i,j}^* \psi_{i,j+1} \right)
\end{aligned} \tag{5.20}$$

For calculation of the time step, we use the first-order accurate one-step forward Euler method:

$$\begin{aligned}
\psi_{i,j}(\tau + d\tau) &= \psi_{i,j}(\tau) + \partial_\tau \psi_{i,j} dt \\
\phi_{i,j}^x(\tau + d\tau) &= \phi_{i,j}^x(\tau) + \partial_\tau \phi_{i,j}^x dt \\
\phi_{i,j}^y(\tau + d\tau) &= \phi_{i,j}^y(\tau) + \partial_\tau \phi_{i,j}^y dt
\end{aligned} \tag{5.21}$$

where  $dt$  is a time step. This explicit method is stable only for a sufficiently small time step  $dt$ . For the TDGL equations, the time step must satisfy a condition [Winiecki, 2002]:

$$d\tau < \frac{d^2}{2\kappa^2} \tag{5.22}$$

where  $d = \max(dx, dy)$  is the biggest grid dimension. In all our simulations, we use  $\kappa = 4$ ,  $dx = dy = 0.5$  (in terms of the coherence length  $\xi$ ) and  $d\tau = 0.001$  (in terms of the GL characteristic time  $\tau_{GL}$ ) that to ensure that this condition is satisfied.

### 2.3 Boundary conditions

For the numerical solution of TDGL, it's crucial to apply the correct discrete form of boundary conditions. In our work, we use two types of boundary conditions for the order parameter. On the boundaries  $x = 0, N_x + 1$ , we implement superconductor-vacuum condition (5.6), setting zero superconducting current through these boundaries. In discrete form, it is written as:

$$\begin{aligned}
\psi_{1,j} &= \psi_{2,j}(t) \exp(-i\phi_{1,j}^x) \\
\psi_{N_x+1,j} &= \psi_{N_x,j}(t) \exp(i\phi_{N_x,j}^x)
\end{aligned} \tag{5.23}$$

On the boundaries  $y = 0, N_y + 1$ , we set order parameter equals zero:

$$\begin{aligned}
\psi_{i,1} &= 0 \\
\psi_{i,N_y+1} &= 0
\end{aligned} \tag{5.24}$$

The boundary conditions for the vector potential  $\mathbf{A}$  are defined via the magnetic field  $\mathbf{B}$ . In 2D geometry, the magnetic field has only a component  $B^z$  perpendicular to the

calculation grid. Using link variables, the magnetic field can be expressed as:

$$B_{i,j}^z = \frac{1}{d_x d_y} \left( \phi_{i,j}^x - \phi_{i,j+1}^x - \phi_{i,j}^y + \phi_{i+1,j}^y \right) \quad (5.25)$$

Based on this equation, boundary conditions for the vector potential  $\mathbf{A}$  through  $\phi^x, \phi^y$  are written as:

$$\begin{aligned} \phi_{i,1}^x &= B_{ext} d_x d_y + \phi_{i,2}^x + \phi_{i,1}^y - \phi_{i+1,1}^y \\ \phi_{i,N_y+1}^x &= -B_{ext} d_x d_y + \phi_{i,N_y}^x - \phi_{i,N_y}^y + \phi_{i+1,N_y}^y \\ \phi_{1,j}^y &= -B_{ext} + \phi_{1,j}^x - \phi_{1,j+1}^x + \phi_{2,j}^y \\ \phi_{N_x+1,j}^y &= B_{ext} - \phi_{N_x,j}^x + \phi_{N_x,j+1}^x + \phi_{N_x,j}^y \end{aligned} \quad (5.26)$$

where  $B_{ext}$  is an external magnetic field perpendicular to the calculation grid.

With these boundary conditions for variables  $\psi_{i,j}, \phi_{i,j}^x, \phi_{i,j}^y$ , it is possible to get a unique solution for the TDGL equations. Code for solution of these equations was written in Julia language, as it represent a fast and free version of Matlab.

### 3 Conclusion

In this chapter, we presented the numerical scheme for solving the TDGL equations, which will be used in the subsequent chapter for modelling superconducting nanowires. This scheme relies on the use of the so-called link-variables to preserve the gauge invariance of the discrete scheme. The discretization is performed on a rectangular 2D staggered mesh using the finite difference method. For the time step, we implement the Euler method. The resulting solution allows us to observe the temporal and spatial dynamics of the order parameter and the magnetic field. From this data, various physical observables can be extracted, including the amplitude of the order parameter, the superconducting and normal current components, and voltage.

# Chapter 6

## Vortex patterns

### Objectives

This chapter is devoted to the theoretical study on the vortex motion in current-carrying superconducting nanowires. We show how the landscape of disorder influences the vortex dynamics and, as a result, DC- and AC- current response of the system. By implementing linear defects, we achieve a complex vortex dynamics which, in some specific cases, leads to the current response similar to the experimentally observed one as discussed in chapter 4. The vortex motion along closely located defects is correlated enabling various synchronization effects and even dynamic metastable energy levels. Some results presented in this chapter are subject of the submitted paper.

### Contents

---

|     |  |            |
|-----|--|------------|
| 1   | Model . . . . .                          | <b>89</b>  |
| 1.1 | One grain boundary . . . . .             | 91         |
| 1.2 | Two identical grain boundaries . . . . . | 96         |
| 1.3 | Two different grain boundaries . . . . . | 101        |
| 2   | Conclusion . . . . .                     | <b>108</b> |

---

In the chapter 4, we delved into the discussion that many transport properties of  $\text{YBa}_2\text{Cu}_3\text{O}_{7-\delta}$  nanowires can be explained through the motion of vortices or phase slips. This motion, however, can be very intricate due to the complex morphology of  $\text{YBa}_2\text{Cu}_3\text{O}_{7-\delta}$  films which own grain boundaries playing role of weak links. In this case, vortices are affected not only by external fields and their mutual interactions but also by the disorder.

Here, we focus on a relatively straightforward case involving a type-II superconducting nanowire with linear defects. Despite its simplicity, we show that this model is enough to reproduce some peculiarities in our experimental results such as Shapiro steps, voltage jumps, and [Negative dynamic resistance \(NDR\)](#).

## 1 Model

As a computational model, we consider a rectangular superconducting sample, representing the central part of a typical nanobridge, as shown in Fig. 6.1a. The model bridge has a length of  $L = 60\xi$  and a width of  $W = 40\xi$ , where  $\xi$  represents the Ginzburg-Landau (GL) coherence length. Real width can vary due to oxygen diffusion from the boundaries. In this 2D case, we neglect all variations of the order parameter in the third ( $z$ ) direction. We investigate the transport properties of this superconducting nanobridge within the framework of TDGL equations using a zero potential gauge. In a dimensionless form (see chapter 5), these equations can be expressed as:

$$\begin{aligned}\partial_t\psi &= \epsilon(\mathbf{r})\psi - |\psi|^2\psi + (\nabla - i\mathbf{A})^2\psi \\ \kappa^2\nabla \times (\nabla \times \mathbf{A}) &= \mathbf{J}_S + \mathbf{J}_N\end{aligned}\tag{6.1}$$

where  $\mathbf{J}_S$ , and  $\mathbf{J}_N$  are superconducting current density and normal current density, correspondingly.

Within the chosen gauge, these can be written, in a dimensionless form, as:

$$\begin{aligned}\mathbf{J}_S &= \text{Im}[\psi^*(\nabla - i\mathbf{A})\psi] \\ \mathbf{J}_N &= -\partial_t\mathbf{A}.\end{aligned}\tag{6.2}$$

This system of equations must be satisfied with appropriate boundary conditions. On boundaries  $y = 0$  and  $y = L$ , we set  $\psi = 0$  and  $\nabla \times \mathbf{A} = \mathbf{0}$ . On boundaries  $x = 0$  and  $x = W$ , we set  $\mathbf{n} \cdot (\nabla - i\mathbf{A})\psi = 0$  and  $\nabla \times \mathbf{A} = \mathbf{H}_{ext}$ .

To compare our simulation results with experiments, we simulate transport properties and retrieve IV curves. We consider the external transport current  $I_{tr}$  to flow between  $y = 0$  and  $y = L$  sides producing an eventual voltage drop  $V$ . To apply the external transport current, we use the boundary conditions for the vector potential at the boundaries  $x = 0, W$  as  $\nabla \times \mathbf{A} = \mathbf{H}_I$ , where  $H_I = 2\pi I_{tr}/c$  represents the magnetic field induced by the

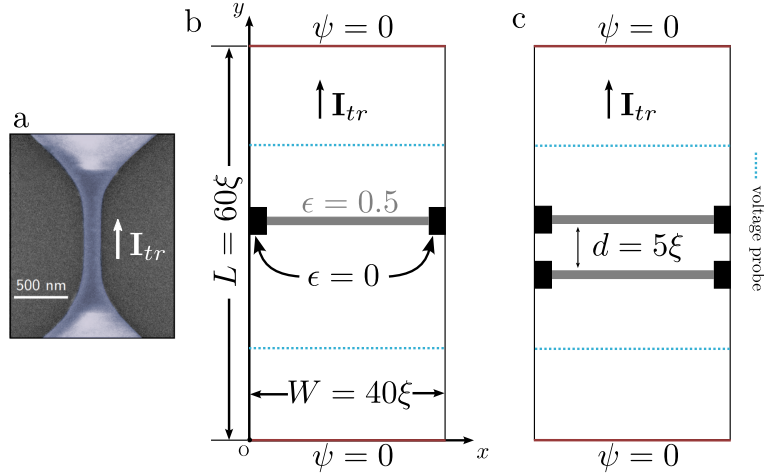


Figure 6.1 – a) Scanning Electron Microscope image of a typical nanobridge studied in experiments [Amari, ]. b) and c) Two sample geometries studied theoretically, representing the central (narrowest) part of the real device. They contain one (b) or two (c) linear defects (grey regions). Edge defects situated at the ends of linear defects are indicated by black rectangles. The direction of the transport current is shown by arrows. The voltage is calculated between the two blue dashed lines. Further details are provided in the text.

transport current.

On the other boundaries, we set  $\nabla \times \mathbf{A} = \mathbf{0}$ . Applying voltage in that direction, the corresponding voltage difference  $V$  is determined by calculating the voltage  $V$  between  $y = 0$  and  $y = L$  boundaries.

In the chosen gauge, the electric field is written as  $\mathbf{E} = -\partial_t \mathbf{A}$ . The corresponding instantaneous voltage drop  $V_{y_1, y_2}$  between two arbitrary points  $y_1, y_2$  in  $y$ -direction can be calculated as:

$$V_{y_1, y_2}(x, t) = - \int_{y_1}^{y_2} E_y(x, y, t) dy = \int_{y_1}^{y_2} \partial_t A_y(x, y, t) dy \quad (6.3)$$

By averaging this voltage over the sample width and time, we get the DC-voltage  $\langle V \rangle$  measured in experiments. To avoid the voltage drops at  $y = 0, L$  boundaries, we calculate the voltage inside the bridge where the order parameter is fully restored ( $\psi = 1$ ), as indicated by the blue dashed lines in Fig. 6.1 b and c.

When simulating the Shapiro step experiments, the microwave illumination is added as an AC-current of amplitude  $I_{AC}$  and frequency  $f_{AC}$ . The total transport current through the bridge is therefore:

$$I_{tr} = I_{DC} + I_{AC} \sin(2\pi f_{AC} t) \quad (6.4)$$

The state of the bridge is determined by calculating the voltage  $V$  between  $y = 0$  and  $y = L$  boundaries for each value of transport current. Averaging this voltage over the sample width and time one gets the DC-voltage  $\langle V \rangle$  measured in experiments.

Discretization and solution procedure are presented in the chapter 5. We use a quadratic grid with a mesh side  $dx = dy = 0.5\xi$ . Code was written in Julia, which is a fast and convenient language for scientific computations. For a stability reasons, as described by eq.5.22, we set a time step as  $d\tau = 0.001$ . As a material parameter, we set  $\kappa = 4$ . While we have used a lower value for  $\kappa$  ( $\kappa = 4$ ) in our simulations compared to typical HTS superconductors ( $\kappa \approx 100$ ), it can be assumed that, for most effects,  $\kappa$  serves as a scale of interaction within a specific geometry. Our results are applicable within a certain scale. For instance, a similar behavior involving the flux flow of vortices and antivortices was observed in a study by [Berdiyrov, 2014] for  $\kappa = 10$ . Nevertheless, our results can be extrapolated to conventional type-II superconductors, making them somewhat general in that sense.

In the model, we neglect all non-equilibrium quasiparticle processes. For all considered frequencies, the RF illumination only affects vortices as an additional periodic Lorentz force.

### 1.1 One grain boundary

As a starting point, we consider a single linear defect, as illustrated in Fig. 6.1b, simulating a grain boundary crossing the bridge. This type of defect is prevalent in  $\text{YBa}_2\text{Cu}_3\text{O}_{7-\delta}$  thin films and significantly influences vortex motion in such systems [Maggio-Aprile, 1997].

Additionally, we introduce two point defects at the ends of the linear defect, representing suppressed superconductivity in the locations where the grain boundary reaches the sample edges. This mimics a strong suppression of superconductivity on the edges in real samples due to fabrication process.

In our model, this defect is introduced by depending on the spatially varying parameter  $\epsilon(\mathbf{r})$ , which is associated with the local critical temperature  $T_c(\mathbf{r})$  and the global sample temperature  $T$ :

$$\epsilon(\mathbf{r}) = \frac{T_c(\mathbf{r}) - T}{T} \quad (6.5)$$

The superconducting part of the bridge is described by  $\epsilon = 1$ , while the defects are characterized by a locally reduced critical temperature  $T_c(\mathbf{r})$  and are described by a lower  $\epsilon(\mathbf{r})$ . For instance, the linear (grey) defect of width  $1 \times \xi$  crossing the bridge is characterized by  $\epsilon = 0.5$ . It represents an extended structural defect, such as a grain boundary crossing the real sample or an artificial weak-link. At a given temperature  $T$ , this defect is superconducting, but its local critical temperature is  $3/4$  of the critical temperature  $T_c$  in the rest of the sample. The two point defects at the edges, presented by black rectangles  $2\xi \times 5\xi$ , are characterized by  $\epsilon = 0$ , corresponding to fully suppressed superconductivity. These edge defects appear at the ends of the grain boundaries as a result of a damage caused during the nanobridge fabrication processes.

The results of the calculations are presented in Fig. 6.2.

When the transport current  $I_{tr}$  is well below a critical value  $I_c$ , the order parameter in the bridge is steady. It is depleted at the two local edge defects and at the linear defect, as shown in Fig. 6.2a, following the imposed  $\epsilon(\mathbf{r})$ .

At  $I_{tr} \lesssim I_c$ , one vortex and one anti-vortex are already pinned on the two edge defects. The entire bridge remains in the superconducting state, with  $V = 0$ , as expected. This is because only a vortex motion introduces dissipation into the system.

Figs. 6.2c-e are snapshots of the temporal evolution of the order parameter amplitude when a constant  $I_{tr} = 0.10 > I_c$  is applied. Under this condition, one vortex and one antivortex simultaneously enter the bridge, as shown in Fig. 6.2c. They accelerate towards each other under the action of the Lorentz force, experience mutual attraction, as depicted in Fig. 6.2d, and annihilate, as illustrated in Fig. 6.2e. The process is periodic, with the period and details of the vortex-antivortex dynamics depending on the applied transport current  $I_{tr}$  and the TDGL parameters. Moving vortices dissipate energy and generate an instantaneous voltage difference  $V(t)$  between the top and bottom part of the nanobridge, proportional to the relative vortex velocity. Fig. 6.2f illustrates the evolution of  $V(t)$ , with points c-e correspond to snapshots in Figs. 6.2c-e. At the moment (c), the voltage rapidly rises as vortices accelerate due to their interaction with the edges and the transport current. In (d),  $V$  crosses a local minimum as the vortex velocity drops in a region where interaction with the edge is already sufficiently small, and the transport current is reduced on the scale of  $\sim \lambda$ . A sharp increase in the vortex velocity due to the vortex-antivortex attraction just before annihilation produces a peak in  $V(t)$  at moment (e). The Fourier spectrum of  $V(t)$  is presented in Fig. 6.2g. It contains the fundamental frequency of an amplitude  $V_1$  and several harmonics with comparable amplitudes. Both  $V(t)$  and the spectrum indicate the strong anharmonicity of the vortex motion. It is important to note that the fundamental frequency is not fixed but grows with  $I_{tr}$  [Al Luhaibi, 2022] as the increasing Lorentz force pushes vortices to move and annihilate faster.

By repeating the calculations for different  $I_{DC}$  and time-averaging  $\langle V(t) \rangle$ , we retrieve  $\langle V \rangle(I_{DC})$  dependencies measured in experiments.

Plots in Fig. 6.3 are the result of these calculations for the range of  $I_{DC}$  around the transition from the non-dissipative to the dissipative state. The plots are presented in reduced coordinates  $\langle V \rangle / \mu_0$  vs  $I_{DC} / (J_0 W)$ . The shape of the curve resembles the  $V(I)$  characteristics of an ordinary Superconductor-Normal metal-Superconductor (SNS) Josephson junction. The latter, represented by the dashed line in Fig. 6.3, was calculated using the RSJ model. Both curves exhibit a non-dissipative branch at low currents, a rise at some critical current, and a smooth increase at higher currents.

However, the resemblance is limited. First, in the present case, the SNS junction does not exist, and the intrinsic critical (depairing) current of the bridge  $\sim 0.301 J_0 W$  is much higher than the calculated value  $I_c \simeq 0.072 J_0 W$ . Second, in SNS junctions,

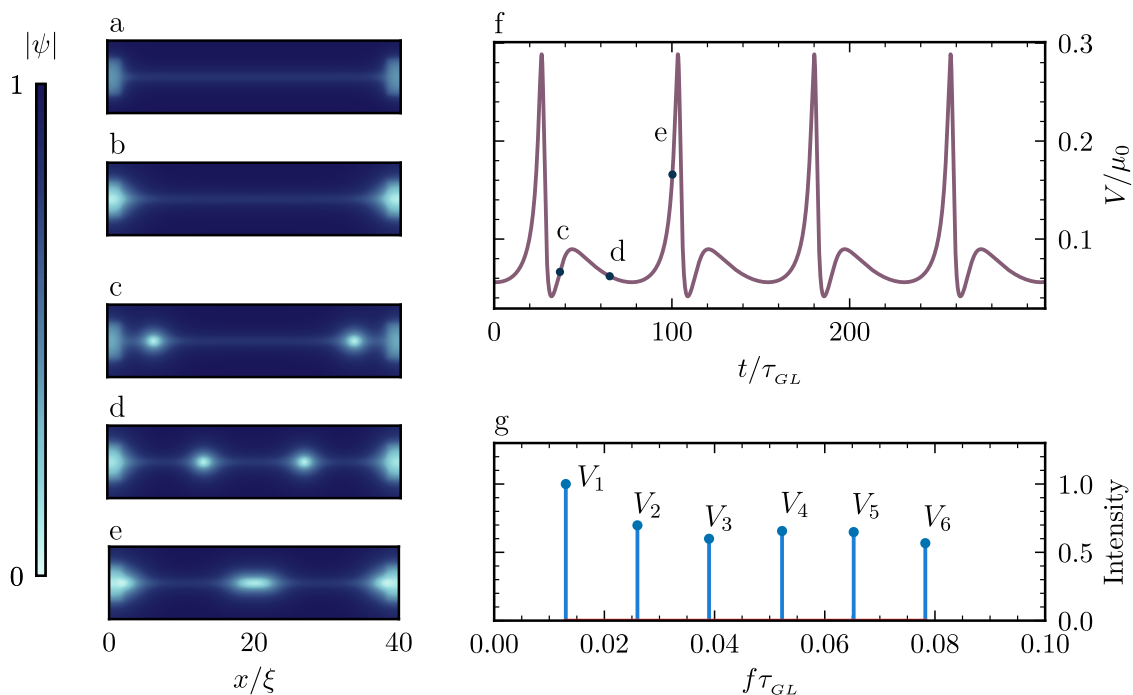


Figure 6.2 – Vortex dynamics in single linear defect with no AC current applied ( $I_{AC} = 0$ ). a) Static map of the order parameter amplitude  $|\psi(\mathbf{r})|$  at low transport currents  $I_{DC} \ll I_c$ . b) Static  $|\psi(\mathbf{r})|$  map at  $I_{DC} \lesssim I_c$  indicates the presence of one vortex and one anti-vortex at the edge defects, ready to enter. d)-e) Snapshots of  $|\psi(\mathbf{r})|$  at different moments of vortex propagation for a fixed  $I_{DC} = 0.10 > I_c$ . f) Periodic temporal evolution of the instantaneous voltage  $V(t)$  at the same conditions. The dots c, d and e on the graph correspond to snapshots c), d) and e). The period of  $V(t)$  oscillations provides the fundamental frequency  $f_1$  of the process. g) Fourier spectrum of  $V(t)$ .

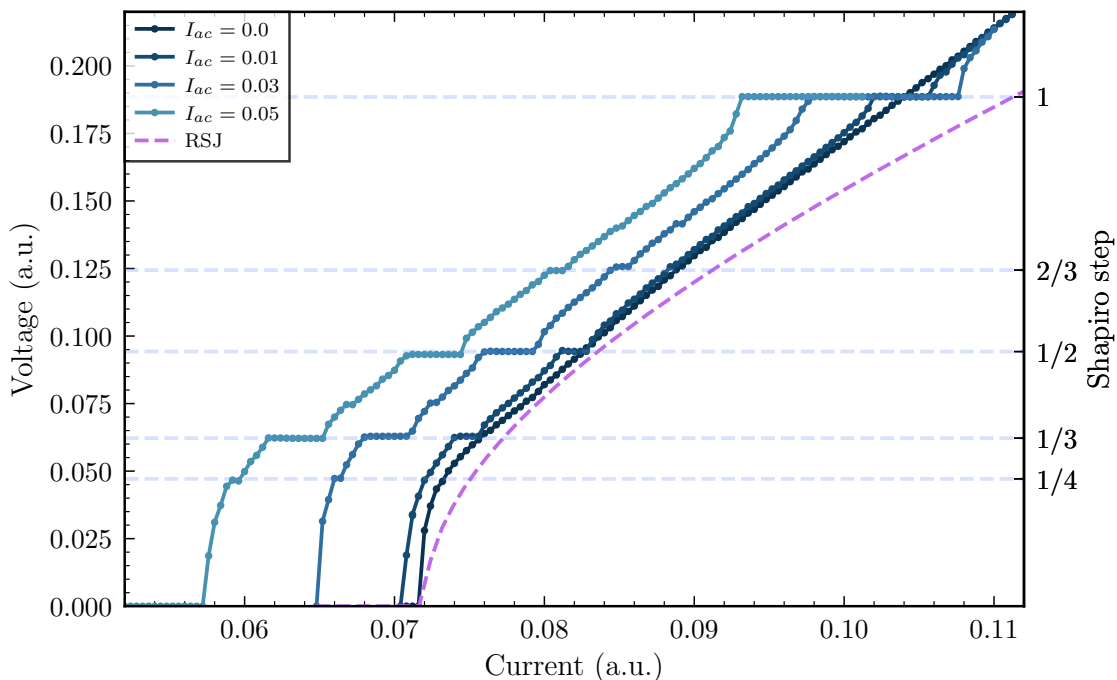


Figure 6.3 – Transport properties of the nanobridge with one linear defect. Solid lines represents normalized  $\langle V \rangle(I_{DC})$  characteristics calculated for different values of the AC component  $I_{AC}$  of the total transport current. The right vertical axis displays the numbers of Shapiro plateaus. Dashed line -  $V(I)$  characteristic of a SNS Josephson junction calculated within the RSJ model [Stewart, 1968; McCumber, 1968]. To fit the curve into the plot window, its vertical scale was divided by a factor of 10.

the  $\langle V \rangle(I_{DC})$  curve asymptotically approaches the normal branch  $\langle V \rangle = R_N I_{DC}$  as  $I_{DC}$  increases. Meanwhile, the bridge "resistance",  $\langle V \rangle / I_{DC} \times (J_0 W / \mu_0)$ , remains much lower than its normal state resistance  $R_N^*$ . Third, the RSJ model fails to reproduce an almost linear rise of  $\langle V \rangle(I_{DC})$  for  $I > I_c$ . These deviations originate from the fact that, contrary to SNS junctions where the voltage appears as a result of the suppression of the proximity-induced superconducting correlations in the normal part, in the nanobridges, it is due to individual vortex motion inside a still superconducting device. This difference is essential, leading to unique transport properties that we focus on in this work.

The SNS-like behaviour of the bridge is further evidenced by simulating its response to RF illumination. When an AC current is added, the resulting oscillating voltage  $V(t)$  can be locked to the frequency  $f_{AC}$  of this external drive, resulting in plateaus of constant voltage on  $\langle V \rangle(I_{DC})$  curve, as shown in Fig. 6.3. This effect resembles the well-known Shapiro steps observed in ordinary Josephson junctions under RF illumination, where the  $n^{th}$  voltage plateau is defined by the locking condition  $f_1 = n \cdot f_{AC}$  (where  $n$  is an integer) and the second Josephson relation  $\langle V(t) \rangle = h f_1 / 2e$ , where  $f_1$  is the fundamental (Josephson) frequency.

In addition to the integer Shapiro plateaus, the fractional ones are also revealed. These

\*. this is why the vertical scale of the RSJ curve was reduced to fit it in the plot window

plateaus appear in Fig. 6.3 at voltages satisfying the general condition

$$\frac{n}{k} \cdot hf_{AC} = 2e\langle V(t) \rangle, \quad (6.6)$$

where  $n$  and  $k$  are integers.

The presence of fractional plateaus is directly linked to a high anharmonicity of  $V(t)$  oscillations in Fig. 6.2f.

The Fourier spectrum of  $V(t)$ , presented in Fig. 6.2g, is indeed characterised by high amplitudes  $V_k$  of  $k^{th}$  voltage harmonics (at a frequency  $f_k$ ) that are comparable to the amplitude  $V_1$  at its fundamental frequency  $f_1$ . This enables efficient locking of these harmonics to the AC-drive when  $f_k = kf_1 = nf_{AC}$ .

In Fig. 6.4, the instantaneous voltage  $V(t)$  and its spectrum for the Shapiro plateau  $\frac{1}{3}$  are shown. When the frequency  $f_{AC}$  is slightly detuned from  $f_k/n$ , a low-frequency envelope of a beat frequency  $|f_{AC} - f_k/n|$  is observed. This effect allows for the detection of higher harmonics experimentally, even when their magnitude is small and imperceptible in  $\langle V \rangle(I_{DC})$  curves in the Shapiro step experiment. Consequently, by tuning the amplitude and frequency of the AC excitation, it becomes possible to induce fractional Shapiro step when  $f_{AC}$  is not only a multiple of  $f_1$  but a multiple of higher  $f_k$  harmonics. All of these features reveal a rich spectral characteristic of the system under consideration. It should be mentioned that when the amplitude  $I_{AC}$  becomes comparable to  $I_{DC}$ , the AC excitation cannot be considered anymore as a perturbation. Instead, one should think of a complex dynamical system whose spectrum (amplitudes  $V_k$  and frequencies  $f_k$ ) depends on both components of  $I_{tr}$ .

The presented results show that, even in such a simple geometry, we can reproduce some remarkable features of our experimental results, such as integer and fractional Shapiro steps. The origin of the integer Shapiro steps lies in the frequency lock of the periodic system by a sinusoidal external AC drive. This effect is very general and is known in the theory of dynamical systems as Arnold's tongues [Rosenblum, 2003; Klimenko, 2013]. This provides a robustness of this effect, and integer Shapiro steps due to the vortex motion were observed not only in constricted nanobridges [Gubankov, 1976; Sivakov, 2003; Schneider, 1993; Nawaz, 2013b] but also, for example, in pinning arrays [Fiory, 1971; Martinoli, 1978; Van Look, 1999; Reichhardt, 2000; Al Luhaibi, 2022]. In our experiments, this robustness is confirmed by the fact that fractional Shapiro steps were only observed at low temperatures, and their amplitudes were small. In contrast, integer Shapiro steps persisted to higher temperatures and exhibit large amplitudes. The key ingredient contributing to the occurrence of the fractional Shapiro steps is the high anharmonicity of the vortex motion realized in our experiment. In the Section 3.3, we discussed and applied the RSJ model for a nanobridge that was based on the CPR function from pioneering works [Aslamazov, 1975b; Likharev, 1975]. These works predicted similarities between the transport properties of Josephson junctions and those of nanobridges crossed by vortices (or phase-slips). Although qualitatively obtaining the same results, we now

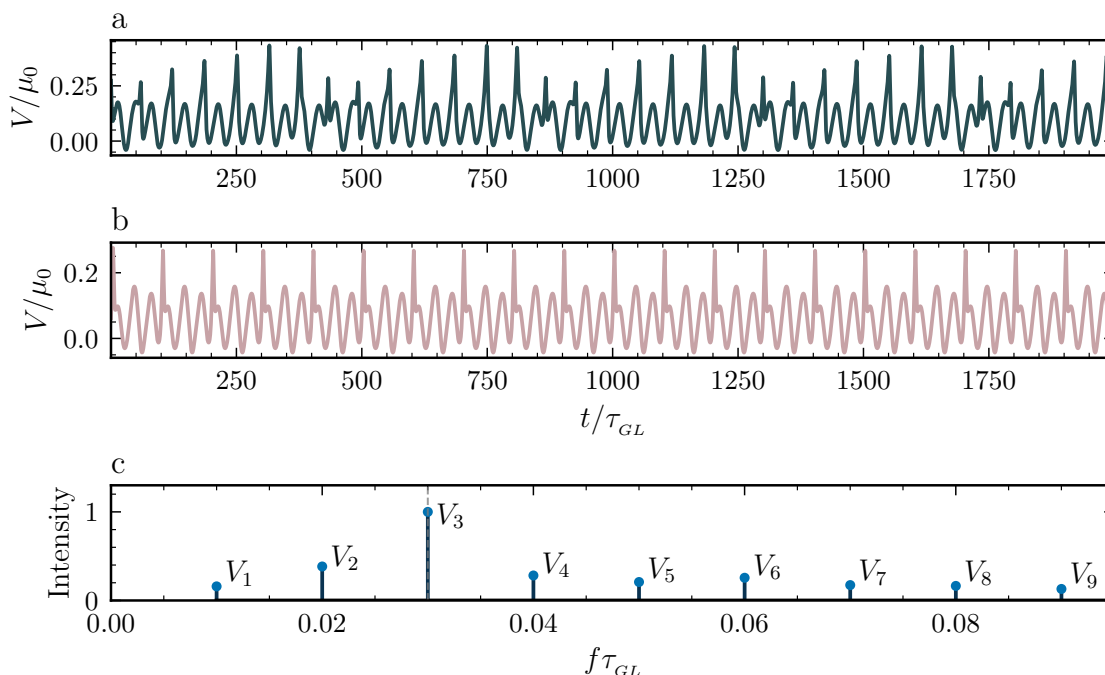


Figure 6.4 – Evolution of the instantaneous voltage  $V(t)$  for the Shapiro plateau  $1/3$  of Fig.3. a)  $V(t)$  at constant  $I_{DC}$  and  $I_{AC}$  for the detuned frequency  $f_{AC} = 0.625 f_3$ . The low-frequency envelope due to the beat effect is visible. b)  $V(t)$  at the resonance  $f_{AC} = f_3$ . c) Frequency spectrum of  $V(t)$  in the case (b).

present them based on the mean-field TDGL theory. This approach allows us to connect our results to material and geometric parameters and provides a foundation for exploring much more complex cases in a real 2D dimension.

## 1.2 Two identical grain boundaries

In experimentally studied nanobridges, the disorder is rarely represented by only one grain boundary. Most non-epitaxial superconducting films exhibit granularity on a scale of  $20 - 200$  nm, which can be significantly shorter than the nanobridge width  $W$ . For instance, nano-meanders studied in [Amari, 2017b] were elaborated out of  $\text{YBa}_2\text{Cu}_3\text{O}_{7-\delta}$  thin films. They possess a specific morphology [Mannhart, 1996] and form a network of grain boundaries. Statistically, several such boundaries can cross the bridge.

The vortex motion in these networks is much more complex than in a single grain boundary studied above. While the vortex cores are confined within the grain boundaries [Maggio-Aprile, 1997], the vortex currents extend far beyond; they circulate on a scale of  $\lambda_L$  or, in ultrathin films, on an even larger scale of the Pearl penetration depth  $\lambda_P$  [Pearl, 1964]. This results in a mutual interaction between vortices present in different grain boundaries, affecting their collective motion.

As a step towards accounting for this complexity, we now consider two linear defects

(grain boundaries) characterized by  $\epsilon = 0.5$ . The defects are separated by a distance  $l = 5\xi \sim \lambda_L$ , Fig. 6.1c, thus inducing an interline vortex-vortex interaction.

The calculated  $\langle V \rangle(I_{DC})$  characteristics in the case of two identical linear defects are presented in Fig. 6.5. When considering the curve without AC current  $I_{AC} = 0$ , we observe that the shape of this curve is almost identical to that obtained in the case of a single linear defect. As in the previous case, at DC-currents just above the critical one  $I_{DC} \gtrsim I_c$ , one vortex-antivortex pair enters the nanobridge and moves along one of the two linear defects, generating a non-zero voltage. The only difference with the single defect case is that after vortex-antivortex annihilation in one line, a new vortex-antivortex pair enters the other line, and the process repeats. Further increase in the DC-current leads to an acceleration of vortices and, consequently, an increase in voltage  $\langle V \rangle$ .

At a high enough DC-current, the system enters a new state in which the second vortex-antivortex pair enters into the second line before the first pair annihilates in the first one. This moment is witnessed by a slight inflexion of  $\langle V \rangle(I_{DC})$  curve at  $I_{DC} \simeq 0.084$ . In this state, there are two vortex-antivortex pairs in the nanobridge at the same time. Due to the mutual repulsion of vortices of the same sign, they attempt to position themselves as far from each other as possible while remaining inside linear defects. This leads to a lateral  $x$ -shift of the vortex positions in neighbouring lines, as shown in Fig. 6.6a. This dynamic vortex pattern is reminiscent of the static Abrikosov vortex lattice. As time advances, the vortex-antivortex pair in the bottom line annihilates, the one in the top line advances towards the centre, and a new one enters the bottom line.

By adding a low AC current, Shapiro plateaus appear that closely resemble those observed in the single defect case (see line  $I_{AC} = 0.01$  in Fig. 6.5). Though, at higher AC currents  $I_{AC} > 0.01$ , new features emerge. Large 2/3 Shapiro plateaus on  $\langle V \rangle(I_{DC})$  curves with a rapid voltage rise on their left side and a voltage drop on their right side (hand-added smooth dashed lines help are included to help appreciate the amplitude of the effect). Unlike other plateaus, the width of the 2/3 plateau rapidly grows with the AC current, as seen in the curves at  $I_{AC} = 0.02, 0.03, \text{ and } 0.05$ ).

To understand the origin of this phenomenon, let us consider the dynamics of the system close to the voltage drops. In the specific case of  $I_{AC} = 0.03$ , this occurs at  $I_{DC}^{drop} \simeq 0.076$ , as indicated by the arrow on the  $\langle V \rangle(I_{DC})$  curve in Fig. 6.5.

The calculations show that just above  $I_{DC}^{drop}$ , the vortex-antivortex motion in the two defects is sequential, as presented in Fig. 6.6a, while just below  $I_{DC}^{drop}$  (that is on the plateau) it is synchronous: Vortex-antivortex pairs enter the defects simultaneously, move in parallel to each other (see the snapshot Fig. 6.6b), and annihilate at the same time. This leads to high peak-to-peak voltage spikes in  $V(t)$ , as those visible on the left side of Fig. 6.6c.

The synchronous configuration itself is not stable. Indeed, when a vortex in one line is located under a vortex in the other, the projection of a vortex-vortex repulsion force

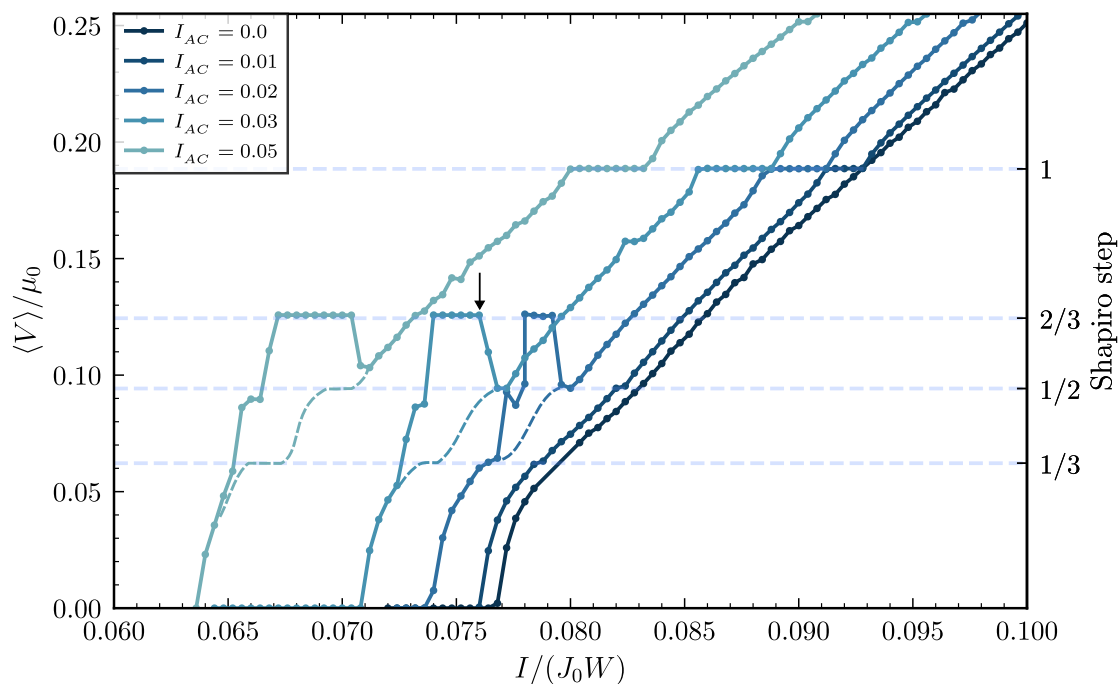


Figure 6.5 –  $\langle V \rangle(I_{DC})$  characteristics for different values of  $I_{AC}$  in the case of two identical linear defects (displayed in Fig. 6.1c). The right vertical axis displays the numbers of Shapiro steps. Dashed lines are used as eye-guides (refer to the text for details).

on a  $x$ -axis is zero. Any  $x$ -shift of their position gives rise to the  $x$ -axis component of vortex-vortex repulsion which drives the system out of this unstable balance towards a more stable checkerboard configuration, illustrated in Fig. 6.6a. Thus, the metastable configuration of Fig. 6.6b is stabilized by the external AC-drive, acting as a periodic force. If the amplitude of this force (proportional to  $I_{AC}$ ) is sufficient, the configuration is stabilized, in some range of external parameters, giving rise to a plateau on  $\langle V \rangle(I_{DC})$  curve.

When the DC current is slightly increased above  $I_{DC}^{drop}$ , the Lorentz force increases, and the system jumps down to the stable configuration of Fig. 6.6a. The corresponding evolution of  $V(t)$  is presented in Fig. 6.6c.

After a few periods of high peak-to-peak voltage oscillations, the system transitions to oscillations with a nearly twice lower peak-to-peak voltage (compare left and right parts of Fig. 6.6c). This change is due to the fact that in the metastable state, the vortex-antivortex annihilation takes place simultaneously in the two lines, while in the stable configuration, the process is sequential. The system is no longer locked to the  $\frac{2}{3}$  Shapiro step in the stable configuration.

The motion of vortices in the two close linear defects can be seen as a system of two coupled identical anharmonic oscillators. In this representation, the two oscillation

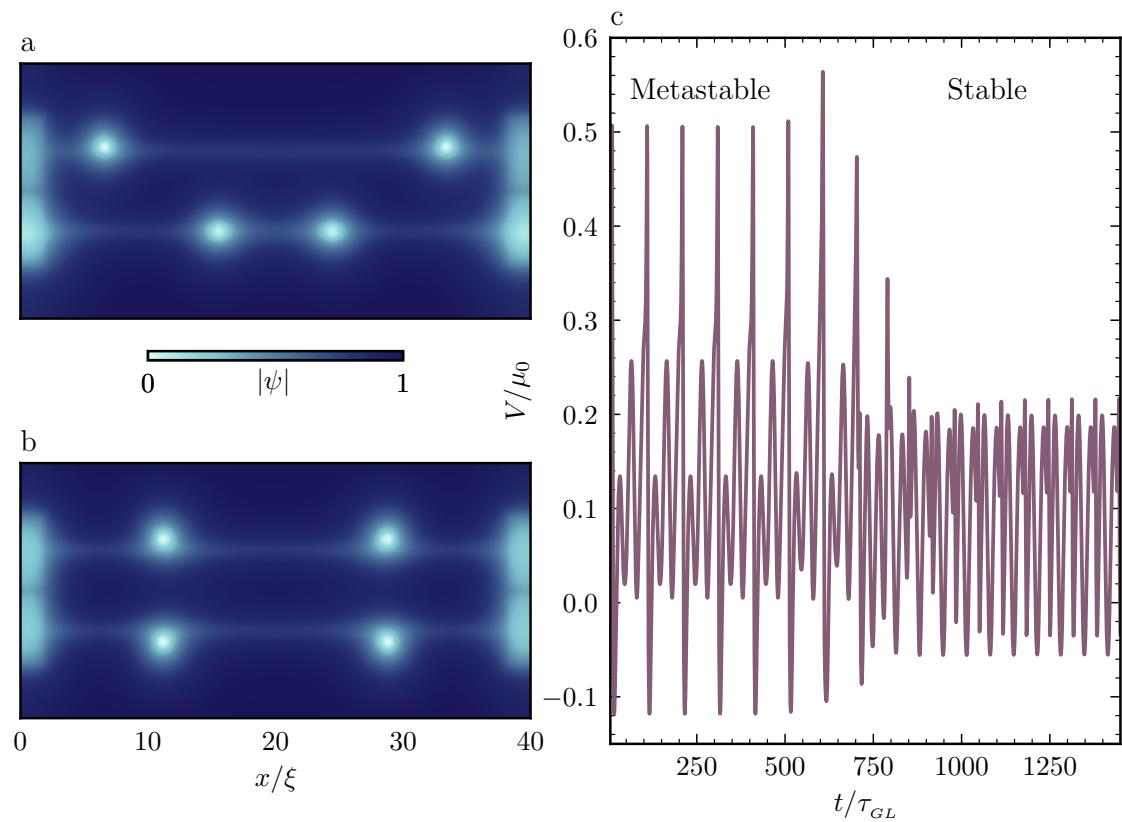


Figure 6.6 – Vortex dynamics in the case of two identical linear defects of Fig. 6.1c. a) and b) Snapshots of the order parameter amplitude in the stable (a) and metastable (b) states near the transition (see in the text). c) Evolution of  $V(t)$  at the transition from the metastable to the stable state at  $I_{AC} = 0.03$ . The initial DC current  $I_{DC} = 0.076$  switches to  $I_{DC} = 0.077$  at the moment  $t = 500$ . A movie illustrating the oscillatory dynamics of this transition is provided by the [link](#).

patterns of Fig. 6.6 can be seen as two modes, one of which is low in energy  $E_0$  and therefore stable, while the other, at higher energy  $E_1$ , is metastable. Each of these modes depends on DC current  $I_{DC}$ , and the evolution of the lowest mode corresponds to  $\langle V \rangle(I_{DC})$  curve at  $I_{AC} = 0$ . The other mode can only be achieved with an external excitation, in a certain range of pumping powers and frequencies.

The calculated Fourier spectra of  $V(t)$  in the states  $E_0$  and  $E_1$  are presented in Fig. 6.7.

In the metastable configuration  $E_1$ , the AC-drive locks to the third harmonic of the system as  $2f_{AC} = 3f_1$ . The Josephson frequency is  $f_1 = (2/3)f_{AC}$  and, consequently, the DC voltage measured in the experiment is  $\langle V(t) \rangle = (2/3)hf_{AC}/2e$ . This voltage remains constant as long as the system is locked to the drive, resulting in the unusual  $\frac{2}{3}$  Shapiro plateau in Fig. 6.5. Immediately after the drop, the drive locks to the second harmonic as  $f_{AC} = 2f_1$ , that is  $f_1 = (1/2)f_{AC}$ , resulting in a lower DC voltage  $\langle V(t) \rangle = (1/2)hf_{AC}/2e$ . In principle, it could be the usual  $\frac{1}{2}$  Shapiro plateau due to anharmonicity. Although, when the AC current increases and the width of the unusual  $\frac{2}{3}$  plateau rapidly grows, the plateau  $\frac{1}{2}$  shrinks and disappears (compare the curves at  $I_{AC} = 0.02, 0.03$  and  $0.05$  in Fig. 6.5). Note that as  $I_{DC}$  is further increased above  $I_{DC}^{drop}$ , the Lorentz force increases, pushing vortices to move faster, the corresponding frequencies grow, and the lock to the fixed frequency of the AC-drive is lost. This roller-coaster ride between different metastable, stable locked, and unlocked states is reflected in voltage spectra and, as a consequence, in a  $\langle V \rangle(I_{DC})$  curve.

Returning to the described analogy we provide a toy example: we consider a system of two coupled identical anharmonic oscillators such as two mathematical pendulums coupled via spring. Each pendulum is an anharmonic oscillator because restoring gravitational force is proportional to  $\sin(\theta)$ . Using the angles of each pendulum as variables we can write the Lagrangian of the system in the small-angle approximation as:

$$\mathcal{L} = \frac{1}{2}ml^2 (\dot{\theta}_1^2 + \dot{\theta}_2^2) - mgl(2 - \cos \theta_1 - \cos \theta_2) - \frac{1}{2}kl^2 (\theta_2 - \theta_1)^2, \quad (6.7)$$

where  $m$  is the mass of each pendulum,  $g$  is gravitational acceleration,  $k$  is the spring constant and  $l$  is the length of each pendulum (see Fig. 6.7b).

The corresponding system of equations is

$$\begin{aligned} \ddot{\theta}_1 + \frac{g}{l} \sin \theta_1 + \frac{k}{m} (\theta_1 - \theta_2) &= 0 \\ \ddot{\theta}_2 + \frac{g}{l} \sin \theta_2 - \frac{k}{m} (\theta_1 - \theta_2) &= 0. \end{aligned} \quad (6.8)$$

Solving this system of equations in the small-angle approximation, we achieve two characteristic frequencies (or modes) of this motion  $\omega_1 = \sqrt{\frac{g}{l}}, \omega_2 = \sqrt{\frac{g}{l} + 2\frac{k}{m}}$ . One of these frequencies is bigger than the other and consequently, the corresponding energy of

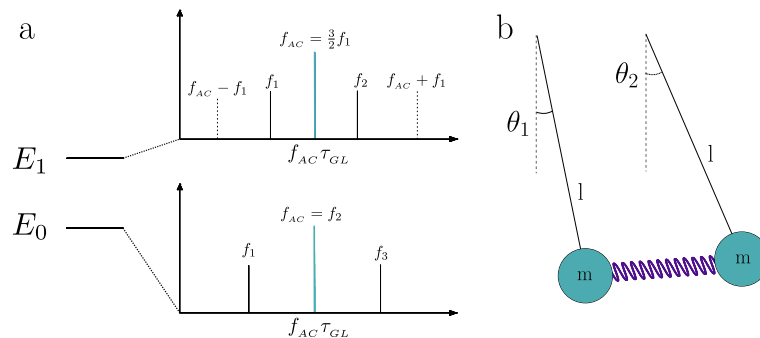


Figure 6.7 – a) Schematic energy diagram of the states considered in Fig.6. Stable ( $E_0$ ) and metastable ( $E_1$ ) states are presented along with their frequency spectra. b) a sketch of two coupled oscillators

the system is bigger. In classical mechanics, this consequence is given by the general expression  $T = \sqrt{2m} \int \frac{dx}{\sqrt{E-U(x)}}$ , where  $E$  is the total energy of the system and  $U(x)$  is the potential energy. The energy difference between these two modes is proportional to  $\sim \sqrt{\frac{k}{m}}$  and is associated with the energy of a spring deformation. In a low-energy mode  $\omega_1$ , pendulums move in phase and their relative distance does not change during oscillations, thus spring's length does not change. In a high-energy mode  $\omega_2$ , the pendulums are out of phase and the spring deforms all the time, adding an additional component to the total energy. In our system, the same role plays as the force of the vortex-vortex repulsion.

### 1.3 Two different grain boundaries

Until now, we have considered a very idealistic case where the two coupled linear defects were identical. This situation could be realised in artificial stacks of SNS junctions [Berdiyrov, 2013], periodic pinning arrays [Al-Khawaja, 2005; Van Look, 1999], but not in nanobridges made of films in which the intrinsic pinning landscape is aperiodic, and the inter-grain coupling varies from one grain boundary to the other. To account for this diversity, we also studied asymmetric linear defects. To introduce this asymmetry we keep the value of  $\epsilon$  of the bottom line the same as before  $\epsilon_1 = 0.5$  while now changing the local critical temperature in the top line via parameter  $\epsilon_2$ .

In the Fig. 6.8  $\langle V \rangle(I_{DC})$  curves for different values of  $\epsilon_2$  are presented.

Now, when the symmetry is broken, transport properties become more complex. We can notice several new features in comparison to the previous symmetric case. The first feature is the abrupt voltage jump that never happens in the symmetric case without an external AC drive. When two lines are different the degeneracy is lifted and the first vortex-antivortex pair enters into the one energetically more favorable line. This leads to the appearance of nonzero voltage  $V(t) \neq 0$ , defining the critical current  $I_c$ . Further increasing the transport current  $I_{DC}$  leads to the entry of the second pair in the second line at some value of the current force. The mutual interaction of vortices leads to perturbations of motions of the whole system due to the lines coupling through vortex-vortex interaction.

As a consequence, it leads to a larger resultant voltage due to 1) an increase in the number of moving vortices in the nanobridge and 2) a change in their velocities. The dependence of the critical current  $I_c$  on different values of the local critical temperature of the top line is shown in Fig. 6.8. This dependence is not monotonic, with a maximum at the value  $\epsilon_2 = 0.5$  i.e., in the symmetric case.

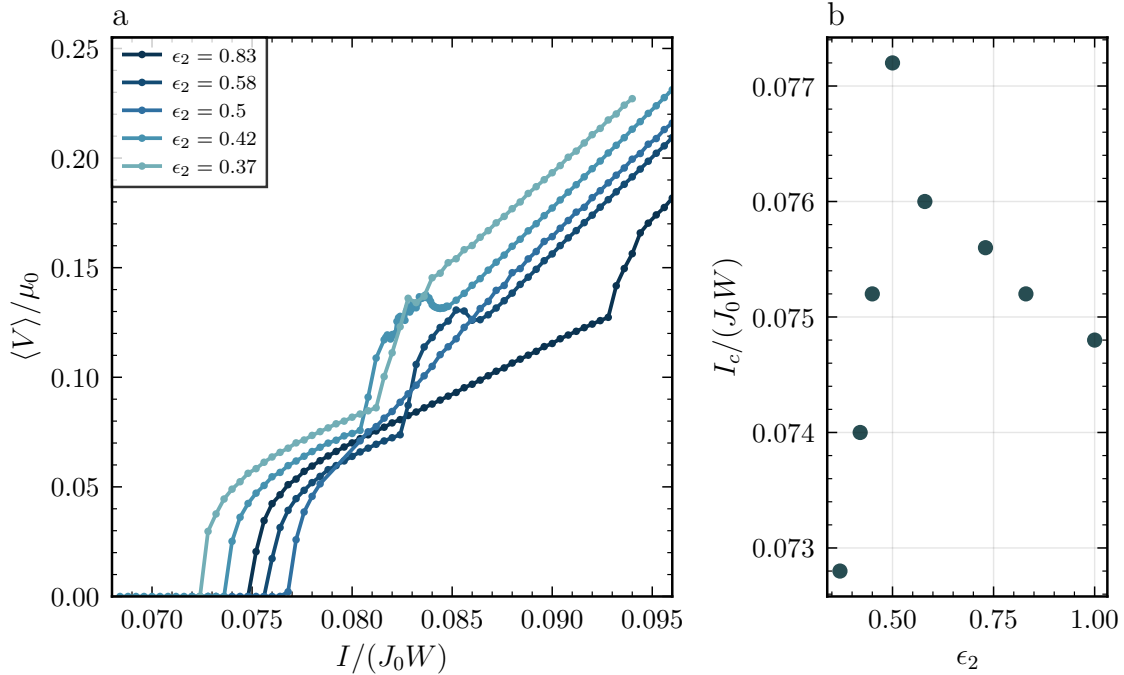


Figure 6.8 – a)  $\langle V \rangle(I_{DC})$  characteristics for different values of  $\epsilon_2$  with fixed  $\epsilon_1 = 0.5$  in the case of two different linear defects (displayed in Fig. 6.1c). b) Corresponding critical current  $I_c$  versus  $\epsilon_2$  dependency.

It would be logical to assume that this dependence increases monotonically with increasing  $\epsilon_2$ , since the pinning force in this line increases, pinning in the line with  $\epsilon_1$  is always higher, and the critical current is determined by the line with  $\epsilon_2$ . Having reached the maximum in the symmetric case when  $\epsilon_1$  equals  $\epsilon_2$ , a further increase in the pinning force through  $\epsilon_2$  should not change the situation, since now the critical current is determined by  $\epsilon_1$ . The graph should go into saturation. However, the calculation shows that this is not the case. Further increase of  $\epsilon_2$  leads to a decrease of the critical current.

We can give a semiclassical picture in a manner of the [Resistive Capacitive Shunted Junction \(RCSJ\)](#) model.

Let us represent vortices as point particles and pinning centres as potential wells with depth proportional to the pinning force. Each vortex is in its own pinning trench, but they interact with each other. This interaction is repulsive and can be represented in the classical case by a connecting spring. Moreover, our defect lines are at such a distance that the spring is initially compressed. By applying a current we lower the barriers in this

potential trench similarly to the RCSJ model with a washboard potential.

Now, we fix the epsilon value of one line and consider two cases:  $\epsilon_2 < \epsilon_1$  and  $\epsilon_2 > \epsilon_1$ . The sweep of the transport current  $I_{DC}$  leads to the lowering and tilting of the vortex entry barriers. The height of the barriers is proportional to the local critical temperature and, correspondingly, to the  $\epsilon$ . The critical current  $I_c$  is determined by the current at which our particle overcomes the barrier.

In the first case, we have  $\epsilon_2 < \epsilon_1$ . Taking into account this condition, we obtain that critical current is proportional to the  $\epsilon_2$ ,  $I_c \sim \epsilon_2$ , which is consistent with the calculations (see Fig. 6.8). Now consider the second case when  $\epsilon_2 > \epsilon_1$ . Then the first pair of vortices will always enter the line with  $\epsilon_1$  because now the weakest point is here. It would seem that now the critical current should not change, but calculations show the opposite - the critical current is inversely proportional to  $\epsilon_2$ ,  $I_c \sim \frac{1}{\epsilon_2}$ .

Let us consider how the interaction of vortices in different lines changes as  $\epsilon_2$  increases. Our vortices-particles are locked in their trenches, so we are interested only in the projection on the x-axis of their repulsive force. When the potential is shallow, the vortices oscillate in potential pits relative to each other and the total force on the x-axis is zero. As  $\epsilon_2$  increases, the barrier increases and the vortex in this line is more strongly localised, the amplitude of its oscillations along the x-axis decreases. Because of this, the total component of the force on the x-axis appears, because the second vortex (in the line with  $\epsilon_1$ ) is now part of the time in the x-axis region inaccessible to the second vortex. This additional force helps to push the vortex into the nanobridge volume, reducing the critical current. And the larger  $\epsilon_2$  is, the more localised the vortex is in this line and the more force it pushes the second vortex out. In the limit, this localised vortex can be considered as an additional source of current of a complex shape. Essentially the maximum critical current will be when this force is equal to zero, i.e. both barriers are the same, hence. Which corresponds to the results in the Fig. 6.8b.

The repulsive vortex-vortex force is defined by the current distribution created by each of them. According to the Ginzburg-Landau theory, the kinetic energy of superconducting electrons that is proportional to  $\sim |(\nabla - i\mathbf{A})\psi|^2$  and so is proportional to  $|\mathbf{J}_s|^2$ , where  $\mathbf{J}_s$  is a superconducting current density. In Fig. 6.9, we plot the superconducting current density  $J_s$  as a function of coordinates  $(x,y)$  for  $\epsilon_2 = 0.83$  and  $\epsilon_2 = \epsilon_1 = 0.5$  at a bias current that is slightly below the critical, current kinetic energy density is distributed nonequally between the lines for the case  $\epsilon_2 = 0.83$ : current lines are squeezed into the nanobridge more than the line with  $\epsilon_1$ .

The nonmonotonic dependence of the critical current on the pinning centres is not unique to our system.

A similar effect was also found in Ref. [Koshelev, 2016; Haddon, 2022; Grishakov, 2012]. According to Koshelev *et al.*[Koshelev, 2016], there are two reasons for this behaviour: the first is an increase in the hopping mobility of vortices at the pinning centres and the

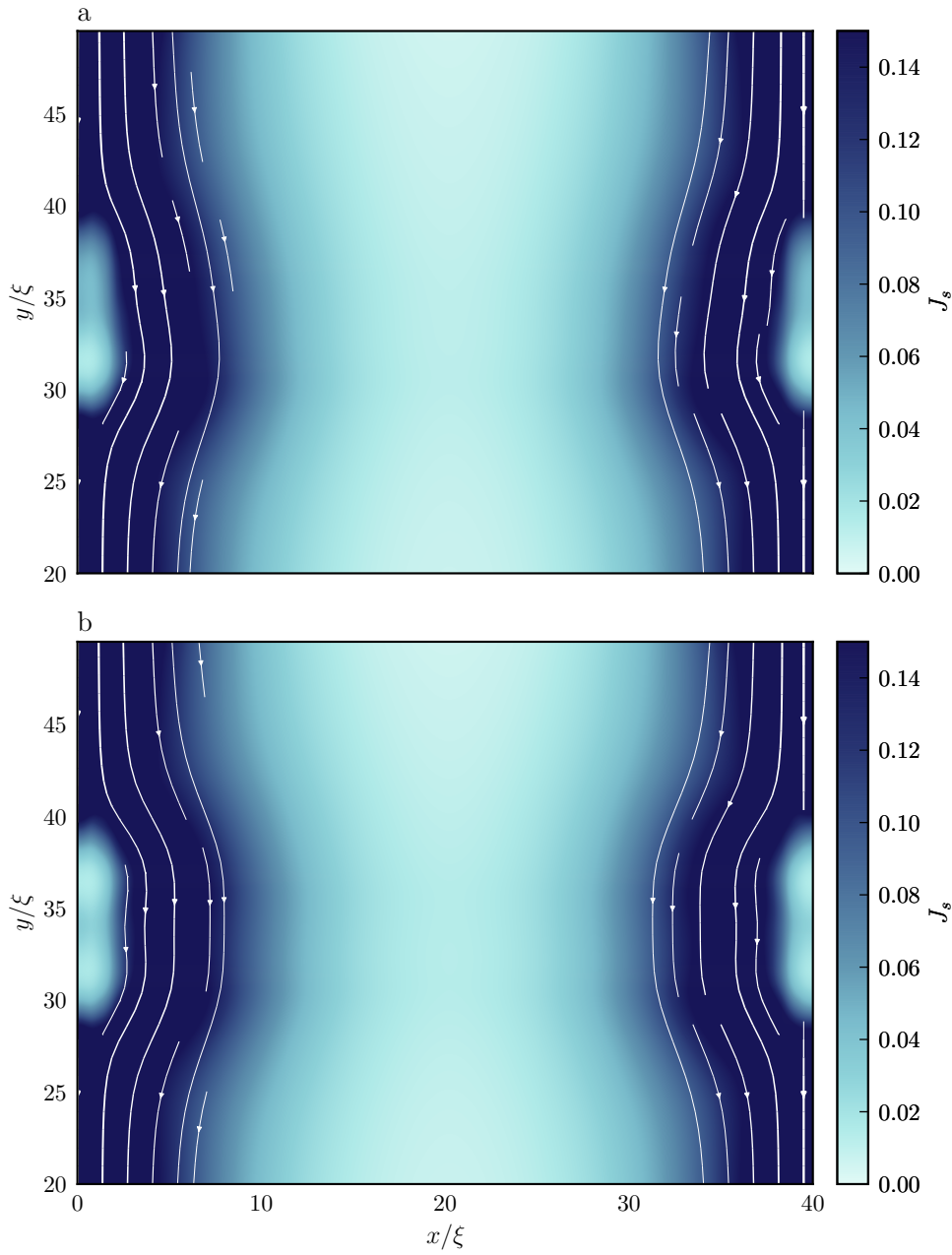


Figure 6.9 – Color-maps of the superconducting current density  $J_s$  distribution when the DC current  $I_{DC}$  is set just below the critical current  $I_c$  for two cases a)  $\epsilon_2 = 0.83$  and b)  $\epsilon_2 = \epsilon_1 = 0.5$

second is a decrease in the effective volume of the superconductor due to an increase in the percentage of defects and nonsuperconducting inclusions and, as a consequence, a decrease in the current-carrying capacity.

In our case at zero magnetic field, the edges play the largest role. From this point on, the critical current is determined by the roughness of the edges. The effect of the edges on the vortex entrance and motion was studied in the Refs.[Benfenati, 2020; Kimmel, 2019].

Additionally, the question of the influence of defects at the boundary on the critical

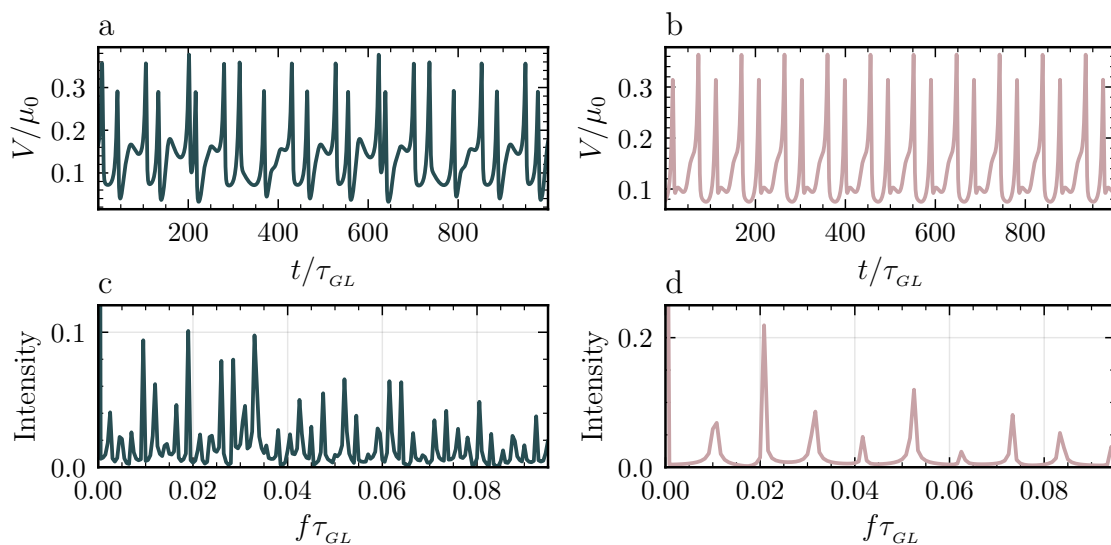


Figure 6.10 – Dynamics of states with (a,c) and without (b,d) NDR for the case  $\epsilon_2 = 0.042$ .

current was studied, for example, in the works [Glatz, 2020; Sadovskyy, 2016a; Sadovskyy, 2017; Sadovskyy, 2019; Kimmel, 2017]. The search for an optimum with respect to the maximum critical current is a separate problem, which leads to the whole area under the paradigm *critical current by design* [Sadovskyy, 2016b].

The second feature is the regions of **Negative dynamic resistance (NDR)**.

In these regions, average voltage  $\langle V \rangle$  decreases with the increasing current  $I_{DC}$ . They appear after a sharp voltage rise when the vortex-antivortex pair enters the second line defect and they are well pronounced if two linear defects differ  $\epsilon_1 \approx \epsilon_2$  slightly. If this is the case, in a picture of coupled pendulums we have two coupled pendulums with slightly different eigenfrequencies. DC current  $I_{DC}$  plays the role of a constant force that acts on the system. Sweep the current we drive the system through different states. As we discussed earlier, several modes exist in this system. It is possible to mix them and synchronize vortex-antivortex pairs motion in neighbouring lines. Because of defects mismatch, this synchronization is not perfect but only partial. In Fig. 6.10a,c voltage versus time and corresponding spectrum for a value  $I_{DC} = 0.083$  that corresponds to a before the dip for  $\epsilon_2 = 0.042$  are presented. One can see that the spectrum is not as narrow as in the case of the NDR region. This indicates that before the NDR region, the system was more chaotic with a bunch of different modes, some of which are high-energy and yield higher voltage. On the other side in the NDR region, instantaneous voltage is more periodic which can be seen in both direct signal (Fig. 6.10b) and its spectrum (Fig. 6.10d). Much fewer oscillation modes appear. And all of them are low-energy checkmate modes.

When AC excitation is added, integer and fractional Shapiro steps are observed, the latter stemming from the anharmonic nature of vortex motion. The transitions to/from

metastable modes are also observed, although their number is larger, their shape is more complex and intricate than in the case of identical defects. Clearly, the vortex dynamics in the presence of asymmetric defects lead to a greater variety of collective motion modes.

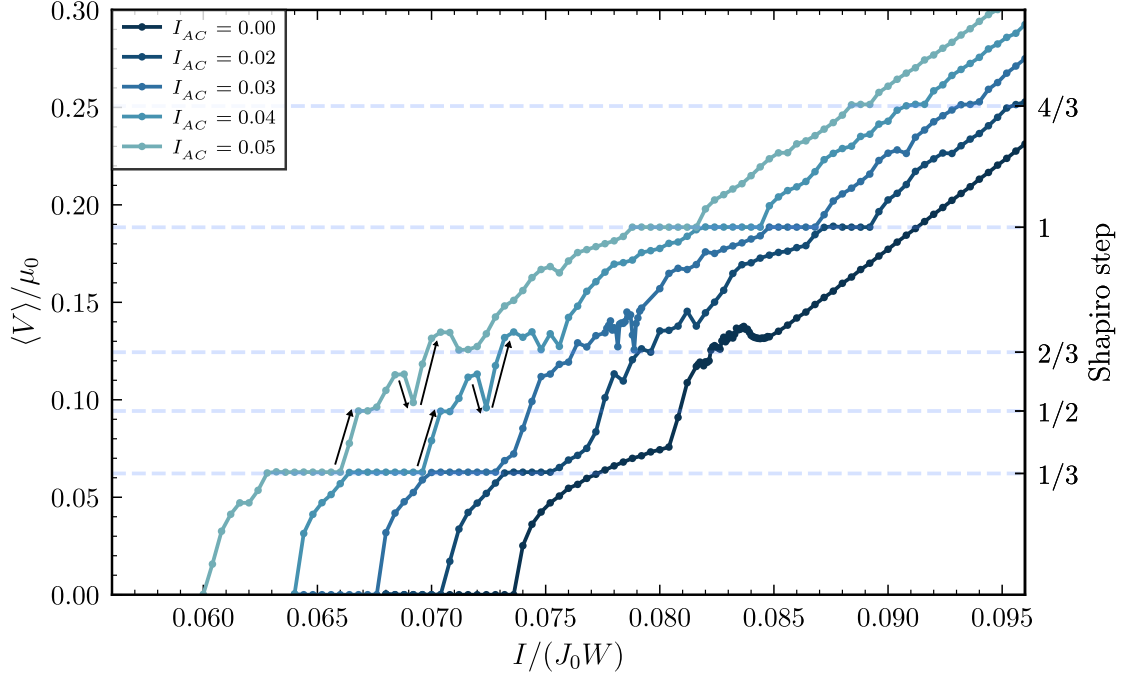


Figure 6.11 –  $\langle V \rangle(I_{DC})$  characteristics for different  $I_{AC}$  in the case of two different linear defects,  $\epsilon = 0.5$  and  $\epsilon = 0.42$ . The right vertical axis displays the numbers of corresponding Shapiro steps.

The evolution of Shapiro features in Figs. 6.5, 6.11 with increasing  $I_{AC}$  is not trivial. At low AC excitation,  $I_{AC} \ll I_{DC}$ , conventional Shapiro plateaus are narrow and no signatures of metastable states are seen. In this regime, the AC component acts as a probe that locks, at a fixed  $f_{AC}$ , onto the spectrum of the vortex motion, solely determined by the main driving (Lorentz) force  $\sim I_{DC}$ . As  $I_{DC}$  increases, the vortices move faster,  $f_1$  and  $f_k$  increase. At some  $I_{DC}$ , a given  $f_k$  gets close enough to  $nf_{AC}$ , and the motion locks to  $f_{AC}$ ;  $f_1$  remains fixed in some range of  $I_{DC}$ . As  $I_{DC}$  increases further, the locking effect is lost. This results in a series of integer and fractional Shapiro plateaus visible on  $\langle V \rangle(I_{DC})$  curve at  $I_{AC} = 0.02$ .

When  $I_{AC}$  increases and becomes comparable with  $I_{DC}$ , two phenomena appear. The first one is the well-known enlargement of Shapiro plateaus, due to a stronger locking effect at higher AC-currents. The second one is related to the perturbation of the vortex motion spectrum by the oscillatory force  $\sim I_{AC}$ , whose amplitude becomes comparable to the Lorentz force due to the AC current. The combined action of  $I_{DC}$  and  $I_{AC}$  allows the existence of metastable states. They can be locked to  $f_{AC}$ , resulting in jump-plateau-drop features as observed in Fig. 6.5. The same phenomenon takes place in Fig. 6.11, where

many more voltage bumps and drops are observed (some jumps to metastable states are indicated by black arrows) as compared to Fig. 6.5. The lift of degeneracy, resulting in a more rich and complex metastable state spectrum, is certainly behind these differences. Finally, the DC current range where the feature appears rapidly extends with increasing  $I_{AC}$ .

In the limit of a dense, on the scale of  $W$ , network of defects, one would expect a huge number of apparently chaotically arranged voltage jump-bump-drops to appear on  $\langle V \rangle(I_{DC})$  curves, reflecting a vast number of accessed vortex motion modes and the complexity of the related spectra. The term "chaotic" is justified here due to the high sensitivity of the accessed metastables configurations to external parameters such as  $I_{DC}$ ,  $I_{AC}$ ,  $f_{AC}$ , the disorder landscape, etc. Indeed, after unlocking from one metastable state, the system can jump down to a more stable configuration or lock up to another metastable state, from the available set. As a result, the position and shape of bumps-drops on  $\langle V \rangle(I_{DC})$  curves would appear arbitrary (see Fig. 6.11), while they are deterministic.

The revealed voltage drops correspond to a negative dynamic resistance  $dV/dI(I_{DC})$ . The latter has been experimentally observed in periodic pinning arrays subject to a specific external magnetic field [Gutierrez, 2009; Misko, 2006; Reichhardt, 1997], where a complex collective dynamics of vortices led to multiple phase transitions in their collective motion, with no need for additional AC-drive, resulting in various features in the  $V(I)$  characteristics [Gutierrez, 2009; Misko, 2006; Reichhardt, 1997]. Another system is a perforated Nb film put in an external magnetic field, where the negative dynamic resistance can appear due to the Ratchet effect under AC drive [Dobrovolskiy, 2017]. More recently, both Shapiro steps and negative dynamic resistance were observed in a MoN strips with artificial cut [Ustavshikov, 2022]. The authors attributed the negative dynamic resistance to the chaotic aperiodic vortex motion at high AC-excitation amplitude.

The ability to use AC excitation both as a pump and as a probe opens up interesting possibilities for realization, spectroscopy and control of metastable states in superconducting weak-links. The obtained results demonstrate the potential for designing artificial disorder landscapes to achieve desired responses to AC-amplitude and/or frequency. The general nature of weak-links suggests that there would be multiple ways of experimental realization of these functionalities. One of the straightforward routes is to engineer superconducting films with a controlled disorder using a focused ion beam approach [Dobrovolskiy, 2017] or to deposit superconducting materials onto faceted structures [Soroka, 2007]. By carefully designing the spatial distribution of defects or grain boundaries, one could tailor the response of the weak-links to both DC- and AC-excitation. Another avenue is to overlap superconducting weak-links by ferromagnetic strips that can locally suppress the superconducting order parameter due to the inverse proximity effect [Carapella, 2016a; Carapella, 2016b; Dobrovolskiy, 2020a; Jaque, 2002; Yuzhelevski, 1999]. This can introduce additional complexity in the vortex dynamics and lead to novel effects under

microwave excitation.

## 2 Conclusion

In this work, we conducted a numerical investigation into the transport properties of superconducting nanobridges carrying current and exposed to microwave illumination. To account for the granularity observed in experimental devices, we introduce one or two linear defects, simulating grain boundaries, oriented perpendicularly to the applied current. Our study unveils the rich and complex dynamics of the vortex motion along these defects. The pronounced anharmonicity in the system enabled us to lock its spectrum with an external periodic drive, resulting in the observation of both integer and fractional Shapiro plateaus in DC voltage-current characteristics.

In the case of two close linear defects, the inter-vortex coupling leads to the appearance of collective modes of correlated motion, featuring multiple stable and metastable states. These transitions manifest as regions of negative differential resistance  $dV/dI(I_{DC})$  in the current-voltage characteristic. Manipulating the amplitude and frequency of the external drive provides a mean to pump the system into higher-resistance metastable modes and stabilise it within a finite range of DC transport currents. Stepping beyond this range initiates a relaxation to lower-resistance modes. The ability to control and stabilise different modes of the vortex motion opens up new possibilities for designing superconducting devices with tunable transport properties and novel functionalities.

# Conclusion

This work aims to investigate the critical behaviour in nanoscale superconducting filaments, both experimentally and theoretically. Recent progress in the fabrication of HTS-based nanoscale devices has stimulated our research. Low-temperature superconductors have already found applications in various fields, including medicine and quantum information science. It is desirable to have all the useful properties of these devices at higher temperatures. The discovery of HTS was promising for practical applications, but their unique nature and difficulty in handling them posed challenges. Although massive studies of HTS have been carried out since its discovery, it is only relatively recently that significant success has been achieved in the fabrication of devices that are close to real-world applications. This understanding is due to the accumulated experience with these materials and knowledge of their properties, as well as the development of nanoscale manufacturing technologies. Further progress in improving the performance of these devices can lead to enhancement of the SSPD domain or used in Magnetoencephalography (MEG).

This manuscript describes the method used to fabricate nanoscale  $\text{YBa}_2\text{Cu}_3\text{O}_{7-\delta}$  wires because wires are the basic building block of various devices, and at the same time, this geometry is simple enough to compare with existing theoretical models. Fabricating such samples is challenging because of the material's high sensitivity to oxygen doping and the presence of defects that significantly affect the transport properties. Simultaneously, we use the sensitivity to disorder to form the nanowires themselves using ion irradiation.

A major part of this work has been the investigation of the transport properties of the fabricated nanowires. We measured  $IV$  curves over a wide range of temperatures. In order to find a consistent explanation for the observed effects, we attempted to interpret the data using various existing models. The vortex scenario appeared to be the most likely. As part of our testing process, we utilized the Shapiro steps measurement to obtain additional data. This involved conducting transport measurements under RF illumination. The results obtained from this method were quite unusual, with some things remaining unexplained and requiring further investigation. In the following section of our work, we attempt to provide explanations for some of these results.

The second main part is devoted to the theoretical study of the motion of Abrikosov vortices in superconducting nanowires with linear defects.

On the basis of numerical solution of [TDGL](#) equations, we managed to show that vortex motion leads not only to the appearance of integer Shapiro steps, but also to the appearance of fractional ones.

The observations at relatively low temperatures align with our experimental findings, and the emergence of these phenomena is attributed to the intricate anharmonic motion of vortices and antivortices. The presence of an additional linear defect in the neighbourhood preserves the existing effects, but under certain conditions qualitatively new ones appear.

Specifically, in the presence of [RF](#) radiation, the system exhibits transitions to metastable states that were previously inaccessible due to their high energy. These transitions manifest as regions with negative dynamical resistance on [IV](#) curves. Our predicted effect is strongest in the sterile symmetric case, but we also discuss its stability under variations in defect parameters. Importantly, the predicted effect is not confined to specific conditions and had potential realizations in various other superconducting systems.

# List of publications

## Peer-reviewed articles

Amari, P., **Kozlov, S.**, Recoba-Pawłowski, E., Velluire-Pellat, Z., Jouan, A., Couëdo, F., ... & Feuillet-Palma, C.. "*Scalable nanofabrication of high-quality  $YBa_2Cu_3O_7 - \delta$  nanowires for single-photon detectors*". *Physical Review Applied*, 20(4), 044025 (2023).

DOI: [10.1103/PhysRevApplied.20.044025](https://doi.org/10.1103/PhysRevApplied.20.044025)

Velluire-Pellat, Z., Maréchal, E., Moulonguet, N., Saiz, G., Ménard, G. C., **Kozlov, S.**, ... Bergeal, N.. "*Hybrid quantum systems with high- $T_c$  superconducting resonators*". *Scientific Reports*, 13(1), 14366 (2023).

DOI: [10.1038/s41598-023-44720-4](https://doi.org/10.1038/s41598-023-44720-4)

Kudriashov, A., Babich, I., Hovhannisyanyan, R. A., Shishkin, A. G., **Kozlov, S. N.**, Fedorov, A., ... Stolyarov, V. S.. "*Revealing Intrinsic Superconductivity of the Nb/BiSbTe<sub>2</sub>Se Interface*". *Advanced Functional Materials*, 32(49), 2209853 (2022).

DOI: [10.1002/adfm.202209853](https://doi.org/10.1002/adfm.202209853)

Pierini, S., Capitani, F., Scimeca, M., **Kozlov, S.**, Pierucci, D., Alchaar, R., ... Lhuillier, E.. "*Vanishing confinement regime in terahertz HgTe nanocrystals studied under extreme conditions of temperature and pressure*". *The Journal of Physical Chemistry Letters*, 13(30), 6919-6926 (2022).

DOI: [10.1021/acs.jpcclett.2c01636](https://doi.org/10.1021/acs.jpcclett.2c01636)

Stolyarov, V. S., Roditchev, D., Gurtovoi, V. L., **Kozlov, S. N.**, Yakovlev, D. S., Skryabina, O. V., ... Golubov, A. A.. "*Resonant Oscillations of Josephson Current in Nb-Bi<sub>2</sub>Te<sub>2.3</sub>Se<sub>0.7</sub>-Nb Junctions*". *Advanced Quantum Technologies*, 5(3), 2100124 (2022).

DOI: [10.1002/qute.202100124](https://doi.org/10.1002/qute.202100124)

Stolyarov, V. S., Yakovlev, D. S., **Kozlov, S. N.**, Skryabina, O. V., Lvov, D. S., Gumarov, A. I., ... & Roditchev, D.. "*Josephson current mediated by ballistic topological states in Bi<sub>2</sub>Te<sub>2.3</sub>Se<sub>0.7</sub> single nanocrystals*". *Communications Materials*, 1(1), 38 (2020).

DOI: [10.1038/s43246-020-0037-y](https://doi.org/10.1038/s43246-020-0037-y)

Skryabina, O. V., **Kozlov, S. N.**, Egorov, S. V., Klimenko, A. A., Ryazanov, V. V., Bakurskiy, S. V., ... Stolyarov, V. S.. "*Anomalous magneto-resistance of Ni-nanowire/Nb hybrid system*". *Scientific reports*, 9(1), 14470 (2019).

DOI: [10.1038/s41598-019-50966-8](https://doi.org/10.1038/s41598-019-50966-8)

**Kozlov, S. N.**, Skryabina, O. V., Egorov, S. V., Golovchanskiy, I. A., Klimenko, A. A., Napolskii, K. S., & Stolyarov, V. S.. "*Magneto-resistance of a single polycrystalline nickel nanowire*". *Journal of Applied Physics*, 125(6) (2019).

DOI: [10.1063/1.5064680](https://doi.org/10.1063/1.5064680)

Golovchanskiy, I. A., Abramov, N. N., Stolyarov, V. S., Shchetinin, I. V., Dzhumaev, P. S., Averkin, A. S., **Kozlov, S. N.** ... & Ustinov, A. V.. "*Probing dynamics of micro-magnets with multi-mode superconducting resonator*". Journal of Applied Physics, 123(17) (2018).

DOI: [10.1063/1.5025028](https://doi.org/10.1063/1.5025028)

Skryabina, O. V., Egorov, S. V., Goncharova, A. S., Klimenko, A. A., **Kozlov, S. N.**, Ryazanov, V. V., ... & Stolyarov, V. S.. "*Josephson coupling across a long single-crystalline Cu nanowire*". Applied physics letters, 110, 222605 (2017).

DOI: [10.1063/1.4984605](https://doi.org/10.1063/1.4984605)

## Articles under review

**Kozlov, S.**, Lesueur, J., Roditchev, D., Feuillet-Palma, C.. "*Dynamic metastable vortex states in interacting vortex lines*". under review in *Communications Physics*.

## International conferences (first author)

**Kozlov, S.**, Lesueur, J., Roditchev, D., Feuillet-Palma, C.. "*Dynamic metastable vortex states in interacting vortex lines*". Advanced Physics of van der Waals heterostructure, Roscoff, France, 2023.

**Kozlov, S.**, Amari, P., Lesueur, J., Roditchev, D., Feuillet-Palma, C.. "*Probing vortex dynamics in YBCO nanowire using RF illumination*". Congrès Général des 150 ans de la Société Française de Physique, Paris, France, 2023.

**Kozlov, S.**, Amari, P., Briatico, J., Bergeal, N., Lesueur, J., Feuillet-Palma, C.. "*Probing vortex dynamics in YBCO nanowire using RF illumination*". Low dimensional superconducting hybrids for novel quantum functionalities, Paris, France, 2021.

**Kozlov, S.**, Amari, P., Briatico, J., Bergeal, N., Lesueur, J., Feuillet-Palma, C.. "*Probing vortex dynamics in YBCO nanowire using RF illumination*". VORTEX 2021, Online, 2021.

**Kozlov, S.**, Skryabina, O. V., Egorov, S. V., Klimenko, A. A., Golovchanskiy, I. A., Napolskii, K. S., and Stolyarov, V. S.. "*Magnetoresistance of a single polycrystalline nickel nanowire at low temperature*". New in Magnetism and Magnetic Materials, Moscow, Russia 2018.

**Kozlov, S.**, Skryabina, O. V., Egorov, S. V., Goncharova, A. S., Klimenko, A. A., Ryazanov, V. V., Bakurskiy, S. V., Kupriyanov, M. Y., Golubov, A. A., Napolskii, K. S., and Stolyarov, V. S.. "*Supercurrent in Nb/Cu-nanowire/Nb Josephson junctions*". Superconducting Hybrid Nanostructures: Physics and Applications, Dolgoprudny, Russia, 2016.

# Bibliography

- [Abrikosov, 1969] Aleksei Alekseevich Abrikosov. « Magnetic impurities in nonmagnetic metals ». *Soviet Physics Uspekhi* 12.2 (1969), p. 168 (cit. on pp. 3, 36).
- [Abrikosov, 1964] Aleksej A Abrikosov, Lev P Gorkov, IE Dzyaloshinski, Richard A Silverman, and George H Weiss. *Methods of quantum field theory in statistical physics*. American Institute of Physics, 1964 (cit. on p. 3).
- [Al Luhaibi, 2022] Abdulwahab Al Luhaibi, A Glatz, and JB Ketterson. « Driven responses of periodically patterned superconducting films ». *Physical Review B* 106.22 (2022), p. 224516 (cit. on pp. 92, 95).
- [Albrecht, 2007] J Albrecht, M Djupmyr, and S Brück. « Universal Temperature Scaling of Flux Line Pinning in High-Temperature Superconducting Thin Films ». *Journal of Physics: Condensed Matter* 19.21 (2007), p. 216211 (cit. on pp. 58–60).
- [Alloul, 2009] H. Alloul, J. Bobroff, M. Gabay, and P. J. Hirschfeld. « Defects in Correlated Metals and Superconductors ». *Rev. Mod. Phys.* 81.1 (2009), pp. 45–108 (cit. on p. 22).
- [Amari, 2017a] P Amari, C Feuillet-Palma, A Jouan, F Couëdo, N Bourlet, E Géron, et al. « High-temperature superconducting nano-meanders made by ion irradiation ». *Superconductor Science and Technology* 31.1 (2017), p. 015019 (cit. on p. 49).
- [Amari, 2017b] Paul Amari, C Feuillet-Palma, A Jouan, F Couëdo, N Bourlet, E Géron, et al. « High-temperature superconducting nano-meanders made by ion irradiation ». *Superconductor Science and Technology* 31.1 (2017), p. 015019 (cit. on pp. 33, 96).
- [Amari, ] P. Amari... « In revision » () (cit. on p. 90).
- [Anderson, 1964] Philip W Anderson and YB Kim. « Hard superconductivity: theory of the motion of Abrikosov flux lines ». *Reviews of modern physics* 36.1 (1964), p. 39 (cit. on pp. 61, 62).
- [Anderson, 1963] Philip W Anderson and John M Rowell. « Probable observation of the Josephson superconducting tunneling effect ». *Physical Review Letters* 10.6 (1963), p. 230 (cit. on p. 3).
- [Andersson, 2020] Eric Andersson, Riccardo Arpaia, Edoardo Trbaldo, Thilo Bauch, and Floriana Lombardi. « Fabrication and electrical transport characterization of high quality underdoped YBa<sub>2</sub>Cu<sub>3</sub>O<sub>7- $\delta$</sub>  nanowires ». *Superconductor Science and Technology* 33.6 (2020), p. 064002 (cit. on p. 33).
- [Andronov, 1993] A Andronov, I Gordion, V Kurin, I Nefedov, and I Shereshevsky. « Kinematic vortices and phase slip lines in the dynamics of the resistive state of narrow superconductive thin film channels ». *Physica C: Superconductivity and its Applications* 213.1-2 (1993), pp. 193–199 (cit. on p. 54).
- [Annunziata, 2010] Anthony J Annunziata, Orlando Quaranta, Daniel F Santavicca, Alessandro Casaburi, Luigi Frunzio, Mikkel Ejrnaes, et al. « Reset dynamics and latching in niobium superconducting nanowire single-photon detectors ». *Journal of Applied Physics* 108.8 (2010) (cit. on p. 33).
- [Arpaia, 2014a] R Arpaia, M Ejrnaes, L Parlato, R Cristiano, M Arzeo, T Bauch, et al. « Highly Homogeneous YBCO/LSMO Nanowires for Photoresponse Experiments ». *Superconductor Science and Technology* 27.4 (2014), p. 044027 (cit. on p. 33).
- [Arpaia, 2015a] R Arpaia, M Ejrnaes, L Parlato, F Tafuri, R Cristiano, D Golubev, et al. « High-Temperature Superconducting Nanowires for Photon Detection ». *Physica C* (2015), p. 7 (cit. on p. 35).
- [Arpaia, 2014b] Riccardo Arpaia, M Ejrnaes, Loredana Parlato, R Cristiano, Marco Arzeo, Thilo Bauch, et al. « Highly homogeneous YBCO/LSMO nanowires for photoresponse experiments ». *Superconductor Science and Technology* 27.4 (2014), p. 044027 (cit. on p. 34).

- [Arpaia, 2015b] Riccardo Arpaia, M Ejrnaes, Loredana Parlato, Francesco Tafuri, R Cristiano, D Golubev, et al. « High-temperature superconducting nanowires for photon detection ». *Physica C: Superconductivity and its Applications* 509 (2015), pp. 16–21 (cit. on p. 33).
- [Arpaia, 2014c] Riccardo Arpaia, D Golubev, Reza Baghdadi, Marco Arzeo, Gunta Kunakova, Sophie Charpentier, et al. « Resistive state triggered by vortex entry in YBa<sub>2</sub>Cu<sub>3</sub>O<sub>7- $\delta$</sub>  nanostructures ». *Physica C: Superconductivity and its Applications* 506 (2014), pp. 165–168 (cit. on p. 49).
- [Arpaia, 2017] Riccardo Arpaia, Dmitri Golubev, Reza Baghdadi, Regina Ciancio, Goran Dražić, Pasquale Orgiani, et al. « Transport Properties of Ultrathin YBa<sub>2</sub>Cu<sub>3</sub>O<sub>7- $\delta$</sub>  Nanowires: A Route to Single Photon Detection ». *Physical Review B* 96.6 (2017), p. 064525. arXiv: [1708.04721](https://arxiv.org/abs/1708.04721) [[cond-mat](#)] (cit. on pp. 33, 34).
- [Arpaia, 2013] Riccardo Arpaia, Shahid Nawaz, Floriana Lombardi, and Thilo Bauch. « Improved nanopatterning for YBCO nanowires approaching the depairing current ». *IEEE transactions on applied superconductivity* 23.3 (2013), pp. 1101505–1101505 (cit. on p. 34).
- [Arutyunov, 2008] K Yu Arutyunov, Dmitri S Golubev, and Andrej Dmitievič Zaikin. « Superconductivity in one dimension ». *Physics Reports* 464.1-2 (2008), pp. 1–70 (cit. on p. 68).
- [Arutyunov, 2012] Konstantin Yu Arutyunov, Terhi T Hongisto, Janne S Lehtinen, Leena I Leino, and Alexander L Vasiliev. « Quantum phase slip phenomenon in ultra-narrow superconducting nanorings ». *Scientific reports* 2.1 (2012), p. 293 (cit. on p. 68).
- [Aslamazov, 1968] LG Aslamazov and AI Larkin. « The influence of fluctuation pairing of electrons on the conductivity of normal metal ». *Physics Letters A* 26.6 (1968), pp. 238–239 (cit. on p. 47).
- [Aslamazov, 1969] LG Aslamazov and AI Larkin. « Josephson effect in superconducting point contacts ». *ZhETF Pisma Redaktsiiu* 9 (1969), p. 150 (cit. on p. 68).
- [Aslamazov, 1975a] LG Aslamazov and AI Larkin. « Josephson effect in wide superconducting bridges ». *Zh. Eksp. Teor. Fiz* 68 (1975), pp. 766–775 (cit. on pp. 67, 69).
- [Aslamazov, 1975b] LG Aslamazov and AI Larkin. « Josephson effect in wide superconducting bridges ». *Zh. Eksp. Teor. Fiz* 68 (1975), pp. 766–775 (cit. on p. 95).
- [Aslamazov, 1978] LG Aslamazov and AI Larkin. « Influence of a microwave field on the critical current of superconducting contacts ». *Soviet Physics-JETP* 47 (1978), pp. 1136–1142 (cit. on p. 73).
- [Assink, 1993] H Assink, AJMVD Harg, CM Schep, NY Chen, D vd Marel, P Hadley, et al. « Critical currents in submicron YBa<sub>2</sub>/Cu<sub>3</sub>O<sub>7</sub>/lines ». *IEEE transactions on applied superconductivity* 3.1 (1993), pp. 2983–2985 (cit. on p. 33).
- [Bardeen, 1957] John Bardeen, Leon N Cooper, and J Robert Schrieffer. « Microscopic theory of superconductivity ». *Physical Review* 106.1 (1957), p. 162 (cit. on p. 3).
- [Bartolf, 2010] Holger Bartolf, Andreas Engel, Andreas Schilling, Konstantin Il'in, Michael Siegel, H-W Hübers, et al. « Current-assisted thermally activated flux liberation in ultrathin nanopatterned NbN superconducting meander structures ». *Physical Review B* 81.2 (2010), p. 024502 (cit. on p. 48).
- [Bednorz, ] J G Bednorz. « Possible High T<sub>c</sub> Superconductivity in the Ba - La- Cu- O System » (), p. 5 (cit. on pp. xii, 19).
- [Benfatto, 2009] L Benfatto, Claudio Castellani, and Thierry Giamarchi. « Broadening of the Berezinskii-Kosterlitz-Thouless superconducting transition by inhomogeneity and finite-size effects ». *Physical Review B* 80.21 (2009), p. 214506 (cit. on pp. 46, 48).
- [Benfenati, 2020] Andrea Benfenati, Andrea Maiani, Filipp N Rybakov, and Egor Babaev. « Vortex nucleation barrier in superconductors beyond the Bean-Livingston approximation: A numerical approach for the sphaleron problem in a gauge theory ». *Physical Review B* 101.22 (2020), p. 220505 (cit. on p. 104).
- [Bennemann, 2008] Karl-Heinz Bennemann and John B Ketterson. *Superconductivity: Volume 1: Conventional and Unconventional Superconductors Volume 2: Novel Superconductors*. Springer Science & Business Media, 2008 (cit. on p. 4).
- [Berdiyorov, 2014] G Berdiyrov, Khalil Harrabi, F Oktasendra, Khaled Gasmi, AI Mansour, JP Maneval, et al. « Dynamics of current-driven phase-slip centers in superconducting strips ». *Physical Review B* 90.5 (2014), p. 054506 (cit. on p. 91).
- [Berdiyorov, 2009a] GR Berdiyrov, MV Milošević, and FM Peeters. « Kinematic vortex-antivortex lines in strongly driven superconducting stripes ». *Physical Review B* 79.18 (2009), p. 184506 (cit. on p. 54).

- [Berdiorov, 2009b] GR Berdiorov, MV Milošević, and FM Peeters. « Tunable kinematics of phase-slip lines in a superconducting stripe with magnetic dots ». *Physical Review B* 80.21 (2009), p. 214509 (cit. on p. 54).
- [Berdiorov, 2013] GR Berdiorov, SE Savel'Ev, MV Milošević, FV Kusmartsev, and FM Peeters. « Synchronized dynamics of Josephson vortices in artificial stacks of SNS Josephson junctions under both dc and ac bias currents ». *Physical Review B* 87.18 (2013), p. 184510 (cit. on p. 101).
- [Bergeal, 2005] N Bergeal, X Grison, J Lesueur, G Faini, M Aprili, and J P Contour. « High-quality planar high-T-c Josephson junctions ». *Applied Physics Letters* 87.10 (2005), p. 102502 (cit. on pp. 25, 36).
- [Bergeal, 2006] N. Bergeal, J. Lesueur, G. Faini, M. Aprili, and J. P. Contour. « High Tc Superconducting Quantum Interference Devices Made by Ion Irradiation ». *Appl. Phys. Lett.* 89.11 (2006), p. 112515 (cit. on p. 36).
- [Bernstein, 1995] P. Bernstein, C. Picard, V. Becker, S. Flament, and N. Beaudet. « Vortex Dynamics in Superconducting Microbridges with Low-vortex Pinning Forces and Superconducting Flux Flow Transistors ». *Journal of Applied Physics* 78.12 (1995), pp. 7358–7367 (cit. on p. 61).
- [Bernstein, 1997] P. Bernstein, C. Picard, M. Pannetier, Ph. Lecoeur, J. F. Hamet, T. D. Doan, et al. « Current–Voltage Characterization of the Vortex Motion in YBa<sub>2</sub>Cu<sub>3</sub>O<sub>7-δ</sub> Microbridges and the Implications on the Development of Superconducting Flux Flow Transistors ». *Journal of Applied Physics* 82.10 (1997), pp. 5030–5038 (cit. on pp. 61, 64).
- [Bezryadin, 2008] Alexey Bezryadin. « Quantum suppression of superconductivity in nanowires ». *Journal of Physics: Condensed Matter* 20.4 (2008), p. 043202 (cit. on p. 68).
- [Blatter, 1994] Gianni Blatter, Mikhail V Feigel'man, Vadim B Geshkenbein, Anatoly I Larkin, and Valerii M Vinokur. « Vortices in high-temperature superconductors ». *Reviews of modern physics* 66.4 (1994), p. 1125 (cit. on p. 59).
- [Bobroff, 2005] J. Bobroff. « Impuretés et systèmes corrélés. Des chaînes aux cuprates supraconducteurs ». *Annales de Physique* 30.1 (2005), pp. 1–151 (cit. on p. 25).
- [Bulaevskii, 2012] LN Bulaevskii, Matthias Graf, and Vladimir G Kogan. « Reply to “Comment on ‘Vortex-assisted photon counts and their magnetic field dependence in single-photon superconducting detectors’” ». *Physical Review B* 86.2 (2012), p. 026502 (cit. on p. 49).
- [Bulaevskii, 2011] LN Bulaevskii, MJ Graf, CD Batista, and VG Kogan. « Vortex-induced dissipation in narrow current-biased thin-film superconducting strips ». *Physical Review B* 83.14 (2011), p. 144526 (cit. on pp. 46, 48).
- [Carapella, 2016a] G Carapella, P Sabatino, C Barone, S Pagano, and M Gombos. « Current driven transition from Abrikosov-Josephson to Josephson-like vortex in mesoscopic lateral S/S'/S superconducting weak links ». *Scientific reports* 6.1 (2016), pp. 1–12 (cit. on p. 107).
- [Carapella, 2016b] G Carapella, P Sabatino, and M Gombos. « Mesoscopic lateral S/N/S weak links: Josephson effects and Josephson-like vortex flow ». *Superconductor Science and Technology* 30.2 (2016), p. 025018 (cit. on p. 107).
- [Charaev, 2022] I. Charaev, D. A. Bandurin, A. T. Bollinger, I. Y. Phinney, I. Drozdov, M. Colangelo, et al. arXiv:2208.05674 (2022). arXiv: [2208.05674](https://arxiv.org/abs/2208.05674) [[cond-mat](#), [physics:quant-ph](#)] (cit. on p. 33).
- [Charaev, 2023] Ilya Charaev, DA Bandurin, AT Bollinger, IY Phinney, I Drozdov, M Colangelo, et al. « Single-photon detection using high-temperature superconductors ». *Nature Nanotechnology* 18.4 (2023), pp. 343–349 (cit. on pp. 33, 35).
- [Charpentier, 2016] S Charpentier, R Arpaia, J Gaudet, D Matte, R Baghdadi, T Löfwander, et al. « Hot spot formation in electron-doped PCCO nanobridges ». *Physical Review B* 94.6 (2016), p. 060503 (cit. on p. 33).
- [Chen, 1989] C. H. Chen, A. E. White, K. T. Short, R. C. Dynes, J. M. Poate, D. C. Jacobson, et al. « Ion Beam Induced Damage and Superlattice Formation in Epitaxial YBa<sub>2</sub>Cu<sub>3</sub>O<sub>7-δ</sub> Thin Films ». *Applied Physics Letters* 54.12 (1989), pp. 1178–1180 (cit. on p. 25).
- [Chiles, 2022] Jeff Chiles, Ilya Charaev, Robert Lasenby, Masha Baryakhtar, Junwu Huang, Alexana Roshko, et al. « New Constraints on Dark Photon Dark Matter with Superconducting Nanowire Detectors in an Optical Haloscope ». *Physical Review Letters* 128.23 (2022), p. 231802 (cit. on p. 32).
- [Christen, 1993] DK Christen and R Thompson. « Current problems at high T c ». *Nature* 364.6433 (1993), pp. 98–99 (cit. on p. 59).

- [Clark, 1968] TD Clark. « Experiments on coupled Josephson junctions ». *Physics Letters A* 27.9 (1968), pp. 585–586 (cit. on p. 3).
- [Clarke, 2004] John Clarke and Alex I Braginski. *The SQUID Handbook: Fundamentals and Technology of SQUIDS and SQUID Systems*. Vol. 1. Wiley-Vch, 2004 (cit. on p. xii).
- [Connolly, 2008] MR Connolly, MV Milošević, SJ Bending, and T Tamegai. « Magneto-optical imaging of flux penetration into arrays of Bi 2 Sr 2 CaCu 2 O 8 microdisks ». *Physical Review B* 78.13 (2008), p. 132501 (cit. on p. 10).
- [Cooper, 1956] Leon N Cooper. « Bound electron pairs in a degenerate Fermi gas ». *Physical Review* 104.4 (1956), p. 1189 (cit. on p. 3).
- [Couëdo, 2020] François Couëdo, Paul Amari, Cheryl Feullet-Palma, Christian Ulysse, Yogesh Kumar Srivastava, Ranjan Singh, et al. « Dynamic Properties of High-Tc Superconducting Nano-Junctions Made with a Focused Helium Ion Beam ». *Scientific Reports* 10.1 (2020), p. 10256 (cit. on pp. 36, 37).
- [Couëdo, 2019] François Couëdo, Eliana Recoba Pawlowski, Julien Kermorvant, Juan Trastoy, Denis Crété, Yves Lemaître, et al. « High-  $T_c$  Superconducting Detector for Highly-Sensitive Microwave Magnetometry ». *Applied Physics Letters* 114.19 (2019), p. 192602 (cit. on p. 36).
- [Cristophe, 1997] Goupil Christophe. « Ph.D. thesis » (1997) (cit. on p. 63).
- [Curtz, 2010] N Curtz, E Koller, H Zbinden, M Decroux, and L Antognazza. « Patterning of Ultrathin YBCO Nanowires Using a New Focused-Ion-Beam Process ». *Supercond. Sci. Technol.* (2010), p. 7 (cit. on pp. 34, 37).
- [Cybart, 2015] Shane A Cybart, E Y Cho, T J Wong, Björn H Wehlin, Meng K Ma, Chuong Huynh, et al. « Nano Josephson superconducting tunnel junctions in YBa ». *Nature Nanotechnology* (2015), pp. 1–5 (cit. on p. 37).
- [Dauler, 2014] Eric A. Dauler, Matthew E. Grein, Andrew J. Kerman, Francesco Marsili, Shigehito Miki, Sae Woo Nam, et al. « Review of Superconducting Nanowire Single-Photon Detector System Design Options and Demonstrated Performance ». *Optical Engineering* 53.8 (2014), p. 081907 (cit. on p. 32).
- [De Gennes, 2018] Pierre-Gilles De Gennes. *Superconductivity of metals and alloys*. CRC press, 2018 (cit. on pp. 8, 82).
- [De Nivelles, 1993] M. J. M. E. De Nivelles, G. J. Gerritsma, and H. Rogalla. « Thermally Activated Coherent Vortex Motion in YBa 2 Cu 3 O 7 -  $\delta$  Thin Film Microbridges ». *Physical Review Letters* 70.10 (1993), pp. 1525–1528 (cit. on pp. 49, 54, 62).
- [Ding, 1996] H. Ding, M. R. Norman, J. C. Campuzano, M. Randeria, A. F. Bellman, T. Yokoya, et al. « Angle-resolved photoemission spectroscopy study of the superconducting gap anisotropy in Bi 2 Sr 2 Ca Cu 2 O 8 + x ». *Physical Review B* 54.14 (1996), R9678–R9681 (cit. on p. 25).
- [Dinsmore, 2008] R. C. Dinsmore, Myung-Ho Bae, and A. Bezryadin. « Fractional order Shapiro steps in superconducting nanowires ». *Applied Physics Letters* 93.19 (2008), p. 192505 (cit. on p. 70).
- [Dmitriev, 2005] VM Dmitriev, IV Zolocheskii, TV Salenkova, and EV Khristenko. « Critical currents, phase slip centers, and phase slip lines in superconducting films in the absence of external magnetic field ». *Low temperature physics* 31.2 (2005), pp. 127–136 (cit. on p. 54).
- [Dobrovolskiy, 2017] Oleksandr V Dobrovolskiy, Michael Huth, Valerij A Shklovskij, and Ruslan V Vovk. « Mobile fluxons as coherent probes of periodic pinning in superconductors ». *Scientific Reports* 7.1 (2017), p. 13740 (cit. on p. 107).
- [Dobrovolskiy, 2020a] OV Dobrovolskiy, E Begun, VM Bevez, R Sachser, and M Huth. « Upper frequency limits for vortex guiding and ratchet effects ». *Physical Review Applied* 13.2 (2020), p. 024012 (cit. on p. 107).
- [Dobrovolskiy, 2020b] OV Dobrovolskiy, D Yu Vodolazov, F Porrati, R Sachser, VM Bevez, M Yu Mikhailov, et al. « Ultra-fast vortex motion in a direct-write Nb-C superconductor ». *Nature communications* 11.1 (2020), p. 3291 (cit. on p. 54).
- [Early, 1994] EA Early, Richard L Steiner, Alan F Clark, and K Char. « Evidence for parallel junctions within high-T c grain-boundary junctions ». *Physical Review B* 50.13 (1994), p. 9409 (cit. on p. 69).
- [Ejrnaes, 2017a] M Ejrnaes, L Parlato, R Arpaia, T Bauch, F Lombardi, R Cristiano, et al. « Observation of Dark Pulses in 10 Nm Thick YBCO Nanostrips Presenting Hysteretic Current Voltage Characteristics ». *Superconductor Science and Technology* 30.12 (2017), 12LT02 (cit. on p. 35).

- [Ejrnaes, 2017b] M Ejrnaes, L Parlato, R Arpaia, T Bauch, F Lombardi, R Cristiano, et al. « Observation of dark pulses in 10 nm thick YBCO nanostrips presenting hysteretic current voltage characteristics ». *Superconductor Science and Technology* 30.12 (2017), 12LT02 (cit. on p. 33).
- [Eliashberg, 1970] G. M. Eliashberg. « Film Superconductivity Stimulated by a High-frequency Field ». *Pisma v Zh. Eksp. Teor. Fiz.* 11 (1970), p. 186 (cit. on p. 73).
- [Eliashberg, 1960] GM Eliashberg. « Interactions between electrons and lattice vibrations in a superconductor ». *Sov. Phys. JETP* 11.3 (1960), pp. 696–702 (cit. on p. 3).
- [Eliashberg, 1969] GM Eliashberg. « Nonstationary equations for superconductors with low concentration of paramagnetic impurities ». *SOV PHYS JETP* 28.6 (1969), pp. 1298–1302 (cit. on p. 15).
- [Esmaeil Zadeh, 2021] Iman Esmaeil Zadeh, J. Chang, Johannes W. N. Los, Samuel Gyger, Ali W. Elshaari, Stephan Steinhauer, et al. « Superconducting Nanowire Single-Photon Detectors: A Perspective on Evolution, State-of-the-Art, Future Developments, and Applications ». *Applied Physics Letters* 118.19 (2021), p. 190502 (cit. on p. xii).
- [Fedotov, 2002] Yu V Fedotov, SM Ryabchenko, EA Pashitski, AV Semenov, VI Vakaryuk, VM Pan, et al. « Magnetic-field and temperature dependence of the critical current in thin epitaxial films of the high-temperature superconductor YBa<sub>2</sub>Cu<sub>3</sub>O<sub>7- $\delta$</sub>  ». *Low Temperature Physics* 28.3 (2002), pp. 172–183 (cit. on p. 59).
- [Fiory, 1971] A. T. Fiory. « Quantum Interference Effects of a Moving Vortex Lattice in Al Films ». *Physical Review Letters* 27.8 (1971), pp. 501–503 (cit. on pp. 69, 95).
- [Fröhlich, 1950] Herbert Fröhlich. « Theory of the superconducting state. I. The ground state at the absolute zero of temperature ». *Physical Review* 79.5 (1950), p. 845 (cit. on p. 3).
- [Ginzburg, 1950] VL Ginzburg and LD Landau. « Theory of superconductivity ». *Zh. Eksp. Teor. Fiz.:(USSR)* 20.12 (1950) (cit. on pp. 2, 6).
- [Glatz, 2020] Andreas Glatz, Ivan A Sadovskyy, Ulrich Welp, Wai-Kwong Kwok, and George W Crabtree. « The quest for high critical current in applied high-temperature superconductors ». *Journal of Superconductivity and Novel Magnetism* 33 (2020), pp. 127–141 (cit. on p. 105).
- [Goltsman, 2001] G. N. Gol'tsman, O. Okunev, G. Chulkova, A. Lipatov, A. Semenov, K. Smirnov, et al. « Picosecond Superconducting Single-Photon Optical Detector ». *Applied Physics Letters* 79.6 (2001), pp. 705–707 (cit. on p. 32).
- [Golubev, 2001] Dmitri S Golubev and Andrei D Zaikin. « Quantum tunneling of the order parameter in superconducting nanowires ». *Physical Review B* 64.1 (2001), p. 014504 (cit. on p. 68).
- [Golubev, 2008] Dmitri S Golubev and Andrei D Zaikin. « Thermally activated phase slips in superconducting nanowires ». *Physical Review B* 78.14 (2008), p. 144502 (cit. on p. 68).
- [GORKOV, 1968] LP GOR'KOV. « Generalization of the Ginzburg-Landau equations for non-stationary problems in the case of alloys with paramagnetic impurities ». *Soviet Phys.-JETP* 27.2 (1968), pp. 328–334 (cit. on p. 15).
- [Gorkov, 1959] Lev Petrovich Gor'kov. « Microscopic derivation of the Ginzburg-Landau equations in the theory of superconductivity ». *Sov. Phys. JETP* 9.6 (1959), pp. 1364–1367 (cit. on p. 3).
- [Griessen, 1994] R. Griessen, Wen Hai-hu, A. J. J. Van Dalen, B. Dam, J. Rector, H. G. Schnack, et al. « Evidence for Mean Free Path Fluctuation Induced Pinning in YBa<sub>2</sub>Cu<sub>3</sub>O<sub>7</sub> and YBa<sub>2</sub>Cu<sub>4</sub>O<sub>8</sub> Films ». *Physical Review Letters* 72.12 (1994), pp. 1910–1913 (cit. on p. 58).
- [Grigorieva, 2007] IV Grigorieva, Walter Escoffier, VR Misko, BJ Baelus, FM Peeters, L Ya Vinnikov, et al. « Pinning-induced formation of vortex clusters and giant vortices in mesoscopic superconducting disks ». *Physical review letters* 99.14 (2007), p. 147003 (cit. on p. 10).
- [Grishakov, 2012] KS Grishakov, PN Degtyarenko, NN Degtyarenko, VF Elesin, and VS Kruglov. « Time dependent Ginzburg-Landau equations for modeling vortices dynamics in type-II superconductors with defects under a transport current ». *Physics Procedia* 36 (2012), pp. 1206–1210 (cit. on p. 103).
- [Gropp, 1996] William D. Gropp, Hans G. Kaper, Gary K. Leaf, David M. Levine, Mario Palumbo, and Valerii M. Vinokur. « Numerical Simulation of Vortex Dynamics in Type-II Superconductors ». *Journal of Computational Physics* 123.2 (1996), pp. 254–266 (cit. on p. 15).
- [Gubankov, 1976] VN Gubankov, VP Koshelets, and GA Ovsyannikov. « Coherent effects in superconducting bridges of variable thickness ». *Sov. Phys. JEPT* 44 (1976), pp. 181–186 (cit. on pp. 69, 73, 95).

- [Gupta, 1991] Raju P. Gupta and Michèle Gupta. « Order-Disorder-Driven Change in Hole Concentration and Superconductivity in  $\text{YBa}_2\text{Cu}_3\text{O}_{6.5}$  ». *Physical Review B* 44.6 (1991), pp. 2739–2746 (cit. on p. 34).
- [Gurevich, 2008] A Gurevich and VM Vinokur. « Size effects in the nonlinear resistance and flux creep in a virtual Berezinskii-Kosterlitz-Thouless state of superconducting films ». *Physical review letters* 100.22 (2008), p. 227007 (cit. on p. 46).
- [Gurevich, 2012] A Gurevich and VM Vinokur. « Comment on “Vortex-assisted photon counts and their magnetic field dependence in single-photon superconducting detectors” ». *Physical Review B* 86.2 (2012), p. 026501 (cit. on p. 49).
- [Gutierrez, 2009] J Gutierrez, AV Silhanek, Joris Van de Vondel, Werner Gillijns, and VV Moshchalkov. « Transition from turbulent to nearly laminar vortex flow in superconductors with periodic pinning ». *Physical Review B* 80.14 (2009), p. 140514 (cit. on p. 107).
- [Gutiérrez, 2007] J Gutiérrez, T Puig, and X Obradors. « Anisotropy and strength of vortex pinning centers in  $\text{YBa}_2\text{Cu}_3\text{O}_{7-x}$  coated conductors ». *Applied physics letters* 90.16 (2007) (cit. on p. 59).
- [Haddon, 2022] CWW Haddon, AI Blair, F Schoofs, and DP Hampshire. « Computational Simulations Using Time-Dependent Ginzburg–Landau Theory for Nb–Ti-Like Microstructures ». *IEEE Transactions on Applied Superconductivity* 32.4 (2022), pp. 1–5 (cit. on p. 103).
- [Hadfield, 2009] Robert H. Hadfield. « Single-Photon Detectors for Optical Quantum Information Applications ». *Nature Photonics* 3.12 (2009), pp. 696–705 (cit. on p. 32).
- [Halperin, 1979] BI Halperin and David R Nelson. « Resistive transition in superconducting films ». *Journal of low temperature physics* 36 (1979), pp. 599–616 (cit. on pp. 47, 75).
- [Hilgenkamp, 2002] Hans Hilgenkamp and Jochen Mannhart. « Grain boundaries in high- $T_c$  superconductors ». *Reviews of Modern Physics* 74.2 (2002), p. 485 (cit. on p. 29).
- [Hilgenkamp, 2003] Hans Hilgenkamp, Henk-Jan H Smilde, Dave H A Blank, Guus Rijnders, Horst Rogalla, John R Kirtley, et al. « Ordering and manipulation of the magnetic moments in large-scale superconducting p-loop arrays ». 422 (2003), p. 4 (cit. on pp. 25, 26).
- [httpwwwscontelru, 2022] <http://www.scontel.ru>, <https://www.idquantique.com/>, <https://singlequantum.com/>, <https://www.qdusa.com/>, and <http://www.sconphoton.com> (2022) (cit. on p. 32).
- [Hwa, 1993] Terence Hwa, Pierre Le Doussal, David R Nelson, and Valerii M Vinokur. « Flux pinning and forced vortex entanglement by splayed columnar defects ». *Physical review letters* 71.21 (1993), p. 3545 (cit. on p. 59).
- [Ijaduola, 2006] Anota O Ijaduola, James R Thompson, Roeland Feenstra, David K Christen, Albert Agcaoili Gapud, and X Song. « Critical currents of ex situ  $\text{YBa}_2\text{Cu}_3\text{O}_{7-\delta}$  thin films on rolling assisted biaxially textured substrates: Thickness, field, and temperature dependencies ». *Physical Review B* 73.13 (2006), p. 134502 (cit. on p. 59).
- [Jaeger, 2002] Richard C. Jaeger. 2nd ed. Modular Series on Solid State Devices v. 5. Upper Saddle River, N.J: Prentice Hall, 2002 (cit. on p. 37).
- [Jaque, 2002] Daniel Jaque, EM González, José Ignacio Martín, José Virgilio Anguita, and JL Vicent. « Anisotropic pinning enhancement in Nb films with arrays of submicrometric Ni lines ». *Applied Physics Letters* 81.15 (2002), pp. 2851–2853 (cit. on p. 107).
- [Johansson, 2009] Jesper Johansson, Karin Cedergren, Thilo Bauch, and Floriana Lombardi. « Properties of inductance and magnetic penetration depth in (103)-oriented  $\text{YBa}_2\text{Cu}_3\text{O}_{7-\delta}$  thin films ». *Physical Review B* 79.21 (2009), p. 214513 (cit. on p. 48).
- [Josephson, 1962] Brian David Josephson. « Possible new effects in superconductive tunnelling ». *Physics letters* 1.7 (1962), pp. 251–253 (cit. on p. 3).
- [Al-Khawaja, 2005] Sameer Al-Khawaja. « Chaotic dynamics of underdamped Josephson junctions in a ratchet potential driven by a quasiperiodic external modulation ». *Physica C: Superconductivity and its applications* 420.1-2 (2005), pp. 30–36 (cit. on p. 101).
- [Kimmel, 2017] Gregory Kimmel, Ivan A Sadovskyy, and Andreas Glatz. « In silico optimization of critical currents in superconductors ». *Physical Review E* 96.1 (2017), p. 013318 (cit. on p. 105).
- [Kimmel, 2019] Gregory J Kimmel, Andreas Glatz, Valerii M Vinokur, and Ivan A Sadovskyy. « Edge effect pinning in mesoscopic superconducting strips with non-uniform distribution of defects ». *Scientific reports* 9.1 (2019), p. 211 (cit. on p. 104).

- [Klimenko, 2013] A Klimenko and O Romaskevich. « Asymptotic properties of Arnold tongues and Josephson effect ». *arXiv preprint arXiv:1305.6746* (2013) (cit. on p. 95).
- [Korneev, 2012] A. Korneev, Yu. Korneeva, I. Florya, B. Voronov, and G. Goltsman. « NbN Nanowire Superconducting Single-Photon Detector for Mid-Infrared ». *Physics Procedia* 36 (2012), pp. 72–76 (cit. on p. 32).
- [Korz, 2020] Boris Korzh, Qing-Yuan Zhao, Jason P. Allmaras, Simone Frasca, Travis M. Autry, Eric A. Bersin, et al. « Demonstration of Sub-3 Ps Temporal Resolution with a Superconducting Nanowire Single-Photon Detector ». *Nature Photonics* 14.4 (2020), pp. 250–255 (cit. on p. 32).
- [Koshelev, 2016] AE Koshelev, IA Sadovskyy, CL Phillips, and A Glatz. « Optimization of vortex pinning by nanoparticles using simulations of the time-dependent Ginzburg-Landau model ». *Physical Review B* 93.6 (2016), p. 060508 (cit. on p. 103).
- [Kramer, 1973] Edward J Kramer. « Scaling laws for flux pinning in hard superconductors ». *Journal of applied physics* 44.3 (1973), pp. 1360–1370 (cit. on p. 64).
- [Kramer, 1977] L Kramer and A Baratoff. « Lossless and dissipative current-carrying states in quasi-one-dimensional superconductors ». *Physical Review Letters* 38.9 (1977), p. 518 (cit. on p. 54).
- [Kramer, 1978] Lorenz Kramer and Richard J Watts-Tobin. « Theory of dissipative current-carrying states in superconducting filaments ». *Physical Review Letters* 40.15 (1978), p. 1041 (cit. on pp. 17, 54).
- [Krishana, 1995] K. Krishana, J. M. Harris, and N. P. Ong. « Quasiparticle Mean Free Path in YBa<sub>2</sub>Cu<sub>3</sub>O<sub>7</sub> Measured by the Thermal Hall Conductivity ». *Phys. Rev. Lett.* 75.19 (1995), pp. 3529–3532 (cit. on p. 26).
- [Kunchur, 2019] Milind N. Kunchur. « Evaluating Superconductors through Current Induced Depairing ». *Condensed Matter* 4.2 (2019), p. 54 (cit. on p. 54).
- [Kuznetsov, 2017] A V Kuznetsov, I I Sannikov, and A A Ivanov. « Temperature Dependence of Critical Current in YBa<sub>2</sub>Cu<sub>3</sub>O<sub>7- $\delta$</sub>  Films ». *Journal of Physics: Conference Series* 941 (2017), p. 012071 (cit. on p. 59).
- [Kwok, 2016] Wai-Kwong Kwok, Ulrich Welp, Andreas Glatz, Alexei E Koshelev, Karen J Kihlstrom, and George W Crabtree. « Vortices in high-performance high-temperature superconductors ». *Reports on Progress in Physics* 79.11 (2016), p. 116501 (cit. on p. 81).
- [Lam, 2019] Simon KH Lam, Avi Bendavid, and Jia Du. « Hot spot formation in focused-ion-beam-fabricated YBa<sub>2</sub>Cu<sub>3</sub>O<sub>7-x</sub> nanobridges with high critical current densities ». *Nanotechnology* 30.32 (2019), p. 325301 (cit. on p. 34).
- [Landau, 1937] Lev Davidovich Landau. « On the theory of phase transitions ». *Zh. Eksp. Teor. Fiz.* 11 (1937), p. 19 (cit. on p. 6).
- [Larkin, 1975] AI Larkin and YUN Ovchinnikov. « Nonlinear conductivity of superconductors in the mixed state ». *Sov. Phys. JETP* 41.5 (1975), pp. 960–965 (cit. on p. 54).
- [Larsson, 2000] Peter Larsson, Bengt Nilsson, and ZG Ivanov. « Fabrication and transport measurements of YBa<sub>2</sub>Cu<sub>3</sub>O<sub>7-x</sub> nanostructures ». *Journal of Vacuum Science & Technology B: Microelectronics and Nanometer Structures Processing, Measurement, and Phenomena* 18.1 (2000), pp. 25–31 (cit. on p. 33).
- [Lau, 2001] Chun Ning Lau, N Markovic, M Bockrath, A Bezryadin, and M Tinkham. « Quantum phase slips in superconducting nanowires ». *Physical review letters* 87.21 (2001), p. 217003 (cit. on p. 68).
- [Lehtinen, 2012] JS Lehtinen, Timo Sajavaara, K Yu Arutyunov, M Yu Presnjakov, and AL Vasiliev. « Evidence of quantum phase slip effect in titanium nanowires ». *Physical Review B* 85.9 (2012), p. 094508 (cit. on p. 68).
- [Lesueur, 1993] J Lesueur, L Dumoulin, S Quillet, and J Radcliffe. « Ion-beam induced metal insulator transition in YBCO films ». *Journal of alloys and compounds* 195 (1993), pp. 527–530 (cit. on pp. 25, 36).
- [Lesueur, 1990] J Lesueur, P Nedellec, H Bernas, JP Burger, and L Dumoulin. « Depairing-like variation of T<sub>c</sub> in YBa<sub>2</sub>Cu<sub>3</sub>O<sub>7- $\delta$</sub>  ». *Physica C: Superconductivity* 167.1-2 (1990), pp. 1–5 (cit. on p. 34).
- [Lesueur, 2007] J. Lesueur, N. Bergeal, M. Sirena, X. Grison, G. Faini, M. Aprili, et al. « High Tc Josephson Nanojunctions Made by Ion Irradiation: Characteristics and Reproducibility ». *IEEE Trans. Appl. Supercond.* 17.2 (2007), pp. 963–966 (cit. on p. 36).

- [Likharev, 1979] KK Likharev. « Superconducting weak links ». *Reviews of Modern Physics* 51.1 (1979), p. 101 (cit. on p. 68).
- [Likharev, 1975] KK Likharev and LA Iakobson. « Steady-state properties of superconducting bridges ». *Zhurnal Tekhnicheskoi Fiziki* 45 (1975), pp. 1503–1509 (cit. on pp. 67, 69, 95).
- [Lindgren, 1999] M Lindgren, M Currie, C Williams, TY Hsiang, PM Fauchet, Roman Sobolewski, et al. « Intrinsic picosecond response times of Y–Ba–Cu–O superconducting photodetectors ». *Applied Physics Letters* 74.6 (1999), pp. 853–855 (cit. on p. 33).
- [London, 1935] Fritz London and Heinz London. « The electromagnetic equations of the supraconductor ». *Proceedings of the Royal Society of London. Series A-Mathematical and Physical Sciences* 149.866 (1935), pp. 71–88 (cit. on pp. 2, 4).
- [Lyatti, 2018] M. Lyatti, M. A. Wolff, A. Savenko, M. Kruth, S. Ferrari, U. Poppe, et al. « Experimental Evidence for Hotspot and Phase-Slip Mechanisms of Voltage Switching in Ultrathin YBa<sub>2</sub>Cu<sub>3</sub>O<sub>7-x</sub> Nanowires ». *Physical Review B* 98.5 (2018), p. 054505 (cit. on p. 33).
- [Lyatti, 2016] Matvey Lyatti, A Savenko, and U Poppe. « Ultra-thin YBa<sub>2</sub>Cu<sub>3</sub>O<sub>7-x</sub> films with high critical current density ». *Superconductor science and technology* 29.6 (2016), p. 065017 (cit. on p. 34).
- [Maeda, 1988] Hiroshi Maeda, Yoshiaki Tanaka, Masao Fukutomi, and Toshihisa Asano. « A new high-Tc oxide superconductor without a rare earth element ». *Japanese Journal of Applied Physics* 27.2A (1988), p. L209 (cit. on p. 3).
- [Maggio-Aprile, 1997] Ivan Maggio-Aprile, Christophe Renner, Andreas Erb, Eric Walker, and Øystein Fischer. « Critical currents approaching the depairing limit at a twin boundary in YBa<sub>2</sub>Cu<sub>3</sub>O<sub>7-δ</sub> ». *Nature* 390.6659 (1997), pp. 487–490 (cit. on pp. 91, 96).
- [Mannhart, 1996] Jochen Mannhart, Hans Hilgenkamp, B Mayer, Ch Gerber, John R Kirtley, Kathryn A Moler, et al. « Generation of Magnetic Flux by Single Grain Boundaries of YBa<sub>2</sub>Cu<sub>3</sub>O<sub>7-x</sub> ». *Physical review letters* 77.13 (1996), p. 2782 (cit. on p. 96).
- [Marsili, 2013] F Marsili. « Detecting Single Infrared Photons with 93% System Efficiency ». *NATURE PHOTONICS* 7 (2013), p. 5 (cit. on p. 32).
- [Marsili, 2012] Francesco Marsili, Francesco Bellei, Faraz Najafi, Andrew E. Dane, Eric A. Dauler, Richard J. Molnar, et al. « Efficient Single Photon Detection from 500 Nm to 5 Mm Wavelength ». *Nano Letters* 12.9 (2012), pp. 4799–4804 (cit. on p. 32).
- [Martinoli, 1978] Piero Martinoli. « Static and dynamic interaction of superconducting vortices with a periodic pinning potential ». *Physical Review B* 17.3 (1978), pp. 1175–1194 (cit. on p. 95).
- [Matveev, 2002] KA Matveev, AI Larkin, and LI Glazman. « Persistent current in superconducting nanorings ». *Physical review letters* 89.9 (2002), p. 096802 (cit. on p. 68).
- [Maxwell, 1950] Emanuel Maxwell. « Isotope effect in the superconductivity of mercury ». *Physical Review* 78.4 (1950), p. 477 (cit. on p. 3).
- [McCumber, 1968] DE McCumber. « Effect of ac impedance on dc voltage-current characteristics of superconductor weak-link junctions ». *Journal of Applied Physics* 39.7 (1968), pp. 3113–3118 (cit. on p. 94).
- [Meissner, 1933] Walther Meissner and Robert Ochsenfeld. « Ein neuer effekt bei eintritt der supraleitfähigkeit ». *Naturwissenschaften* 21.44 (1933), pp. 787–788 (cit. on p. 2).
- [Misko, 2006] Vyacheslav R Misko, Sergey Savel'ev, Alexander L Rakhmanov, and Franco Nori. « Nonuniform self-organized dynamical states in superconductors with periodic pinning ». *Physical review letters* 96.12 (2006), p. 127004 (cit. on p. 107).
- [Miura, 2011] M. Miura, B. Maiorov, S. A. Baily, N. Haberkorn, J. O. Willis, K. Marken, et al. « Mixed Pinning Landscape in Nanoparticle-Introduced YGdBa<sub>2</sub>Cu<sub>3</sub>O<sub>y</sub> Films Grown by Metal Organic Deposition ». *Physical Review B* 83.18 (2011), p. 184519 (cit. on p. 59).
- [Mooij, 2006] JE Mooij and Yu V Nazarov. « Superconducting nanowires as quantum phase-slip junctions ». *Nature Physics* 2.3 (2006), pp. 169–172 (cit. on p. 68).
- [Nahum, 1991] M. Nahum, S. Verghese, P. L. Richards, and K. Char. « Thermal Boundary Resistance for YBa<sub>2</sub>Cu<sub>3</sub>O<sub>7-δ</sub> Films ». *Applied Physics Letters* 59.16 (1991), pp. 2034–2036 (cit. on p. 56).
- [Natarajan, 2012] Chandra M Natarajan, Michael G Tanner, and Robert H Hadfield. « Superconducting nanowire single-photon detectors: physics and applications ». *Superconductor science and technology* 25.6 (2012), p. 063001 (cit. on p. 32).

- [Nawaz, 2013a] Shahid Nawaz, Riccardo Arpaia, Thilo Bauch, and Floriana Lombardi. « Approaching the theoretical depairing current in YBa<sub>2</sub>Cu<sub>3</sub>O<sub>7-x</sub> nanowires ». *Physica C: Superconductivity* 495 (2013), pp. 33–38 (cit. on p. 33).
- [Nawaz, 2013b] Shahid Nawaz, Riccardo Arpaia, Floriana Lombardi, and Thilo Bauch. « Microwave Response of Superconducting Y Ba<sub>2</sub> Cu<sub>3</sub> O<sub>7-δ</sub> Nanowire Bridges Sustaining the Critical Depairing Current: Evidence of Josephson-like Behavior ». *Physical review letters* 110.16 (2013), p. 167004 (cit. on pp. 69, 95).
- [Nelson, 1993] David R Nelson and VM Vinokur. « Boson localization and correlated pinning of superconducting vortex arrays ». *Physical Review B* 48.17 (1993), p. 13060 (cit. on p. 59).
- [Ning, 2010] YX Ning, CL Song, YL Wang, Xi Chen, JF Jia, QK Xue, et al. « Vortex properties of two-dimensional superconducting Pb films ». *Journal of Physics: Condensed Matter* 22.6 (2010), p. 065701 (cit. on p. 10).
- [OMahony, 2022] Shane M. O’Mahony, Wangping Ren, Weijiong Chen, Yi Xue Chong, Xiaolong Liu, H. Eisaki, et al. « On the electron pairing mechanism of copper-oxide high temperature superconductivity ». *Proceedings of the National Academy of Sciences* 119.37 (2022), e2207449119 (cit. on p. 25).
- [Olson, 1998] CJ Olson, C Reichhardt, and Franco Nori. « Fractal networks, braiding channels, and voltage noise in intermittently flowing rivers of quantized magnetic flux ». *Physical review letters* 80.10 (1998), p. 2197 (cit. on p. 54).
- [Onnes, 1911] H Kamerlingh Onnes. « The superconductivity of mercury ». *Comm. Phys. Lab. Univ. Leiden* 122 (1911), p. 124 (cit. on p. 2).
- [Oreg, 1999] Yuval Oreg and Alexander M Finkel’stein. « Suppression of T<sub>c</sub> in superconducting amorphous wires ». *Physical review letters* 83.1 (1999), p. 191 (cit. on p. 68).
- [Ouanani, 2016a] S Ouanani, J Kermorvant, C Ulysse, M Malnou, Y Lemaitre, B Marcilhac, et al. « High-Tc Superconducting Quantum Interference Filters (SQIFs) Made by Ion Irradiation ». *Superconductor Science and Technology* 29.9 (2016), p. 094002 (cit. on p. 36).
- [Ouanani, 2016b] S Ouanani, J Kermorvant, C Ulysse, M Malnou, Y Lemaitre, B Marcilhac, et al. « High-Tc superconducting quantum interference filters (SQIFs) made by ion irradiation ». *Superconductor science and technology* 29.9 (2016), p. 094002 (cit. on p. 48).
- [Païdassi, 1979] S. Païdassi. « Superconductivity at 23 K in A15 Nb<sub>3</sub> (Ge,Si) prepared by CVD ». *Journal of Applied Physics* 50.5 (1979), pp. 3556–3559 (cit. on p. 19).
- [Pannetier, 2000] M. Pannetier, Ph. Lecoœur, P. Bernstein, T. D. Doan, and J. F. Hamet. « Characterization of Pinning and Vortex Motion in Thin Superconducting Microbridges ». *Phys. Rev. B* 62.22 (2000), pp. 15162–15171 (cit. on p. 61).
- [Papari, 2014] G Papari, F Carillo, Daniela Stornaiuolo, Davide Massarotti, L Longobardi, F Beltram, et al. « Dynamics of vortex matter in YBCO sub-micron bridges ». *Physica C: Superconductivity and its Applications* 506 (2014), pp. 188–194 (cit. on p. 34).
- [Papari, 2012] G Papari, Franco Carillo, Daniela Stornaiuolo, L Longobardi, F Beltram, and Francesco Tafuri. « High critical current density and scaling of phase-slip processes in YBaCuO nanowires ». *Superconductor Science and Technology* 25.3 (2012), p. 035011 (cit. on p. 34).
- [Pawlowski, 2018] Eliana Recoba Pawlowski, Julien Kermorvant, Denis Crété, Yves Lemaitre, Bruno Marcilhac, Christian Ulysse, et al. « Static and radio frequency magnetic response of high T<sub>c</sub> superconducting quantum interference filters made by ion irradiation ». *Superconductor Science and Technology* 31.9 (2018), pp. 095005–11 (cit. on p. 36).
- [Pearl, 1964] J. Pearl. « Current distribution in superconducting films carrying fluxoids ». *Appl. Phys. Lett.* 5.4 (1964), pp. 65–66 (cit. on p. 96).
- [Plain, 2002] J Plain, T Puig, F Sandiumenge, X Obradors, and J Rabier. « Microstructural influence on critical currents and irreversibility line in melt-textured YBa<sub>2</sub> Cu<sub>3</sub> O<sub>7-x</sub> reannealed at high oxygen pressure ». *Physical Review B* 65.10 (2002), p. 104526 (cit. on pp. 58, 59).
- [Polat, 2011] Ö Polat, JW Sinclair, YL Zuev, JR Thompson, DK Christen, SW Cook, et al. « Thickness dependence of magnetic relaxation and E-J characteristics in superconducting (Gd-Y)-Ba-Cu-O films with strong vortex pinning ». *Physical review B* 84.2 (2011), p. 024519 (cit. on p. 59).
- [Protte, 2022] Maximilian Protte, Varun B Verma, Jan Philipp Höpker, Richard P Mirin, Sae Woo Nam, and Tim J Bartley. « Laser-lithographically written micron-wide superconducting nanowire single-photon detectors ». *Superconductor Science and Technology* 35.5 (2022), p. 055005 (cit. on p. 33).

- [Qiu, 2008] Chunyin Qiu and Tiezheng Qian. « Numerical study of the phase slip in two-dimensional superconducting strips ». *Physical Review B* 77.17 (2008), p. 174517 (cit. on p. 48).
- [Rauch, 1993] W Rauch, E Gornik, G Sölkner, AA Valenzuela, F Fox, and H Behner. « Microwave properties of YBa<sub>2</sub>Cu<sub>3</sub>O<sub>7-x</sub> thin films studied with coplanar transmission line resonators ». *Journal of applied Physics* 73.4 (1993), pp. 1866–1872 (cit. on p. 48).
- [Ray, 2015] Pia Jensen Ray. « Structural Investigation of La(2-x)Sr(x)CuO(4+y) » (2015) (cit. on p. 20).
- [Reichhardt, 1997] C Reichhardt, CJ Olson, and Franco Nori. « Dynamic phases of vortices in superconductors with periodic pinning ». *Physical Review Letters* 78.13 (1997), p. 2648 (cit. on p. 107).
- [Reichhardt, 2000] Charles Reichhardt, Richard T Scalettar, Gergely T Zimányi, and Niels Grønbech-Jensen. « Phase-locking of vortex lattices interacting with periodic pinning ». *Physical Review B* 61.18 (2000), R11914 (cit. on p. 95).
- [Repaci, 1996] JM Repaci, C Kwon, Qi Li, Xiuguang Jiang, T Venkatesan, RE Glover III, et al. « Absence of a Kosterlitz-Thouless transition in ultrathin Y Ba 2 Cu 3 O 7-  $\delta$  films ». *Physical Review B* 54.14 (1996), R9674 (cit. on p. 75).
- [Romano, 2018] P Romano, M Riccio, A Guarino, N Martucciello, G Grimaldi, A Leo, et al. « Electron doped superconducting cuprates for photon detectors ». *Measurement* 122 (2018), pp. 502–506 (cit. on p. 33).
- [Rosenblum, 2003] Michael Rosenblum and Arkady Pikovsky. « Synchronization: from pendulum clocks to chaotic lasers and chemical oscillators ». *Contemporary Physics* 44.5 (2003), pp. 401–416 (cit. on p. 95).
- [Rudenko, 1991] EM Rudenko, IV Korotash, IP Nevirkovets, Yu M Boguslavskii, PA Zhukov, and AG Sivakov. « Stimulation of critical current and vortices movement in wide microbridges based on epitaxial YBCO films ». *Superconductor Science and Technology* 4.1 (1991), p. 1 (cit. on p. 73).
- [Rullier-Albenque, 2001] F. Rullier-Albenque, H. Alloul, and R. Tourbot. « Disorder and Transport in Cuprates: Weak Localization and Magnetic Contributions ». *Phys. Rev. Lett.* 87.15 (2001), p. 157001 (cit. on p. 25).
- [Sadovskyy, 2015] I. A. Sadovskyy, A. E. Koshelev, C. L. Phillips, D. A. Karpeyev, and A. Glatz. « Stable Large-Scale Solver for Ginzburg-Landau Equations for Superconductors ». *Journal of Computational Physics* 294 (2015), pp. 639–654 (cit. on p. 81).
- [Sadovskyy, 2016a] IA Sadovskyy, AE Koshelev, Andreas Glatz, Volkan Ortalan, MW Rupich, and Maxime Leroux. « Simulation of the vortex dynamics in a real pinning landscape of YBa<sub>2</sub>Cu<sub>3</sub>O<sub>7- $\delta$</sub>  coated conductors ». *Physical Review Applied* 5.1 (2016), p. 014011 (cit. on p. 105).
- [Sadovskyy, 2017] IA Sadovskyy, YL Wang, Z-L Xiao, W-K Kwok, and Andreas Glatz. « Effect of hexagonal patterned arrays and defect geometry on the critical current of superconducting films ». *Physical Review B* 95.7 (2017), p. 075303 (cit. on p. 105).
- [Sadovskyy, 2016b] Ivan A Sadovskyy, Ying Jia, Maxime Leroux, Jihwan Kwon, Hefei Hu, Lei Fang, et al. « Toward superconducting critical current by design ». *Advanced Materials* 28.23 (2016), pp. 4593–4600 (cit. on p. 105).
- [Sadovskyy, 2019] Ivan A Sadovskyy, Alexei E Koshelev, Wai-Kwong Kwok, Ulrich Welp, and Andreas Glatz. « Targeted evolution of pinning landscapes for large superconducting critical currents ». *Proceedings of the National Academy of Sciences* 116.21 (2019), pp. 10291–10296 (cit. on p. 105).
- [Santavica, 2018] Daniel F Santavica. « Prospects for faster, higher-temperature superconducting nanowire single-photon detectors ». *Superconductor Science and Technology* 31.4 (2018), p. 040502 (cit. on p. 33).
- [Schmid, 1966] Albert Schmid. « A time dependent Ginzburg-Landau equation and its application to the problem of resistivity in the mixed state ». *Physik der kondensierten Materie* 5.4 (1966), pp. 302–317 (cit. on p. 15).
- [Schneider, 1993] J Schneider, H Kohlstedt, and R Wördenweber. « Nanobridges of optimized YBa<sub>2</sub>Cu<sub>3</sub>O<sub>7</sub> thin films for superconducting flux-flow type devices ». *Applied physics letters* 63.17 (1993), pp. 2426–2428 (cit. on p. 95).
- [Segawa, 2003] Kouji Segawa and Yoichi Ando. « Transport Properties of Untwinned YBa<sub>2</sub>Cu<sub>3</sub>O<sub>y</sub> Single Crystals and the Origin of the 60-K Plateau ». *Journal of Low Temperature Physics* 131.5 (2003), pp. 821–830 (cit. on p. 25).

- [Senoussi, 1988] S Senoussi, M Osséna, G Collin, and IA Campbell. « Exponential H and T decay of the critical current density in YBa<sub>2</sub>Cu<sub>3</sub>O<sub>7-δ</sub> single crystals ». *Physical Review B* 37.16 (1988), p. 9792 (cit. on p. 59).
- [Sergeev, 1994] A. Sergeev, A. Semenov, V. Trifonov, B. Karasik, G. Gol'tsman, and E. Gershenzon. « Heat Transfer in YBaCuO Thin Film/Sapphire Substrate System ». *Journal of Superconductivity* 7.2 (1994), pp. 341–344 (cit. on p. 56).
- [Sharafiev, 2016] A Sharafiev, M Malnou, C Feuillet-Palma, C Ulysse, P Febvre, J Lesueur, et al. « Josephson Oscillation Linewidth of Ion-Irradiated YBa<sub>2</sub>Cu<sub>3</sub>O<sub>7</sub> Junctions ». *Superconductor Science and Technology* 29.7 (2016), p. 074001 (cit. on p. 36).
- [Shibata, 2016] H Shibata, H Takesue, T Honjo, T Akazaki, and Y Tokura. « Single-Photon Detection Using Magnesium Diboride Superconducting Nanowires ». *Appl. Phys. Lett.* (2016), p. 4 (cit. on p. 35).
- [Shibata, 2017] Hiroyuki Shibata, Naoto Kirigane, Kentaro Fukao, Daisuke Sakai, Shinichi Karimoto, and Hideki Yamamoto. « Photoresponse of a La<sub>1.85</sub>Sr<sub>0.15</sub>CuO<sub>4</sub> nanostrip ». *Superconductor Science and Technology* 30.7 (2017), p. 074001 (cit. on p. 33).
- [Silhanek, 2010a] AV Silhanek, RGB Kramer, Joris Van de Vondel, VV Moshchalkov, MV Milošević, GR Berdiyrov, et al. « Freezing vortex rivers ». *Physica C: Superconductivity* 470.19 (2010), pp. 726–729 (cit. on p. 54).
- [Silhanek, 2010b] AV Silhanek, MV Milošević, RBG Kramer, GR Berdiyrov, Joris Van de Vondel, RF Luccas, et al. « Formation of stripelike flux patterns obtained by freezing kinematic vortices in a superconducting Pb film ». *Physical review letters* 104.1 (2010), p. 017001 (cit. on p. 55).
- [Sirena, 2007a] M. Sirena, N. Bergeal, J. Lesueur, G. Faini, R. Bernard, J. Briatico, et al. « Study and Optimization of Ion-Irradiated High Tc Josephson Junctions by Monte Carlo Simulations ». *Journal of Applied Physics* 101.12 (2007), p. 123925 (cit. on p. 36).
- [Sirena, 2007b] M. Sirena, X. Fabrèges, N. Bergeal, J. Lesueur, G. Faini, R. Bernard, et al. « Improving the IcRn Product and the Reproducibility of High Tc Josephson Junctions Made by Ion Irradiation ». *Applied Physics Letters* 91.26 (2007), p. 262508 (cit. on p. 36).
- [Sivakov, 2003] A. G. Sivakov, A. M. Glukhov, A. N. Omelyanchouk, Y. Koval, P. Müller, and A. V. Ustinov. « Josephson Behavior of Phase-Slip Lines in Wide Superconducting Strips ». *Physical Review Letters* 91.26 (2003), p. 267001 (cit. on p. 95).
- [Skocpol, 1974] W. J. Skocpol, M. R. Beasley, and M. Tinkham. « Self-heating Hotspots in Superconducting Thin-film Microbridges ». *Journal of Applied Physics* 45.9 (1974), pp. 4054–4066 (cit. on p. 55).
- [Smirnov, 2018] Konstantin Smirnov, Alexander Divochiy, Yury Vakhtomin, Pavel Morozov, Philipp Zolotov, Andrey Antipov, et al. « NbN Single-Photon Detectors with Saturated Dependence of Quantum Efficiency ». *Superconductor Science and Technology* 31.3 (2018), p. 035011 (cit. on p. 32).
- [Sobolewski, 1998] Roman Sobolewski. « Ultrafast Dynamics of Nonequilibrium Quasi-Particles in High-Temperature Superconductors ». *SPIE's International Symposium*. Ed. by Davor Pavuna and Ivan Bozovic. 1998, p. 480 (cit. on p. 33).
- [Sonin, 1989] EB Sonin and AK Tagantsev. « Electrodynamics of the Josephson medium in high-Tc superconductors ». *Physics Letters A* 140.3 (1989), pp. 127–132 (cit. on p. 79).
- [Soroka, 2007] Oleksiy K Soroka, Valerij A Shklovskij, and Michael Huth. « Guiding of vortices under competing isotropic and anisotropic pinning conditions: Theory and experiment ». *Physical Review B* 76.1 (2007), p. 014504 (cit. on p. 107).
- [Souto, 2021] Vinícius S Souto, Elwis CS Duarte, Edson Sardella, and Rafael Zadorosny. « Kinematic vortices induced by defects in gapless superconductors ». *Physics Letters A* 419 (2021), p. 127742 (cit. on p. 54).
- [Stewart, 1968] WC Stewart. « Current-voltage characteristics of Josephson junctions ». *Applied physics letters* 12.8 (1968), pp. 277–280 (cit. on p. 94).
- [Stolyarov, 2018] Vasily S Stolyarov, Tristan Cren, Christophe Brun, Igor A Golovchanskiy, Olga V Skryabina, Daniil I Kasatonov, et al. « Expansion of a superconducting vortex core into a diffusive metal ». *Nature communications* 9.1 (2018), p. 2277 (cit. on p. 10).
- [Tafari, 2006] Francesco Tafuri, JR Kirtley, D Born, Daniela Stornaiuolo, PG Medaglia, Pasquale Orgiani, et al. « Dissipation in ultra-thin current-carrying superconducting bridges; evidence for quantum tunneling of Pearl vortices ». *Europhysics letters* 73.6 (2006), p. 948 (cit. on pp. 75, 76).

- [Tang, 2000] W H Tang, C Y Ng, C Y Yau, and J Gao. « Thickness Dependence of Superconductivity for  $\text{YBa}_2\text{Cu}_3\text{O}_y$  Ultra-Thin Films ». *Supercond. Sci. Technol.* 13.5 (2000), pp. 580–583 (cit. on p. 26).
- [Tinkham, 2002] M Tinkham and CN Lau. « Quantum limit to phase coherence in thin superconducting wires ». *Applied physics letters* 80.16 (2002), pp. 2946–2948 (cit. on p. 68).
- [Trabaldo, 2019] E Trabaldo, R Arpaia, M Arzeo, E Andersson, D Golubev, F Lombardi, et al. « Transport and noise properties of YBCO nanowire based nanoSQUIDs ». *Superconductor Science and Technology* 32.7 (2019), p. 073001 (cit. on p. 33).
- [Tsuei, 2000] C. C. Tsuei and J. R. Kirtley. « Pairing symmetry in cuprate superconductors ». *Reviews of Modern Physics* 72.4 (2000), pp. 969–1016 (cit. on p. 25).
- [Tsuei, 1994] C. C. Tsuei, J. R. Kirtley, C. C. Chi, Lock See Yu-Jahnes, A. Gupta, T. Shaw, et al. « Pairing Symmetry and Flux Quantization in a Tricrystal Superconducting Ring of  $\text{YBa}_2\text{Cu}_3\text{O}_{7-\delta}$  ». *Physical Review Letters* 73.4 (1994), pp. 593–596 (cit. on pp. 25, 26).
- [Ustavshnikov, 2022] SS Ustavshnikov, M Yu Levichev, I Yu Pashen'kin, NS Gusev, SA Gusev, and D Yu Vodolazov. « Negative Differential Resistance and Shapiro Steps in a Superconducting MoN Strip with a Cut ». *JETP Letters* 115.10 (2022), pp. 626–633 (cit. on p. 107).
- [Van Look, 1999] Lieve Van Look, Erik Rosseel, MJ Van Bael, Kristiaan Temst, VV Moshchalkov, and Yvan Bruynseraede. « Shapiro steps in a superconducting film with an antidot lattice ». *Physical Review B* 60.10 (1999), R6998 (cit. on pp. 95, 101).
- [Verma, 2021] V. B. Verma, B. Korzh, A. B. Walter, A. E. Lita, R. M. Briggs, M. Colangelo, et al. « Single-photon detection in the mid-infrared up to  $10 \mu\text{m}$  wavelength using tungsten silicide superconducting nanowire detectors ». *APL Photonics* 6.5 (2021), p. 056101 (cit. on p. 33).
- [Vetter, 2016] Andreas Vetter, Simone Ferrari, Patrik Rath, Rasoul Alaei, Oliver Kahl, Vadim Kovalyuk, et al. « Cavity-Enhanced and Ultrafast Superconducting Single-Photon Detectors ». *Nano Lett.* (2016), p. 8 (cit. on p. 32).
- [Vinnikov, 2003] L Ya Vinnikov, J Karpinski, SM Kazakov, J Jun, J Anderegg, SL Bud'ko, et al. « Bitter decoration of vortex structure in  $\text{MgB}_2$  single crystals ». *Physica C: Superconductivity* 385.1-2 (2003), pp. 177–179 (cit. on p. 10).
- [Vinokur, 1995] VM Vinokur, PH Kes, and AE Koshelev. « The 2D collective creep exponents reconsidered ». *Physica C: Superconductivity* 248.1-2 (1995), pp. 179–184 (cit. on p. 75).
- [Vishik, 2018] I. M. Vishik. « Photoemission Perspective on Pseudogap, Superconducting Fluctuations, and Charge Order in Cuprates: A Review of Recent Progress ». *Rep. Prog. Phys.* 81.6 (2018), p. 062501 (cit. on p. 24).
- [Vodolazov, 2012] D Yu Vodolazov. « Saddle point states in two-dimensional superconducting films biased near the depairing current ». *Physical Review B* 85.17 (2012), p. 174507 (cit. on p. 46).
- [Vodolazov, 2007] D Yu Vodolazov and FM Peeters. « Rearrangement of the vortex lattice due to instabilities of vortex flow ». *Physical Review B* 76.1 (2007), p. 014521 (cit. on p. 54).
- [Vodolazov, 2017] D. Yu. Vodolazov. « Single-Photon Detection by a Dirty Current-Carrying Superconducting Strip Based on the Kinetic-Equation Approach ». *Physical Review Applied* 7.3 (2017), p. 034014 (cit. on p. 34).
- [Weber, 1991] Andreas Weber and Lorenz Kramer. « Dissipative states in a current-carrying superconducting film ». *Journal of low temperature physics* 84 (1991), pp. 289–299 (cit. on p. 54).
- [Wells, 2015a] Frederick S Wells, Alexey V Pan, X Renshaw Wang, Sergey A Fedoseev, and Hans Hilgenkamp. « Analysis of low-field isotropic vortex glass containing vortex groups in  $\text{YBa}_2\text{Cu}_3\text{O}_{7-x}$  thin films visualized by scanning SQUID microscopy ». *Scientific reports* 5.1 (2015), p. 8677 (cit. on p. 11).
- [Wells, 2015b] Frederick S. Wells, Alexey V. Pan, X. Renshaw Wang, Sergey A. Fedoseev, and Hans Hilgenkamp. « Analysis of Low-Field Isotropic Vortex Glass Containing Vortex Groups in  $\text{YBa}_2\text{Cu}_3\text{O}_{7-x}$  Thin Films Visualized by Scanning SQUID Microscopy ». *Sci Rep* 5.1 (2015), p. 8677 (cit. on p. 26).
- [Winiiecki, 2002] T. Winiiecki and C. S. Adams. « A Fast Semi-Implicit Finite Difference Method for the TDGL Equations ». *Journal of Computational Physics* 179.1 (2002), pp. 127–139. arXiv: [cond-mat/0106466](https://arxiv.org/abs/cond-mat/0106466) (cit. on pp. 84, 86).

- 
- [Wolf, 2013] Thomas Wolf, Nicolas Bergeal, Jérôme Lesueur, Coenrad J Fourie, Giancarlo Faini, Christian Ulysse, et al. « YBCO Josephson junctions and striplines for RSFQ circuits made by ion irradiation ». *IEEE Transactions on applied superconductivity* 23.2 (2013), pp. 1101205–1101205 (cit. on p. 48).
- [Wollman, 1993] D. A. Wollman, D. J. Van Harlingen, W. C. Lee, D. M. Ginsberg, and A. J. Leggett. « Experimental determination of the superconducting pairing state in YBCO from the phase coherence of YBCO-Pb dc SQUIDS ». *Physical Review Letters* 71.13 (1993), pp. 2134–2137 (cit. on p. 25).
- [Wu, 1987a] M. K. Wu, J. R. Ashburn, C. J. Torng, P. H. Hor, R. L. Meng, L. Gao, et al. « Superconductivity at 93 K in a New Mixed-Phase Y-Ba-Cu-O Compound System at Ambient Pressure ». *Physical Review Letters* 58.9 (1987), pp. 908–910 (cit. on p. 19).
- [Wu, 1987b] Maw-Kuen Wu, Jo R Ashburn, Clj Torng, Pei-Herng Hor, Rl L Meng, Lo Gao, et al. « Superconductivity at 93 K in a new mixed-phase Y-Ba-Cu-O compound system at ambient pressure ». *Physical review letters* 58.9 (1987), p. 908 (cit. on p. 3).
- [wwwmicroresistde, 2022] www.microresist.de (2022) (cit. on p. 40).
- [Yuzhelevski, 1999] Y Yuzhelevski and G Jung. « Artificial reversible and programmable magnetic pinning for high-Tc superconducting thin films ». *Physica C: Superconductivity* 314.3-4 (1999), pp. 163–171 (cit. on p. 107).
- [Zeldov, 1990] E Zeldov, NM Amer, G Koren, A Gupta, MW McElfresh, and RJ Gambino. « Flux creep characteristics in high-temperature superconductors ». *Applied physics letters* 56.7 (1990), pp. 680–682 (cit. on p. 75).
- [Zeldov, 1994] Eli Zeldov, AI Larkin, VB Geshkenbein, M Konczykowski, D Majer, B Khaykovich, et al. « Geometrical barriers in high-temperature superconductors ». *Physical Review Letters* 73.10 (1994), p. 1428 (cit. on p. 75).
- [Ziegler, 2004] J. F. Ziegler and J. P. Biersack. « The Stopping and Range of Ions in Matter IBM, New York » (2004) (cit. on p. 38).

## RÉSUMÉ

---

Les détecteurs de photons uniques basés sur des nanofils supraconducteurs à basse température ont déjà démontré d'excellentes propriétés et des performances remarquables dans diverses applications en dessous de 1K, allant de l'information quantique au test de circuits intégrés. Dans ce contexte, l'idée de créer un tel détecteur basé sur des supraconducteurs à haute température fonctionnant autour de 40 K est très séduisante. Cependant, la tâche s'avère difficile, non seulement en raison des obstacles technologiques liés à la fabrication de nanofils ultramincés, mais aussi en raison de la nature distincte de la supraconductivité dans ces matériaux.

Ce travail est divisé en deux parties : une étude expérimentale des caractéristiques de transport des nanofils YBCO et une étude numérique de l'influence du mouvement vortex sur les caractéristiques de transport des nanorubans supraconducteurs.

Dans la partie expérimentale, nous présentons la fabrication de nanofils supraconducteurs à l'aide de la technique d'irradiation ionique. Leur caractérisation par transport DC et RF a permis de démontrer le rôle de la dynamique des vortex sur les propriétés supraconductrices critiques.

Les observations expérimentales sont soutenues par notre étude numérique, développée spécifiquement pour la géométrie de notre système et consacrée aux effets du mouvement vortex d'Abrikosov sur les propriétés de transport. Dans le cadre de la théorie de Ginzburg-Landau dépendante du temps, nous avons confirmé les signatures de la synchronisation des vortex conduisant à l'apparition de marches de Shapiro fractionnaires et, dans un paysage de désordre spécifique, cette synchronisation peut créer des états métastables dynamiques, observés dans nos nanofils supraconducteurs.

## MOTS CLÉS

---

Supraconducteurs, Cuprates, Nanofils, Simulations numériques, Ginzburg Landau dépendant du temps, Vortex Abrikosov

## ABSTRACT

---

Single-photon detectors based on low-temperature superconducting nanowires have already demonstrated excellent properties and remarkable performance in various applications below 1K, ranging from quantum information to integrated circuit testing. In this context, the idea of creating such a detector based on high-temperature superconductors operating around 40 K is highly appealing. However, the task is proving challenging not only due to technological barriers associated with the manufacture of ultra-thin nanowires but also because of the distinct nature of superconductivity in these materials.

This work is divided into two parts: an experimental study of the transport characteristics of YBCO nanowires, and a numerical study of the influence of vortex motion on the transport characteristics of superconducting nanostripes.

In the experimental part, we present the fabrication of superconducting nanowires using the ion irradiation technique. Their characterisation by DC and RF transport has enabled demonstrating the role of the vortex dynamics on critical superconducting properties.

The experimental observations are supported by our numerical study, developed specifically for the geometry of our system and devoted to the effects of Abrikosov vortex motion on the transport properties. Within the framework of the time-dependent Ginzburg-Landau theory, we have confirmed the signatures of vortex synchronisation leading to the appearance of fractional Shapiro steps. Moreover, in a specific disorder landscape, this synchronisation can create dynamic metastable states, leading to phenomena experimentally observed in the studied nanowires.

## KEYWORDS

---

Superconductivity, Cuprates, Nanowires, Numerical simulations, Time Dependent Ginzburg Landau, Abrikosov vortices